EFFECTIVE RESERVOIR MANAGEMENT USING STREAMLINE-BASED RESERVOIR SIMULATION, HISTORY MATCHING AND RATE ALLOCATION OPTIMIZATION

A Dissertation

by

SHUSEI TANAKA

Submitted to the Office of Graduate and Professional Studies of
Texas A&M University
in partial fulfillment of the requirements for the degree of

DOCTOR OF PHILOSOPHY

Chair of Committee,	Akhil Datta-Gupta
Committee Members,	Michael J. King
	Eduardo Gildin
	Yalchin Efendiev
Head of Department,	A. Daniel Hill

December 2014

Major Subject: Petroleum Engineering

ABSTRACT

The use of the streamline-based method for reservoir management is receiving increased interest in recent years because of its computational advantages and intuitive appeal for reservoir simulation, history matching and rate allocation optimization. Streamline-based method uses snapshots of flow path of convective flow. Previous studies proved its applicability for convection dominated process such as waterflooding and tracer transport. However, for a case with gas injection with strong capillarity and gravity effects, the streamline-based method tends to lose its advantages for reservoir simulation and may result in loss of accuracy and applicability for history-matching and optimization problems.

In this study, we first present the development of a 3D 3-phase black oil and compositional streamline simulator. Then, we introduce a novel approach to incorporate capillary and gravity effects via orthogonal projection method. The novel aspect of our approach is the ability to incorporate transverse effects into streamline simulation without adversely affecting its computational efficiency. We demonstrate our proposed method for various cases, including CO_2 injection scenario. The streamline model is shown to be particularly effective to examine and visualize the interactions between heterogeneity which resulting impact on the vertical and areal sweep efficiencies.

Next, we apply the streamline simulator to history matching and rate optimization problems. In the conventional approach of streamline-based history matching, the objective is to match flow rate history, assuming that reservoir energy was matched

already, such as pressure distribution. The proposed approach incorporates pressure information as well as production flow rates, aiming that reservoir energy are also reproduced during production rate matching.

Finally, we develop an NPV-based optimization method using streamline-based rate reallocation algorithm. The NPV is calculated along streamline and used to generate diagnostic plots of the effectiveness of wells. The rate is updated to maximize the field NPV. The proposed approach avoids the use of complex optimization tools. Instead, we emphasize the visual and the intuitive appeal of streamline methods and utilize flow diagnostic plots for optimal rate allocation.

We concluded that our proposed approach of streamline-based simulation, inversion and optimization algorithm improves computational efficiency and accuracy of the solution, which leads to a highly effective reservoir management tool that satisfies industry demands.

ACKNOWLEDGEMENTS

I would like to express my sincere gratitude to my committee chair, Dr. Datta-Gupta for his academic guidance and financial support throughout the course of this research. I would also like to extend my sincere appreciation to my co-chair, Dr. King, for the kind advice to advance and improve my research. I would also like to extend my appreciation to Dr. Gildin, Dr. Efendiev and Dr. Nasrabadi for their thoughtful discussions and suggestions that improved the contents of this dissertation.

Thanks also go to MCERI alumni and current students for their mentorship, partnership and friendship throughout my study life.

Finally, thanks to my family for their support.

TABLE OF CONTENTS

Page

LIST OF FIGURES

Page

LIST OF TABLES

Page

CHAPTER I

INTRODUCTION

The quality of reservoir performance prediction depends upon the reliability of the geological models and the methodology adopted for numerical simulation. As the surveillance technology advances, the resolution of the geological model increases. Also, as we understand the detailed process of the fluid transport, the system of equations gets difficult to solve. Thus, the demand of the computer resources and power increases exponentially as time goes. The unknown variable was up to thousand in the 1950s, however, it is common to use over a million grid cells to describe the reservoir in recent years. This means that the reservoir management process, not only reservoir simulation but also history matching and optimization process needs to handle high resolution geological models efficiently. This chapter identifies the problems related to reservoir management in large scale field operations and describes the challenges regarding this problem. Then, we describe the objective of this study.

1.1 Statement of the Problem

The main objective of a reservoir engineer is to provide a plan to maximize oil and gas recovery from a reservoir by controlling the well while reducing risk and uncertainty at the same time. All of the steps through the reservoir management process require simulation for the forecasting of future production rate under the current estimated geological model. These processes are now largely automated and quick response is required to consider the dynamical change of the asset. However, the process tends to

become complicated as the number of well and production history increases, in addition to the geological information. The reservoir management process requires a number of simulations. However, it is not possible to complete the simulations in time with multimillion cell problem.

Often the detailed distribution of reservoir property, such as permeability and porosity, is upscaled to reduce the number of grid cells and to increase computational efficiency while attempting to preserve the production profile of the original geological model. This step helps to solve history matching and optimization problems with significant improvement in computational efficiency. However, there is an increasing attempt to conduct reservoir simulation on the actual geological scale or close to the seismic resolution model using non-traditional simulation methods, such as multiscale simulation with multicore processing (Atan, Kazemi, and Caldwell 2006). These approaches are expected to improve the reliability of production forecast by exploring multiple subsurface models and by capturing high contrast geological features such as fractures or facies structures. Streamline simulation is one of the candidates to perform reservoir simulation efficiently with such fine scale geologic models. The early development of streamline simulation was limited in its ability to describe flow physics such as compressibility and transverse fluxes such as gravity and capillary. These limitations have largely been resolved through the use of operating splitting techniques (Bratvedt, Gimse, and Tegnander 1996, Berenblyum *et al.* 2003, Jessen and Orr 2004). In addition to that, the method can be applied to the dual-continuum models or to compositional models (Crane *et al.* 2000, Di Donato, Huang, and Blunt 2003).

Although streamline-based simulation is applicable for the majority of field applications, there are still difficulties with highly nonlinear problems. This problem is mainly caused by the decoupling of the system of the equations into several pieces, such as pressure equation, convection equation and transverse flux (Datta-Gupta and King 2007). Because of this aspect, problems with high mobility contrast as well as strong capillarity and gravity limit the time step size, and undermining the computational advantages of the streamline based method. In other words, the streamline simulation is accurate for linear processes, but as level of the non-linearity increases, the solution loses its accuracy with increasing of time step lengths. The EOR processes with WAG, chemical injection create highly nonlinear problems and have been applied in many field (Stoll *et al.* 2011, Brodie *et al.* 2012). Hence, it is highly desired to formulate a novel approach which attains the large time step without losing the accuracy of the solution. This will provide not only computational advantages of streamline-based simulation for highly nonlinear processes, but also give insights into the further applications such as history matching and optimization problems.

In addition, not only reservoir simulation but also the reservoir management becomes difficult with multimillion grid cell models having a large number of wells and long term production data. For the history matching with large number of cells, it is common to define regions which describe compartments of the reservoir (Sahni and Horne 2005) and change static properties manually or in an automated fashion using stochastic algorithms. One may often find after history matching that a certain number of wells do not match the historical data. This often occurs in reservoirs with displacement

processes like waterfloods, where inter-well properties are important in determining production history. In this case, changing the static properties of the reservoir between injector and producer pairs is an efficient approach to calibrate production result. However, it is difficult to locate the regions where inter well flow is involved. In addition, one needs to identify how much static properties need to be changed. Typically, the inter well regions are chosen subjectively and then the static parameter is changed manually. Although this may result in a history match, it often loses geological consistency. One might be able to set a large number of model parameters, however, it results in a significant computational expense for deriving sensitivities of model parameters to production response to calibrate geological parameter.

Finally, the allocation of the flow rate of the injector and producer is another important aspect of the overall development strategy of a field. Because the reservoirs are heterogeneous and often described by complicated geology, the choice of uniform, constant injection rate will not be the best approach to recover the hydrocarbon from the field. The optimal injection/production scenario is required for individual project considering geology, dynamic well performance and operation constraints. Forecasting of the performance of an EOR process and finding ways to get a quick quantitative estimation of the performance is key to achieving this goal. This is particularly challenging for large mature fields with a number of injector and producer well set. Prudhoe bay, Alaska, for an example, has over one thousand of wells with 30 years of the production history. The focus of the optimization is wide and complicated, such as defining a life of the well from design to abandonment (Anders *et al.* 2008). As in most

of the field application, the solution space of the optimization problem is large and constrained, the applicable algorithms for the optimization process is limited. For instance, it is feasible for a stochastic algorithm to make a plan of the schedule of all the wells existing in a field but requires fast and robust simulators to evaluate the quality of the well and propose better option.

1.2 Motivation and Challenges of the Study

The integrated work flow of the streamline-based simulation, history-matching and rate allocation study can be found in many papers (Agarwal and Blunt 2001, Thiele and Batycky 2003, Watanabe *et al.* 2013). The essential idea of the streamline-based method is founded on capturing the convective flow pattern by streamlines. For reservoir simulation, we solve 1D flow equation along these lines. For history-matching or optimization, streamline property or pattern is used to find the sensitivity of model parameter to production information (Aziz and Settari 1979, Wen, Deutsch, and Cullick 1998, Datta-Gupta 2000, Wang and Kovscek 2000). Although the advantages of the streamline-based methods are mainly discussed in previous studies, we have limitations, however. The main limitation for streamline is caused by linearization of the nonlinear problem. In other words, we generate set of 'snapshot' out of the nonlinear problem assuming that some parameters are constant through that snapshot period. Thus, once the problem gets highly nonlinear, it is difficult to apply the streamline-based approach. This is the main reason why the streamline-based method is often used for waterflooding, but it is difficult to apply to multicomponent gas injection scenario. Many processes of oil and gas recovery involve transfer of fluid components between the phases, which causes

the fluid properties to be dependent on phase compositions and pressure. Such processes are highly nonlinear, and thus multiple pressure and streamline update is required. In addition, simulation of these processes requires solution of the flow equation associated with phase equilibrium calculations (Coats 1980, Nghiem, Fong, and Aziz 1981) which are computationally expensive. Streamline models for compositional simulation model with transverse effects are yet to be improved, particularly keeping computational efficiency while retaining accurate solution.

Also, the 'snapshot' describes the convective flow and transverse effect is not taken into account. Several previous studies have discussed the incorporation of transverse flux such as capillarity and gravity for streamline simulation, by operator splitting method. Using their approach, transverse mechanisms are resolved using two sets of spatial discretization. The operator splitting of transverse flow occurs on the three dimensional simulation grids, right after we solve the convective processes along the streamlines. This solution is accurate for linear processes, but as non-linearity increases, the solution deteriorates for large time step lengths. The improved operator-splitting with correction term has also been studied by several authors (Holden, Karlsen, and Lie 2000, Karlsen *et al.* 2001, Karlsen and Espedal 2007). The basic idea to improve the operator-splitting approach is to take into account the unphysical entropy loss produced by the hyperbolic solver during the convective step. For reservoir simulation, this is done by introducing anti-diffusive concave envelope correction derived from the fractional flow equations (Datta-Gupta and King 2007). This self-sharpening effect provides unique solutions which satisfy the entropy condition, even for large time steps. However, this

approach has not been introduced into commercial streamline reservoir simulators because of the complexity in handling the concave envelope construction for general reservoir simulation. Hence, the solutions shown in the literature are for simple cases, such as 1-dimensional homogeneous model. The multidimensional heterogeneous cases are also described in some papers, however, the fluids are immiscible, rock and fluids are incompressible and the viscosity or mobility does not depend upon pressure. Once problems become more general, such as multiphase multicomponent miscible and compressible cases, this approach is not feasible because concave envelope becomes a function of pressure, temperature as well as the composition. Thus, the approach requires finding an anti-diffusive correction term for every grid during each time step of a simulation.

Integrating dynamic data into high-resolution reservoir models requires an efficient inverse problem. The number of simulation and amount of computational resources are limited in comparison and history matching often needs to be carried out with a small number of reservoir simulation. Typically, the stochastic method is often used to find the global parameter, and then a deterministic approach is used to update the fine scale static parameters. In the deterministic approach, the efficiency to find parameter sensitivities for production data is a key to conduct such high resolution reservoir model updating. In order to calculate parameter sensitivities, following approaches are used in common: perturbation methods, gradient-simulator methods (Anterion, Eymard, and Karcher 1989), and adjoint or optimal control methods (Chavent, Dupuy, and Lemmonier 1975, Li, Reynolds, and Oliver 2003). The gradient simulator method or adjoint method is

often used to achieve this since it requires the solution of a linear system and one additional forward simulation. Streamline based approaches has advantages compared with other approach. In this study, we present an algorithm based on streamline-based assisted data integration method.

The streamline-based data integration was first introduced for fast evaluation of reservoir-response sensitivities (Vasco, Seongsik, and Datta-Gupta 1999). The novelty of the streamline based approach is that it requires a single forward simulation with post-processing step to find parameter sensitivity by analytical formulation. In addition, generalized travel time inversion (GTTI) has been introduced (He, Yoon, and Datta-Gupta 2002) to combine travel time matching (Wu and Datta-Gupta 2002) and amplitude matching keeping the time-shift information as well as the magnitude of the response of the objective function. The GTTI minimizes the misfit function by maximizing the coefficient of determination of observed and calculated data. Because of this, the size of inverse matrix is reduced compared with full amplitude matching and thus it helps high resolution reservoir modeling and model updating.

Traditionally, the streamline based history matching is used to integrate water cut data, assuming that pressure data is integrated with prior model and the match is kept during the history matching process of water-cut. However, the posterior model often deteriorates pressure data match after the water cut matching by streamline based method. In order to prevent this issue, an iterative process is required to match pressure and water cut by combining stochastic algorithm and streamline-based inversion. However, this process is computationally expensive and tends to lose the advantage of

the streamline-based history matching process. Because of these reasons, it is highly desired to develop an algorithm to integrate pressure information during streamline-based flow rate history matching.

Streamline-based rate allocation optimization is getting popular because of visual based flow diagnostics and analytical sensitivity or derivative free optimization algorithm. The previous study (Thiele and Batycky 2003, Alhuthali, Oyerinde, and Datta-Gupta 2007) indicates that the streamline-based optimization method is robust and particularly suited for field scale water flooding with large amount of wells. The previous study of streamline based method maximizes oil production rate. This type of the objective function is quite applicable to waterflooding problem. However, one limitation is that streamline-based optimization does not explore setting the objective function as the Net Present Value (NPV). Instead, the algorithm often uses penalized misfit function to reduce the water production rate as well as accelerating oil production rate to improve NPV. One question is that if this penalized function can be generalized or not. In other words, it often requires subjective tuning factors for field study and may not be robust. Thus, the streamline-based optimization method should consider an alternative objective function such as NPV, in order to avoid these penalized factors. The challenge here is that we need to achieve this goal without losing the computational advantages presented by previous work. In other words, the proposed approach is able to diagnose NPV with streamline-based flux distribution. Also, the algorithm can be derivative free or able to calculate sensitivity analytically.

1.3 Research Objective and Thesis Outline

The main goal of this study is to develop streamline-based algorithms to make the process of reservoir simulation, history matching and optimization efficient and robust. Considering study background, the objective of this research is stated as follows.

First, we develop a general purpose streamline-based reservoir simulator. The simulator takes into account black oil and compositional models. Then, we propose a novel approach to incorporate capillarity and gravity along streamlines. The proposed method has computational advantages compared to conventional approaches in terms of larger time-stepping. With the introduction of the new approach with an iterative IMPES technique, it is now possible to take a large time step with highly nonlinear gas injection process with strong capillary and gravity effects.

Second, we apply the developed simulator for history-matching problems. The main objective is to integrate water cut response and bottom hole pressure data simultaneously. To achieve that, we derive the equation of pressure drop sensitivities with respect to reservoir properties along streamlines. Using this pressure sensitivity, we aim to reduce the average observation error of bottom hole pressure data through time as we do in water cut. This method has analogies with previous authors (Wang and Kovscek 2000, Milliken, Emanuel, and Chakravarty 2001) and more recently, Watanabe *et al.* (2013). Wang and Kovscek tried to match pressure and water cut using effective properties along streamline. The difference between their method and this approach is that we try to integrate production data based on parameter sensitivity calculations while their method utilizes property multipliers to adjust parameter to match effective

properties. Advantages of our method is that we do not use tuning factors while matching the production data while the use of effective properties require subjective parameters to reduce objective function smoothly and avoid overshoot through the iteration.

Last, we apply the developed model for rate allocation optimization problem. This study presents a new approach to optimize well injection/production rate allocation based on NPV and a flow diagnostic method. The proposed method measures reservoir flow dynamics quantitatively between injector/producer well pairs. The well-rate reallocation is conducted based on injection/production relative efficiencies derived from flow diagnostics. The method does not require an adjoint formulation and, thus, can be applied to any numerical simulator.

The main objectives of this research and corresponding chapters of this dissertation are as follows.

Chapter I: General introduction, problem statement and challenges of this study

Chapter II: Development of a streamline-based black oil and compositional simulator. Stating with the governing equations, the numerical scheme of the streamline-based simulation is discussed. The verification of the simulator is conducted based on the black oil system.

Chapter III: The application of the developed model. The inclusion of the transverse flux along streamline is highlighted. The application is shown in black oil and compositional models. A series of verification is conducted and field application is demonstrated.

Chapter IV: The application of the developed simulator for history-matching problems. The new approach to including pressure data is described and the application is shown in synthetic models including the 3D Brugge benchmark field.

Chapter V: Develop an NPV-based rate optimization method. The proposed approach is demonstrated using a series of numerical experiments, including the Brugge benchmark case. The results are compared with the non-NPV-based optimization methods that have been previously proposed. Overall, the proposed method results in greater economic value than the non-NPV-based methods and is easily incorporated into a variety of reservoir modeling applications.

Chapter VI: States conclusion of this study and future work.

CHAPTER II

DEVELOPMENT OF A GENERAL PURPOSE STREAMLINE-BASED RESERVOIR SIMULATOR*

2.1 Chapter Summary

This chapter discusses the general background of streamline simulation. Then, starting from governing equation, we derive the pressure and flow equations for streamline-based simulation of three phase black oil and general multicomponent compositional system. We also describe how to incorporate the compressibility effect into the streamline simulation in addition to discretization techniques for space and time. Then we demonstrate our approach using a series of synthetic cases, including the SPE10 and Brugge waterflooding benchmark. The demonstration of the model for black oil model and compositional simulations will be discussed in the next chapter including capillarity.

2.2 Literature Review

Streamline approach was first applied in the study of well patterns and total recovery by Muskat and Wyckoff (1934). Muskat used electrical conduction models to simulate different well configuration and defined streamlines based on equipotential surfaces. The reservoir was considered to be homogeneous and tracer-flow assumptions were used in the calculations. From their research Muscat and Wyckoff concluded that channeling

*Part of the data reported in this chapter is reprinted with permission from "Effects of Oil Compressibility on Production Performance of Fractured Reservoirs Evaluated by Streamline Dual-Porosity Simulation" by Tanaka, S., Arihara, N. and Al-Marhoun, M. A. 2010: Paper SPE-130397-MS Presented at the SPE EUROPEC/EAGE Annual Conference and Exhibition, 14-17 June, Barcelona, Spain. Copyright 2014 Society of Petroleum Engineers

along high-permeability zones within the main sand body was the dominant factor in the ultimate recovery more so than the well spacing and pattern. Muskat continued his research on the use of streamlines for two-dimensional problems using the potential-theory method (Muskat and Wyckoff 1937).

The use of streamtube in two phase flow was first introduced by Higgins and Leighton (1962). The reservoir was assumed homogeneous in these calculations. The method consisted of dividing the streamtubes into elements of equal volume. Average mobility and geometric shape factors were calculated for each element, and the total resistance along each streamtube was used to calculate the total flow rate for each streamtube.

Parsons (1972) introduced the concept of time-of-flight along the streamlines while modeling a reservoir with anisotropic permeability. Time-of-flight was defined as the time which a particle travels from an injection point to a sink or production point, and it was different for each streamline. The time-of-flight is directly related to the reservoir heterogeneity, and accounts for the reservoir driving forces at the time the velocity field is calculated.

Bommer and Schechter (1979) solved the transport equations for modeling the in-situ uranium leaching using a one-dimensional, finite-difference formulation along streamlines. With this approach, they were able to account for chemical reactions and physical diffusion in the main direction of flow while accounting for the relevant physics of the leaching process.

Using physical data from laboratory experiments, Lake, Johnston, and Stegemeier (1981) modeled flow in the vertical cross-section for polymer flood using streamlines. They introduce the concept of decoupling the vertical response from the areal one in the polymer/surfactant displacement. The areal flow, as assumed by Lake *et al*., was influenced by well pattern, whereas the vertical flow was dependent on the reservoir rock property variations and type of displacement.

Pollock (1988) incorporated a particle-tracking algorithm that uses a simple linear interpolation of the velocity field vector to create three-dimensional streamlines. Pollock's algorithm has been widely used in most streamline simulation models because of its simplicity and accuracy. Also, his algorithm produces streamlines that are emanated from an injector well and terminated on a producer based on the velocity field in the reservoir. In this method a large number of cells could be found in many regions without a streamline going through the regions, because the pressure gradient in these regions is small.

Since the key concept was established until 1990, streamline simulators have received increased attention in the petroleum industry.

Bratvedt *et al.* (1992) introduced a front-tracking approach into the streamline method, which derives analytic solution for streamline one-dimensional saturation equation by the Buckley-Leverett concept. They also introduced an operator splitting technique into the streamline concept in order to describe gravity effect (Bratvedt, Gimse, and Tegnander 1996), which decouples gravity, and transfer term.

Datta-Gupta and King (1995) used the time-of-flight for fluid transport as one-dimensional flow equation instead of two-dimensional fluid transport equations. Their model showed significant reduction of computation time in comparisons with the conventional finite difference method, and also appealed the advantage of less numerical dispersion and grid orientation effects.

Batycky, Blunt, and Thiele (1997) introduced a three-dimensional streamline-based fluid flow simulator. This simulator accounted for the effects of changing well conditions as well as gravity for incompressible multiphase flow. Also they introduced a 3D field-scale compositional reservoir simulator based on streamline concept, and demonstrated its applicability. Their model treated fluid transfer and phase equilibrium on streamlines, with fluid compressibility and volume change on mixing by "dimensionless distance" which was derived from fluid velocity on streamlines.

Ponting (1998) addressed the limitations of the streamline technology, particularly numerical balance errors and rate allocations. Streamline modeling is not a conservative formulation; therefore, material balance errors are inherent in this approach. On the other hand most finite difference methods use conservative formulations where material balance is honored.

Ingebrigtsen, Bratvedt, and Berge (1999) introduced a three-phase streamline simulator which addressed the issues of multiphase flow as well as compressibility effects on streamlines. Two different methods were presented in the paper to solve the three-phase flow along the streamlines. The first one was a sequential method, which adjusts pressure-volume relations during saturation calculation on streamlines. The

second method solved for pressure and saturation simultaneously. This method allowed a consistent material balance within the streamlines.

Fundamentally, there should be no crossflow across streamlines. On the other hand, for mathematical convenience gravity and capillary forces have been dealt with in the streamline models by means of operator splitting techniques reported by several authors (Berenblyum *et al.* 2003, Jessen and Orr 2004, Rodriguez, Segura, and Moreno 2003). Rodriguez, Segura, and Moreno (2003) proposed to modify the streamline pressure equations to account for both capillary and gravity forces directly. The modified pressure equations were solved on the finite difference grid and velocities were back calculated from the solution including the gravity and capillary forces as well.

Di Donato, Huang, and Blunt (2003) presented a streamline-based dual-porosity simulator to model waterflooding in fractured reservoirs. Streamlines were traced through the fracture, and the transfer flow from the matrix to fracture region was modeled as a sink/source term on the streamline with operator splitting technique. They also introduced three forms of the transfer function: the conventional steady-state model and two linear transfer functions that match experimental measurements on cores. Their study revealed that an appropriate linear transfer function gives results similar to the conventional non-linear model with efficient computational time.

Al-Harbi *et al.* (2005) introduced streamline-based fractured reservoir simulation based on the dual-media approach. The fractures and matrix were treated as separate continua that are connected through a transfer function. While they modeled the dual-

porosity dual-permeability formulation based on streamline, the problem remained regarding stable time-stepping control for transfer function.

Although several authors have studied fractured reservoir simulation based on streamlines, most of the studies have been done on 2-phase incompressible flow. Moreno, Kazemi, and Gilman (2004) modeled a dual-porosity model for oil-gas and water-oil flow and Kozlova *et al.* (2006) modeled a dual-porosity model for three phase flow. The model proposed by Kozlova *et al* included fluid compressibility by the effective density idea with implicit streamline formulation (Andrianov, Bratvedt, and Myasnikov 2007) on saturation solver. Their model showed good agreement with the conventional finite difference method and reduced computation time.

The other aspect of the streamline-based method is that it is possible to identify well to well connections with flow distributions, apply history-matching techniques and optimize flow patterns and production profiles simultaneously (LeBlanc and Caudle 1971). In addition to this, streamline-based simulation has been applied to model ranking such as screening of geologic model to reduce number of realizations, upscaling from detailed geologic models to flow models of coarser grids (Stenerud *et al.* 2008), analyzing tracer tests (Iino, Arihara, and Okatsu 2006) and assessing the efficiency of waterflooding (Alhuthali, Oyerinde, and Datta-Gupta 2007, Iino and Arihara 2007, Thiele and Batycky 2003). The details are discussed in the following chapters related to the application of history-matching and optimization.

2.3 Mathematical Model

2.3.1 Mass and Momentum Balance Equation

The fundamental principle that underlies flow in a porous medium is conservation of mass. The amount of a component present at any location is changed by the motion of fluid with varying composition through the porous medium. Thus, the first issue to be faced in constructing a model of a flow process is to define and describe the flow mechanisms that contribute to the transport of each component. The components move due to following phenomena:

1. *Convection*: the movement of components within a permeable medium.
2. *Accumulation*: the total amount of mass due to immobilization or adsorbed components.
3. *Sink/source*: the total amount of injected/produced fluid components.

In this chapter, the differential equations solved in the subsequent chapters are derived and assumptions are discussed, which are required to reduce the equation of the general material balance to the special cases considered in this study. The major assumptions addressed first are that neither the effects of chemical reactions are included in the flow problems considered here, nor adsorption or temperature variation.

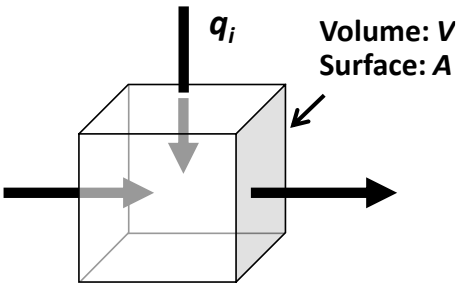

Figure 2.1: Flow path in a cell.

Consider an arbitrary volume, *V*, of the porous medium bounded by a surface, *A* shown in Figure 2.1. If there is no dispersion or diffusion, the material balance on component *i* in the control volume can be stated as by following (Bird and Stewart 1960),

$$\frac{\partial}{\partial t}\int_V M_i dV = -\int_\Gamma \mathbf{F}_i \bullet \mathbf{n} dA + \int_V q_i dV \quad \cdots\cdots\cdots\cdots\cdots\cdots\cdots\cdots\cdots\cdots \quad (2.1)$$

where *M* stands for accumulation of the component, **F** and **n** are flux and inward unit normal vector, and *q* is component flux by sink/source. The equation states that the rate at which the amount of component *i* in *V* changes is exactly balanced by the net inflow of component *i* carried with the flow of each phase (referred as *convection*) and the net inflow that arises from production and injection by well or boundary structure. This can be written as follows

$$\begin{bmatrix}\text{Rate of change in}\\ \text{amount of component}\\ i \text{ in } V\end{bmatrix} = -\begin{bmatrix}\text{Net rate of inflow}\\ \text{of component } i \text{ into } V\\ \text{due to flow of phases}\end{bmatrix} + \begin{bmatrix}\text{Net rate of inflow}\\ \text{due to sink/source}\\ \text{flow } q\end{bmatrix} \quad \cdots\cdots \quad (2.2)$$

Accumulation Term

The amount of phase *j* present in a differential element of volume in a cell is:

$$\left\{\begin{array}{c}\text{Moles of}\\ \text{phase } j \text{ in a cell}\end{array}\right\} = \phi\rho_j S_j V \quad \cdots\cdots\cdots\cdots\cdots\cdots\cdots\cdots\cdots\cdots\cdots\cdots \quad (2.3)$$

where ϕ is the porosity, and ρ_j and S_j are the molar density and saturation of phase *j*, respectively. The amount of the component *i* present in phase *j* is:

$$\left\{\begin{array}{c}\text{Moles of}\\ \text{component } i\\ \text{in phse } j \text{ in a cell}\end{array}\right\} = \phi y_{ij}\rho_j S_j V \quad \cdots\cdots\cdots\cdots\cdots\cdots\cdots\cdots\cdots\cdots\cdots\cdots \quad (2.4)$$

where y_{ij} is the mole fraction of component *i* in phase *j*. The total amount of component *i* present in volume *V* is obtained by summing over the n_p phases present, which gives:

$$\left\{\begin{array}{c}\text{Total moles of}\\ \text{component}\\ i \text{ in a cell}\end{array}\right\} = \phi\sum_{j=1}^{n_p} y_{ij}\rho_j S_j V \quad \cdots\cdots\cdots\cdots\cdots\cdots\cdots\cdots\cdots\cdots\cdots\cdots \quad (2.5)$$

Thus, the total accumulation in a volume, *V*, is described as follows:

$$\left\{\begin{array}{c}\text{Rate of change}\\ \text{in moles}\\ \text{of component } i \text{ in } V\end{array}\right\} = \frac{\partial}{\partial t}\int_V M^i dV = \frac{d}{dt}\phi\sum_{j=1}^{n_p} y_{ij}\rho_j S_j V \quad \cdots\cdots\cdots\cdots\cdots\cdots \quad (2.6)$$

Convection Term

At any differential element of area, the convective molar flux (moles per unit area/unit time) of component *i* in the phase *j* is shown as:

$$\left\{\begin{array}{c}\text{Molar flux of}\\ \text{component } i\\ \text{in phase } j\end{array}\right\} = y_{ij}\rho_j\vec{u}_j \quad \cdots\cdots\cdots\cdots\cdots\cdots\cdots\cdots\cdots\cdots\cdots\cdots \quad (2.7)$$

where $\vec{u}_j$ is the Darcy flow velocity of phase *j*, the volume of phase *j* flowing per unit area of porous medium per unit time. Here we assume that the flux vector may be normal to the surface, *A*, and hence the magnitude of the vector component of the flow crossing the surface is:

$$\left\{\begin{array}{l}\text{Net rate of inflow}\\ \text{of component } i \text{ by}\\ \text{convection}\end{array}\right\} = -\int_{\Gamma}\mathbf{F}\bullet\mathbf{n}dA = -\sum_{j=1}^{n_p} y_{ij}\rho_j\vec{u}_j A \quad \cdots\cdots\cdots\cdots\cdots\cdots \quad (2.8)$$

Sink/source Term

The mass change from injection/production must be taken into account of the mass conservation law. Define $\tilde{q}$ as sink/source fluid molar rate per unit time and unit volume, the mole change in a cell due to well flow is described as follows:

$$\left\{\begin{array}{l}\text{Net rate of inflow}\\ \text{of component } i\\ \text{due to sink/source}\end{array}\right\} = \int_V q^i dV = \sum_{j=1}^{n_p} y_{ij}\tilde{q}_j V \quad \cdots\cdots\cdots\cdots\cdots\cdots\cdots\cdots \quad (2.9)$$

where $\tilde{q}$ <0 for production and $\tilde{q}$ >0 for injection.

Continuity Equation

The accumulation, convection and sink/source terms can be combined to yield an integral material balance for a component *i* as:

$$-\sum_{j=1}^{n_p} y_{ij}\rho_j \vec{u}_j A + \sum_{j=1}^{n_p} y_{ij}\tilde{q}_j V = \frac{d}{dt}\phi \sum_{j=1}^{n_p} y_{ij}\rho_j S_j V \quad \cdots\cdots\cdots\cdots\cdots\cdots\cdots\cdots \quad (2.10)$$

Eq. 2.10 is the mole-rate balance of the component *i* in the control volume *V*. If information about the spatial distribution of component *i* is needed, then a differential material balance known as the continuity equation must be divided. Here, we assume that phase vector $\vec{v}$ is constant at each grid surface. In addition, because the integral of accumulation and convection becomes zero everywhere, each equation can be divided by control volume *V*. Hence the final form of the continuity equations for multicomponent, multiphase flow becomes as follows by using divergence operation

$$-\nabla \bullet \sum_{j=1}^{n_p} y_{ij}\rho_j \vec{u}_j + \sum_{j=1}^{n_p} y_{ij}\tilde{q}_j = \frac{d}{dt}\phi \sum_{j=1}^{n_p} y_{ij}\rho_j S_j \quad \cdots\cdots\cdots\cdots\cdots\cdots\cdots\cdots \quad (2.11)$$

To compute specification of the flow problem, a number of additional functions and conditions must be available. The flow velocity is the most important part of Eq. 2.11 yet to be determined, because it controls the connective part of the flow. In principle, this term is derived by momentum balance equation. In practice, however, the solutions of the resulting Navier-Stokes equation for the detailed velocity distributions are not required for the reservoir simulation and impractical for computational aspect. Instead, an averaged version of the momentum equations is used. For fluid flow through porous medium, volume averaging of the momentum equations yields a form equivalent to Darcy's law, which describe that the local flow velocity is proportional to the pressure gradient. Considering the flow of multiphase problem, the each flow velocity of a phase *j* is assumed to be given by:

$$\vec{u}_j = -\frac{kk_{rj}}{\mu_j}\left(\nabla p_j - \rho_{mj} g \nabla D\right) \quad \cdots\cdots\cdots\cdots\cdots\cdots\cdots\cdots\cdots\cdots\cdots\cdots \quad (2.12)$$

where k is permeability, and k_{rj}, μ_j, ρ_{mj}, and p_j are relative permeability, viscosity, mass density, and pressure of phase j, respectively. The phase subscript, j, on the pressure in Eq. 2.12 implies that the pressure is different in different phases. The relationships between these pressures are always assumed to be represented by capillary pressure functions.

2.3.2 Constraint Equation

Recall that the governing equation can be described as follows using Darcy's law.

$$\sum_{j=1}^{n_p}\left[\frac{\partial}{\partial t}\left(\phi y_{ij}\rho_j S_j\right) + \nabla \bullet \left(y_{ij}\rho_j \vec{u}_j\right) - y_{ij}\tilde{q}_j\right] = 0$$

The governing equation describes n_c (number of components) conservation equations for a reservoir domain with unknown variables such as pressure, saturation for n_p phases, and $n_p \times n_c$ mole fractions. In addition, the constraint equations for each component and phases can be established. The remaining equations which complete the description of arbitrary phases with arbitrary components are obtained from:

1. Capillary pressure relations: n_p-*1* equations

$$\begin{aligned} P_{c,ow} &= p_o - p_w \\ P_{c,go} &= p_g - p_o \end{aligned} \quad \cdots\cdots\cdots\cdots\cdots\cdots\cdots\cdots\cdots\cdots\cdots\cdots \quad (2.13)$$

2. Phase equilibrium relations: $n_c \times n_p$ equations

$$K_{ij} = y_{ij} / y_{jj} \quad \cdots\cdots\cdots\cdots\cdots\cdots\cdots\cdots\cdots\cdots\cdots\cdots \quad (2.14)$$

3. Phase constraints: n_p equations

$$\sum_{i=1}^{n_c} y_{i,j} = 1 \quad \cdots\cdots \quad (2.15)$$

4. Saturation constraint: 1 equation

$$\sum_{j=1}^{n_p} S_j = 1 \quad \cdots\cdots \quad (2.16)$$

2.3.3 Multicomponent Formulation

Here, we need to simplify the model because the mutual interaction of each phase with arbitrary components is quite difficult to handle using the equilibrium definitions. If we simplify the description of the multiple hydrocarbon components into two pseudo components, we handle 3 phases of oil, gas and water with mutual components of oil, gas and water. This assumption is quite common approach in the oil industry and called "black oil model".(Aziz and Settari 1979, Fagin and Stewart 1966). The mass balance equations and unknown variables of the general black oil equation becomes

$$\left.\begin{array}{l} \begin{pmatrix} S_o & S_g & S_w \\ p_o & p_g & p_w \end{pmatrix} \\ \begin{pmatrix} y_{oo} & y_{og} & y_{ow} \\ y_{go} & y_{gg} & y_{gw} \\ y_{wo} & y_{wg} & y_{ww} \end{pmatrix} \end{array}\right\} = 15 \text{ unknown variables} \quad \cdots\cdots \quad (2.17)$$

To solve for the above unknown variables, 15 equations must be derived. We have three mass-balance equations along with other equations as follows.

1. Capillary pressure relations: 2 equations

$$P_{cgo} = p_g - p_o$$
$$P_{cow} = p_o - p_w \quad \cdots\cdots (2.18)$$

2. Phase equilibrium relations: 6 equations

$$K_{go} = y_{go}/y_{oo}; \quad K_{wo} = y_{wo}/y_{oo}$$
$$K_{og} = y_{og}/y_{gg}; \quad K_{wg} = y_{wg}/y_{gg} \quad \cdots\cdots (2.19)$$
$$K_{gw} = y_{gw}/y_{ww}; \quad K_{ow} = y_{ow}/y_{ww}$$

3. Phase constraints: 3 equations

$$y_{oo} + y_{og} + y_{ow} = 1$$
$$y_{gg} + y_{go} + y_{gw} = 1 \quad \cdots\cdots (2.20)$$
$$y_{ww} + y_{wo} + y_{wg} = 1$$

4. Saturation constraint: 1 equation

$$S_o + S_g + S_w = 1 \quad \cdots\cdots (2.21)$$

5. Component conservation equation: 3 equations

$$\sum_{j=owg} \left[\frac{\partial}{\partial t} \left(\phi y_{ij} \rho_j S_j \right) + \nabla \bullet \left(y_{ij} \rho_j \vec{u}_j \right) - y_{ij} \tilde{q}_j \right] = 0$$

As we describe a three-phase black oil model above, however, the general three-phase mutual model is still not reasonable for practical applications, because the general three-phase flash computations can be quite complex and not efficient from computational aspect. Specifically, the water phase is usually composed with water component only, and the vaporized water is usually negligible in the hydrocarbon phases for isothermal problems.

$$\left.\begin{matrix} \begin{pmatrix} S_o & S_g & S_w \\ p_o & p_g & p_w \end{pmatrix} \\ \begin{pmatrix} y_{oo} & 0 & 0 \\ y_{go} & 1 & 0 \\ 0 & 0 & 1 \end{pmatrix} \end{matrix}\right\} = 8 \text{ unknown variables} \quad \cdots\cdots\cdots\cdots\cdots\cdots \quad (2.22)$$

The following are the corresponding 8 equations.

1. Capillary pressure relations: 2 equations

$$\begin{aligned} P_{cgo} &= p_g - p_o \\ P_{cow} &= p_o - p_w \end{aligned} \quad \cdots\cdots\cdots\cdots\cdots\cdots \quad (2.23)$$

2. Phase equilibrium relations: 1 equations

$$K_{go} = y_{go} / y_{oo} \quad \cdots\cdots\cdots\cdots\cdots\cdots \quad (2.24)$$

3. Phase constraints: 1 equations

$$y_{oo} + y_{go} = 1 \quad \cdots\cdots\cdots\cdots\cdots\cdots \quad (2.25)$$

4. Saturation constraint: 1 equation

$$S_o + S_g + S_w = 1 \quad \cdots\cdots\cdots\cdots\cdots\cdots \quad (2.26)$$

5. Component conservation equation: 3 equation

$$\sum_{j=owg} \left[\frac{\partial}{\partial t} \left(\phi y_{ij} \rho_j S_j \right) + \nabla \bullet \left(y_{ij} \rho_j \vec{u}_j \right) - y_{ij} \tilde{q}_j \right] = 0$$

2.3.4 Black Oil Formulation

Since the black-oil model is the simplified version of the compositional model, it is important to keep a clear definition of phases and components. In the black oil model,

the relationship between phases and components is simply defined by the volume of the reservoir and standard conditions.

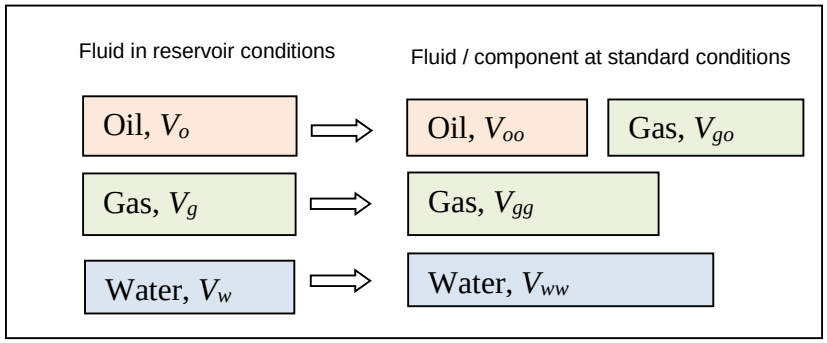

Figure 2.2: Fluid in standard conditions and reservoir conditions in black-oil system.

The V_α in Figure 2.2 stand for the volume of phase α at reservoir conditions, and $V_{i\alpha}$ is the volume of component i in phase α at standard conditions. Again, this study modeled the dissolved gas component in the oil phase, which is described by symbol V_{go} in Figure 2.2. The phase volume change and component mixing by pressure is defined by formation volume factor and solubility, respectively. The formation volume factor of phase α at some specified conditions to the volume of the component associated with that phase at standard conditions is defined as B_α as follows:

$$B_\alpha = 1/b_\alpha = V_\alpha / V_{i\alpha}\,; i, \alpha = owg \quad \cdots\cdots\cdots\cdots\cdots\cdots\cdots\cdots\cdots\cdots \quad (2.27)$$

In the compositional model, exchange of component between phases are found by *K*-value. For black-oil models, *K*-value are simplified functions of pressure which is

given by a solubility table for this study. The solubility of the component *i* in phase α, measured with respect to reference reservoir condition is defined as

$$R_{i\alpha} = V_{i\alpha} / V_{\alpha\alpha} \quad \cdots\cdots \quad (2.28)$$

With formation volume factor and solubility, the relationships for mass fraction and equilibrium ratios used in Eqs. 2.15-16 are shown as

$$\rho_\alpha y_{i\alpha} = \rho_\alpha^{stc} R_{i\alpha} b_\alpha \quad \cdots\cdots \quad (2.29)$$

Using Eqs. 2.27-29, we can rewrite Eq. 2.11 to the following black oil form

$$\sum_{j=owg} \left[\frac{\partial}{\partial t} \left(\phi R_{ij} b_j S_j \right) + \nabla \bullet \left(R_{ij} b_j \vec{u}_j \right) - q_j \right] = 0 \quad \cdots\cdots \quad (2.30)$$

where $q_j = \sum_i R_{ij} b_j \tilde{q}_j / \rho_j$. The black oil model here assumes immiscible oil and water, which makes $R_{oo,ww}$=1.0 and $R_{ow,wo,og}$=0.0. Thus the solubility is only gas component in the oil phase, $R_{go}=R_s$, the phase density is calculated as follows.

$$\rho_\alpha = b_\alpha \rho_\alpha^{stc}, \alpha = gw \quad \cdots\cdots \quad (2.31)$$

$$\rho_o = b_o \left(\rho_o^{stc} + \rho_g^{stc} R_s \right) \quad \cdots\cdots \quad (2.32)$$

2.4 Solution of Pressure Equation

The main objectives of the section is to verify the pressure equation derived in Appendix A for both black oil and compositional model by single phase single component system.

2.4.1 Pressure Equation

The final form of the pressure equation for IMPES method is shown below. The detailed description of the derivation of pressure equation is shown in Appendix A. For black oil model and compositional model, we get final form as:

$$\phi c_t \frac{\partial p_o}{\partial t} + \nabla p_o \sum_{j=ogw} c_j \vec{u}_j + \nabla \bullet \sum_{j=ogw} \vec{u}_j - \sum_{j=ogw} Q_j = 0 \quad \cdots\cdots\cdots\cdots\cdots\cdots\cdots \quad (2.33)$$

The objective of this section is to verify the above equation by single component single phase problem. The streamline tracing is not required to calculate production rate. The results are compared with commercial simulator and analytical solution as a reference.

2.4.2 Verification of Single Phase Model-Black Oil Model

To verify the pressure equation, numerical simulation is conducted by single component single phase problem. The main objective to verify the accuracy of the numerical simulation and compare the simulation results with analytical solution (Brown *et al.* 2011) and results by commercial numerical simulator. To test the developed pressure equation for the general case, a horizontal well with multiple transverse fracture case is prepared. Figure 2.3 shows the overview of the geological model and well configuration used for reservoir simulation.

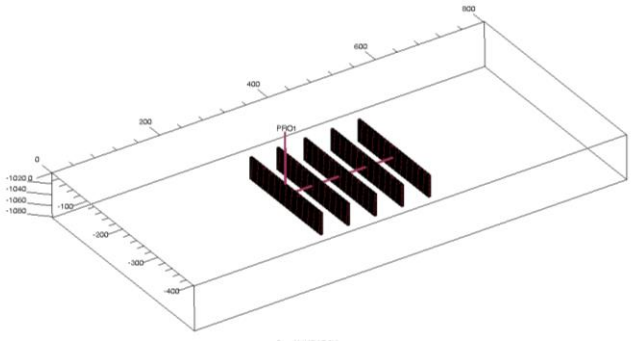

Figure 2.3: Reservoir and well geometry with multiple transverse fractures used for verification of pressure solver.

To describe the reservoir used in analytical solution, the reservoir model uses over 3 million grid blocks. The general information about this reservoir is summarized in Table 2.1 and 2.2.

Table 2.1: General parameters for numerical simulator

Parameters	Input Values
Dimensions	(nx,ny,nz) = (401,201,41)
Grid block size	(dx,dy,dz) = (2.0,2.0,2.0) [ft]
Reservoir dimension	(Dx,Dy,Dz) = (802,402,82) [ft]
Horizontal permeability	kx,ky = 0.001
Vertical permeability	kz = 0.0001
Porosity	0.05
Reservoir top depth	5000 [ft]
Initial pressure	5000 [psi] at 5000 [ft]
Rock compressibility	0.000001 [psi^{-1}]
Gas surface density	0.05508 [lb/cft]
Fluid PVT	Table input
Initial time step size	1 [second]
Maximum time step size	10 [days]
Time increment factor	1.20
Simulation period	10000 [days]

Table 2.2: Well/fracture parameters for numerical simulator		
Parameters	Input	Equivalent Values
Fracture porosity	0.001	0.5
Fracture width	2 grid block (4 [ft])	0.008 [ft] (4*0.001)
Fracture conductivity	-	100
Fracture half length	50 grids	100 [ft]
Number of fractures	5	5
Perf/Frac location 1	(151,101,21)	(301,201,41) [ft]
Perf/Frac location 2	(176,101,21)	(351,201,41) [ft]
Perf/Frac location 3	(201,101,21)	(401,201,41) [ft]
Perf/Frac location 4	(226,101,21)	(351,201,41) [ft]
Perf/Frac location 5	(251,101,21)	(401,201,41) [ft]
Well radius	0.3 [ft]	0.3 [ft]
Well constraint	BHP, 2000 [psi]	BHP, 2000 [psi]

The fracture parameters for numerical model can be non-unique to setup equivalent values used in analytical solution, such as fracture conductivity. This is because the analytical model does not have explicit fracture volume, but use dimensionless number. In order to keep consistency between numerical simulation and analytical solution, following assumptions are made:

- Actual fracture has 0.008 ft of width, with a porosity of 0.5.
- Use of 2 grid blocks to describe the width of the fracture, by assigning porosity of 0.001.
- Use of 10000 mD for fracture permeability, to have dimensionless fracture conductivity = 100.0.
- No anisotropy and heterogeneity in fracture domain.
- No hydraulic pressure loss or frictional pressure loss along horizontal well.

The PVT properties are given as tables in Appendix F. This is a black oil simulation and formation volume factor and viscosity is referred from pure methane component. The initial condition of the reservoir is single phase gas. The production rate is shown in Figure 2.4 below.

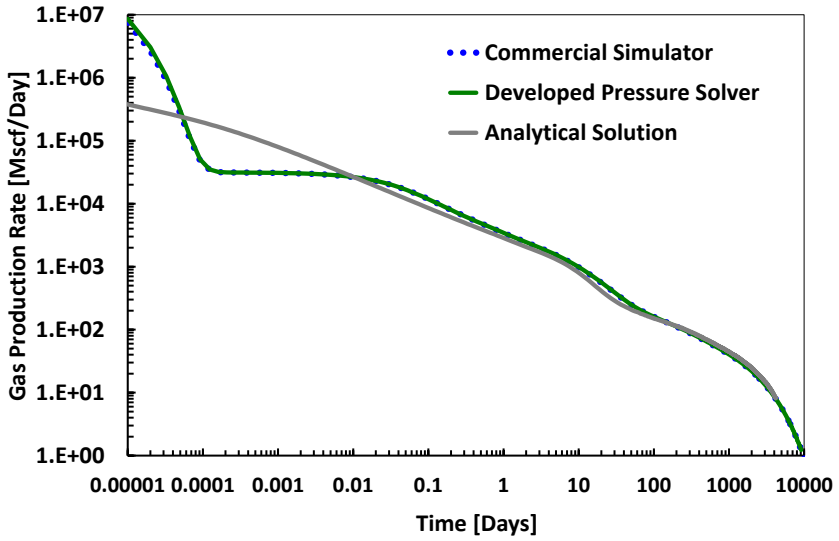

Figure 2.4: Production rate of multiple transverse fracture model. Black oil simulation with single component gas model.

The production rate of each hydraulic fracture is calculated by Peaceman's model shown in Appendix A in detail. The total gas production rate is displayed. As shown in Figure 2.4, the production rates of the developed model and commercial numerical simulation results showed good agreement. The analytical solution is following the same trend, however, showed differences at the beginning of the production period. This is because the numerical model is a full 3D model while the analytical solution does not

have gravity effect. In addition, the analytical solution does not include trilinear flow and cannot describe correctly at the beginning of the production period.

2.4.3 Verification by Single Phase Single Component EOS-based Simulation

The pressure equation is tested again using single component single phase EOS-based phase equilibrium model. The component is pure methane and PVT properties are calculated by Equation of State (Peng and Robinson 1976), viscosity by LBK model (Lohrenz, Bray, and Clark 1964) as shown in Appendix F. The critical properties are given to describe methane. The volumetric flow rate and molar rate of the well are calculated by (Nghiem, Fong, and Aziz 1981) as described in Appendix A. The production rate is compared with commercial Equation-of-State simulator (Schlumberger, E300) shown in Figure 2.5 below.

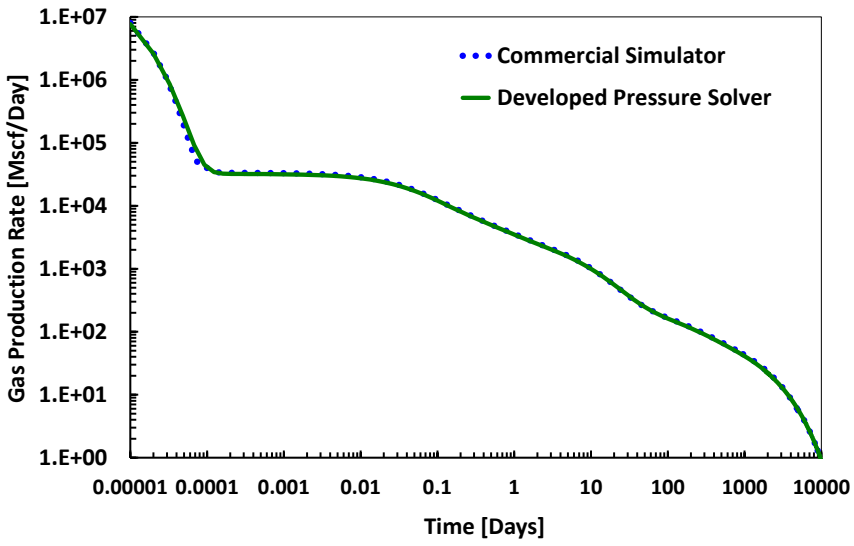

Figure 2.5: Production rate of multiple transverse fracture model. Single component Methane, Equation-of-State based simulation model.

Again the result of gas production rate from compositional run showed good agreement with commercial simulator. Based on these results we conclude that pressure equation derived in Appendix A shows good performance in both black oil and compositional simulation for a single component system.

2.5 Streamline-Based Reservoir Simulation

Streamline simulation is based on the same partial differential equations for fluid flow in porous media as used for finite differential simulators. However, streamline simulation uses a different computational scheme. Streamline simulation has become increasingly popular for high resolution reservoir simulation using multimillion cell geologic models. For incompressible or slightly compressible flow and under convection dominated conditions, streamline models are well-known to outperform conventional finite-difference simulation in terms of computational speed.

Streamline models can also improve accuracy because of subgrid resolution, and reduce numerical dispersion and grid orientation effects. To a large extent, the efficiency of the current streamline formulation is the consequence of the incompressibility assumption that allows us to easily and effectively decouple the pressure and conservation equations during flow simulation. This decoupling is greatly facilitated by the introduction of the streamline time-of-flight coordinate. Specifically, utilizing the time-of-flight as the spatial coordinate, the multidimensional conservation equations are reduced to a series of one-dimensional equations along streamlines. Solutions of these 1-D equations can take large time steps and still produce stable solutions. In contrast, the finite difference IMPES method can suffer from stability problems and be severely

restricted by the time step size (Coats 2000). Fully-implicit finite difference methods are unconditionally stable, but time steps can still be limited due to convergence and/or time truncation errors (Au *et al.* 1980, Aziz and Settari 1979). Furthermore, they are known to introduce large numerical dispersion if the grid block size is large.

In addition, for heterogeneity-dominated flow and adverse mobility-ratio conditions, the streamlines need to be updated infrequently, leading to further savings in computation time. The basic steps of streamline simulation is shown in Figure 2.6.

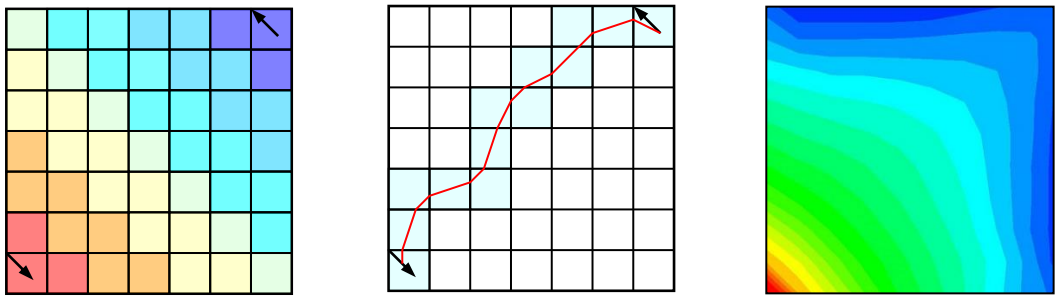

(a) Pressure field **(b) Streamline tracing** **(c) Saturation distribution**

Figure 2.6: Basic steps in streamline-based reservoir simulation.

In the streamline method, the system pressure is solved implicitly using iterative methods (Figure 2.6 (a) or Appendix A). After pressure is solved, the velocity field is calculated from pressure gradient, and streamlines are traced semi-analytically using Pollock's method (Figure 2.6b). This method assumes piecewise linear pressure gradient within a grid. Each streamline represents a constant volumetric rate and acts as an one-dimensional space for the saturation solver. Saturations are moved along the streamlines using smaller incremental time steps derived by sub-dividing the duration of the pressure

time (Figure 2.6c). Moving saturations along streamlines implies that the resulting saturation distribution is not affected by grid orientation. The reduction of the 3D grid-block problem into a set of one dimensional flow problems results in huge efficiency when resolving high-resolution geological scale models. At the end of the time step, saturations are mapped from streamline space to grid-blocks, and the process is repeated for the next time step.

Advantages of streamline simulation are as follows:

1. Computation time efficiency. Streamline simulation can be orders of magnitude faster than finite difference simulation of incompressible or slightly compressible, heterogeneity-dominated advective fluid flow.
2. Visualizing flow patterns. Streamline geometries and densities reveal the impact of the geometry on the flow paths showing high and low flow zones.
3. Can derive specific "well-to-well" rate by streamline volumes. We can see the specific well-to-well flow and this information is useful for history matching and a waterflood management system.
4. Enable tracing accurate saturation front. In general, streamline simulation can reduce numerical smearing because of the 1D flow calculation algorithm. In general, it can lessen grid orientation effects.

In this study, the IMPES (Implicit Pressure Explicit Saturation) and SIM (Sequential Implicit) method was incorporated to solve the system of unknowns. Thus, the pressure is always solved implicitly while saturation solved explicitly or implicitly along 1-D streamlines.

2.5.1 Time-of-Flight

A fundamental concept of the streamline method is based on a coordinate transformation from physical space to a coordinate system following the flow direction. We first review this transformation before introducing the streamline-based flow equations. The transformation is based on the bi-streamfuctions and an additional time-of-flight coordinate. Introducing the bi-streamfuctions, ψ, and χ, we construct a velocity field, $\vec{u}$, as:

$$\vec{u} = \nabla\psi \times \nabla\chi \quad \cdots\cdots\cdots\cdots\cdots\cdots\cdots\cdots\cdots\cdots\cdots\cdots\cdots\cdots\cdots\cdots \quad (2.34)$$

Conventional streamline simulation assumes no velocity divergence on streamline. This can be expressed as $\nabla\bullet(\nabla\psi\times\nabla\chi)=0$ using Eq. 2.34. A streamline is defined by the intersection of a constant value for ψ with a constant value for χ. In two dimensional application, $\psi=\psi(x,y)$, $\chi=z$, and ψ is recognized to be the streamfunction. The time-of-flight, τ, is defined as the travel time of the particle along the streamlines.

$$\tau(x,y,z) = \int \frac{\phi ds}{|\vec{u}|} \quad \cdots\cdots\cdots\cdots\cdots\cdots\cdots\cdots\cdots\cdots\cdots\cdots\cdots\cdots\cdots\cdots \quad (2.35)$$

The transformation from the physical space to the time-of-flight coordinates can be derived from streamlines in which the lines are traced on straight lines of varying length through the grid-blocks. The Eq. 2.35 can be written as $\vec{u}\cdot\nabla\tau = \phi$, and we can derive the following relations.

$$\left\| \frac{\partial(\tau,\psi,\chi)}{\partial(x,y,z)} \right\| = \nabla\tau\cdot(\nabla\psi\times\nabla\chi) = \nabla\tau\cdot\vec{u} = \phi \quad \cdots\cdots\cdots\cdots\cdots\cdots\cdots\cdots \quad (2.36)$$

This expression gives us the relationship between the physical space and the time-of-flight coordinates following the flow direction, as follows:

$$\phi dxdydz = d\tau d\psi d\chi \quad \cdots\cdots (2.37)$$

Eq. 2.37 indicates that the coordinate transformation preserves pore volume. Using this time-of-flight coordinate, (τ,ψ,χ), we can consider the conservation equation of incompressible fluid flow. For compressible fluids, we need redefinition of the streamfuction shown in Eq. 2.34. This redefinition is described later by using effective-density.

2.5.2 Time-of-Flight Coordinate and Underlying Grid

The fundamental idea of time-of-flight, τ is that the time required for a neutral tracer to reach a distance, *s*, along a streamline. Mathematically, this idea is expressed as:

$$\tau(s) = \int_0^s \frac{\phi(\xi)}{u_t(\xi)} d\xi \quad \cdots\cdots (2.38)$$

In order to make time-of-flight clear, define that q_{sl} as a total flow rate of one streamline and also define $u_t(s)$ as the total velocity at an arbitrary location, *s*, along a streamline. The derivation here assumes incompressible flow and flow rate is constant along streamline. Then, the cross-sectional area of streamline at the location *s* is expressed as:

$$A_{sl}(s) = \frac{q_{sl}}{\left|u_t(s)\right|} \quad \cdots\cdots (2.39)$$

Multiply porosity to the both sides of Eq. 2.39, and we get

$$A_{sl}(s)\phi(s) = q_{sl}\frac{\phi(s)}{|u_t(s)|} \quad \cdots\cdots\cdots\cdots\cdots\cdots\cdots\cdots\cdots\cdots\cdots\cdots\cdots\cdots \quad (2.40)$$

Eq. 2.40 can be integrated at the location *s* as follows:

$$\int_0^s A_{sl}(s)\phi(s)ds = \int_0^s q_{sl}\frac{\phi(s)}{|u_t(s)|}ds = q_{sl}\int_0^s \frac{\phi(s)}{|u_t(s)|}ds = q_{sl}\tau \quad \cdots\cdots\cdots\cdots\cdots\cdots \quad (2.41)$$

The integrated value of the cross sectional area from 0 to *s* is the volume of one streamline. As shown in the left hand side of the equation, the streamline is often described as line but has its associated pore volume, calculated as $PV_{sl} = \tau \cdot q_{sl}$.

The definition of the time-of-flight at the well is important because well grid property is quite sensitive to the production results. In this model, we define the time-of-flight at a sink/source grid, τ_0, as follows;

$$\tau_0 = \frac{V_p}{q_{wel}} = \frac{V_b\phi\eta}{q_{wel}} \quad \cdots\cdots\cdots\cdots\cdots\cdots\cdots\cdots\cdots\cdots\cdots\cdots\cdots\cdots\cdots\cdots \quad (2.42)$$

where η is net gross ratio, which describe the ratio of pay or non-pay region of a pore volume. The above definition does not distinguish the cell and inter flux properties of the grid. The time-of-flight at well grid is identical for all the streamlines at launch. The number of streamlines, however, is assigned to each surface based on the ratio of the strength of the velocity or the amount of flux.

2.5.3 Streamline Tracing in a Cell

A streamline is defined as the instantaneous curve in space along which every point is tangent to the local velocity vector. Tracing streamlines from injectors to producers is based on the analytical description of a streamline path within a grid-block as outlined

by Pollock (1988). The underlying assumption is that the velocity field in each coordinate direction varies linearly and is independent of the velocities in the other directions. The Pollock's method is attractive because it is analytical and consistent with the governing material balance equation. Although original Pollock's equation are assuming orthogonal grid blocks, it can be extended into general corner point grids (Cordes and Kinzelbach 1992, Prevost, Edwards, and Blunt 2002). In order to trace streamlines in general corner point geometry, we first rewrite the equations in dimensionless variables using the fractional distances through each coordinate directions as

$$\alpha = x/DX \quad \beta = y/DY \quad \gamma = z/DZ \quad \cdots\cdots\cdots\cdots\cdots\cdots\cdots\cdots\cdots\cdots \quad (2.43)$$

Here α,β,γ and x, y, z stand for the dimensionless and original coordinate, respectively. The general idea of this dimensionless transform is that we trace streamlines in unit cube and map back to the original unit system by isoparametric mapping.

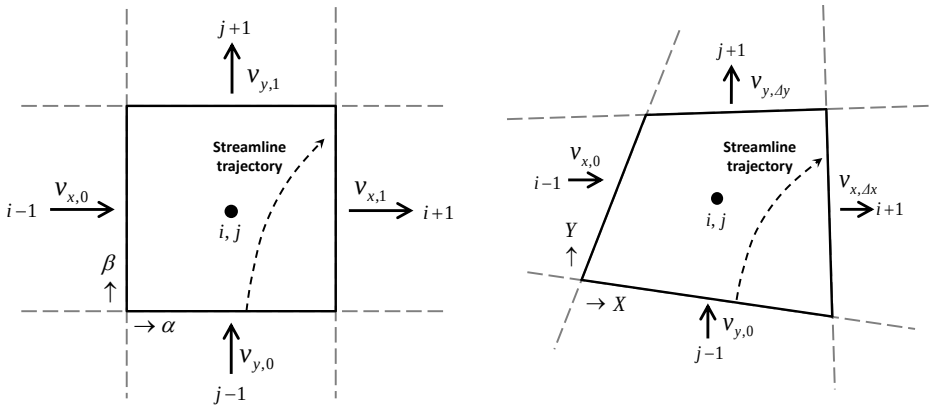

Figure 2.7: Streamline tracing in a 2D single cell: Unit space (left) and physical space (right).

We first define Darcy velocity and cell length in a single grid block. The Pollock's piecewise linear approximation is defined as the following equation

$$\frac{dx}{dt} = \vec{v}_t = v_{x,0} + x\delta v_t \quad \cdots\cdots\cdots\cdots\cdots\cdots\cdots\cdots\cdots\cdots\cdots\cdots\cdots\cdots\cdots\cdots \quad (2.44)$$

The transformation of the above equation into dimensionless unit space is done using volumetric flux $\{q_\upsilon | \upsilon = \alpha, \beta, \gamma\} = \{q_x, q_y, q_z\}$ and cross sectional flow area. These fluxes each varies linearly across the cell same as the velocity and thus

$$\mathbf{q} = \vec{u}_t \cdot A \quad \cdots\cdots\cdots\cdots\cdots\cdots\cdots\cdots\cdots\cdots\cdots\cdots\cdots\cdots\cdots\cdots \quad (2.45)$$

The gradient of the flux and velocity is described as

$$\delta\mathbf{q} = V_b \cdot \delta\vec{u}_t \quad \cdots\cdots\cdots\cdots\cdots\cdots\cdots\cdots\cdots\cdots\cdots\cdots\cdots\cdots\cdots\cdots \quad (2.46)$$

Consider the 2D grid-block shown in Figure 2.7, where the interstitial velocity field and a local coordinate system and origin are already defined. In a case with Cartesian grid, the total velocity for the x-direction, v_x, is calculated as:

$$v_x = v_{x,0} + \delta v_x (x - x_0) \quad \cdots\cdots\cdots\cdots\cdots\cdots\cdots\cdots\cdots\cdots\cdots\cdots\cdots\cdots\cdots\cdots \quad (2.47)$$

$$\delta v_x = \frac{(v_{x,\Delta x} - v_{x,0})}{\Delta x} \quad \cdots\cdots\cdots\cdots\cdots\cdots\cdots\cdots\cdots\cdots\cdots\cdots\cdots\cdots\cdots\cdots \quad (2.48)$$

$$dt = \frac{dx}{v_{x,0} + \delta v_x (x - x_0)} \quad \cdots\cdots\cdots\cdots\cdots\cdots\cdots\cdots\cdots\cdots\cdots\cdots\cdots\cdots\cdots\cdots \quad (2.49)$$

The velocities $v_{x,\Delta x}$ and $v_{x,0}$ represent the flux vectors at the location of 0 and Δx on x-axis. Here, introduce equivalent property in dimensionless form as follows

$$q_\alpha = q_{\alpha,0} + \delta q_\alpha \alpha \quad \cdots\cdots\cdots\cdots\cdots\cdots\cdots\cdots\cdots\cdots\cdots\cdots\cdots\cdots\cdots\cdots \quad (2.50)$$

$$\delta q_\alpha = \delta u_x V_b \quad \cdots\cdots\cdots\cdots\cdots\cdots\cdots\cdots\cdots\cdots\cdots\cdots\cdots\cdots\cdots\cdots \quad (2.51)$$

$$dT = \frac{d\alpha}{q_{\alpha,0} + \delta q_\alpha \alpha} \quad \cdots\cdots\cdots\cdots\cdots\cdots\cdots\cdots\cdots\cdots\cdots\cdots\cdots\cdots\cdots\cdots \quad (2.52)$$

where α is the end position, α_0 is the position of the origin coordinate – all in the x-coordinate direction. The dimensionless time from entry point to the exit coordinate, T can be calculated by taking the integral of Eq. 2.52 from the entry point (α,*0*) to arbitrary coordinate α as

$$T = \int_0 dT = \int\limits_{a_0(Initial)} \frac{d\alpha}{q_{a,0} + \delta q_\alpha \alpha} = \frac{1}{\delta q_\alpha} In\left(\frac{q_a}{q_a + \delta q_\alpha (\alpha_0 - 1)}\right) + C \quad \cdots\cdots\cdots \quad (2.53)$$

Here, C=0 at the initial condition. Knowing that $V_x = dx/dt$, Eq. 2.52 can be integrated to yield the time required to reach an α ,β, γ direction, $\Delta T_{e,\upsilon}$ as:

$$\Delta T_{e,\upsilon} = \frac{1}{\delta q_\upsilon} In\left(\frac{q_{\upsilon_0} + \delta q_\upsilon \upsilon}{q_{\upsilon_0} + \delta q_\upsilon \upsilon_0}\right); \upsilon = \alpha, \beta, \gamma \quad \cdots\cdots\cdots\cdots\cdots\cdots\cdots\cdots\cdots\cdots \quad (2.54)$$

The correct face at which a streamline exits are the face requiring the smallest value of ΔT_e calculated from Eq. 2.54. In order to find the exit location of the streamline from multiple choice of time and location, choose a minimum time to reach the exit point. The minimum time is simply the positive value calculated by Eq. 2.54 as

$$\Delta T = \min(\Delta \mathbf{T}) \quad \cdots\cdots\cdots\cdots\cdots\cdots\cdots\cdots\cdots\cdots\cdots\cdots\cdots\cdots\cdots\cdots \quad (2.55)$$

Once the minimum pseudo-time of flight T is found, the exit coordinate of the particle is calculated using the general solution of Eq. 2.50 in all three directions and solving for each unit coordinate.

$$\upsilon_e = \upsilon_0 + \left(\upsilon + \upsilon_0 \delta q_\upsilon\right)\left(\frac{e^{\delta q_\upsilon \Delta T} - 1}{\delta q_\upsilon}\right); \upsilon = \alpha, \beta, \gamma \quad \cdots\cdots\cdots\cdots\cdots\cdots\cdots\cdots \quad (2.56)$$

If there exists no flux gradient or negligible flux gradient (e.g. δq < 1.e-20) vector within grid-blocks, Eqs. 2.54 and 2.56 becomes the following equation.

$$\Delta T_{e,\upsilon} = \upsilon / q_{\upsilon,0};\ \upsilon = \alpha, \beta, \gamma \quad \cdots\cdots\cdots\cdots\cdots\cdots\cdots\cdots\cdots\cdots\cdots\cdots\cdots \quad (2.57)$$

$$\upsilon_e = \upsilon_0 + \Delta T_{e,\upsilon} q_{\upsilon,0};\ \upsilon = \alpha, \beta, \gamma \quad \cdots\cdots\cdots\cdots\cdots\cdots\cdots\cdots\cdots\cdots\cdots\cdots\cdots \quad (2.58)$$

The time obtained through these equations are the dimensionless time in the unit cube. Use the Jacobian to relate dimensionless time to find actual time and time-of-flight as

$$\Delta T = \frac{1}{\phi}\frac{d\tau}{J(\alpha, \beta, \gamma)} \text{ and hence, } \Delta\tau = \Delta T \cdot J(\alpha, \beta, \gamma) \cdot \phi \cdot \eta \quad \cdots\cdots\cdots\cdots\cdots \quad (2.59)$$

The estimation of the Jacobian equation is discussed in the pressure equation in the Appendix A.

Consider the case that there exists a contradicting flow vector at each cell surface. In that case, the result of Eqs. 2.54 and 2.56 can have the possibility of negative logarithm or erroneous exponential calculation. To avoid such kind of calculation error, assume a flow divide in the grid block. For the situation where a flow divide exists in the x direction within a grid-block, shown as Figure 2.8, the streamline will not cross the flow divide within the grid-block. This treatment can be pre-processed before starting

streamline tracing and improve performance of computation by avoiding unnecessary calculation of time-of-flight and exit location.

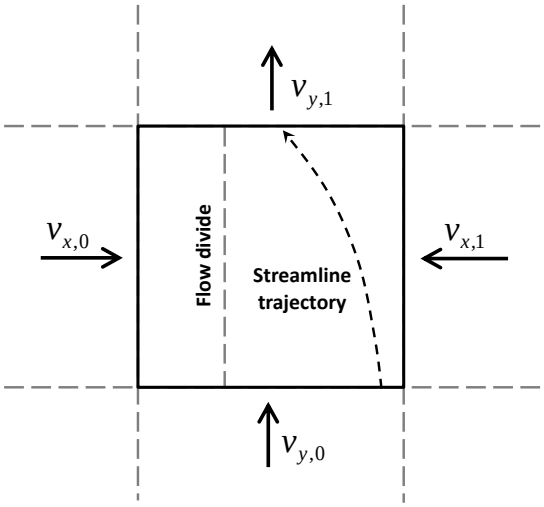

Figure 2.8: Flow divide and streamline tracing.

Each parameter will depend upon T through the Jacobian with a polynomial in α, β and γ, which can be integrated analytically. The implemented formulation recognizes the importance of taking into account the variation in the Jacobian within the cell to accurately reflect the velocity variations along a trajectory; however, variation of the time-of-flight along cell is computationally expensive and not required for the simulation, we use Eqs. 2.56 and 2.59 to find the coordinate and corresponding time-of-flight by approximating the Jacobian with the grid pore volume.

2.5.4 Discretization of Space Along Streamline

In this study, calculations along streamlines are conducted with an irregular grid. In the streamline method for incompressible fluids, an irregular grid is usually transformed into

a regular grid. In incompressible fluid flow, because the total velocity does not change steeply along a streamline, and time-of-flight increments vary corresponding mostly to the distance between nodes. Therefore, the regular grid transformation that tends to smooth time-of-flight does not degrade the solution. On the other hand, compressible fluids cause a time-of-flight value distribution of a wider range than incompressible fluids. Fluid compressibility causes larger variations in velocity between positions of faster and slower velocities. As time-of-flight for compressible fluid flow is determined with flow distance and velocity, uniform averaging of time-of-flight requires quite many nodes to correctly describe velocity effects. A large number of nodes, however, cause an increase in computation time. Therefore, an irregular-grid approach was utilized for 1D computation in this study including treatment to remove small time-of-flight with adaptive merge technique.

Along streamlines, there are two cases to observe small time-of-flight values. In one case with small time-of-flight with fast velocity, and another case, due to extremely short distances regardless of velocity such as flow crossing a corner of the grid, in another case. An advantage of the regular grid transformation is that it can avoid restrictions on the time-step size caused by small time-of-flight values as in the latter case. Care needs to be taken when an irregular grid is used. In this study, a regular grid is partly used for extremely small time-of-flight values

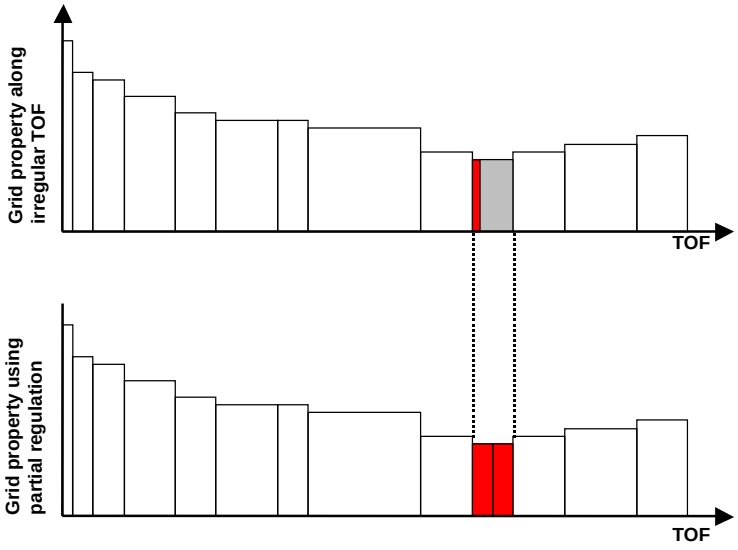

Figure 2.9: The partial regularization of the irregular streamline coordinate.

In the upper picture of Figure 2.9, there is an extremely small time-of-flight. As shown in the figure, it can be transformed into a regular grid after it is combined with the neighbor node.

2.5.5 Streamline Method for Compressible Fluids

Cheng *et al.* (2006) proposed a streamline method for compressible fluids with the concept of effective density that made it possible to treat changes in fluid volumes on streamlines. We also used their approach in the present study.

First, the effective density, ρ, is defined as follows:

$$\nabla \bullet \left(\rho \vec{u}_t\right) = 0 \quad \cdots\cdots\cdots\cdots\cdots\cdots\cdots\cdots\cdots\cdots\cdots\cdots\cdots\cdots\cdots\cdots \quad (2.60)$$

Using the divergence theorem, we get

$$\nabla \bullet \left(\rho \vec{u}_t\right) = \phi \frac{\partial \rho}{\partial \tau} + \rho \nabla \bullet \vec{u}_t = 0 \quad \cdots\cdots\cdots\cdots\cdots\cdots\cdots\cdots\cdots\cdots\cdots\cdots\cdots\cdots \quad (2.61)$$

Therefore, $\nabla \bullet u_t$ can be expressed as follows:

$$\nabla \bullet \vec{u}_t = -\frac{\phi}{\rho}\frac{\partial \rho}{\partial \tau} \quad \cdots\cdots\cdots\cdots\cdots\cdots\cdots\cdots\cdots\cdots\cdots\cdots\cdots\cdots\cdots\cdots \quad (2.62)$$

Here, if ρ = constant, $\nabla \bullet u_t = 0$, which represents incompressible fluids and the flux is constant along streamline.

Eq. 2.62 for compressible fluids can be used to determine the variation of effective density, ρ, along a streamline. According to Pollock (1988), the total velocity is constant and thus the divergence $\nabla \bullet u_t$ becomes as follows

$$\nabla \bullet \vec{u}_t = \frac{\partial u_x}{\partial x} + \frac{\partial u_y}{\partial y} + \frac{\partial u_z}{\partial z} = c \quad \cdots\cdots\cdots\cdots\cdots\cdots\cdots\cdots\cdots\cdots\cdots\cdots\cdots\cdots\cdots\cdots \quad (2.63)$$

Eq. 2.63 is applicable only in Cartesian grid. The divergence of the corner point geometry is calculated as follows

$$\nabla \bullet \vec{u}_t = \frac{1}{V_b}\left(\Delta q_x + \Delta q_y + \Delta q_z\right) = c \quad \cdots\cdots\cdots\cdots\cdots\cdots\cdots\cdots\cdots\cdots\cdots\cdots\cdots\cdots\cdots\cdots \quad (2.64)$$

Therefore, for compressible fluids, $\nabla \bullet u_t$ is a scalar constant in a grid-block. Integrating Eq. 2.62, we can get the following equation for ρ:

$$\rho = \rho_0 e^{-c\tau/\phi} \quad \cdots\cdots\cdots\cdots\cdots\cdots\cdots\cdots\cdots\cdots\cdots\cdots\cdots\cdots\cdots\cdots \quad (2.65)$$

Here, ρ_0 is ρ at the injector block. Setting ρ_0 = 1.0, we can determine a relative fluid volume at every node on the streamline. To evaluate compressibility at well grid, it is required to extract the divergence effect due to the sink/source. In other words, it is required to evaluate only ‘compressible’ effect at the well grid.

$$\nabla \bullet \vec{u}_t\big|_{well} = \frac{1}{V_b}\left(\Delta q_x + \Delta q_y + \Delta q_z + q_{well}\right) \quad \cdots\cdots\cdots\cdots\cdots\cdots\cdots\cdots \quad (2.66)$$

This divergence is used exclusively to estimate the effective density along streamline.

2.6 Solution of 1D Equation

Streamline simulation solve primary variables along 1D transport equation. The derivation of the saturation/component transport equation along streamlines is described in Appendix B for black oil and compositional model. This section, we discuss discretization methods of transport equation and describe numerical advantages. All the equation is discretized first order in time and space for this study.

Once we discretize 1D transport equation by explicit method, the overall workflow becomes IMPES approach. Recall general 1D equation is

$$\frac{\partial}{\partial t}U + \frac{\partial}{\partial \tau}F(U) = H(U) \quad \cdots\cdots\cdots\cdots\cdots\cdots\cdots\cdots\cdots\cdots\cdots\cdots\cdots\cdots \quad (2.67)$$

where *U,F,H* stands for primary variables, fractional flow and compressibility in general. The general form of explicit method becomes as follows

$$U^{n+1} = U_i^{\,n} - \frac{\Delta t}{\Delta \tau}\left[F(U_i^{\,n}) - F(U_{i-1}^{\,n})\right] + \Delta t H(U^n) \quad \cdots\cdots\cdots\cdots\cdots\cdots \quad (2.68)$$

This approach has smaller space discretization error (Aziz and Settari 1979) compared to implicit method while time step is limited to provide the stable solution by Courant-Friderichs-Lewy (CFL) condition (Lax and Wendroff 1960, Coats 2003b). The other approach is to discretize equation by implicit method, which can be called Sequential Implicit Method (SIM) (Dontchev and Rockafellar 2010, Nedelcheva 2012, Kozlova *et*

al. 2006) because we solve saturation equation implicitly after implicit pressure equation. We employ a formulation for the 1D transport equation implicitly as follows:

$$U^{n+1} - U_i^{\,n} + \frac{\Delta t}{\Delta \tau}\left[F(U_i^{\,n+1}) - F(U_{i-1}^{\,n+1})\right] + \Delta t H(U^{n+1}) = 0 \quad \cdots\cdots\cdots\cdots \quad (2.69)$$

Because the solution is unconditionally stable and do not have the CFL condition (Higham 2002), the SIM allows to take a larger time step than those obtained with the IMPES method in general, and it is demonstrated by streamline-based simulation in dual-porosity model by Kozlova *et al.* (2006). However, it is known that truncation error is larger than explicit method as described by problem in porous media by Aziz and Settari (1979) and large time step will introduce significant numerical diffusion.

2.6.1 Saturation Calculation via Explicit Method

We first discretize the equation by explicit method using three phase black oil formulation. The components of the vectors of the saturation equation, Eq. 2.68 is described as follows.

$$U = \begin{bmatrix} S_o b_o \\ S_w b_w \\ S_g b_g + R_s S_o b_o \end{bmatrix}, \quad F = \begin{bmatrix} b_o f_o \\ b_w f_w \\ f_g b_g + R_s f_o b_o \end{bmatrix}, \quad H = \begin{bmatrix} \phi^{-1} b_o \left(f_o c\right) \\ \phi^{-1} b_w \left(f_w c\right) \\ \phi^{-1} c\left(f_g b_g + R_s f_o b_o\right) \end{bmatrix} \quad (2.70)$$

Here we demonstrate the procedure to solve the 1-D saturation equation of gas phase by the explicit discretization method. The oil and water equations can be solved same procedure without miscible component. First, define the volume of gas phase as $m_g^n = S_g^n b_g^n + R_s^n S_o^n b_o^n$ and the volumetric fractional flow as

$$F_g^n = \left(\frac{k_{rg}^n / \mu_g^{n+1}}{k_{ro}^n / \mu_o^{n+1} + k_{rw}^n / \mu_w^{n+1} + k_{rg}^n / \mu_g^{n+1}} \right) b_g^{n+1} + R_s^n \left(\frac{k_{rg}^n / \mu_g^{n+1}}{k_{ro}^n / \mu_o^{n+1} + k_{rw}^n / \mu_w^{n+1} + k_{rg}^n / \mu_g^{n+1}} \right) b_o^{n+1} \quad \cdots\cdots$$

$$\cdots\cdots \quad (2.71)$$

where the superscript '*n+1*' denotes the function of pressure or saturation in the next time level, and '*n*' is the function of the previous or updated value by CFL time step. Repeat oil and water phase and Eq. 2.68 becomes

$$m_{\alpha,i}^{n+1} = m_{\alpha,i}^n - \frac{\Delta t}{\Delta \tau} \left(F_{\alpha,i}^n - F_{\alpha,i-1}^n \right) - \frac{c}{\phi} F_{\alpha,i} \ , \ \alpha = owg \quad \cdots\cdots\cdots\cdots\cdots\cdots \quad (2.72)$$

The procedure to solve above equation is shown below (Tanaka, Arihara, and Al-Marhoun 2010a).

1) Calculate a stable time step size for the convective flow of streamline 1D equation to keep the CFL condition.
2) Calculate the convective flow equation and update primary variable for intermediate time level, for instance, the total mole fraction z_i for compositional model or S_o,S_w,S_g or R_s for the black oil model.
3) Update formation volume factor and viscosity for black oil model if gas component changes during saturation time step. Conduct flash calculation for compositional model. Then proceed to next time step.

The procedure continues until the total sub time steps (stable CFL time step) reach the overall pressure time step. The detailed procedure is shown below.

1) By definition, the time step of the explicit calculation is restricted by stability condition named the CFL condition. The following equation is used in this model.

$$\Delta t \le \frac{N_c \Delta \tau}{v_{\max}} \quad \cdots\cdots \quad (2.73)$$

In the above conditional equation, $\Delta\tau$ is a node of time-of-flight on streamline, v_{max} is maximum velocity and N_c is the Courant number. The Courant number is usually given by user input and should be less than 1.0 for a stable time-step. We usually give less than 1.0 for this study, and the minimum Δt, which satisfies the above conditional equation becomes a stable CFL time-step, is named "CFLΔt".

2) Then, we consider the convective flow with the given CFL time-step. We call this intermediate saturation as "Intermediate CFL saturation, $S_p^{n+CFL\Delta t}$. In this model, the flow is treated as volume constraint and hence, the following volume balance equation is solved for the next time level.

$$m_{\alpha,i}^{n+CFL\Delta t} = m_{\alpha,i}^{n} - \frac{CFL\Delta t}{\Delta \tau}\left(F_{\alpha,i}^{n} - F_{\alpha,i-1}^{n}\right) - \frac{c}{\phi}\Big|_i^{n+1} F_{\alpha,i}^{n} \quad \cdots\cdots \quad (2.74)$$

3) Proceed time step until the sum of CFL time-step reaches given pressure update step. Whenever saturation is required (to update relative permeability, for instance) it is able to calculate from volume m_α^n by

$$S_o^{n+CFL\Delta t} = m_o^{n+CFL\Delta t} / b_o^n$$

$$S_w^{n+CFL\Delta t} = m_w^{n+CFL\Delta t} / b_w^n \quad \cdots\cdots \quad (2.75)$$

$$S_g^{n+CFL\Delta t} = \left(m_g^{n+CFL\Delta t} - R_s^{n+CFL\Delta t} m_o^{n+CFL\Delta t}\right) / b_g^n$$

Once CFL time step reaches pressure step, saturation is updated to match the volume of given pressure of the next time level using formation volume factor as

$$S_o^{n+1} = m_o^{n+1} / b_o^{n+1}$$

$$S_w^{n+1} = m_w^{n+1} / b_w^{n+1} \quad \cdots\cdots (2.76)$$

$$S_g^{n+1} = \left(m_g^{n+1} - R_s^{n+1} m_o^{n+1}\right) / b_g^{n+1}$$

Whenever the gas saturation becomes less than zero, R_s is updated based on the volume of gas and oil.

$$\begin{aligned} R_s &= m_g / m_o \ \ if \ \ S_g \le 0 \\ R_s &= 0 \ \ if \ \ S_o = 0 \end{aligned} \quad \cdots\cdots (2.77)$$

This is always monitored after computing Eqs. 2.75 and 2.76, and primary variable is switched to R_s whenever Eq. 2.77 is satisfied. The bubble point pressure is interpolated from table (e.g. Figure F.2 in Appendix F) or using equation and is always equal or lower than the oil phase pressure. Oil phase properties need to be updated too due to the changes of the bubble point.

Verification of Explicit Method with 1D Model

The verification is presented in this section. The tested model is a simple 1-D linear model with single-porosity. This model treats oil-water 2-phase compressible flow. Table 2.3 summarizes the detailed conditions of the reservoir. An injection well is defined as the rate-constraint of water by 1 rb/day, and a production is also rate-constraint with the same rate of the injector for total fluid rate. The relative permeability is given as the square of the phase saturation, and the oil properties are shown in Table. 2.3. The oil fluid properties were chosen to emphasize the effect of the compressibility and we could analyze this effect well.

Table 2.3: Reservoir parameters used for 1D simulation verification

Parameter Name	Value
Grid Dimension	(nx,ny,nz) = (100,1,1)
Permeability	1 [md]
Pore compressibility	1.0E-20 [psi^{-1}]
Injection fluid compressibility	1.0E-20 [psi^{-1}]
Reservoir fluid compressibility	1.0E-4 [psi^{-1}]
Relative permeability	$k_{rw} = S_w^2$, $k_{ro} = S_o^2$
Injection/production rate	1.0 [rb/day] (1PVI/day)
Simulation time	0.5 [day]
Pressure time step	0.01 [day]

The results of this model are compared to the commercial simulator (Schlumberger, ECLIPSE100) that is based on Finite Difference Fully Implicit Method (FDFIM). Our approach is Streamline-based Implicit Pressure Explicit Saturation method (SLIMPES).

The pressure is updated time step both SLIMPES and FDFIM. The saturation distribution at the last time-step is shown in Figure 2.10

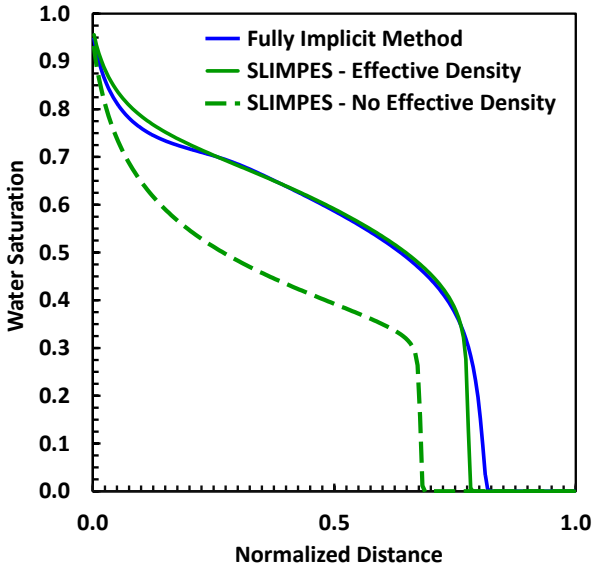

Figure 2.10: Saturation distribution of water phase by SLIMPES (green) and commercial finite difference simulator FDFIM (blue).

The result of commercial simulator (FDFIM) is shown in blue-solid line and the result of this model (SLIMPES) is shown in green-dashed line. For validation of compressible effects, we have also shown the result of incompressible flows (SLIMPES-No Effective Density). By omitting the term of effective density, we can remove the compressibility effects on streamlines. It is clear that the compressibility effect is quite significant in this simulation scenario. Both the incompressible and compressible methods have slight differences from FDFIM at front position. Behind the front, it is obvious that the result of the SLIMPES without effective density shows large differences from FDFIM, while SLIMPES shows good agreements with FDFIM.

2.6.2 Saturation Calculation via Implicit Method

Usually the CFL restriction for the gas flow is quite severe because of low viscosity and high mobility contrast between liquid phases. Also, high permeability contrast also increases the velocity field and will induce severe stability time-step. Hence, the time step is strongly restricted in gas-liquid problem. This problem diminishes the advantages of the streamline-based technique. Implicit calculations can be a useful to overcome this stability problem (Andrianov, Bratvedt, and Myasnikov 2007, Tanaka, Arihara, and Al-Marhoun 2010b), because implicit calculations give us unconditionally stable time-step and it is applicable to the streamline method.

The discretized forms of Eqs. 2.69 and 2.70 with Eqs. B.20-32 in Appendix B with Single Point Upstream weighting (SPU) become as follows.

$$\frac{1}{\Delta t}\left[\left(S_w b_w\right)_i^{n+1}-\left(S_w b_w\right)_i^{n}\right]+\frac{1}{\Delta \tau_i}\left[\left(f_w b_w\right)_i-\left(f_w b_w\right)_{i-1}\right]^{n+1}+\left[\frac{b_w}{\phi}\left(f_w c\right)\right]_i^{n+1}=0 \quad \cdots\cdots \quad (2.78)$$

$$\begin{aligned}&\frac{1}{\Delta t}\left[\left\{S_g b_g+R_s b_o\left(1-S_w-S_g\right)\right\}_i^{n+1}-\left\{S_g b_g+R_s b_o\left(1-S_w-S_g\right)\right\}_i^{n}\right]\\&+\frac{1}{\Delta \tau_i}\left\{\left(b_g f_g+R_s b_o f_o\right)_i^{n+1}-\left(b_g f_g+R_s b_o f_o\right)_{i-1}^{n+1}\right\}+\left[\phi c\left(b_g f_g+b_o R_s f_o\right)\right]_i^{n+1}=0\end{aligned} \quad \cdots \quad (2.79)$$

Here the variables, S_w,S_g, are calculated implicitly by solving above equations and then oil saturation is calculated from phase constraint as $S_o=1-S_w-S_g$. Because the equations are non-linear, the Newton-Raphson method is used to solve the solution. The basic idea of the Newton-Raphson method was described in the Appendix A. The general form of the non-linear set of equations for the Newton-Raphson method is shown as

$$dRx\cdot\delta x=-R \quad \cdots\cdots \quad (2.80)$$

Because the streamline formulation is discretized by nodes and thus, the matrix formed from a number of nodes "*N*" can be constructed as:

$$\begin{bmatrix} \mathbf{A}_1 & \mathbf{C}_2 & & & \\ \mathbf{B}_2 & \mathbf{A}_2 & \mathbf{C}_3 & & \\ & \mathbf{B}_3 & \ddots & & \\ & & \ddots & \mathbf{A}_{N-1} & \mathbf{C}_N \\ & & & \mathbf{B}_N & \mathbf{A}_N \end{bmatrix} \cdot \begin{bmatrix} \delta\mathbf{x}_1 \\ \delta\mathbf{x}_2 \\ \vdots \\ \delta\mathbf{x}_{N-1} \\ \delta\mathbf{x}_N \end{bmatrix} = -\begin{bmatrix} \mathbf{R}_1 \\ \mathbf{R}_2 \\ \vdots \\ \mathbf{R}_{N-1} \\ \mathbf{R}_N \end{bmatrix} \quad \cdots\cdots\cdots\cdots \quad (2.81)$$

where $\mathbf{C}=0$ for normal convective flow simulation along streamline. This term will have value only if cross flow occurs along streamline due to capillary or gravity, which discussed in Chapter III. Because we have two unknown variables at each node along a streamline, **A** and **B** in matrix elements is formed with derivatives of the flow equations, R_w, R_g, as follows:

$$\mathbf{A}_i = \begin{bmatrix} \dfrac{\partial R_{w,i}}{\partial S_{w,i}} & \dfrac{\partial R_{w,i}}{\partial S_{g,i}} \\ \dfrac{\partial R_{g,i}}{\partial S_{w,i}} & \dfrac{\partial R_{g,i}}{\partial S_{g,i}} \end{bmatrix}, \mathbf{B}_i = \begin{bmatrix} \dfrac{\partial R_{w,i}}{\partial S_{w,i-1}} & \dfrac{\partial R_{w,i}}{\partial S_{g,i-1}} \\ \dfrac{\partial R_{g,i}}{\partial S_{w,i-1}} & \dfrac{\partial R_{g,i}}{\partial S_{g,i-1}} \end{bmatrix} \quad \cdots\cdots\cdots\cdots\cdots\cdots \quad (2.82)$$

where δx_i and R_i are defined as:

$$\delta\mathbf{x}_i = \begin{bmatrix} \delta S_{w,i} \\ \delta S_{g,i} \end{bmatrix} \quad \cdots\cdots\cdots\cdots\cdots\cdots\cdots\cdots\cdots\cdots\cdots\cdots\cdots\cdots\cdots\cdots \quad (2.83a)$$

$$\mathbf{R}_i = \begin{bmatrix} R_{w,i} \\ R_{g,i} \end{bmatrix} \quad \cdots\cdots\cdots\cdots\cdots\cdots\cdots\cdots\cdots\cdots\cdots\cdots\cdots\cdots\cdots\cdots \quad (2.83b)$$

Then, the elements of matrix A_i and B_i are calculated as follows:

$$\frac{\partial R_{w,i}}{\partial S_{w,i}} = \frac{b_{w,i}^{n}}{\Delta t} + \frac{b_{w,i}}{\Delta \tau_i}\frac{\partial f_{w,i}}{\partial S_{w,i}} + \frac{b_{w,i}}{\phi_i}\left(\frac{\partial f_{w,i}}{\partial S_{w,i}} c_i\right) \quad \cdots\cdots \quad (2.84)$$

$$\frac{\partial R_{w,i}}{\partial S_{g,i}} = \frac{b_{w,i}}{\Delta \tau_i}\frac{\partial f_{w,i}}{\partial S_{g,i}} + c_i \frac{b_{w,i}}{\phi_i}\frac{\partial f_{w,i}}{\partial S_{g,i}} \quad \cdots\cdots \quad (2.85)$$

$$\frac{\partial R_{g,i}}{\partial S_{w,i}} = -\frac{(R_s b_o)_i^{n}}{\Delta t} + \frac{1}{\Delta \tau_i}\left(b_{g,i}\frac{\partial f_{g,i}}{\partial S_{w,i}} + R_{s,i} b_{o,i}\frac{\partial f_{o,i}}{\partial S_{w,i}}\right) + \frac{1}{\phi_i}\left\{c_i b_{g,i}\frac{\partial f_{g,i}}{\partial S_{w,i}} + R_{s,i} b_{o,i}\left(\frac{\partial f_{o,i}}{\partial S_{w,i}} c_i\right)\right\} \quad (2.86)$$

$$\frac{\partial R_{g,i}}{\partial S_{g,i}} = \frac{1}{\Delta t}\left(b_g - R_s b_o\right)_i^{n} + \frac{1}{\Delta \tau_i}\left(b_{g,i}\frac{\partial f_{g,i}}{\partial S_{g,i}} + R_{s,i} b_{o,i}\frac{\partial f_{o,i}}{\partial S_{g,i}}\right) + \frac{1}{\phi_i}\left\{b_{g,i}\left(\frac{\partial f_{g,i}}{\partial S_{g,i}} c_i\right) + R_{s,i} b_{o,i}\left(\frac{\partial f_{o,i}}{\partial S_{g,i}} c_i\right)\right\}$$

$\cdots\cdots$ (2.87)

$$\frac{\partial R_{w,i}}{\partial S_{w,i-1}} = -\frac{b_{w,i-1}}{\Delta \tau_i}\frac{\partial f_{w,i-1}}{\partial S_{w,i-1}} \quad \cdots\cdots \quad (2.88)$$

$$\frac{\partial R_{w,i}}{\partial S_{g,i-1}} = -\frac{b_{w,i-1}}{\Delta \tau_i}\frac{\partial f_{w,i-1}}{\partial S_{g,i-1}} \quad \cdots\cdots \quad (2.89)$$

$$\frac{\partial R_{g,i}}{\partial S_{w,i-1}} = -\frac{1}{\Delta \tau_i}\left(b_{g,i-1}\frac{\partial f_{g,i-1}}{\partial S_{w,i-1}} + b_{o,i-1} R_{s,i-1}\frac{\partial f_{o,i-1}}{\partial S_{w,i-1}}\right) \quad \cdots\cdots \quad (2.90)$$

$$\frac{\partial R_{g,i}}{\partial S_{g,i-1}} = -\frac{1}{\Delta \tau_i}\left(b_{g,i-1}\frac{\partial f_{g,i-1}}{\partial S_{g,i-1}} + b_{o,i-1} R_{s,i-1}\frac{\partial f_{o,i-1}}{\partial S_{g,i-1}}\right) \quad \cdots\cdots \quad (2.91)$$

When $S_g < 0$, the primary variable is switched to solution GOR by $\delta \mathbf{x}_i = \begin{bmatrix} \delta S_{w,i} \\ \delta R_{g,i} \end{bmatrix}$ and also include in Jacobian component of **A** as well as **B**. The elements of the matrix $\mathbf{A}_i$ and $\mathbf{B}_i$ of solution gas terms are calculated as follows:

$$\frac{\partial R_{w,i}}{\partial R_{s,i}} = \frac{\partial R_{w,i}}{\partial R_{s,i-1}} = 0 \quad \cdots\cdots \quad (2.92)$$

$$\frac{\partial R_{g,i}}{\partial R_{s,i}} = \frac{b_{o,i}^{n}\left(1-S_{w,i}\right)^{n}}{\Delta t} + \frac{b_{o,i} f_{o,i}}{\Delta \tau_i} + b_{o,i} f_{o,i} \frac{c}{\phi_i} \quad \cdots\cdots \quad (2.93)$$

$$\frac{\partial R_{g,i}}{\partial R_{s,i-1}} = -\frac{f_{o,i-1} b_{o,i-1}}{\Delta \tau_i} \quad \cdots\cdots \quad (2.94)$$

The summarized procedure of saturation calculations in the program is as follows. Here the superscript *ite* stands for iteration level and *S* is the saturation.

(1) Set iteration level = 1, and store the initial time-level saturation as.

$$S^{ite} = S^{n} \quad \cdots\cdots \quad (2.95)$$

(2) Construct Jacobian matrix, and find ΔS for the next iteration level by solving linear matrix by Eq. 2.81 by band matrix solver

(3) Update primary variables for next iteration level, $ite+1$

$$S^{ite+1} = S^{ite} + \Delta S \quad \cdots\cdots \quad (2.96)$$

(4) Set *ite* = *ite*+1 and go to the step (2). The convergence criteria is evaluated by change of saturation per iteration, e.g. $\Delta S < 10^{-4}$. In case it is not able find convergence point, we reduce the time step size and go back to the step (1).

(5) To update saturation for the next time-level.

$$S^{n+1} = S^{ite} \quad \cdots\cdots \quad (2.97)$$

In this study, we use the band matrix solver to find the solution of a set of linear equations and implementation is described in Appendix. C. The matrix-form of saturation equations has no off-diagonal elements and thus, the band matrix solver is well suited to solve this matrix form.

Verification of Implicit Method with 1D Model

Verification is conducted for the developed implicit solver, where the fluid and reservoir properties are the same as used in the explicit case. The reservoir model is 1-D linear and water flooding is performed by an injection well. The detailed reservoir conditions are shown in Table.2.3. Again the results are compared between commercial simulator ECLIPSE (FDFIM) and developed method by Streamline-Based Implicit Saturation calculation (SLSIM). The pressure is updated with same time step in both SLSIM and FDFIM. The comparisons of the saturation distribution at the end of the simulation are shown in Figure 2.11 below.

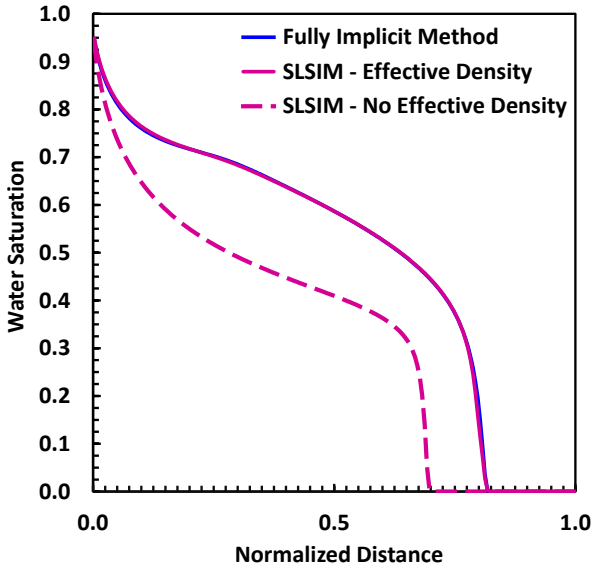

Figure 2.11: Saturation distribution of water phase by SLSIM (red) and commercial finite difference simulator FDFIM (blue).

Again the result of FDFIM is shown in blue dashed line and the result of the streamline (SLSIM) is shown in red solid line. The dotted line shows the result of the

streamline model without including effective density. Now it is obvious that the solution with compressibility effects by effective density shows an exact match with the result of FDFIM. In this simulation case, the finite difference method and streamline method solve the same equation with the same time and space discretization and thus, the equivalent result is reasonable. In addition, this result certifies that the idea of effective density is correct and our implementation seems reasonable for oil water 2 phase problem.

2.6.3 Summary of Discretization Method

The results of the implicit (SLSIM) and explicit (SLIMPES) methods of the saturation equation are demonstrated in Figs. 2.10 and 2.11 and there are differences between implicit and explicit discretization scheme. Also without including the effect of compressibility, the results of the streamline explicit and implicit models have poor agreements with commercial finite difference simulator as shown in Figure 2.10 while the results of compressible flow by including effective density (Figs. 2.10 and 2.11) show good agreements with commercial simulator. The notable point is that the streamline-based explicit treatment has a sharp front compared to FDFIM and SLSIM. Figure 2.12 shows the superposition of the solution by SLIMPES, SLSIM and commercial fully-implicit finite difference simulation result.

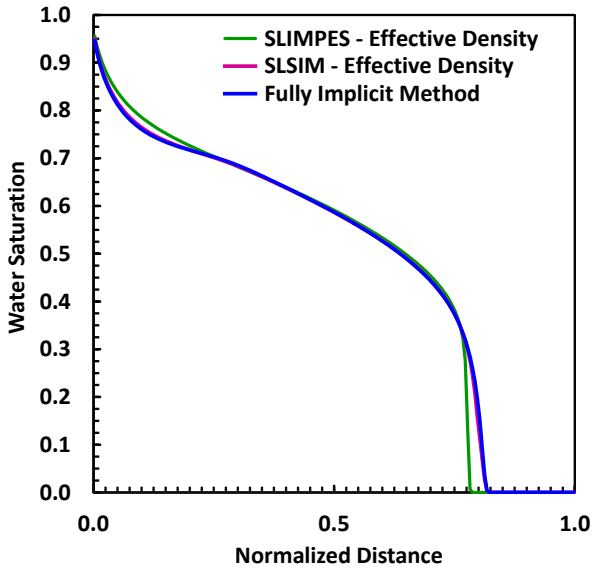

Figure 2.12: Saturation distribution of water phase by SLIMPES (green), SLSIM and commercial FIM (blue).

As discussed previously, one of the advantages of the implicit scheme is that it is able to take larger time step size compared with explicit approach and thus improves the computational efficiency under severe CFL condition in explicit approach. However, it needs to mention that large time step introduces the significant amount of time truncation error. In contrast, the time step of explicit approach is limited by CFL condition, and thus the solution is less sensitive as long as it keeps the stable time step. Figure 2.13 shows the difference of the solution with respect to the selection of time step size. Here both implicit and explicit scheme take the same pressure update step. The saturation equation takes different step between SLIMPES and SLSIM time step selection is up to the CFL for explicit and convergence limit for implicit method.

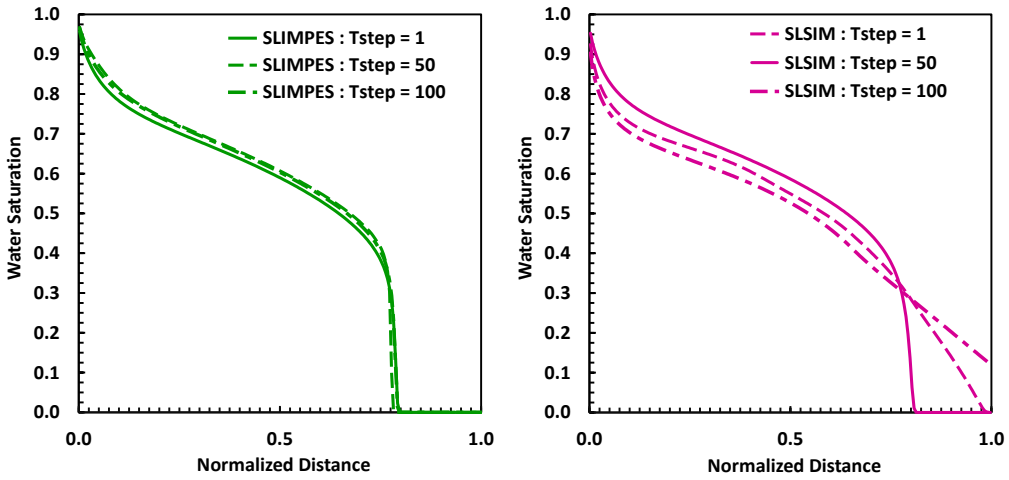

Figure 2.13: Saturation distribution of SLIMPES (left) and SLSIM (right), with 3 different time stepping size (solid line by 1 day, break line by 50 days and dotted line by 100 days).

It is clear that SLSIM is able to obtain larger time step size to solve saturation equation while solution is too diffusive. In contrast, solutions by explicit discretization (SLIMPES) are insensitive to pressure update step size because of limited saturation step due to CFL and also it has smaller discretization error with same step size with implicit discretization.

2.7 Model Validation by 3phase Black Oil Simulation

In this section, we demonstrate our developed streamline-based black oil simulator using three-phase-flow conditions by water-alternate-gas (WAG) injection scenario by series of synthetic cases and field scale examples. These examples emphasize the validation of the solution of our developed streamline simulator and clarify the difference between conventional grid based finite difference simulation methods. As the numerical discretization method and solution are demonstrated by the 1D 2phase oil-water problem in the previous section, 3phase WAG injection is conducted for 1D, 2D and 3D for both homogeneous and heterogeneous media to validate the developed model. Figure 2.14 shows the injection scenario used for all the synthetic cases.

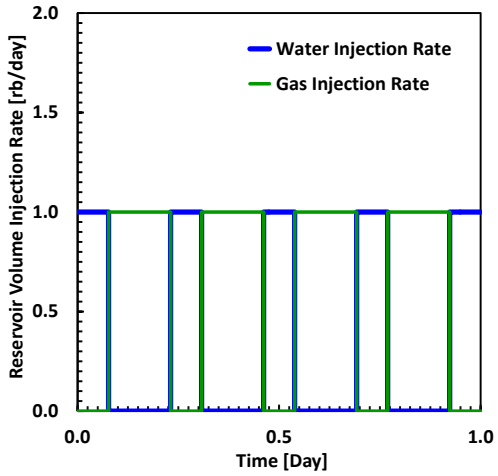

Figure 2.14: Water-Alternation-Gas injection strategy.

The fluid PVT properties of oil, water and gas phase are shown in Appendix. F. The rock table is given by Figure. F.2 in Appendix F with the water wet condition except for

capillary pressure data. The effect of the capillary pressure is the main topic of the Chapter III and is not included through the simulation cases discussed in this section, except for the field case scenario.

The convergence criteria for linear and nonlinear process are assigned for both commercial and developed simulator. For the commercial simulator, the convergence errors for each phase are normalized and Newton-Raphson iteration is continued until the largest in the entire reservoir becomes less than criteria. In addition, a convergence criterion for the linear system is also specified. These numbers are assigned as Table 2.4 and same numbers are used through this study.

Table 2.4: Linear and nonlinear convergence criteria

Parameter Name	Value
CFL number along streamline	0.8
Minimum time step size at saturation	1E-5 [days]
Pressure convergence criteria (This model)	0.01 [psi]
Maximum number of iterative IMPES	5
Linear convergence criteria	1.0E-9
Nonlinear convergence error (commercial)	0.01
Linear convergence criteria (commercial)	1E-5

The nonlinear and linear convergence criteria are also assigned in developed model during pressure calculation. The definition of the nonlinear convergence criteria is a maximum change of the pressure though the iteration, and linear convergence error is residual of the linear solver shown in Appendix C.

2.7.1 1-Dimension Case

First we demonstrate the developed model using 1D core flooding case. The schematic view of the case is shown in Figure 2.15 below and the initial and boundary conditions are summarized by Table 2.5.

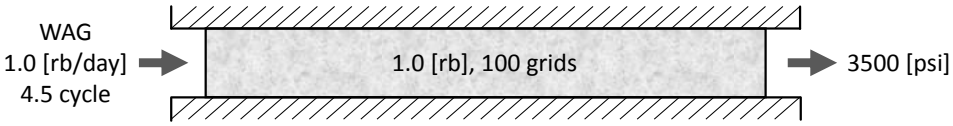

Figure 2.15: 1D injection schematic view.

Through the simulation, the boundary condition is assigned as reservoir volume rate constraint of gas or water, and fixed pressure is given by right side. Unlike previous oil-water scenario, the WAG injection case is a highly nonlinear problem because PVT data are the strong function of pressure and R_s in addition to the high mobility contrast between gas to liquid phase. Thus the simulation is conducted with IMPES based approach with several time step scenario to see the accuracy of the solution and its sensitivity. The results of saturation distribution and pressures are shown in Figure 2.16. Here the solutions of our IMPES method are shown in blue brake lines and solid red line shows the reference solution, which obtained by a commercial simulator by using equivalent PVT and initial/boundary condition with 10000 pressure recalculations. As shown in multiple break lines in Figure 2.16, our simulation results could not reproduce the reference solution. As the number of time step decreases, then the differences with the reference solution increases, especially pressure distribution.

Table 2.5: Reservoir parameters for 1D wag scenario	
Parameter Name	Value
Grid dimension	(nx,ny,nz) = (100,1,1)
Grid block size	dx=dy=dz = 0.824972 [ft]
Porosity	0.1
Permeability	k_x=k_y = 157.93742 [md]
Pore compressibility	4.0E-6 [psi^{-1}]
B_w,μ_w,c_w	1.0,1.0,1.0E-6 [psi^{-1}]
Initial pressure	4000 [psi]
Initial Rs,p_b	0.8 [Mscf/stb], 4000 [psi]
Initial saturation	(S_o,S_w,S_g) = (0.8,0.2,0.0)
Wellbore diameter	0.25
Time step size (commercial)	1E-4 [day]

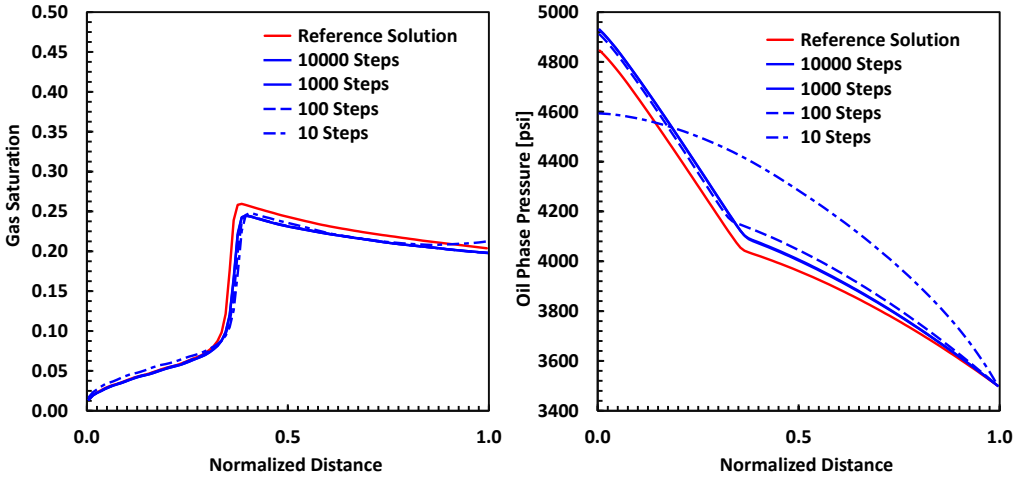

Figure 2.16: Gas saturation distribution (left) and pressure distribution (right) at the end of the simulation. The red line by commercial simulator with 10000 time steps and blue lines are solutions by our model with different time steps without iterative IMPES method.

The production history is compared with reference solution, shown in Figure 2.17. The scatter plot shows our results with different time step. The production results also

showing that we could not reproduce the same results with 10000 time step simulation, and thus our presented IMPES method could not take into account nonlinearity of the problem.

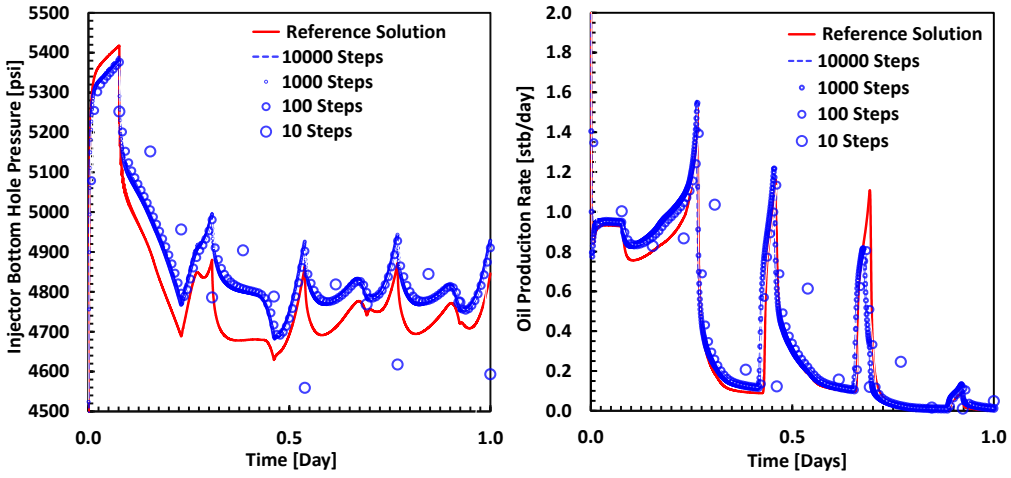

Figure 2.17: The history of the injection bottom hole pressure (left) and oil production rate (right). The red line by commercial simulator with 10000 time steps and blue circles are solutions by our model with different time steps without iterative IMPES method.

The main reason of this discrepancy of the solution between reference solution and developed IMPES method is described as 3 main reasons as follows. First reason is the time truncation error which is caused by differences by the selection of time step size. With increasing time step size, solution gets inaccurate in general. In this case study, we introduced large amount of truncation error in pressure equation as we increase the time step size. The time truncation error of the saturation is difficult to discuss but not sensitive due to CFL limitation by explicit approach. The second reason is the space truncation error and this is negligible for this case study because same discretization is

taken by our approach and we do not conduct any regularization on streamline coordinates. Considering space and time discretization error, the selection of 10000 pressure recalculation should show the good agreement with the reference solution obtained by commercial simulator which is also conducted by equivalent time step size.

Here we have third reason that introduces the difference for the same amount of the space and time discretization, which is the effect of the linearization due to IMPES approach. As described in the pressure equation in the Appendix A, or most of the literatures of IMPES discretization (Aziz and Settari 1979, Ertekin, Abou-Kassem, and King 2001), the pressure equation is solved by following equation

$$\phi c_t \frac{\partial p}{\partial t} + \nabla \bullet \sum_{\alpha=ogw} \vec{u}_\alpha - \sum_{\alpha=ogw} Q_\alpha = 0 \quad \cdots\cdots\cdots\cdots\cdots\cdots\cdots\cdots\cdots\cdots \quad (2.1)$$

where the higher order term of the gradient of the velocity is ignored for the black oil discretization. In black oil system, we assume the accumulation term as follows

$$\left(\frac{b_g - b_o R_s}{b_o b_g} \right) R_o + \frac{R_w}{b_w} + \frac{R_g}{b_g} \approx \phi c_t \frac{\partial p}{\partial t} \quad \cdots\cdots\cdots\cdots\cdots\cdots\cdots\cdots\cdots\cdots \quad (2.2)$$

Again the derivation of this linearization process is described in the appendix A. This equation assumes that the compressibility of oil, water and gas phase is constant through the step. This assumption is applicable for oil-water system, however, is questionable with gas phase with miscible components. Also the time discretization of the solution gas is linearized by $\frac{\partial R_s}{\partial t} = \frac{\partial R_s}{\partial p_o} \frac{\partial p_o}{\partial t}$, however, this can be applied if phase appearance and disappearance does not occur through the step (Fanchi 1987). In other words, in a case

with WAG injection scenario, gas phase appear or disappear in entire reservoir and thus the R_s is not the function of pressure but bubble point. The bubble point pressure moves less than oil phase pressure and thus, linearization will cause material balance error and numerical error due to explicit treatment of the mobility (Fang 1986, MacDonald 1970). This error will introduce over or lower estimates of pressure during pressure calculation to keep incorrect accumulation by adjusting transfer and sink/source term. This is the stability problem of the IMPES method, which velocity or production rate is calculated using saturation (relative permeability) of time level *n*. These assumptions provide large errors in the solution and material balance. The detail of this stability problem and time stepping is discussed next chapter with capillarity effects. It is known that the introduction of a capillary pressure will cause severe stability issues due to explicit treatment of the saturation (Aziz and Settari 1979, Coats 2003a, Lu, Alshaalan, and Wheeler 2007).

In order to avoid these numerical error and stability problem, we introduce an iterative IMPES approach which pressure and saturation equation is solved iteratively to satisfy the convergence between two equations.

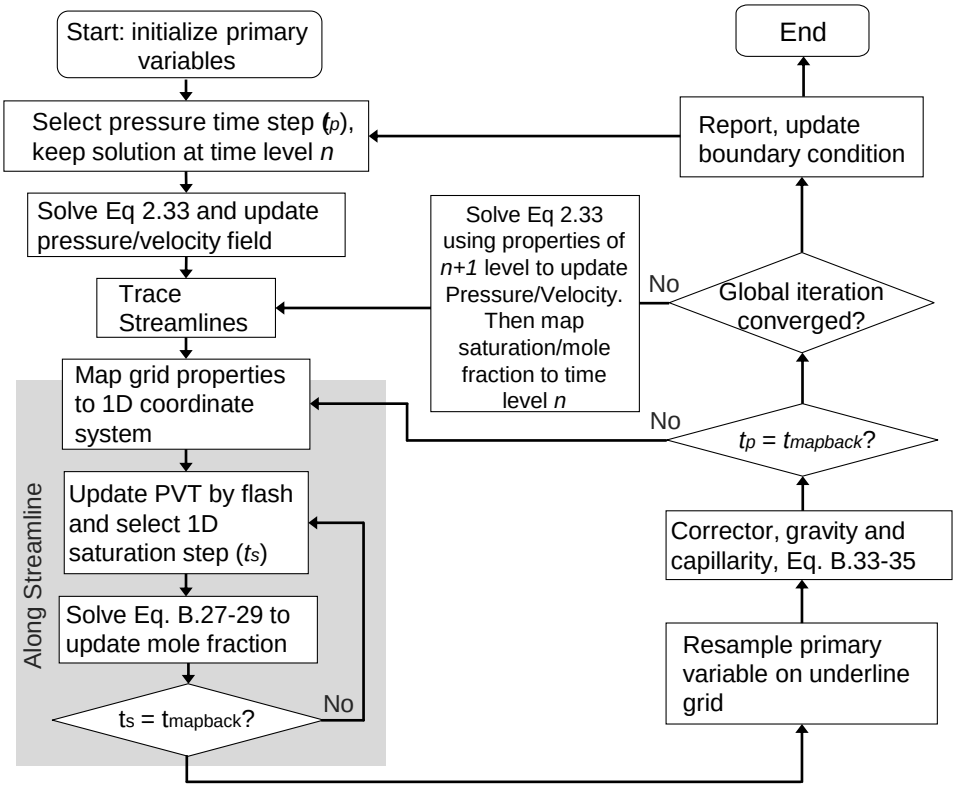

Figure 2.18: Flow chart of iterative IMPES approach.

The implementation of the iterative IMPES approach for the developed streamline-based method is shown in Figure 2.18 as a flow chart. The implementation is done by general multicomponent problem including black oil simulation (Tanaka, Datta-Gupta, and King 2014). The advantages of this iterative method is the reduction of the sensitivity of the time step selection by using mobility (relative permeability) of time level *n+1*. It increases the flexibility of the time stepping strategy and computational advantages of the IMPES approach, reported by several authors (MacDonald 1970,

Ammer, Brummert, and Sams 1991). It also avoids stability problem, especially reservoir simulation with strong capillarity. The effect of stability with capillarity and gravity is discussed in Chapter III. The effect of capillarity is not assigned for all the synthetic case study in this chapter. Also, the iterative approach is able to reduce material balance error by solving the pressure equation before it is linearized, shown in Eq. A.13 of Appendix A.

The 1D case with WAG injection scenario is conducted again using iterative IMPES approach. Results of the gas saturation distribution and production history are shown in Figs 2.19-20. As we expected, the good agreement is obtained compared with reference solution obtained by smaller time step size size.

Using the iterative technique, the solution of saturation and pressure is less sensitive to the selection of the pressure time step size shown in Figure 2.19 and all of the solution with different time step selection shown in the 1D case study converged to the reference solution. The same behavior can be seen in the result of the production history, shown in Figure 2.20.

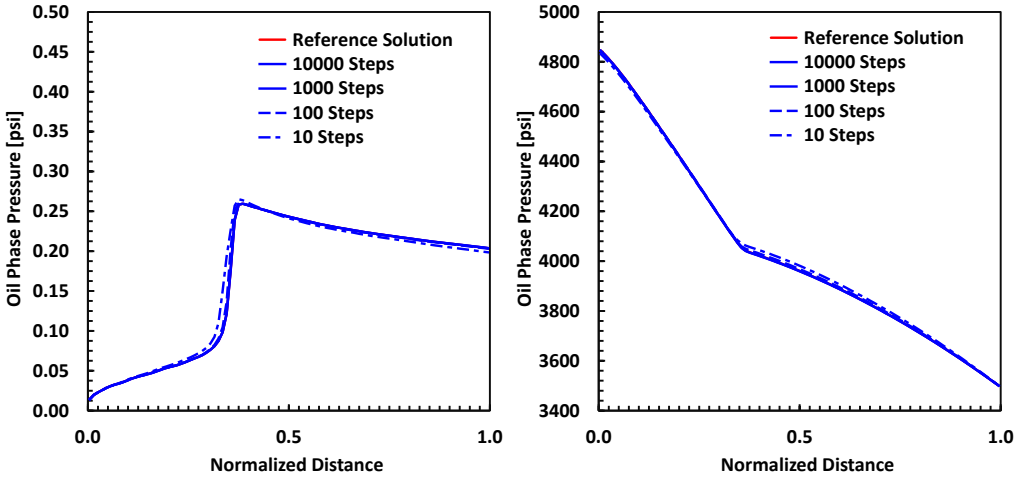

Figure 2.19: Gas saturation distribution (left) and pressure distribution (right) at the end of the simulation. The red line by commercial simulator with 10000 time steps and blue lines are solutions by our model with different time steps iterative IMPES method.

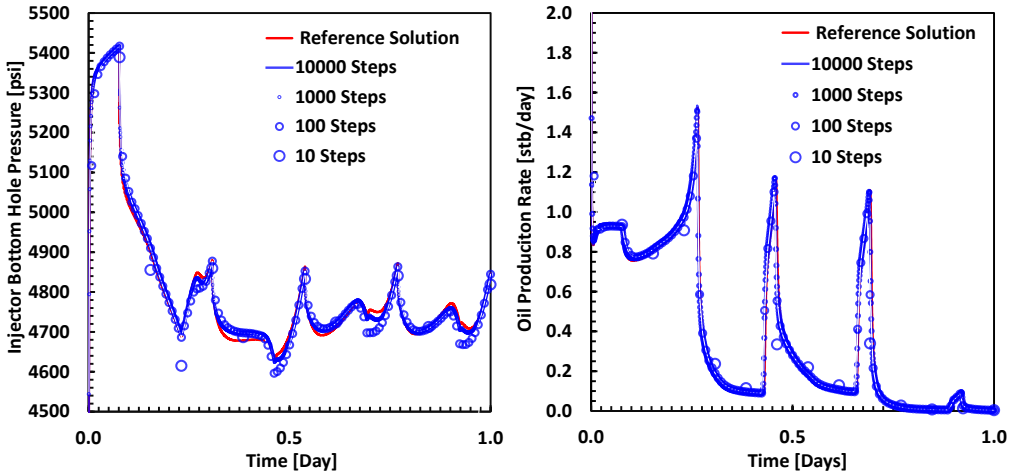

Figure 2.20: The history of the injection bottom hole pressure (left) and oil production rate (right). The red line by commercial simulator with 10000 time steps and blue circles are solutions by our model with different time steps with iterative IMPES method.

2.7.2 2-Dimension Areal Problem

This example demonstrates 2D homogeneous WAG injection scenario using the areal sweep problem. The other properties used for this case study is same as previous 1D case study, summarized in Table F.2 in Appendix F. The schematic figure of a quarter-five spot pattern problem is shown in Figure 2.21 below.

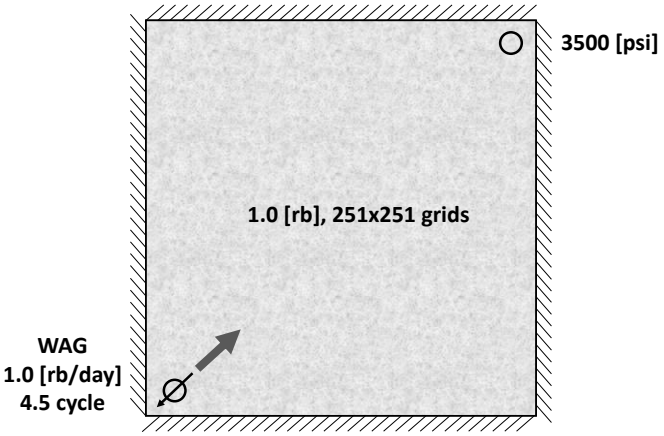

Figure 2.21: 2D areal quarter five spot problem.

The mesh is divided into 251 grids for both *x* and *y* direction, and injector is located at left bottom corner with reservoir volume rate constraint. The producer is located at the opposite diagonal corner with constant pressure constraint by 3500 psi. Initial condition is assigned same as previous case study, shown in Table 2.5. Again the reservoir volume is 1 bbl at initial condition and inject water and gas cycle by 5 cycles, 1PVI for a day.

Figure 2.22 shows the comparisons of oil phase pressure distribution at 1st WAG cycle with commercial finite difference simulator (Fully Implicit Method) and our simulation results. Note that our solution is obtained by iterative IMPES approach after

saturation calculation by SLIMPES approach, including compressibility by effective density. The pressure distribution has small differences but it is acceptable because the maximum differences in the field are less than 1.0 psi. The streamline is traced using total flux field calculated from the oil phase pressure, shown in Figure 2.23. The number of streamlines displayed in Figure is 10% of the actual streamlines used for the saturation calculation. The contour of the streamline shows time-of-flight, which indicates the time of neutral tracer starting from injector to producer. The figure shows break through around 1 day, however, the actual speed of the component is a function of the phase fractional flow and it can be shorter or longer.

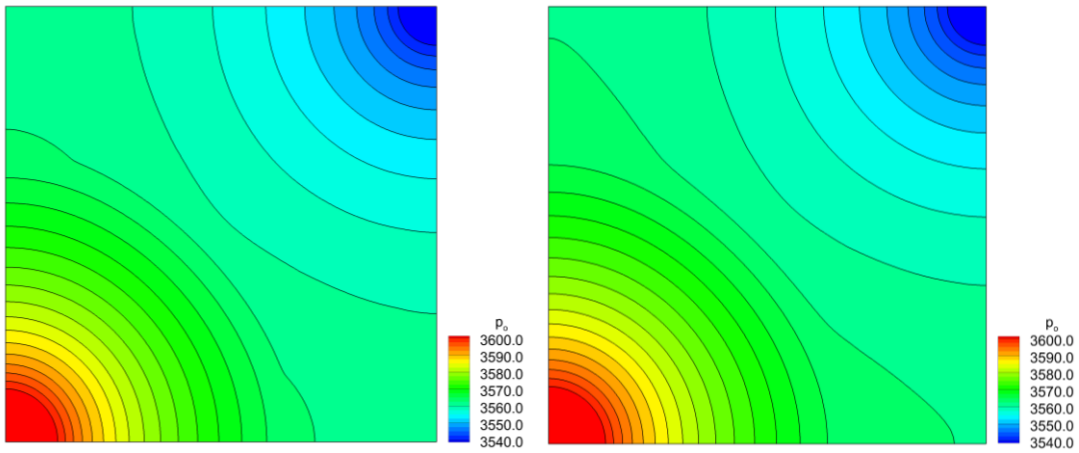

Figure 2.22: The oil phase pressure distribution of commercial simulator (left) and developed model (right), at the 1st cycle of WAG injection.

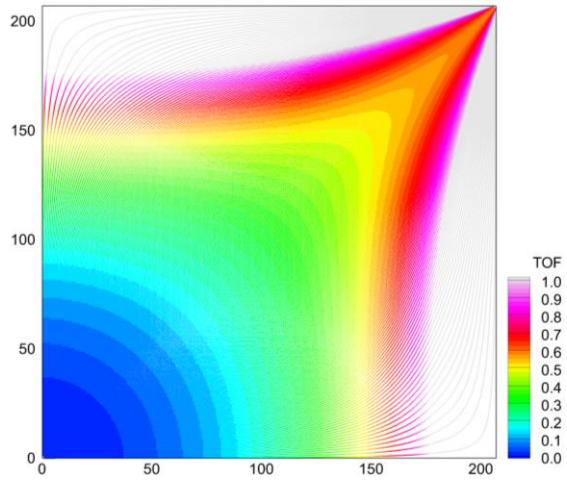

Figure 2.23: The streamline distribution traced in the 2D homogeneous field, contoured by time-of-flight.

Figs. 2.24-25 shows water saturation distribution and gas saturation distribution, respectively. Each of the figure is compared with the result of the commercial finite difference simulator. The results indicate that our simulation results have sharper results compared with the commercial finite difference simulator. This difference is caused because the results of the commercial finite difference simulator are obtained by the fully implicit method, while our simulation result is generated by the iterative IMPES approach. Explicit saturation equation along streamlines generated lower discretization errors and the front of water and gas is clear.

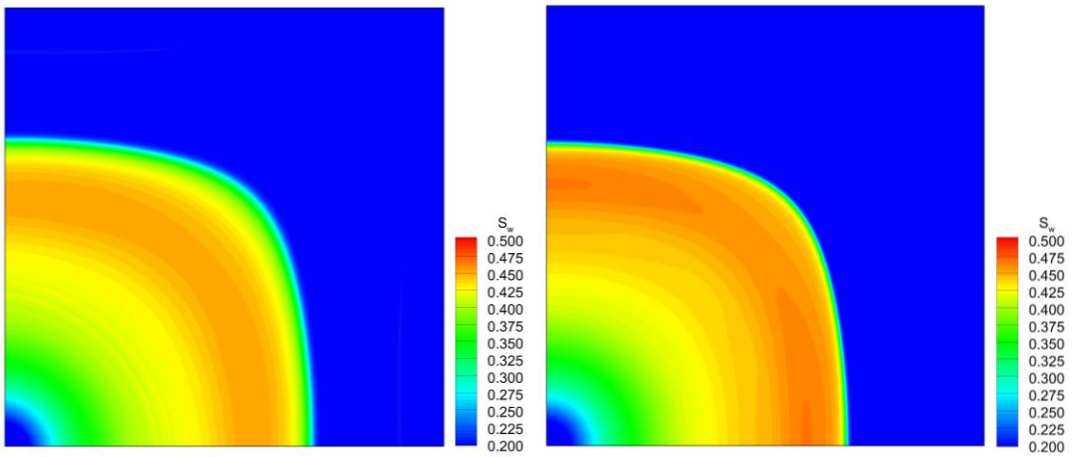

Figure 2.24: The water phase saturation distribution of commercial simulator (left) and developed model (right) by 2D homogeneous model, at the 1st cycle of WAG injection.

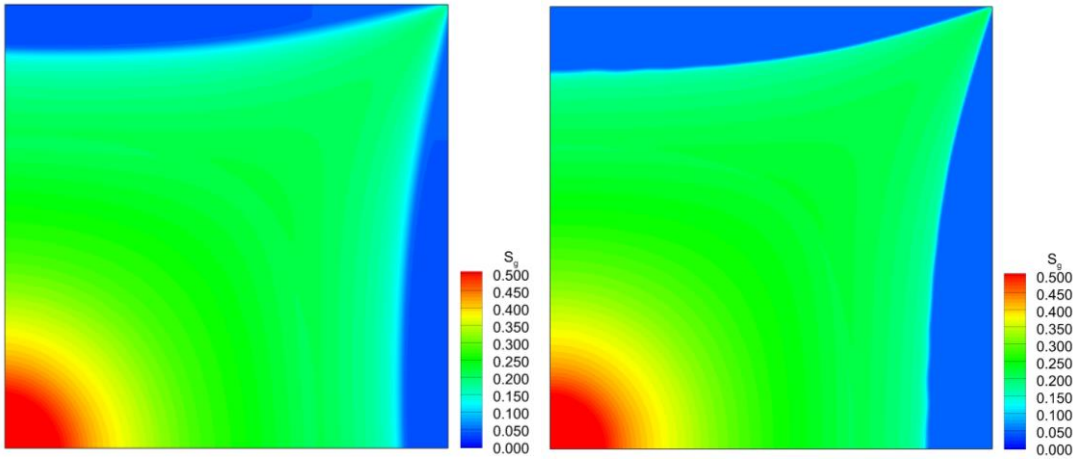

Figure 2.25: The gas phase saturation distribution of commercial simulator (left) and developed model (right) by 2D homogeneous model, at the 1st cycle of WAG injection.

Figure 2.26 shows the bottom hole pressure of the injector and the oil production rate. The result shows good agreement with injector bottom hole pressure. It can be seen that oil production rate of the developed model is a bit lower compared with commercial

simulator, however, it is acceptable considering the differences in gas phase saturation distribution in Figure. 2.25

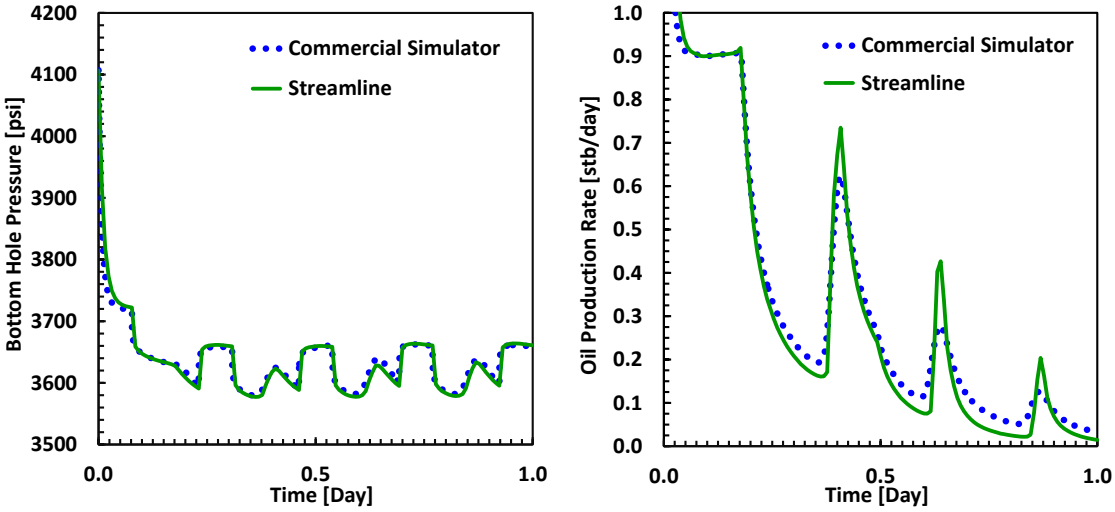

Figure 2.26: The history of the injection bottom hole pressure (left) and oil production rate (right) by 2D homogeneous problem. The blue dot by commercial simulator and green line by developed model.

2.7.3 2-Dimension Areal Heterogeneous Problem

The model is tested by heterogeneous permeability media with the same parameters as in the homogeneous model. The permeability field is given in Figure 2.27 with isotropic (k_x=k_y) condition. The permeability is in log scale and actual range is between 10^{-4}mD to 10^{4}mD. With given PVT and the contrast of permeability field, it is expected that this WAG process will generate viscous fingering behavior (Blunt and Christie 1994)

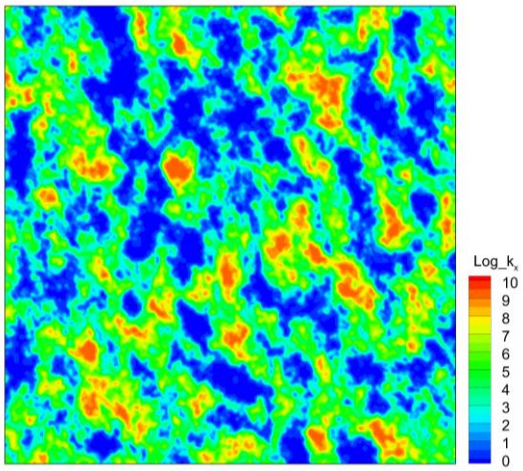

Figure 2.27: Permeability field of 2D areal heterogeneous model, by natural log scale.

Given the permeability field, the streamline distribution is shown in Figure 2.28 contoured shown by time-of-flight). The density of streamline refers to amount of flux in the reservoir and it captures reservoir heterogeneity. The contour indicates the travel time of a neutral tracer along streamlines and the breakthrough can be estimated much earlier compared with the one from the homogeneous case. Figs. 2.29 and 2.30 show the water saturation distribution and gas saturation distribution after 1st cycle of WAG

injection by heterogeneous media. Because of the strong contrast of the permeability field, the sweep area of the reservoir is much less compared with homogeneous media, especially gas saturation distribution. Each of the figure is compared with the result of the commercial finite difference simulator.

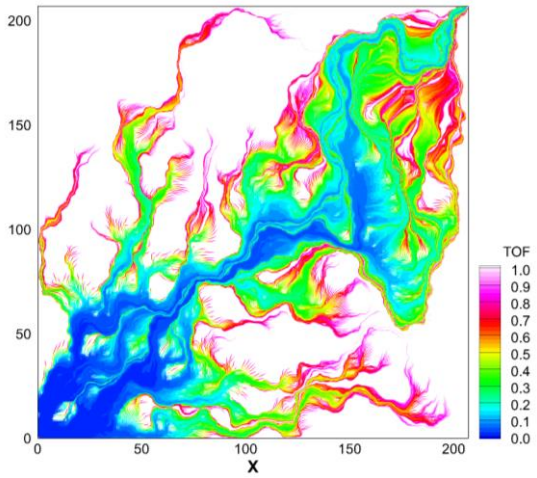

Figure 2.28: Streamline distribution by 2D heterogeneous model, captured at 2nd cycle of WAG injection sequence, contoured by time-of-flight.

Here again shaper saturation front is obtained compared with commercial simulator. The left side of the Figs. 2.29 and 2.30 shows the result of the commercial simulator. The main difference of the two results is that our result shows the breakthrough of water and gas while commercial simulator does not, especially gas phase. The main reason is because of the difference of the numerical scheme, but one key factor needs to be mentioned here is a selection of the number of the streamlines. In heterogeneous media, number of streamline is sensitive compared with a homogeneous scenario because it generates stagnant grid blocks or untraced grids as shown in Figure 2.28. Although this

stagnant cell will not affect significant differences in simulation results because of negligible amount of flux passing through the cell, however, will cause differences compared with grid-based finite difference method will because grid based finite difference method introduce numerical dispersion.

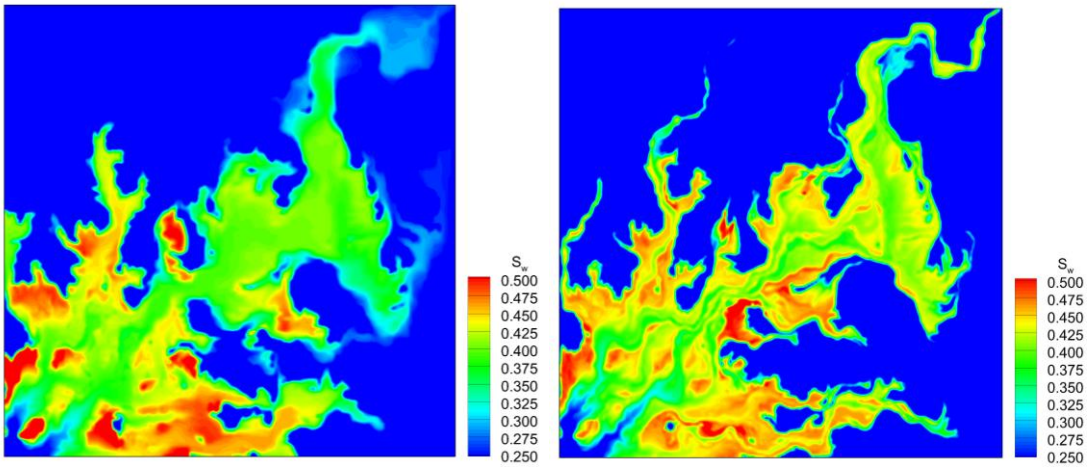

Figure 2.29: The water phase saturation distribution by 2D heterogeneous model: Commercial simulator (left) and our results (right), at the 1st cycle of WAG injection.

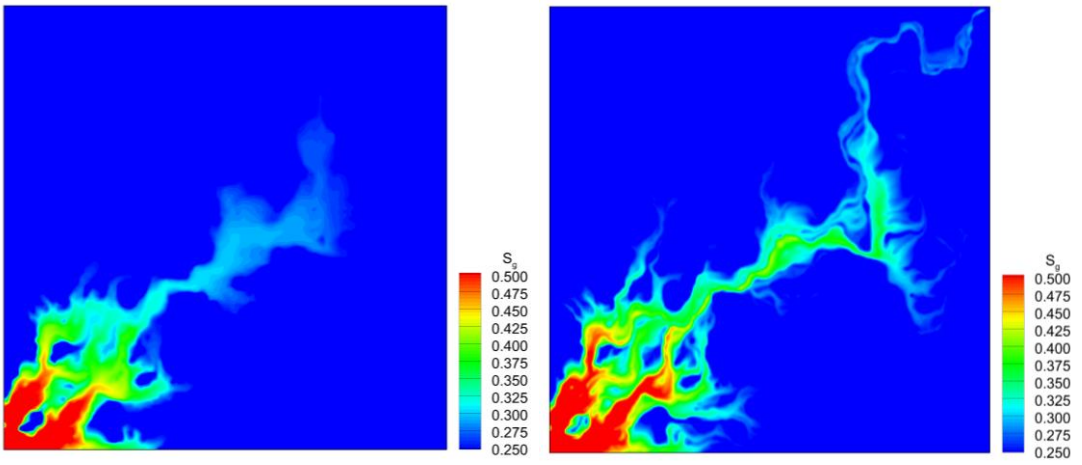

Figure 2.30: The gas phase saturation distribution by 2D heterogeneous model: Commercial simulator (left) and our results (right), at the 1st cycle of WAG injection.

The production history is shown in Figure 2.31. Good agreement is obtained, and we can see lower oil production rate is obtained by the streamline based method. This is because gas and water production rate was higher due to the faster breakthrough as seen in saturation distribution, so that overall oil production is less compared with the commercial finite difference simulator.

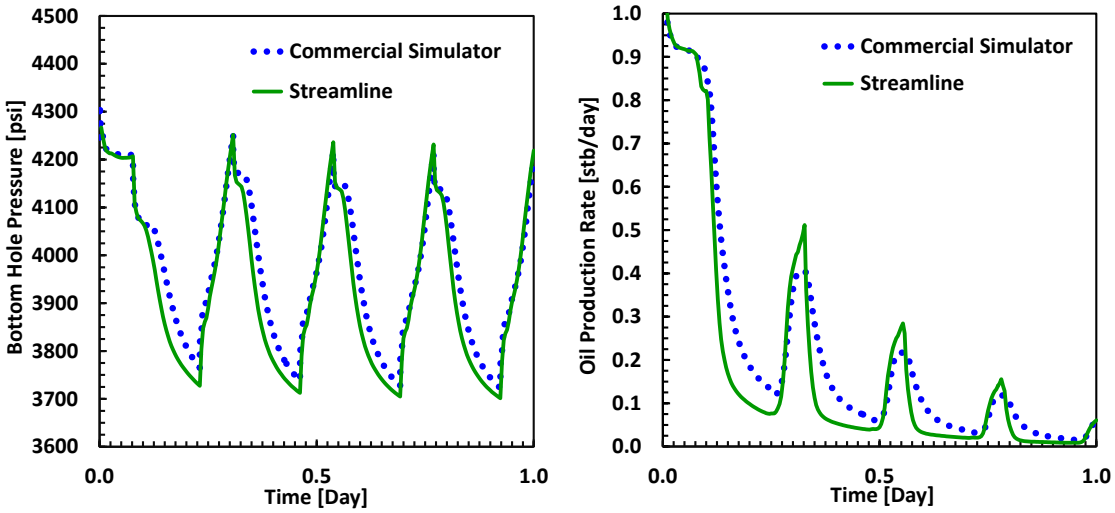

Figure 2.31: The simulation results of the injection bottom hole pressure (left) and oil production rate (right) by 2D heterogeneous problem. The blue dot by commercial simulator and green line by developed model.

2.7.4 2-Dimension Cross-Section

The model is tested with 2D cross section homogeneous media. Figure 2.32 shows the schematic view of the cross section case with streamlines. The injector is now located on the top left side of the reservoir. Because of isotropic media (k_v = k_h), the effect of the gravity is dominant in this case. Now the streamline-based simulation uses operator splitting method to describe the effects of the gravity. The gas-oil and oil-water contact is outside of the reservoir domain.

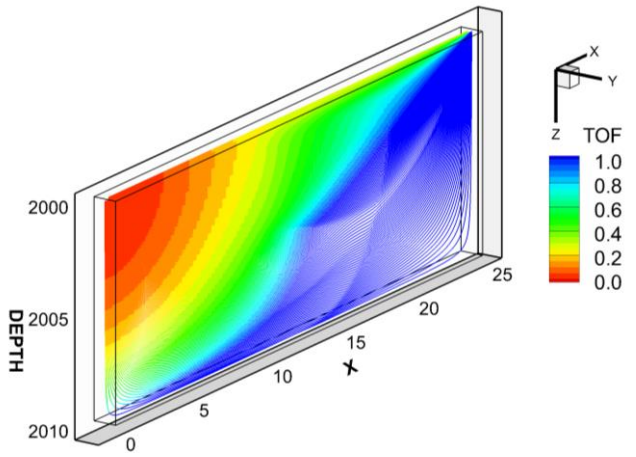

Figure 2.32: The Streamline distribution by cross section homogeneous case, contoured with time-of-flight.

The contrast of the density of water/oil = 2.0 and oil/gas = 10 at initial average reservoir pressure. Through the WAG process, the injected water is going to sweep the bottom and gas will sweep the top part of the reservoir. The counter-flow occurs at the middle depth of the reservoir. The result of saturation distribution is shown in Figs. 2.33-36.

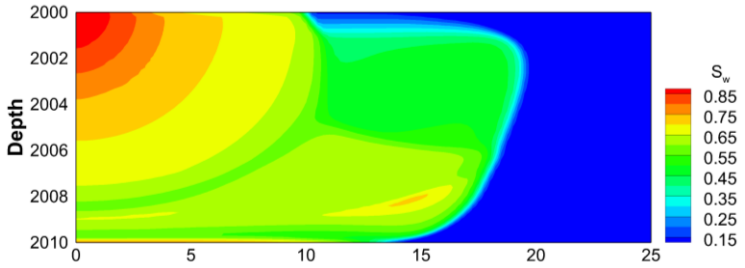

Figure 2.33: Water saturation at 2nd WAG cycle, commercial simulator.

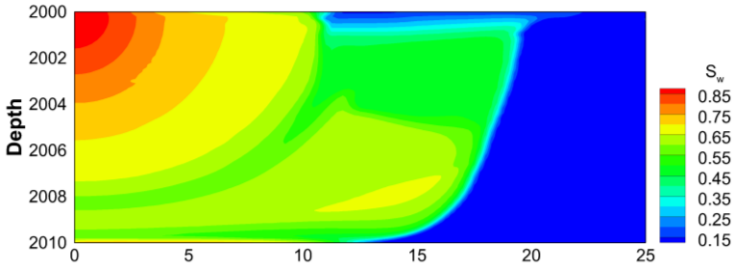

Figure 2.34: Water saturation at 2nd WAG cycle, developed model.

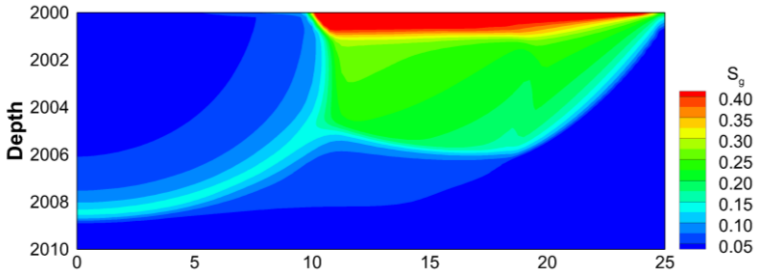

Figure 2.35: Gas saturation at 2nd WAG cycle, commercial simulator.

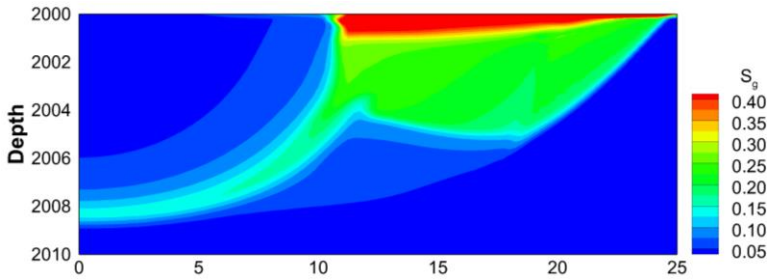

Figure 2.36: Gas saturation at 2nd WAG cycle, developed model.

Figure 2.37 shows the production result of the injector bottom hole pressure and production rate. Again the result of bottom hole pressure showed a good agreement with commercial simulator. The oil production rate, however, showed some fluctuation at the beginning of the simulation. It can be seen that the commercial simulator, however, has larger fluctuation compared to the developed model. The possible reason for this is because of the large time stepping compared with commercial simulator.

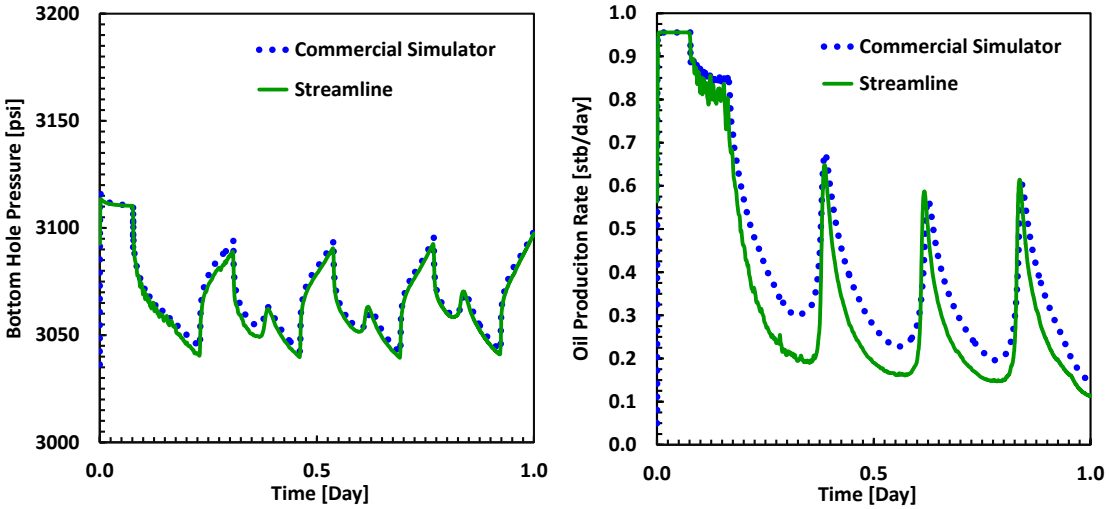

Figure 2.37: The simulation results of the injection bottom hole pressure (left) and oil production rate (right) by 2D cross-section problem. The blue dot by commercial simulator and green line by developed model.

2.7.5 SPE10 Comparative Model

We now demonstrate the applicability of the proposed streamline simulation for the Tenth SPE comparative model (Christie and Blunt 2001). The original purpose of the benchmark case is to compare the performance of different simulators or algorithms, as well as upscaling techniques. Here, we use original model to verify our developed simulator. The model has a simple geometry, with no top structure or faults, as shown in Figure 2.38.

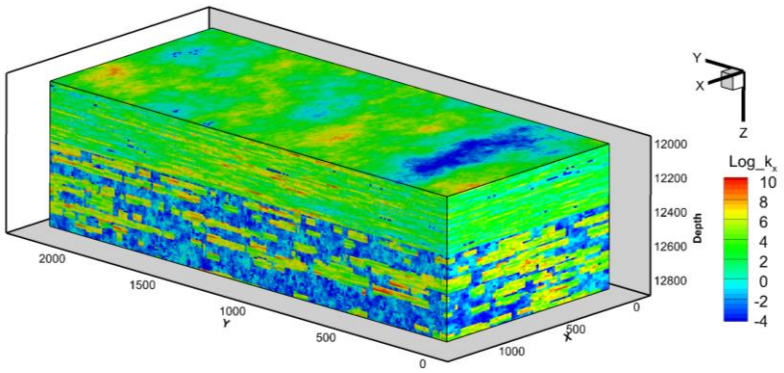

Figure 2.38: Permeability distribution of the 10th SPE comparative model (Natural log scale)

As we see in the permeability field, it is over million cells with a fluvial system. The top part of the model is a Tarbert formation, and is a representation of a prograding near shore environment. The lower part is fluvial system and has strong contrast in both permeability and porosity.

We use this model to compare the commercial simulator and the developed model. The original PVT and rock properties are used. The well configuration is a quarter five

spot, while well is penetrated through top to bottom of the layer. The other parameters are summarized in Table 2.6.

Table 2.6: Reservoir parameters for SPE10 comparative solution

Parameter Name	Value
Grid Dimension	(nx,ny,nz) = (60,220,85)
Permeability	Figure 2.38
Pore compressibility	1.0E-6 [psi^{-1}]
B_w, c_w μ_w	1.1, 3.1E-6 [psi^{-1}] 0.3 [cp]
B_o, μ_o (mean of table)	1.025, 3.0
ρ_o, ρ_w (surface)	53,64 [lb/cft]
Relative permeability	$k_{rw} = S_w^2$, $k_{ro} = S_o^2$
Injector constraint	1000 [rb/day] (0.75PVI)
Producer constraint	4000 [psi], top
Simulation time	6000 [day]
Pressure time step	30.0 [day]

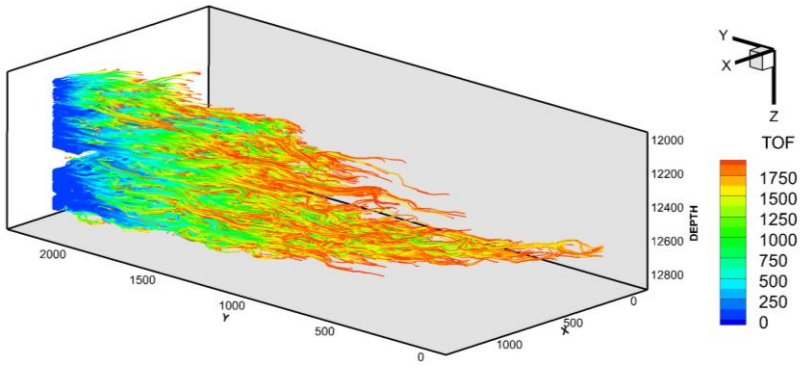

Figure 2.39: Streamline distribution contoured by time-of-flight, SPE10 quarter five spot pattern.

Figure 2.39 shows the streamline distribution at the beginning of the simulation, contoured by time-of-flight. As shown in streamline distribution, there is no injection at

the middle of the injector. This is due to either low permeability or no cross flow allowed within a well for the developed simulator, same as commercial model. In general, faster water front propagation can be expected at the lower part of the reservoir.

Figs. 2.40-41 shows the pressure and water saturation distribution calculated by commercial simulator and the developed model. The pressure distribution has the same profile and we could not find any clear differences. The overall shape of the saturation map is similar, while there are difference in the shape and location of the front.

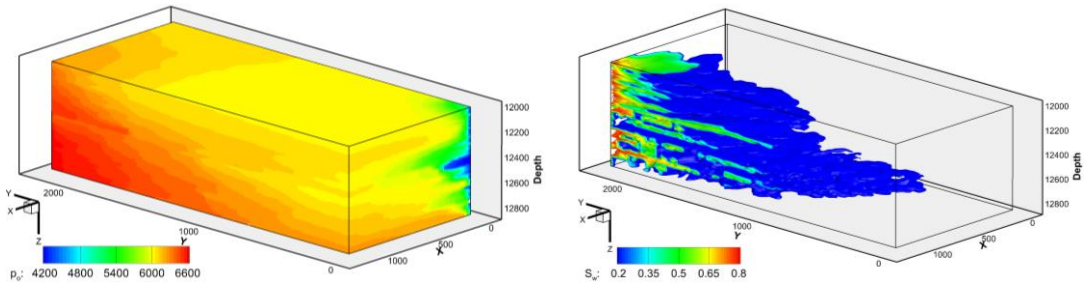

Figure 2.40: Pressure (left) and water saturation distribution (right), by commercial simulator.

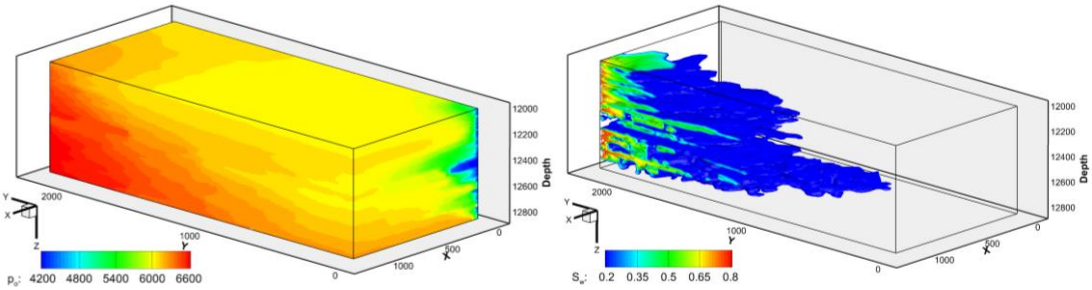

Figure 2.41: Pressure (left) and water saturation distribution (right), by streamline-based simulator.

Figure 2.42 shows the oil production rate of a production well. The overall level of agreement is good, despite the fact that the time step size is 10 times larger for the streamline-base a simulation.

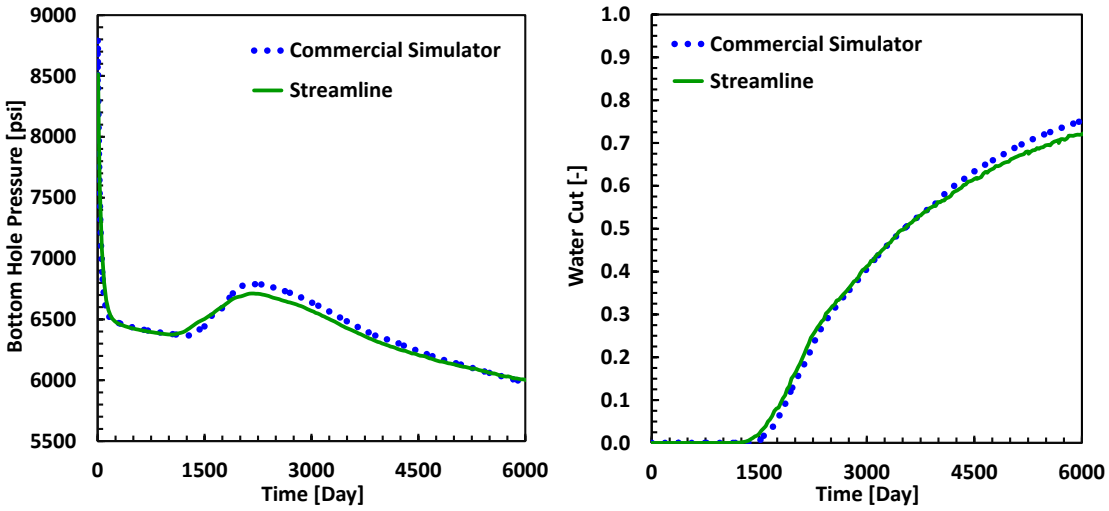

Figure 2.42: The simulation results of the injection bottom hole pressure (left) and oil production rate (right) by SPE10 model. The blue dot by commercial simulator and green line by developed model.

2.7.6 Brugge Waterflood Benchmark

The Brugge reservoir model was used for an international benchmark study of history matching and water flooding optimization (Peters *et al.* 2009). The structure of the Brugge field consists of an east/west elongated half-dome with a large boundary fault at its northern edge and one internal fault with a modest throw as shown in Figs. 2.43-46. The model has 10 years of production history with 20 producers and 10 injectors, with 3 dimensional field discretized by 139×48×9 grid blocks. The Figure 2.43 shows the overall view of the Brugge field contoured by oil saturation distribution.

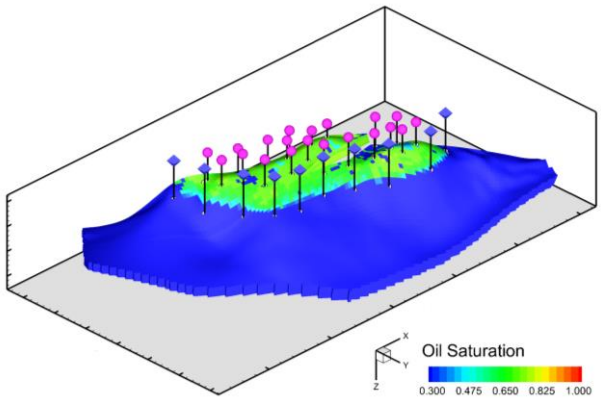

Figure 2.43: Brugge benchmark case, well locations and initial oil saturation distribution.

The Brugge benchmark case is designed for history matching. A total of 104 realizations of permeability and porosity are available. Here, the objective is to demonstrate the developed streamline simulator and thus, we use first realization of permeability, porosity, saturation table (facies ids) and net to gross ratio. The difficulties of this model are as follows. First, equilibrium condition needs to be calculated using

given oil-water contact and capillary pressure table. Second, the model is given by the corner point grid with complex well trajectory. The treatment of the corner point model for grid transmissibility and well transmissibility is described in Appendix. A. The net to gross ratio and saturation table needs to be handled correctly to simulate Brugge field correctly. The given major reservoir static properties are shown in Figure 2.44.

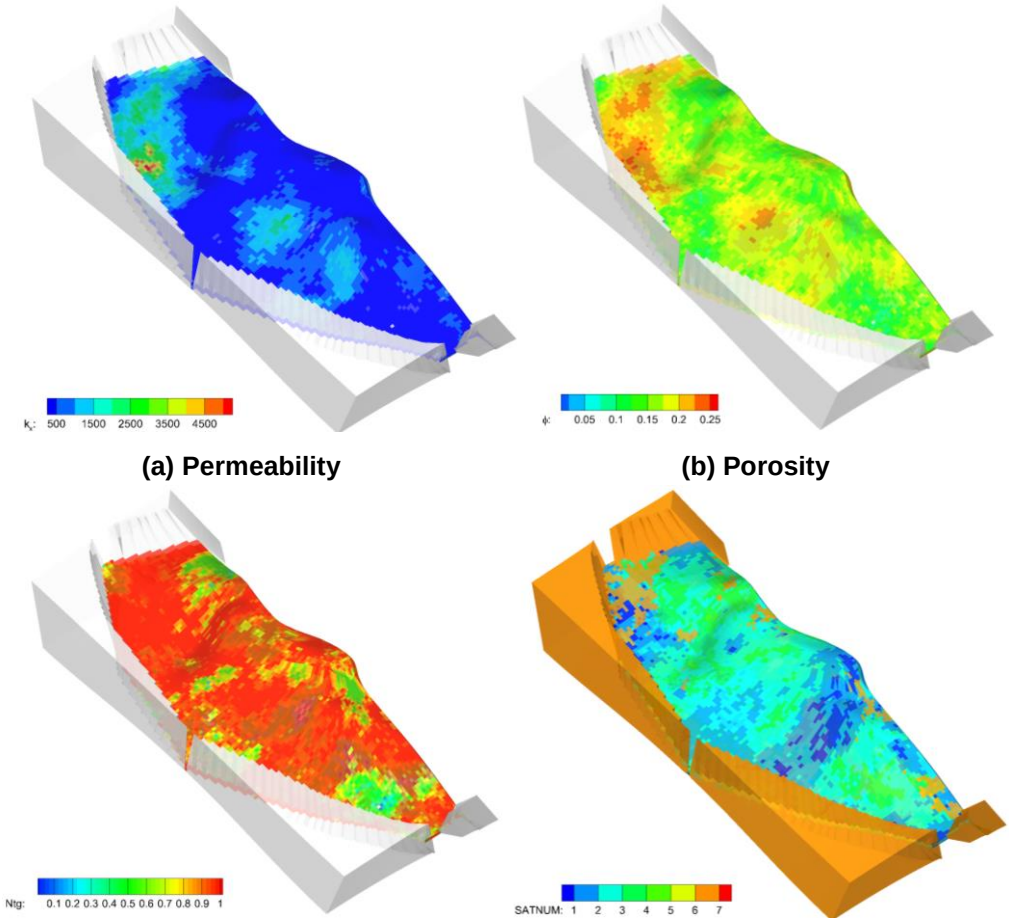

(a) Permeability **(b) Porosity**

(c) Net to gross ratio **(d) Saturation table**

Figure 2.44: Initial static properties of the Brugge benchmark case.

The simulation is conducted for 10 years with a constant injection rate of 1000 bbl/day for each well. The producer is given by the bottom hole pressure. The other properties used for Brugge benchmark scenario is summarized in Table 2.7.

Table 2.7: Reservoir parameters for Brugge benchmark scenario

Parameter Name	Value
Grid dimension	(nx,ny,nz) = (139,48,9)
Permeability	Fig. 2.44 (a)
Porosity	Fig. 2.44 (b)
Net to Gross Ratio	Fig. 2.44 (c)
Rock table	Fig. 2.44 (d)
Pore compressibility	3.5E-6 [psi^{-1}]
B_w, c_w, μ_w	1.0[rb/stb], 3.E-6 [psi^{-1}] 0.32 [cp]
B_o, μ_o (mean of table)	0.98[rb/stb], 1.25 [cp]
Surface density (oil,water)	56,62.6 [lb/cft]
Maximum capillary pressure	26 [psi]
Injector constraint	1000 [rb/day] (0.75PVI)
Producer constraint	4000 [psi], top
Simulation time	6000 [day]
Pressure time step	30.0 [day]

Figure 2.45 shows the oil phase pressure distribution of top view after 0.5 year of the simulation. The pressure field is compared with commercial simulator and a good agreement was obtained. One point needs to be addressed here is that due to the existence of the fault, the pressure field has discontinuities at the top of the reservoir. The difference between commercial simulator and our model can be seen near the fault, which is caused by the difference of fault treatment.

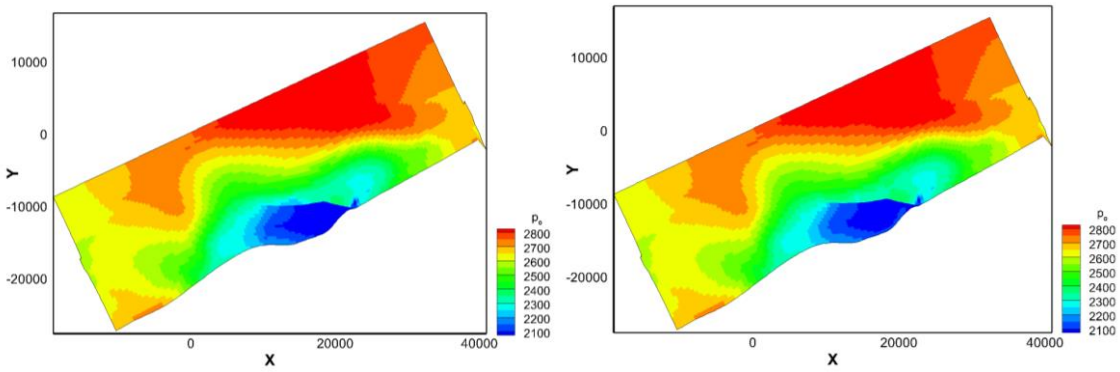

Figure 2.45: Pressure distribution of 2nd time step: Left figure by commercial simulator with non-neighbor connection, right figure by developed model.

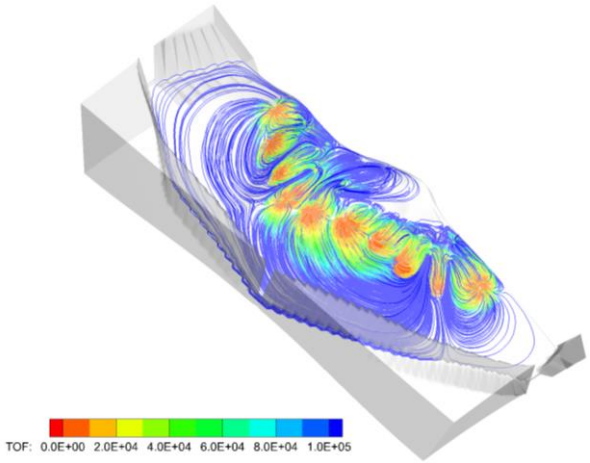

Figure 2.46: Streamline distribution of Brugge benchmark case, contoured by time-of-flight.

Streamline is traced using pressure and flux field, shown in Figure 2.46. The contour describes the time-of-flight and it clearly captures the existence of the fault. Both field water production rate and oil rate are plotted and compared with the result provided by commercial reservoir simulator, in Figure 2.47. An excellent agreement is

obtained here. The break through start right after the injection and production begins, and the difference of the breakthrough time is negligible.

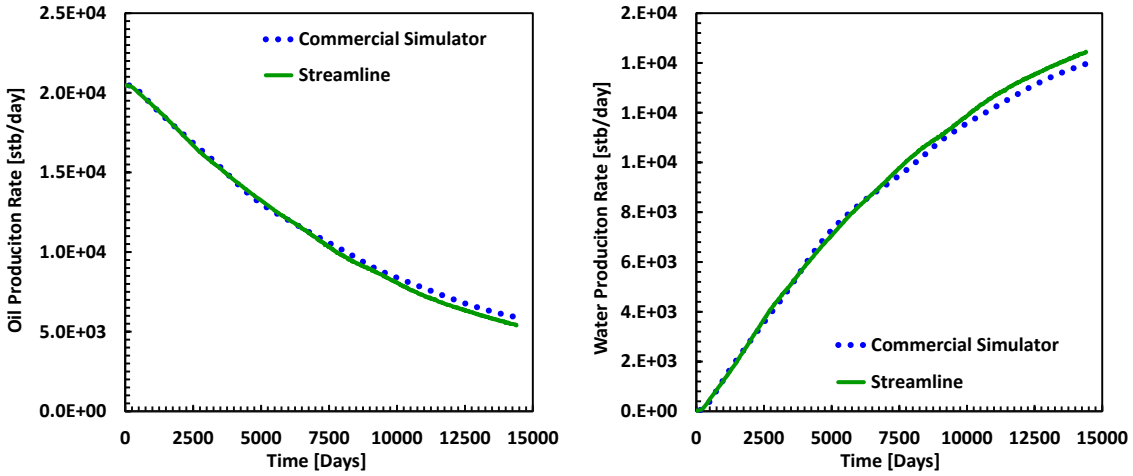

Figure 2.47: The simulation results of the field oil production rate (left) and water production rate (right). The blue dot by commercial simulator and green line by developed model.

The oil saturation is compared at the beginning of simulation to verify the equilibrium calculations. Figure 2.48(a)(b) shows the oil saturation distribution superimposed with oil-water contour plane. Here, the location of the oil-water contact is correctly evaluated by equilibrium calculation. Figure 2.48(c)(d) shows the result after 10 years of water flooding. Here, the overall contact shows good agreement. However, there is faster water front propagation in the commercial simulator near the edge of the fault. This main reason is due to the difference in the treatment of the fault. The commercial simulator creates non-neighbor connection while the developed model does not treat it that way.

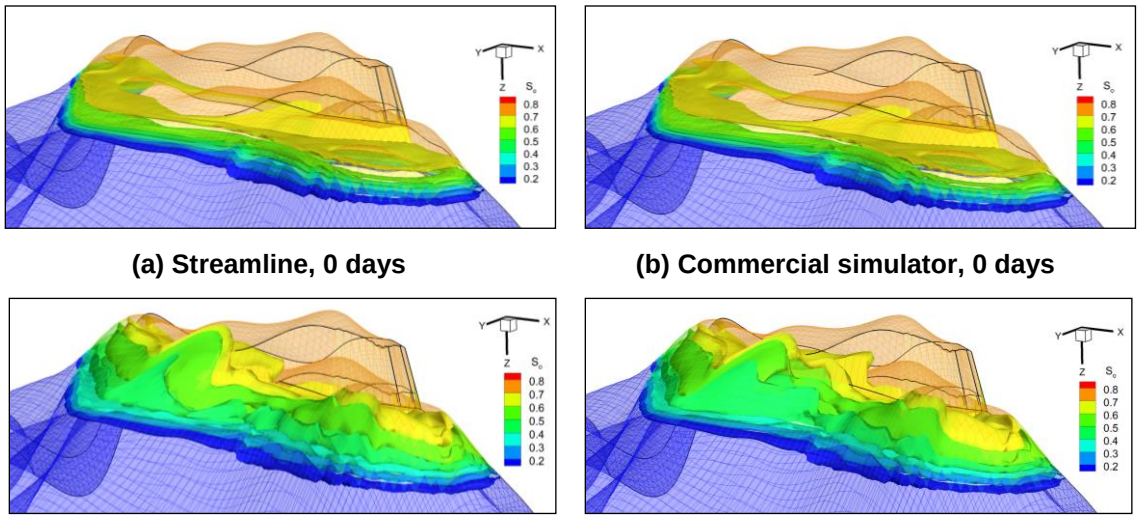

(a) Streamline, 0 days **(b) Commercial simulator, 0 days**

(c) Streamline, 10 years **(d) Commercial simulator, 10 years**

Figure 2.48:Satuarion distribution of (a)(b) beginning of the simulation and (c)(d) after 10 years of waterflood. (a)(c) by streamline method and (b)(d) by commercial simulator.

The one possible reason of the difference in oil production and pressure distribution is due to the treatment of the fault. It is described in technical description that the commercial simulator generates non-neighbor connection between the fault (Schlumberger, 2012b). In order to confirm that, the non-neighbor option is deactivated and we conducted the simulation again. The Figure 2.49 and 2.50 show the water-cut of four individual well and field oil and water producer rate, respectively.

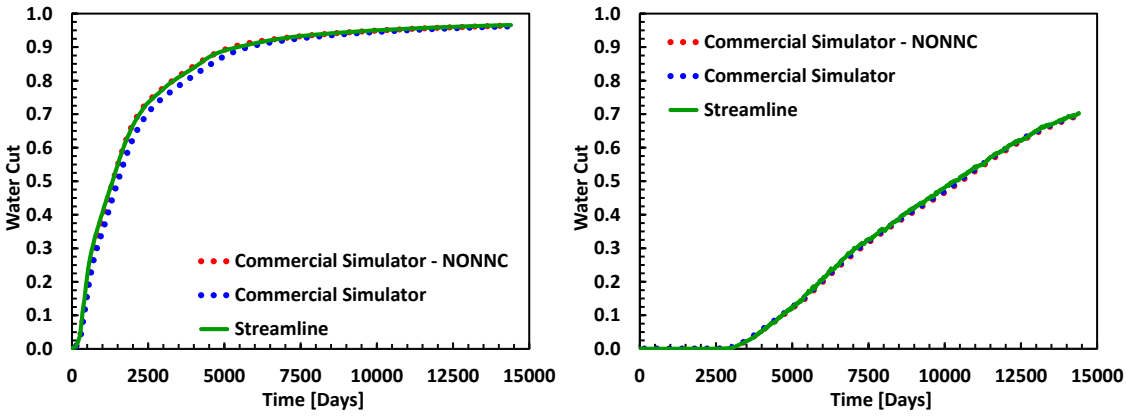

(a) PRD-IP-30

(b) PRD-IP-17

(c) PRD-IP-6

(d) PRD-IP-8

Figure 2.49: The simulation results of the Water-Cut of 4 different producers the red dot line by commercial simulator without non-neighbor connection, the blue dot includes non-neighbor connection.

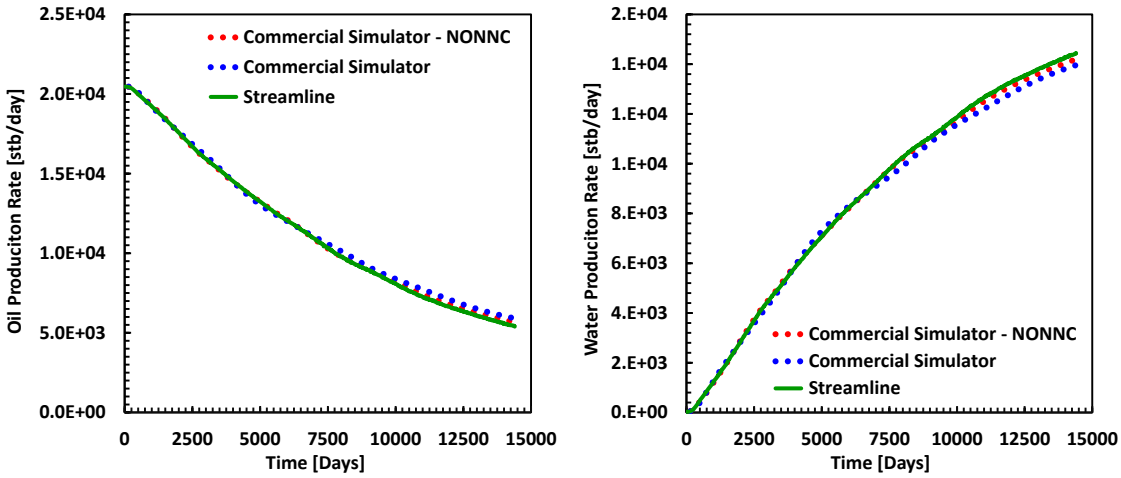

Figure 2.50: The simulation results of the field oil production rate (left) and water production rate (right). The blue dot by commercial simulator and green line by developed model, the red dot line by commercial simulator without non-neighbor connection.

It is clear that without non-neighbor connection, the result of the commercial simulator shows the good agreement with our developed model for both field wise production and well by well comparisons. The treatment of the non-neighbor connection is going to be future work of streamline-based simulation model to make it general for field application to correctly handle complex geometry such as fault, local-grid-refinements (Jimenez, Datta-Gupta, and King 2010, Zhang, King, and Datta-Gupta 2012).

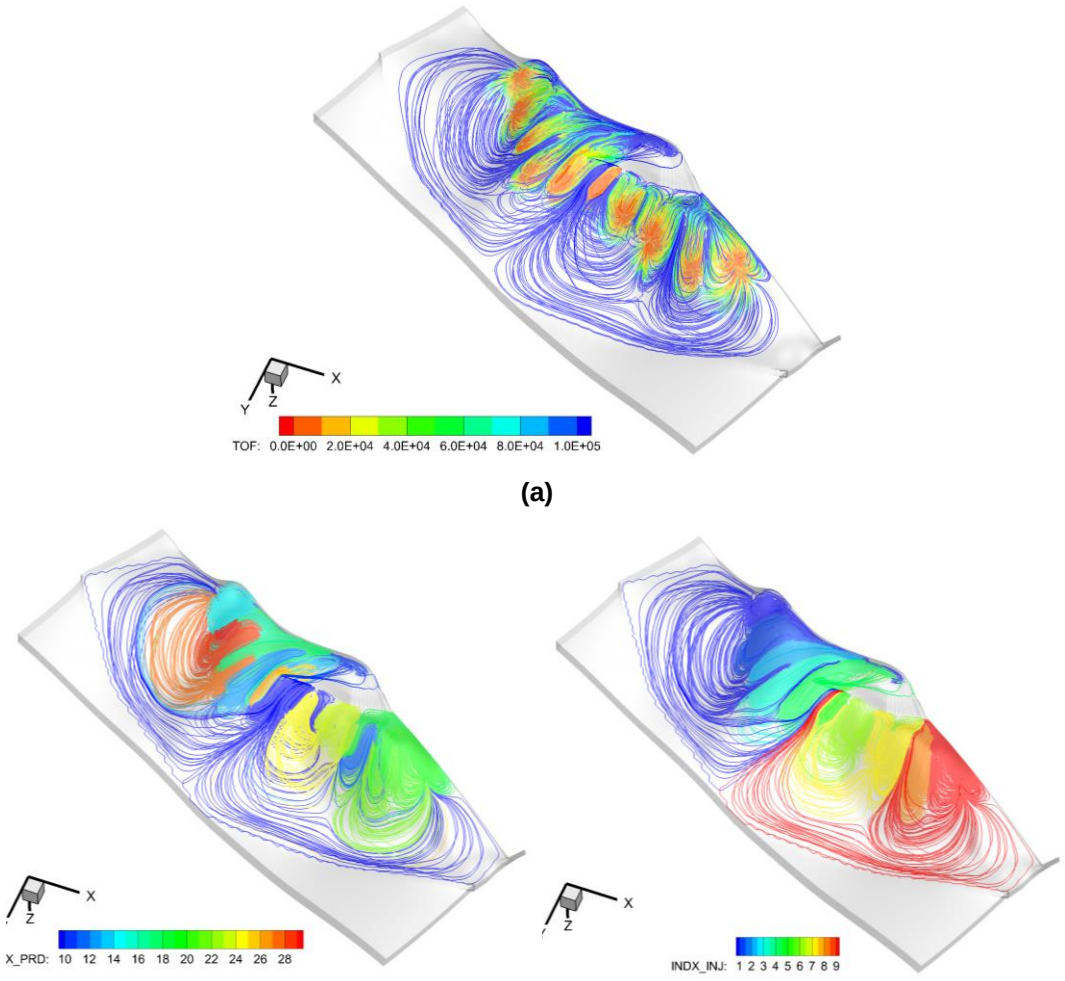

Figure 2.51:Streamline distribution of Brugge benchmark example contoured by (a) Time-of-flight (b) Production well IDs (c) Injection well IDs.

Figure 2.51 shows the streamline distribution colored by time-of-flight (a), producer (b) and injector (c). Using streamlines, it is able to identify drainage region of the individual well and well pair, which is helpful for the application of the history matching and optimization problem, discussed in detail in Chapter IV and V, respectively.

2.8 Chapter Conclusions

In this chapter, we developed a flow simulation model for black oil model and compositional model using the streamline method. We tested the model for 1D, 2D and 3D reservoir, including general corner-point examples. Our approaches with streamline simulation reduce the numerical dispersion and CPU time in some reservoir examples. The conclusions of this chapter are summarized as follows:

1. A streamline-based 3D 3-phase multicomponent model was developed with effect of compressibility and gravity flow by operator splitting technique Implicit and explicit saturation solvers were also implemented and solutions were examined.
2. The formulation with the effective density, expressed in the right-hand side of Eq. 2.67 was confirmed to be a valid and satisfactory approach for the simulation of compressible fluid flow. The high-order discretization scheme of the 1-D saturation equation is also effective to correctly calculate and track displacement fronts.
3. The explicit saturation solver showed accurate fronts in all the tested models. The result of a 1-D reservoir example clearly showed the differences compared with the implicit saturation solver and commercial Fully Implicit method.
4. The implicit saturation solver showed exact matches with commercial fully implicit method for saturation distributions in a 1-D reservoir example.
5. A simulation approach with iterative IMPES was developed, which is a sequential iterative approach for pressure and saturation. In a tested case of WAG injection scenario, the result of the iterative IMPES method showed improvement of the solution.

6. The modeling of the non-neighbor connection is the future work needed for the application to the Brugge benchmark model. The algorithm needs to be developed to detect which grids has a connection between faults and tracing algorithm needs to be implemented accordingly.

CHAPTER III

INCLUSION OF CAPIRRALITY AND GRAVITY ALONG STREMLINE 1D FORMULATION VIA ORTHOGONAL PROJECTION METHOD*

3.1 Chapter Summary

Capillary dominated flows restricts the application of the streamline-based simulation and it is often ignored. One reason is that reservoir simulation by streamline-based approach is well-suited for convection dominant process and often the effect of the capillary is small, and it is convenient to ignore the effect to avoid stability and additional computational cost. However, not only capillary but gravity effects also introduce same problem and gravity is not negligible for water or gas flooding. Hence, in this chapter, we review the treatment of the transverse effects such as gravity and capillarity, and provide an efficient method to properly take into account these effects for streamline simulation without losing computational advantages.

3.2 Literature Review

Several previous studies have discussed the incorporation of capillarity and gravity for streamline simulation. As streamlines are traced to follow the convective flux, there

---

*Part of the data reported in this chapter is reprinted with permission from "A Novel Approach for Incorporation of Capillarity and Gravity Into Streamline Simulation Using Orthogonal Projection" by Tanaka, S., Datta-Gupta, A. and King, M. J. 2013. Paper SPE-163640-MS Presented at the SPE Reservoir Simulation Symposium, 18-20 February, The Woodlands, Texas, U.S.A. Copyright 2014 Society of Petroleum Engineers

Part of the data reported in this chapter is reprinted with permission from "Compositional Streamline Simulation of CO2 Injection Accounting for Gravity and Capillary Effects Using Orthogonal Projection" by Tanaka, S., Datta-Gupta, A. and King, M. J. 2014. Paper SPE-169066-MS Presented at the SPE Improved Oil Recovery Symposium, 12-16 April, Tulsa, Oklahoma, U.S.A. Copyright 2014 Society of Petroleum Engineers

should be no cross flow across streamlines. In order to fully account for capillarity and gravity, operator splitting techniques were first reported by Bratvedt, Gimse, and Tegnander (1996) for gravitational flow and the same approach was applied for capillary driven flow by (Berenblyum *et al.* 2003, Rodriguez, Segura, and Moreno 2003). Berenblyum *et al*. proposed to modify the streamline pressure equations to account for both capillary and gravity forces directly. The modified pressure equation was solved on the finite difference grid and velocities were calculated from the solution. Using their approach, transverse mechanisms are resolved using two sets of spatial discretization. The operator splitting of transverse flow occurs on the three dimensional simulation grid, right after we solve the convective processes along the streamlines. This solution is accurate for linear processes, but as non-linearity increases, the solution deteriorates for large time step lengths. Hence, it is difficult to represent transverse flux especially when the flow is not convective dominant. All of the transverse flows such as gravity segregation, capillarity and diffusion, and unsteady state velocity effects act transverse to the streamlines and need to be represented appropriately.

The improved operator-splitting with correction term has also been studied by several authors (Holden, Karlsen, and Lie 2000, Karlsen *et al.* 2001, Karlsen and Espedal 2007). The basic idea to improve the operator-splitting approach is to take into account the unphysical entropy loss produced by the hyperbolic solver during the convective step. For reservoir simulation, this is done by introducing anti-diffusive concave envelope correction derived from the fractional flow equations. This self-sharpening effect provides unique solutions which satisfy the entropy condition, even for

large time steps. However, this approach has not been introduced into commercial streamline reservoir simulators because of the complexity in handling the concave envelope construction for general reservoir simulation. Hence, the solutions shown in the literature are for simple cases, such as 1-dimenstional homogeneous model. Multidimensional heterogeneous cases are also described in some papers, however, fluids are immiscible, rock and fluids are incompressible and the viscosity or mobility does not depend upon pressure. Once problems become more general, such as multi-phase multicomponent miscible and compressible cases, this approach is not feasible because if the complexity of finding a different anti-diffusive correction term for every cell face during each time step of a simulation.

In order to avoid the need for a concave envelope correction, we introduce an orthogonal projection method which includes components of gravity and capillarity along streamline. Using orthogonal projection, the flux contributed by capillary and gravity is decomposed into components parallel and perpendicular to the total velocity. Conventionally, convective flow is solved by operator-split approach and capillary and gravity flux is solved later on the grid. Our approach includes longitudinal flux of capillary and gravity together with convection along the streamline. The decomposed capillarity and gravity flux components parallel to the streamline are included within the solution of the convective flow equations. As we mentioned previously, streamlines follows total velocity and not all of the flux is aligned with the streamlines. The non-parallel transverse flux needs to be evaluated on the three dimensional grid in the corrector step after calculating saturations along streamlines. Using orthogonal

projection, we also reduce the magnitude of the transverse flux corrections, allowing for larger time steps. However, the most important aspect of this approach is that it removes the requirement for anti-diffusive corrections.

3.3 Background and Methodology

For clarity of exposition, we will first illustrate the approaches to the incorporation of capillarity and gravity using operator splitting and orthogonal projection using 1D Buckley-Leverett flow for a homogeneous model. The saturation transport equation for incompressible flow with uniform porosity and permeability is given by the following equation:

$$\phi \frac{\partial S_w}{\partial t} + \frac{\partial u_w}{\partial x} = 0 \quad \cdots\cdots\cdots\cdots\cdots\cdots\cdots\cdots\cdots\cdots\cdots\cdots\cdots\cdots\cdots\cdots \quad (3.1)$$

The water phase velocity construction includes both convection and capillary diffusion terms ((Datta-Gupta and King 2007).

$$u_w = u_t \frac{\lambda_w}{\lambda_t} + k \frac{\lambda_o \lambda_w}{\lambda_t} \frac{\partial p_{cow}}{\partial x} \quad \cdots\cdots\cdots\cdots\cdots\cdots\cdots\cdots\cdots\cdots\cdots\cdots\cdots\cdots\cdots\cdots \quad (3.2)$$

In the operator splitting approach, the time step in Eq. 3.1 is split into two, each corresponding to different components of the flux of Eq. 3.2, that is, $\frac{\partial}{\partial t} \rightarrow \frac{\partial}{\partial t_1} + \frac{\partial}{\partial t_2}$. In order to illustrate our approach, we will find the solution to Eqs. 3.1-2 using operator splitting including the anti-diffusive correction (Datta-Gupta and King 2007). The relevant equations are:

$$\phi \frac{\partial S_w}{\partial t_1} + u_t \frac{\partial F_w}{\partial x} = 0 \quad where \quad F_w = \frac{\lambda_w}{\lambda_t} \qquad \cdots\cdots\cdots\cdots\cdots\cdots\cdots\cdots \quad (3.3a)$$

$$\phi \frac{\partial S_w}{\partial t_2} + \frac{\partial}{\partial x}\left(u_t \cdot \left(F_w - \tilde{F}_w\right) + \frac{\lambda_w \lambda_o}{\lambda_t} \frac{\partial p_{cow}}{\partial x} \right) = 0 \qquad \cdots\cdots\cdots\cdots\cdots\cdots\cdots\cdots \quad (3.3b)$$

Here $\tilde{F}_w$ is the concave envelope of F_w in Figure 3.1, which depends upon the fluid viscosity and the left and right states for the local Riemann problem. In Figure 3.1, the left (initial) state is at a saturation of 0.1. For a full field simulation with variable saturation and intersecting flood fronts, this construction will vary throughout the reservoir. With the inclusion of gravity, the Riemann problem would also depend upon the permeability and velocity. The convective flux term in Eq. 3.3b is anti-diffusive: $\left(F_w - \tilde{F}_w\right) < 0$. This construction recognizes that the solution to Eq. 3.3a converges to the concave envelope, and so the flux which should be included in the second equation has a convective term which includes the difference.

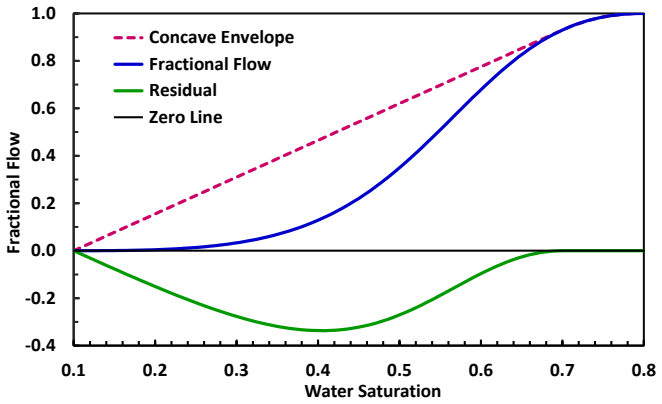

Figure 3.1: Fractional flow and concave envelope construction, example of water saturation from 0.1 to 0.8.

When this approach is implemented in multiple dimensions, we need a corrector time step to include all of the terms transverse to the streamline. However, because the anti-diffusive corrections are parallel to the total velocity, they have no contribution to the corrector step, and need not be calculated. Specifically, if $\vec{u}_w$ is the water flux including gravity and capillarity, then operator splitting with the anti-diffusive correction solves the sequence of equations:

$$\phi \frac{\partial S_w}{\partial t_1} + \nabla \bullet \left(\vec{u}_t F_w \right) = 0 \quad \cdots\cdots\cdots\cdots\cdots\cdots\cdots\cdots\cdots\cdots\cdots\cdots\cdots\cdots \quad (3.4a)$$

$$\phi \frac{\partial S_w}{\partial t_2} + \nabla \bullet \left(\vec{u}_w - \vec{u}_t \cdot \tilde{F}_w \right) = 0 \quad \cdots\cdots\cdots\cdots\cdots\cdots\cdots\cdots\cdots\cdots\cdots\cdots\cdots\cdots \quad (3.4b)$$

The leading convective flux term in the second equation consists of the anti-diffusive correction, $\vec{u}_t \cdot \left(F_w - \tilde{F}_w \right)$ as shown in Eq. 3.3b. If the anti-diffusive corrections are not included, the pair of equations is solved as

$$\phi \frac{\partial S_w}{\partial t_1} + \nabla \bullet \left(\vec{u}_t F_w \right) = 0 \quad \cdots\cdots\cdots\cdots\cdots\cdots\cdots\cdots\cdots\cdots\cdots\cdots\cdots\cdots \quad (3.5a)$$

$$\phi \frac{\partial S_w}{\partial t_2} + \nabla \bullet \left(\vec{u}_w \right) = 0 \quad \cdots\cdots\cdots\cdots\cdots\cdots\cdots\cdots\cdots\cdots\cdots\cdots\cdots\cdots \quad (3.5b)$$

The fractional flow F_w in Eq. 3.3a is defined in the absence of gravity and capillarity. From Eq. 3.2 we can define a total fractional flow f_w including capillarity and solve the saturation transport equation without splitting the capillary term.

$$\phi \frac{\partial S_w}{\partial t} + u_t \frac{\partial f_w}{\partial x} = 0 \quad where \quad f_w = \frac{u_w}{u_t} = \frac{\lambda_w}{\lambda_t} + \frac{k}{u_t} \frac{\lambda_o \lambda_w}{\lambda_t} \frac{\partial p_{cow}}{\partial x} \quad \cdots\cdots\cdots\cdots \quad (3.6)$$

The dominant effect of capillarity is to spread the saturation profile in the vicinity of the Buckley-Leverett saturation front and to enhance the fractional flow, F_w, until the fractional flow f_w approaches the concave envelope, $\tilde{\tilde{F}}_w$. With capillarity included in the solution to the convective equations, there is no need for an anti-diffusive correction. This forms the basic for our proposed orthogonal projection.

In contrast to Eq. 3.4, when utilizing orthogonal projection, we utilize the fractional flow including gravity and capillarity. The water fractional flow parallel to the total velocity is given by $f_w = \vec{u}_w \bullet \vec{u}_t / u_t^2$. This leads to the following sequence of equations:

$$\phi \frac{\partial S_w}{\partial t_1} + \nabla \bullet \left(\vec{u}_t f_w \right) = 0 \quad \cdots\cdots\cdots\cdots\cdots\cdots\cdots\cdots\cdots\cdots\cdots\cdots\cdots\cdots\cdots\cdots \quad (3.7a)$$

$$\phi \frac{\partial S_w}{\partial t_2} + \nabla \bullet \left(\vec{u}_w - \vec{u}_t \cdot f_w \right) = 0 \quad \cdots\cdots\cdots\cdots\cdots\cdots\cdots\cdots\cdots\cdots\cdots\cdots\cdots\cdots\cdots\cdots \quad (3.7b)$$

If the anti-diffusive term had appeared in the second equation, it would have been of the form $\vec{u}_t \cdot \left(f_w - \tilde{\tilde{F}}_w \right)$. Unlike the other formulation, this term vanishes since f_w converges to $\tilde{\tilde{F}}_w$ (King and Dunayevsky 1989). In addition, by construction, the flux in the second equation is orthogonal to the total velocity:

$$\vec{u}_w - \vec{u}_t \cdot f_w = \vec{u}_w - \vec{u}_t \cdot \vec{u}_w \bullet \vec{u}_t / u_t^2 = \left(\vec{\vec{1}} - \hat{u}_t \hat{u}_t \right) \bullet \vec{u}_w = \vec{u}_{w\perp} \quad \cdots\cdots\cdots\cdots\cdots\cdots \quad (3.7c)$$

The Eq. 3.7b consists solely of the transverse flux. By projecting the water velocity in terms of its components parallel and transverse to the total velocity is illustrated in Figure 3.2.

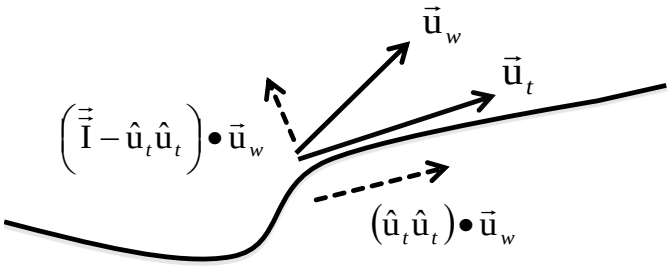

Figure 3.2: Schematic view of water flow along a streamline; dotted arrows show the split of the water flux parallel and perpendicular to the streamline (total velocity).

Although all of the formulations use operator splitting in some form, for convenience we will call the solution of the flow equations following Eq. 3.4 as "Operator Splitting with Anti-Diffusive corrections" (OSAD), the solution of Eq. 3.5 as "Operator Splitting" (OS), and we call the solution of the flow equations following Eq. 3.7 as "Orthogonal Projection" (OP).

3.3.1 Orthogonal Projection in Multidimensions

To illustrate our proposed approach in multidimension, we consider compressible 2-phase immiscible oil and water flow with capillarity and gravity effects. As with any streamline simulator to start with, pressures are solved in a 3D domain using conventional finite difference calculations, and the saturation equations are solved along 1D streamlines. This is followed by a corrector step, again back in the 3D domain. The advantage of the "predictor" step along streamline is that it allows large time steps (King, Osako, and Datta-Gupta 2005). Previous work has shown that the time step is limited by a CFL construction based upon the change in velocity during a time step, not

the velocity itself (Osako, Datta-Gupta, and King 2004, Cheng *et al.* 2006). The governing equations are established from the material balance of each fluid phase.

$$\frac{\partial}{\partial t}\left(\phi\,\rho_\alpha S_\alpha\right)+\nabla\bullet\left(\rho_\alpha\vec{u}_\alpha\right)+\rho_\alpha q_\alpha=0\ ,\ \alpha=o,w \quad \cdots\cdots\cdots\cdots\cdots\cdots \quad (3.8)$$

The phase velocity of each phase is defined using Darcy's law as

$$\vec{u}_\alpha=-\lambda_\alpha\vec{\vec{k}}\bullet\left(\nabla p_\alpha-\rho_\alpha g\nabla D\right) \quad \cdots\cdots\cdots\cdots\cdots\cdots\cdots\cdots\cdots\cdots \quad (3.9)$$

The expression in Eq. 3.9 includes the gradient of the phase pressure and the gravitational potential multiplied by the relative phase mobility and the permeability. The latter may be anisotropic and a tensor. We supply the capillary pressure as a function of water saturation for this model, $p_{cow}=\left(p_o-p_w\right)$, and also define the density difference, $\Delta\rho=\rho_w-\rho_o$, and the total velocity, $\vec{u}_t=\vec{u}_w+\vec{u}_o$. This allows us to express the phase velocity, for example for water, as a fractional flow as given below.

$$\vec{u}_w=F_w\cdot\vec{u}_t+\frac{\lambda_w\lambda_o}{\lambda_t}\vec{\vec{k}}\bullet\left(\nabla p_{cow}+\Delta\rho g\nabla D\right)=f_w\cdot\vec{u}_t+\vec{u}_{w\perp} \quad \cdots\cdots\cdots\cdots \quad (3.10a)$$

$$f_w=\frac{\vec{u}_t\bullet\vec{u}_w}{u_t^2}=F_w+\frac{\lambda_w\lambda_o}{\lambda_t}\frac{\vec{u}_t}{u_t^2}\bullet\vec{\vec{k}}\bullet\left(\nabla p_{cow}+\Delta\rho g\nabla D\right) \quad \cdots\cdots\cdots\cdots\cdots\cdots \quad (3.10b)$$

This equation includes convective, capillary driven and gravity driven contributions to the fractional flow

3.3.2 1D Orthogonal Projection of Saturation Equation

All of the operator splitting formulations utilize the time-of-flight as a spatial coordinate, although the details of the implementation can be different for each. For instance, for Eq. (3.7a), $\nabla \bullet (\vec{u}_t f_w) = \vec{u}_t \bullet \nabla f_w + f_w \nabla \bullet \vec{u}_t = \phi \frac{\partial f_w}{\partial \tau} + f_w \nabla \bullet \vec{u}_t$ and we obtain:

$$\frac{\partial S_w}{\partial t_1} + \frac{\partial f_w}{\partial \tau} = -\frac{f_w}{\phi}(\nabla \bullet \vec{u}_t) \quad \cdots\cdots\cdots\cdots\cdots\cdots\cdots\cdots\cdots\cdots\cdots\cdots\cdots\cdots \quad (3.11)$$

This is the one dimensional saturation equation expressed using the time-of-flight as the spatial coordinate. Eqs. 3.5a and 3.6a are of the same form with f_w replaced by F_w.

Of all the operator split formulations, our proposed orthogonal projection includes more of the physics of the flow in its 1D flow equation than the others. Given the velocity field obtained from the solution of Eq. 3.9, we need to express the fractional flow, Eq. 3.10b, as an expression along the streamlines. We first need to approximate the spatial derivative of the capillary pressure.

$$\begin{aligned} \vec{u}_t \bullet \vec{\vec{k}} \bullet \nabla p_{cow} \approx \vec{u}_t \bullet \vec{\vec{k}} \bullet \hat{u}_t \hat{u}_t \bullet \nabla p_{cow} &= \left(\hat{u}_t \bullet \vec{\vec{k}} \bullet \hat{u}_t \right) \left(\vec{u}_t \bullet \nabla p_{cow} \right) \\ &= \left(\hat{u}_t \bullet \vec{\vec{k}} \bullet \hat{u}_t \right) \left(\phi \frac{\partial p_{cow}}{\partial \tau} \right) \end{aligned} \quad \cdots\cdots\cdots \quad (3.12)$$

The effective permeability is in the direction of convective flow, as is the spatial derivative of the capillary pressure. In other words, this term dominates compared to the transverse components. The latter might be small compared to this term due to the small off-diagonal terms in the permeability tensor or due to relatively small capillary pressure gradients. In a formulation that only considers isotropic permeability, the transverse

terms vanish identically. In contrast, the gravity term always depends upon the vertical permeability.

$$\vec{u}_t \bullet \vec{\vec{k}} \bullet \nabla D = (\vec{u}_t \bullet \nabla D)\left(\nabla D \bullet \vec{\vec{k}} \bullet \nabla D\right) = k_v \cdot (\vec{u}_t \bullet \nabla D) \quad \cdots\cdots\cdots\cdots\cdots\cdots\cdots \quad (3.13)$$

We use depth, D, as the vertical coordinate, to avoid any ambiguity in the direction of *z*.

3.3.3 Corrector Term for the Underlying Grid

Eq. 3.7a is the "predictor" step and Eq. 3.7b is the "corrector" step. In each of the operator split formulations, the initial condition for $\frac{\partial}{\partial t_2}$ is the solution to the first equation at time t_1. As we examine the performance of these methods we will also show the impact of refining the split formulation, i.e., of solving the equations for $\frac{\partial}{\partial t_1}$ and $\frac{\partial}{\partial t_2}$ sequentially multiple times with smaller sub-time steps instead of solving them with a single large time step. As you might expect, as the degree of non-linearity increases, the requirement for sub-time steps also increases.

Of the three formulations, OSAD is the most difficult to implement, because of the need for the concave envelope construction. OS and OSAD each includes both longitudinal and transverse flux terms in the corrector step. OP only includes the transverse flux in its corrector step. From Eq. 3.10b we have water flux along streamlines:

$$\vec{u}_w = F_w \cdot \vec{u}_t + \frac{\lambda_w \lambda_o}{\lambda_t} \vec{\vec{k}} \bullet \left(\nabla p_{cow} + \Delta \rho g \nabla D \right) \quad \cdots\cdots\cdots\cdots\cdots\cdots\cdots\cdots \quad (3.14a)$$

And water flux across streamlines:

$$\vec{u}_{w\perp} = \left(\vec{\vec{I}} - \hat{u}_t \hat{u}_t \right) \bullet \vec{u}_w = \frac{\lambda_w \lambda_o}{\lambda_t} \left(\vec{\vec{I}} - \hat{u}_t \hat{u}_t \right) \bullet \vec{\vec{k}} \bullet \left(\nabla p_{cow} + \Delta \rho g \nabla D \right) \quad \cdots\cdots\cdots \quad (3.14b)$$

OP has the smallest corrector term of the three methods, making it most effective candidate for operator splitting (Tanaka, Datta-Gupta, and King 2013).

3.4 Numerical Examples by Black Oil Model

In this section we apply the OP approach to a series of test problems in 1-D, 2-D and 3-D and compare performance with the conventional operator splitting method and with anti-diffusive correction (OS, OSAD). To start with, we specify relative-permeability and capillary pressure functions. For simplicity we will use relative permeability and capillary pressures following Corey's and Ferreira's models (Corey 1954, Ferreira and Descant 1986), respectively. These models describe the relative-permeability and capillary pressures as a function of saturation.

$$k_{ro} = k_{ro}(S_{wc}) \left(\frac{1 - S_w - S_{or}}{1 - S_{wr} - S_{or}} \right)^{n_o} \quad \cdots\cdots\cdots\cdots\cdots\cdots\cdots\cdots\cdots\cdots\cdots\cdots \quad (3.15a)$$

$$k_{rw} = k_{rw}(S_{oir}) \left(\frac{S_w - S_{wr}}{1 - S_{wr} - S_{or}} \right)^{n_w} \quad \cdots\cdots\cdots\cdots\cdots\cdots\cdots\cdots\cdots\cdots\cdots\cdots \quad (3.15b)$$

$$p_{cowt} = c_{pc} \sqrt{\phi k_h^{-1}} \cdot \begin{cases} \left(S_{wn} - S_w \right)^{n_{pc}} & S_{wr} \le S_w \le S_{wn} \le 1 - S_{or} \\ -\left(S_w - S_{wn} \right)^{n_{pc}} & S_{wn} \le S_w \le 1 - S_{or} \end{cases} \quad \cdots\cdots\cdots\cdots \quad (3.15c)$$

For the relative permeability curves, S_{or}, = 0.2 and S_{wr} = 0.1 are used as the residual oil and irreducible water saturations. The other parameters are defined as $k_{ro}(S_{wr})$ = 1.0, $k_{rw}(S_{or})$ = 0.4, n_o, = 2 and n_w = 2.5. These parameters describe a water-wet relative permeability. The capillary pressure curve scales as a function of porosity and permeability according to the Leverett J-function and we have used S_{wn}=0.7. The water density is ρ_w=60 lb/cft and the oil density is taken as half that of water. Viscosity of water is used as a constant value, 1cp through all the cases. Oil viscosity is also 1cp and constant value through 1D verification.

The workflow for the OP formulation is summarized in Figure 3.3.

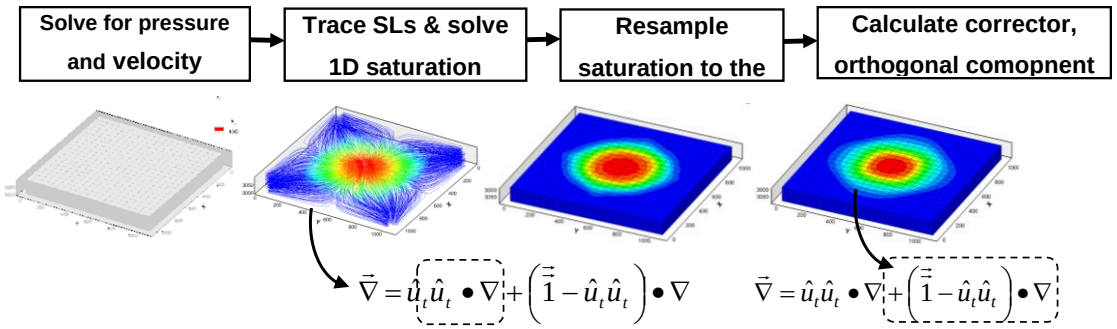

Figure 3.3: Flowchart of the orthogonal projection method.

3.4.1 Illustration by 1D Space

The Orthogonal Projection (OP) approach is first evaluated using a simple 1D homogeneous reservoir model. Porosity and permeability are constant and the rock and fluids are treated as incompressible. The injection rate is specified on the left boundary and the pressure is specified on the right. The water saturation distribution at 4000 days

(0.35 PVI) is compared with the results from a commercial finite difference simulator (ECLIPSE). For the comparisons of the time stepping, the commercial simulator takes 100 pressure and saturation recalculations while other methods (OS, OP, and OSAD) takes a single IMPES step. This allows us to observe the effect of the large time step.

Figure 3.4a shows the operator split solution with anti-diffusive corrections (OSAD). The three curves shown are for the commercial simulator without capillarity (to indicate the magnitude of capillarity), the commercial simulation with capillarity, and OSAD. The results demonstrate that the OSAD formulation works properly, as expected. Figure 3.4b compares the results from the commercial simulation with capillarity and the OP results. This is a one dimensional incompressible problem, and thus the problem is nonlinear in terms of relative-permeability and capillary pressure without transverse flux. The results showed excellent agreement between OP and the commercial simulation. Comparison with Figure 3.4a indicates that OSAD anti-diffusive correction leads to a rather sharp solution, although it is clearly converging to the entropy satisfying solution.

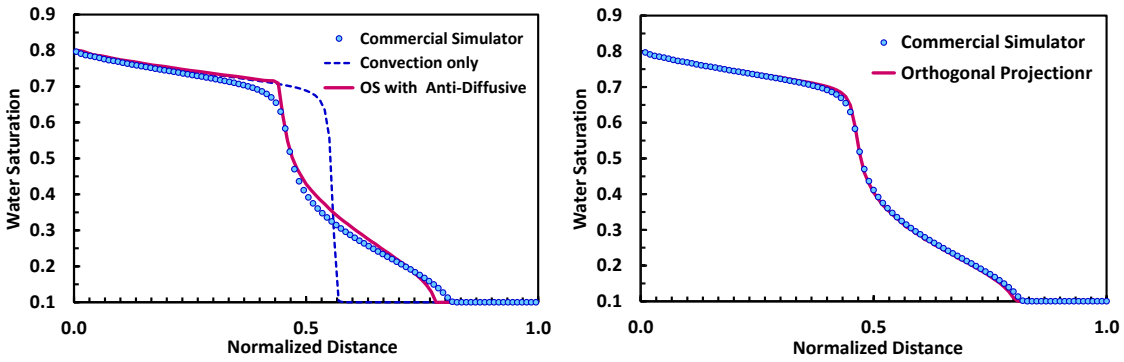

(a) Solution by operator-split **(b) Solution by orthogonal projection**

Figure 3.4: Water saturation distribution at 0.35 PVI for the 1D horizontal model: (a) Dashed blue curve is the result of convective flow, the blue circle is the commercial simulator with capillarity, and the solid red curve is operator split with anti-diffusive correction

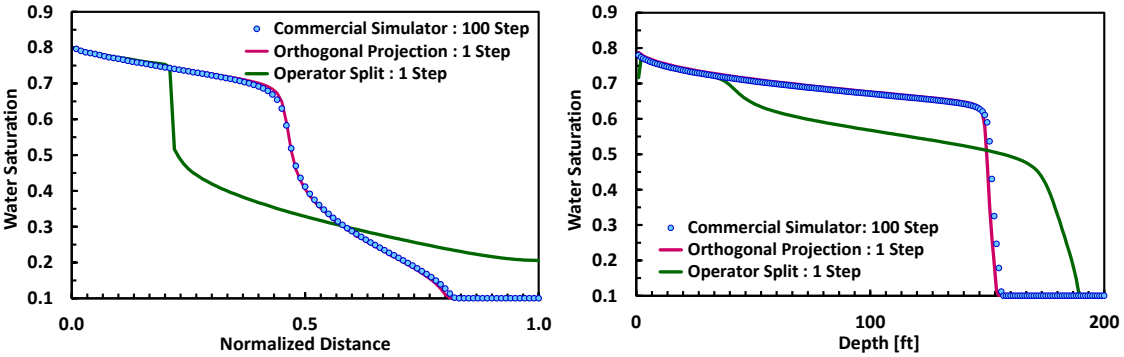

(a) 1D horizontal reservoir **(b) 1D vertical reservoir**

Figure 3.5: Water saturation distribution at 0.35 PVI showing the impact of gravity and the use of operator splitting without the anti-diffusive correction. Commercial simulator (blue circle), orthogonal projection (red solid) and operator splitting (green)

Figure 3.5 demonstrates the necessity of including the anti-diffusive correction with the conventional operator splitting, while taking single large time steps. The commercial simulation results are shown in pink, orthogonal projection in blue and operating split in

green. Irrespective of whether the flow is horizontal (Figure 3.5a) or vertical (Figure 3.5b), the OS solution is too dispersed. For the vertical case, water injection is from the top of the model and the impact of gravity is to segregate the flow leading to a sharp front. The OP calculation does not have a corrector step, while the OS calculation does. The OS calculation is being performed with a large time step, i.e., the convective predictor step calculates the solution at 0.35 PVI and then the corrector step is run to include the effects of capillarity and gravity.

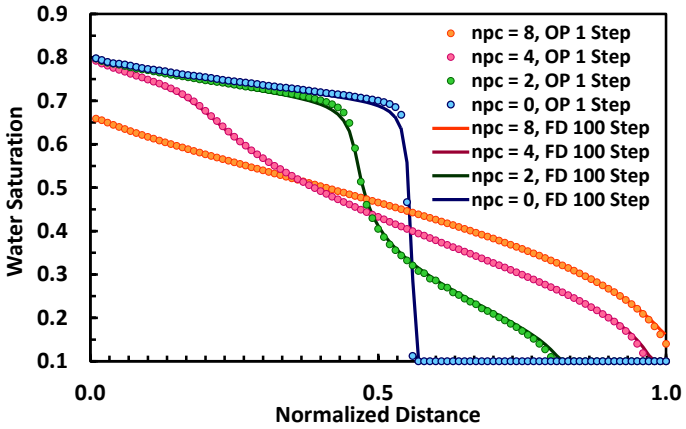

Figure 3.6: Water saturation distribution at 0.35 PVI for the 1D horizontal model, contrasting commercial simulation and the OP calculation, for four different capillary pressure curves (n_{pc} = 0, 2, 4, 8). The commercial simulation includes a recomputation of the pressure equation 100 times while the OP solution uses only a single pressure solution.

Figure 3.6 shows the excellent agreement between the commercial simulation results and OP for four different capillary pressure functions (n_{pc} = 0, 2, 4, 8). The commercial simulation includes re-computation of the pressure equation 100 times while the OP solution uses only a single pressure solution.

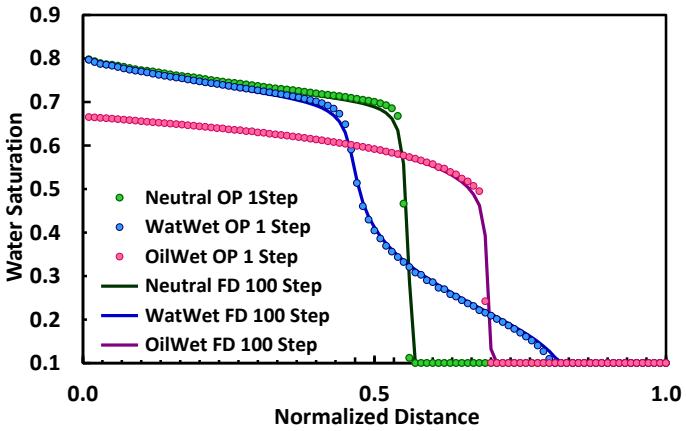

Figure 3.7: Water saturation distributions at 0.35 PVI for the 1D horizontal model with different wettability computed by the commercial simulation (FIM) and orthogonal projection. Green: neutral (zero capillary pressure), Blue: water-wet, Red: oil-wet, Green: zero capillary pressure as a reference.

Figure 3.7 shows a similar comparison, but now for a different wettability scenarios: neutral, water-wet and oil-wet. The water wet condition generate saturation fringe as seen previous results while oil wet case generate shock front. Again, the agreement is excellent.

In order to examine the effect of capillarity and gravity on operator splitting and orthogonal projection, sensitivity analysis is conducted by changing time step size with a different fractional flow curve. The following fractional flow models are tested (a) linear fractional flow (b) fractional flow with concave down (c) fractional flow with concave up. To find the effect on capillarity and gravity, 3 reservoir models are prepared: (a) 1D vertical including gravity effect (b) 1D horizontal reservoir including capillary effect (c) 1D vertical reservoir including both capillary and gravity.

The Table 3.1 shows the parameters used to construct 3 mobility cases with 3 reservoir model. The Figure 3.8 shows the 3 different fractional flow (mobility) scenarios with capillary pressure as a function of water saturation. They are defined as straight line, concave down, and concave up fractional flow from top to bottom, respectively.

Table 3.1: Parameters used for 1D simulation verification

Simulation Case	Permeability [mD]	Rel-Perm	Capillary Equation
Gravity	5.0	$K_{rw}=S_w, K_{ro}=S_o$	-
Gravity	6.3	$K_{rw}=S_w^{0.25}, K_{ro}=S_o^{0.25}$	$10* S_o^2$
Gravity	6.3	$K_{rw}=S_w^{0.25}, K_{ro}=S_o^{0.25}$	$-100* S_w^2$
Capillary	5.0	$K_{rw}=S_w, K_{ro}=S_o$	$erfc^{-1}$
Capillary	6.3	$K_{rw}=S_w^{0.25}, K_{ro}=S_o^{0.25}$	$10* S_o^2$
Capillary	6.3	$K_{rw}=S_w^{0.25}, K_{ro}=S_o^{0.25}$	$-100* S_w^2$
Gravity+Capillary	3.1	$K_{rw}=S_w, K_{ro}=S_o$	$500* S_o^2$
Gravity+Capillary	6.3	$K_{rw}=S_w^{0.25}, K_{ro}=S_o^{0.25}$	$10* S_o^2$
Gravity+Capillary	6.3	$K_{rw}=S_w^{0.25}, K_{ro}=S_o^{0.25}$	$-100* S_w^2$

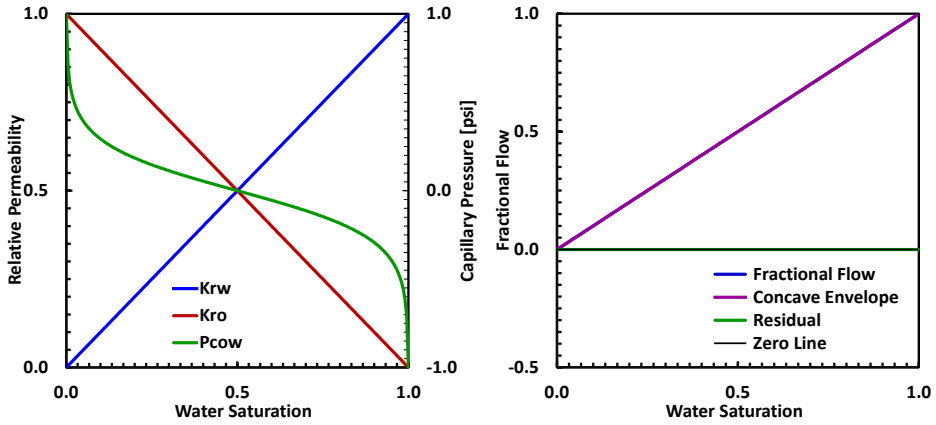

(a) Straight fractional flow model

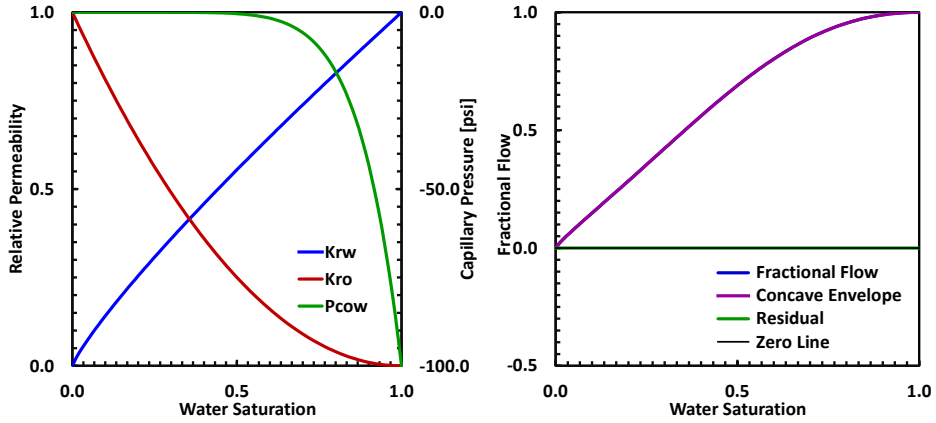

(b) Concave-down fractional flow model

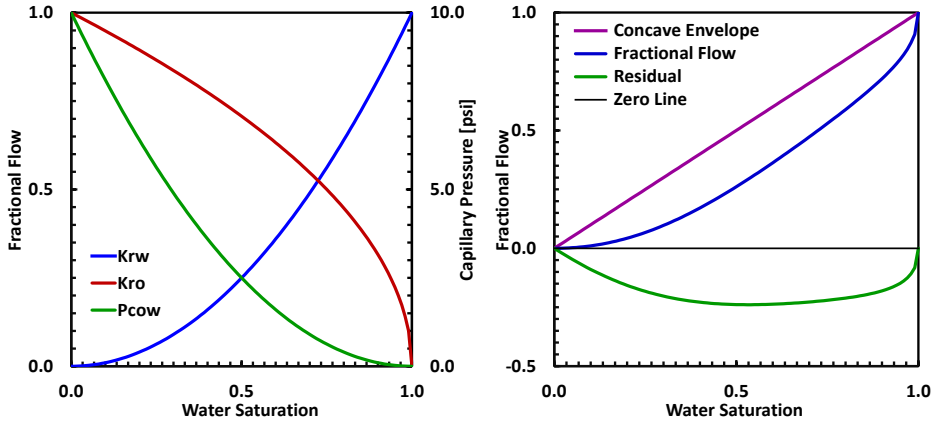

(c) Concave-up fractional flow model

Figure 3.8: Relative permeability and capillary pressure (3 figures in the left) and corresponding fractional flow and concave envelope (3 figure sin the right), by (a) Straight (b) Concave up (c) Concave-down fractional flow model.

Figure 3.9 shows the result of the saturation distribution by vertical gravity flow with 3 different scenarios. The reference solution is shown in blue circles, which is obtained by the commercial IMPES simulator with 256 time steps or more. The actual time steps depend on the convergence and stability analysis which is controlled internally and thus it can be more than specified steps. The green and red dotted lines are solutions by the OS and OP, respectively, with different pressure update frequency. The pressure update is conducted by 7 scenarios, from 1 step to maximum 256 steps. Figure 3.9 (a) shows the result of the OS by linear fractional flow. It is expected that with linear fractional flow, the concave envelope construction and anti-diffusive correction is not required and thus the solution is not sensitive to the selection of the time step size. However, it can be observed that the solution by OS shows the large differences with the selection of the time step size. This difference happens because of the treatment of the boundary condition. Once convection and gravity effect is split, the boundary condition is the constant injection rate during convection period, and then it becomes closed boundary during gravity step. Because of the closed boundary condition during gravity step, the water is purely segregated during the injection period and we do not need concave envelope construction. This splitting error due to boundary condition is observed for both fractional flow with concave up and concave down, shown as Figure 3.8 (b,c). The solution by fractional flow of concave up case has no concave envelope and is expected to be insensitive to time step selection, however, it has large differences with reference solution especially around the boundary condition. The result of Figure

3.8(c) is same trend, but has different behavior. Not only the saturation front, but also shape showed large differences.

Compared with the result of OS shown in Figure 3.9 (a,b,c), the effect of the time stepping is negligible for the result of OP, shown in Figure 3.9 (d,e,f). The nonlinearity of this case study is only mobility (relative permeability) and capillarity. Again it needs to be mention that the time discretization error of the saturation calculati8on step constrained by CFL condition. This treatment is also applied to the OS, however, only OP could avoid this error.

The sensitivity is evaluated again by taking RMS error from the reference solution for both OP and OS, shown in Figure 3.10. The result shows that the solution by the OS is always sensitive to the time step selection, including the linear fractional flow problem, and it requires 256 time steps to converge to the reference solution. This error is introduced by treatment of the boundary condition by convection and gravity step. The result of OP has slight differences in the RMSE, however, the solution is less sensitive and always showed a better solution compared with the OS.

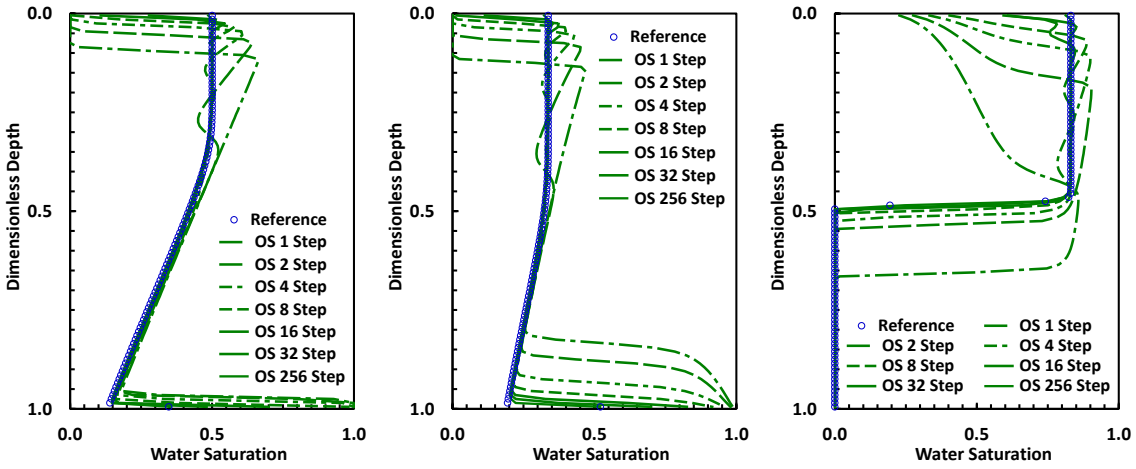

(a) Straight FFlow (b) Concave-down FFlow (c) Concave-up FFlow

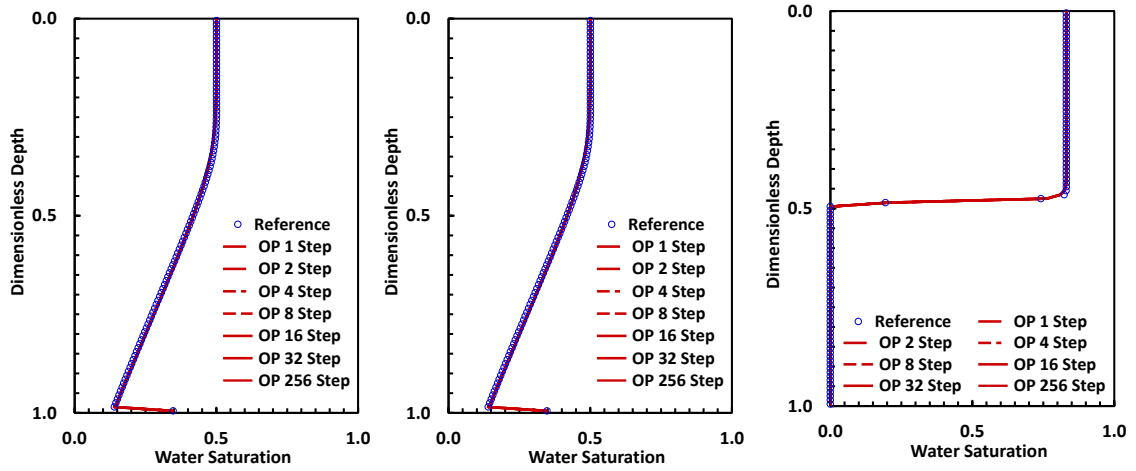

(d) Straight FFlow (e) Concave-down FFlow (f) Concave-up FFlow

Figure 3.9: Water saturation distribution at 0.4 PVI, operator splitting without the anti-diffusive correction (green), orthogonal projection (red) and reference (blue circle).

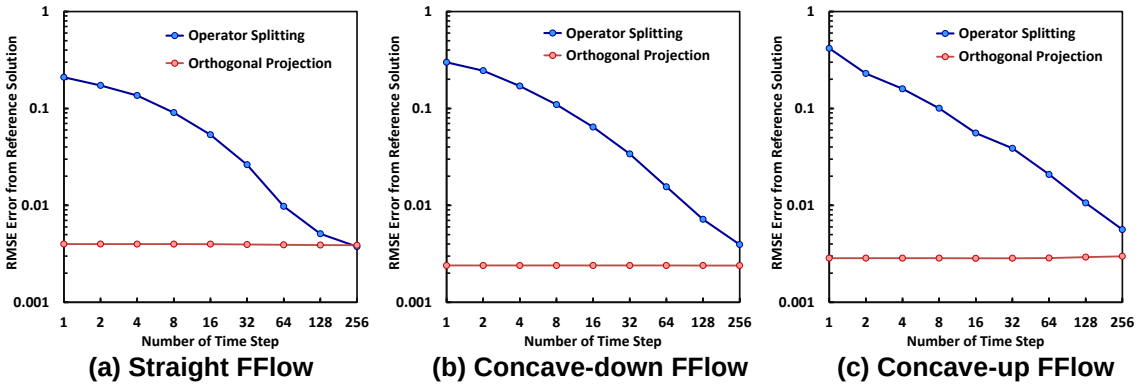

Figure 3.10: Water saturation distribution at 0.4 PVI showing the impact of gravity and the use of operator splitting without the anti-diffusive correction. Commercial simulator (blue circle), orthogonal projection (red solid) and operator splitting (green).

Now we compare the effect of the capillarity using a horizontal reservoir. Again the 3 different mobility cases are tested and results are shown in Figure 3.11. In the figure, the (a,b,c) shows the result from OS and (d,e,f) by OP, respectively. Unlike gravity case, the capillary does not have a clear difference near the boundary and the linear model has small differences for both OP and OS. However, the result from concave up fractional flow was expected to be insensitive to the selection of the time step size while it has clear differences in the solution of the OS. The result of the concave down fractional flow has a similar error shown in Figure 3.5 (a) and thus the solution is too diffusive. The result of OP showed good agreement with the reference case for all the fractional flow models.

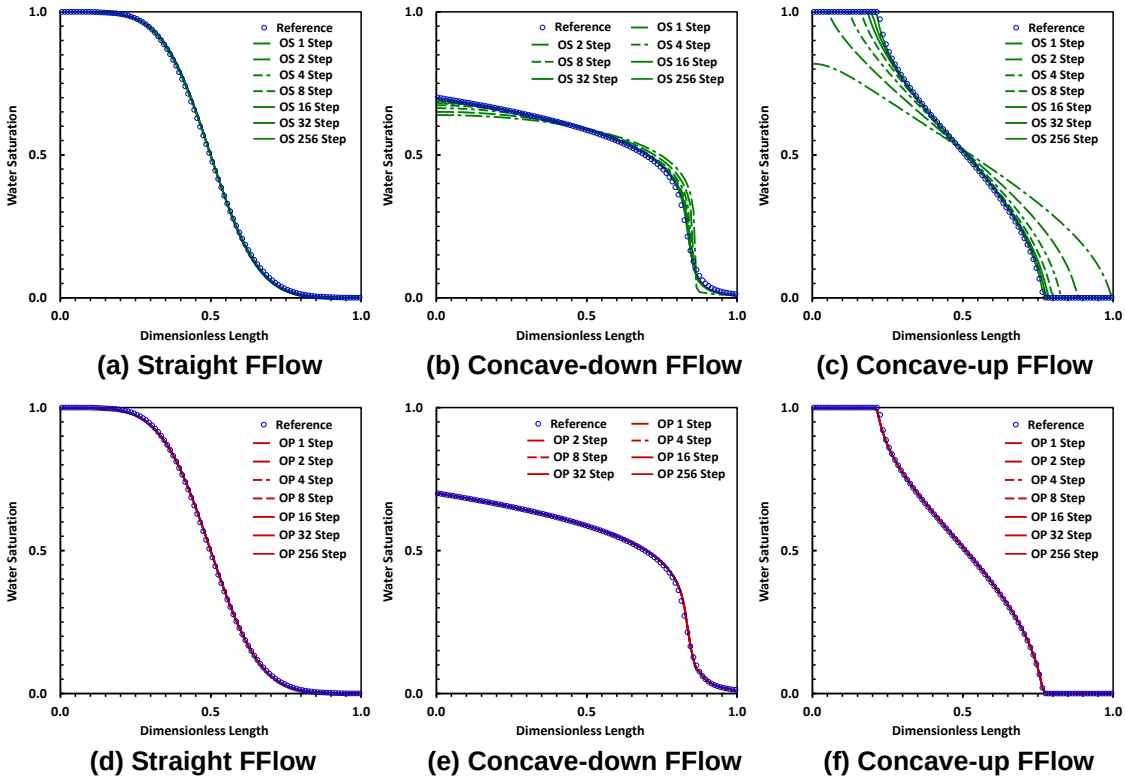

Figure 3.11: Water saturation distribution at 0.4 PVI, operator splitting without the anti-diffusive correction (green), orthogonal projection (red) and reference (blue circle).

The sensitivity is evaluated again by taking RMSE from the reference solution for both OP and OS, shown in Figure 3.12. The result shows that the solution by the OS is always sensitive to the time step selection, except the linear fractional flow problem. The result from non-linear fractional flow model, both concave up and down model showed large RMS error and it took 256 time step to converge to the reference solution, while result of OP showed good agreement with all the fractional flow scenario with different time step strategy.

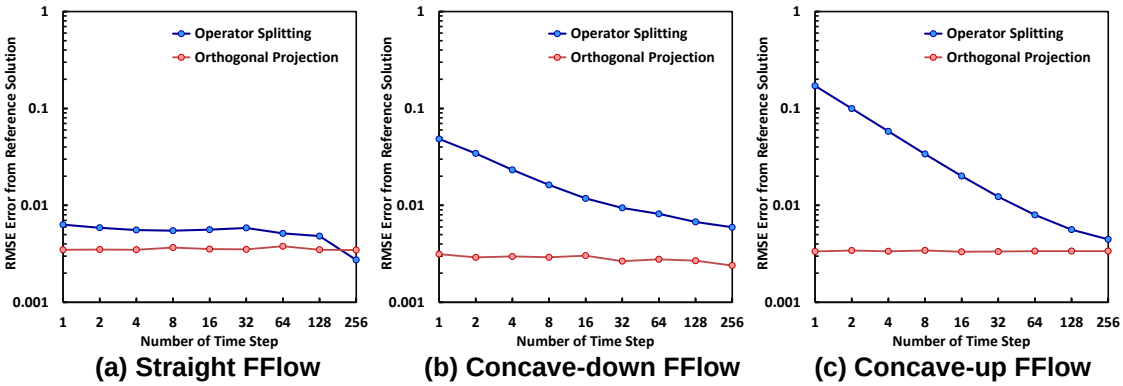

Figure 3.12: Water saturation distribution at 0.4 PVI, operator splitting without the anti-diffusive correction (green), orthogonal projection (red) and reference (blue circle).

The final case evaluates the effect of the capillary as well as gravity using a vertical reservoir. Figure 3.13 shows the result of the saturation distribution. The result shows large differences between reference and OS, for all the fractional flow models. There is a significant difference near the injector and producer as well as the saturation front.

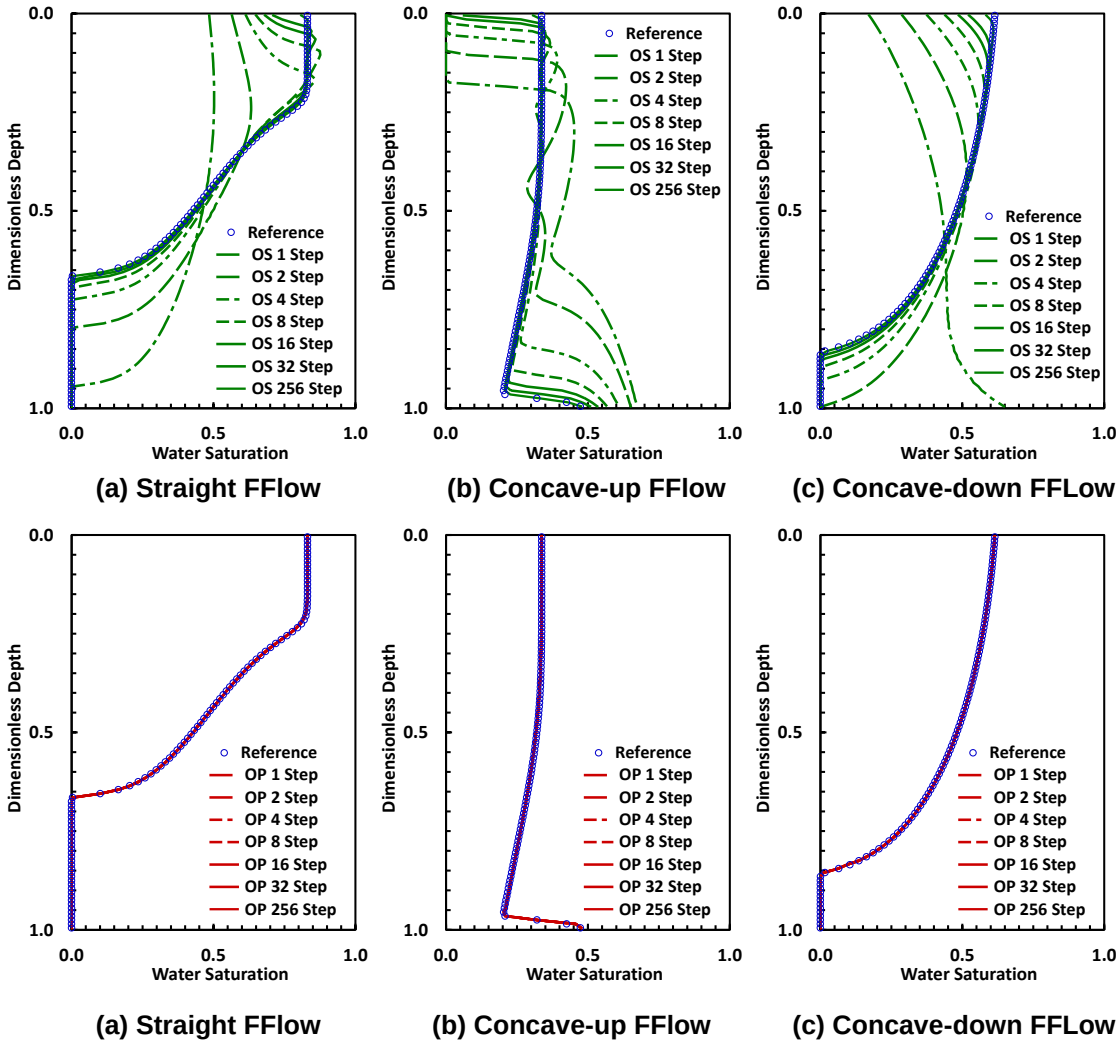

Figure 3.13: Water saturation distribution at 0.4 PVI, operator splitting without the anti-diffusive correction (green), orthogonal projection (red) and reference (blue circle).

With the existence of gravity and capillary, the solution from the OS is always sensitive to time step selection even linear fractional flow model. We can conclude that, it is not possible to reproduce the reference solution by OS with large time step size. This is a severe limitation for the application of the conventional streamline-based approach because the gravity effects cannot be ignored for oil water problem. The proposed approach, however, could reproduce the reference solution as long as the effect of the mobility is evaluated correctly by the iterative IMPES approach.

The time step sensitivity of capillary and gravity scenario is evaluated again by taking RMSE from the reference solution for both OP and OS, shown in Figure 3.14. The result shows that the solution by OS requires 256 time steps to converge to the reference solution same as the gravity scenario shown in Figure 3.8.

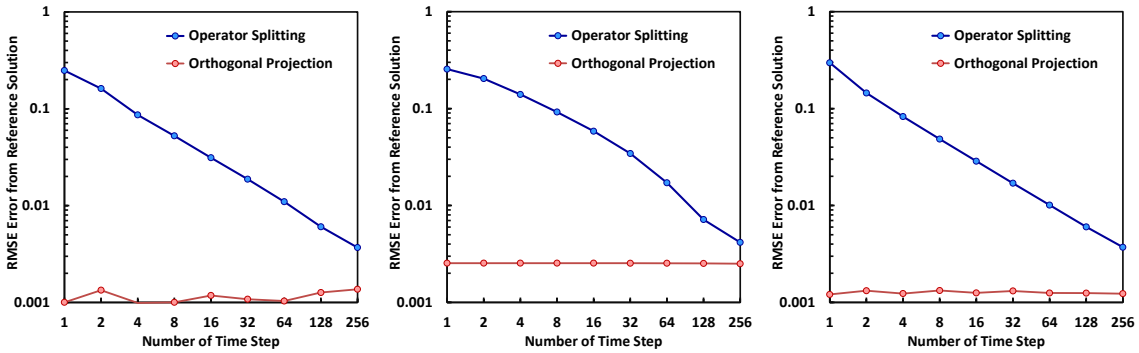

Figure 3.14: Water saturation distribution at 0.4 PVI, operator splitting without the anti-diffusive correction (green), orthogonal projection (red) and reference (blue circle).

The evaluation of gravity, capillary, and gravity and capillary scenario is carried out with by different permeability and capillary curve. These parameters are selected to set

the capillary and gravity number to be of the same range. Because the mobility is different in 3 different fractional flow scenario, the capillary and gravity number changes dynamically and cannot specify single number. Instead, the maximum capillary and gravity number is measured during simulation by calculating convection, capillary and gravity separately. For instance, the maximum capillary number is the maximum ratio of convection flux to capillary flux of all the cell faces. The results are summarized in Table 3.2 as follows.

Table 3.2: Maximum capillary/gravity number and RMS error from reference solution

Simulation Case	Fractional Flow	Gravity Number	Capillary Number
Gravity	Straight	1.02	-
Gravity	Concave down	1.05	-
Gravity	Concave up	0.89	-
Capillary	Straight	-	0.45
Capillary	Concave down	-	0.42
Capillary	Concave up	-	0.52
Gravity+Capillary	Straight	0.75	0.32
Gravity+Capillary	Concave down	0.82	0.29
Gravity+Capillary	Concave up	0.65	0.42

3.4.2 Illustration by 2D Space

The orthogonal projection method splits the transverse flux into parallel and perpendicular to the total velocity. In a 1D scenario, the capillarity and gravity always follow the transverse flux and thus all the capillarity and gravity can be available along streamlines. In 2D scenario, however, the introduction of the capillary will generate transverse flux and predictor-corrector approach is necessary. The 2D quarter five spot model of water and gas injection is tested to evaluate the flux of capillarity along the total velocity and perpendicular to the total velocity, as follows.

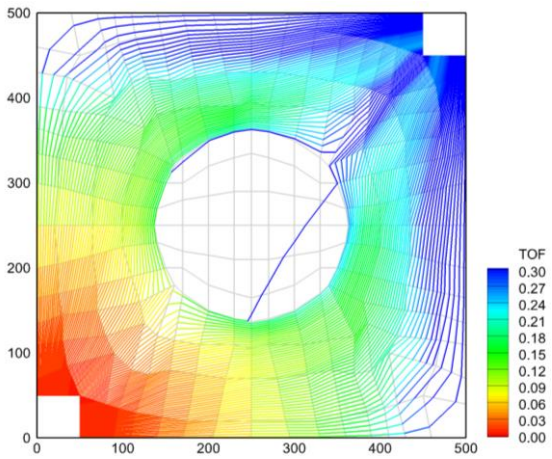

Figure 3.15: Streamline distribution of 2D illustrative example.

The model is quarter five spot case with low permeability (5 mD) at the center and surrounded high permeability region (100 mD). The capillary is given as J-function and thus the low permeability region has lower water phase pressure and thus the water behave as if it is absorbed into the center by capillary flux. As shown in streamline distribution in Figure 3.15, the convection flow does not carry water at low permeability

region. The capillarity flows water to the low permeability region and immobile it. The water injection is conducted by 0.2 PVI and then the reservoir fluid is injected again by 0.2PVI, and observe the water flux and capillarity.

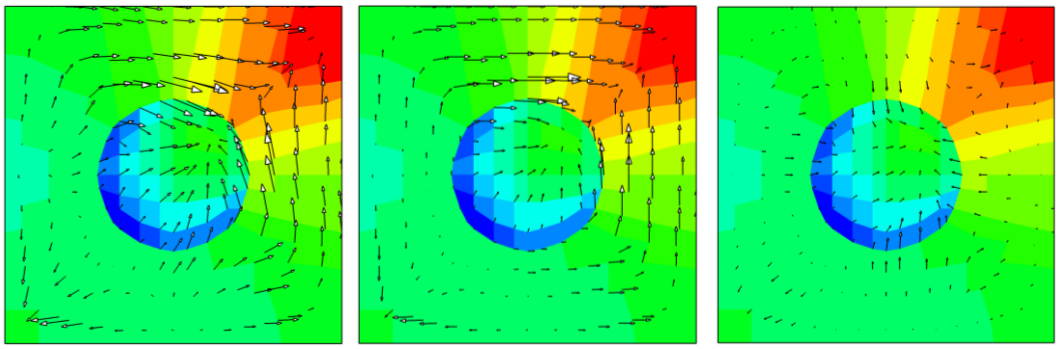

(a) Total capillary(b) Capillary parallel to total velocity (c) Capillary transverse flux

Figure 3.16: Snapshot of the capillary flux, total (a) and after split by parallel (b) and transverse (c) to the total velocity.

Figure 3.16 shows the result of the water saturation distribution and capillary flux is shown as black arrow. The total capillary flux is shown by Figure 3.16a. It clearly shows that the water around the low permeability region moves into the low permeability region. On the other hand, the capillary at the high permeability region seems to be following convective flow or streamline trajectory. Then the total capillary flux is split into parallel and transverse shown in Figure 3.16b and 3.16c respectively. Now the capillary along the total velocity has the majority of the component of overall capillary flux. All the flux shown here can be calculated along streamlines by orthogonal projection method and does not require any concave envelope correction. The Figure 3.16c, however, needs to be evaluated as a corrector term on the grid. Although the

concave envelope correction is required to evaluate this remaining capillary flux, however, this component is small and the splitting error can be ignored.

3.4.3 2D Areal, Homogeneous and Heterogeneous Models

2D areal simulations are used for the next set of comparisons. Here we compare and contrast commercial simulation, orthogonal projection (OP) and operating splitting (OS). As mentioned earlier, because of the difficulty in constructing a multidimensional OS code with anti-diffusive corrections, we only provide a comparison with OS, not OSAD. These calculations are performed for water-wet capillary pressures only. Both the homogeneous and heterogeneous reservoir models here have an average permeability of 1000 mD. The range of permeability in the heterogeneous reservoir is 0.1 to 4000 mD. Injection rates and bottom hole flowing pressures at the producer are specified. Fluid compressibility is 1.0E-6 psi^{-1} for both the water and oil phases. Unlike the 1D case, we now calculate saturation corrections from transverse flux for both OP and OS.

In these examples, we have treated the frequency of pressure recalculation as a sensitivity parameter with 1, 5, 10, 50 or 100 recalculations. The commercial simulator is set as 100 recalculations. For each pressure recalculation, there is a single predictor step followed by a single corrector step. Physically we expect a certain amount of flux redistribution because of the self-stabilization of the waterflood because of the reduced mobility of two phase flow compared to single phase. Figure 3.17 shows the performance of the orthogonal projection with 5 pressure recalculations compared to the commercial simulator. The agreement of the saturation distribution between OP and the

commercial simulator is quite satisfactory regardless of larger pressure step size taken by OP.

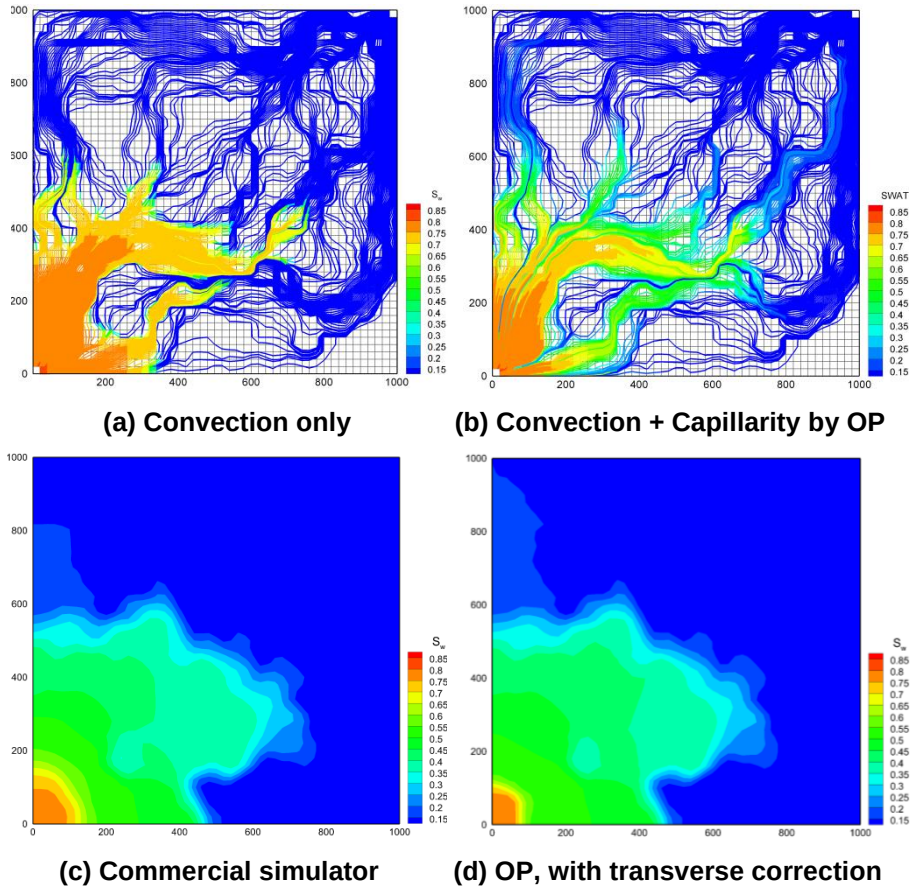

(a) Convection only **(b) Convection + Capillarity by OP**

(c) Commercial simulator **(d) OP, with transverse correction**

Figure 3.17: Heterogeneous reservoir water saturation distribution obtained from: (a) Commercial simulation with 100 pressure calculations (b) OP, no capillarity, with 5 pressure calculations(c) OP with capillarity, with 5 pressure calculations (d) OP after transverse correction, with 5 pressure calculations.

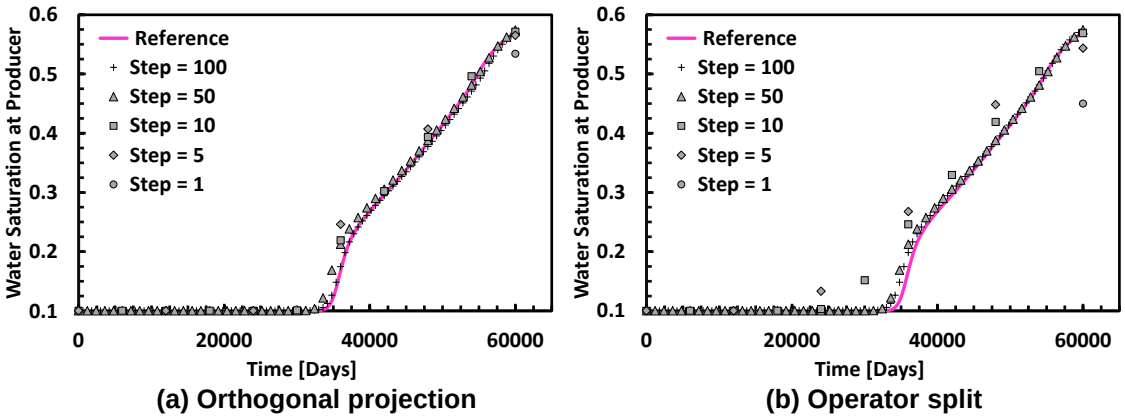

Figure 3.18: Water saturation at the producer grid block versus time for the heterogeneous areal model with 5 different frequencies of pressure recalculation. The pink curve (Reference) obtained by finite difference method. The gray points show the solution at a given frequency of pressure recalculations (1, 5, 10, 50 and 100 recalculations). (a) OP (b) OS.

To better understand these results, we have examined the outlet water saturation as a function of the number of pressure recalculations for both the homogeneous and heterogeneous models and for both the OP and the OS methods. Figure 3.18a shows the impact of pressure recalculation on the outlet saturation, with the pink curve being the reference result from the commercial simulator. With even a few recalculations, the OP saturations are close to the reference results for most of the profile, with the exception of the time of water breakthrough. This is expected in part particularly at an early time, unless the pressure is recalculated sufficient times to capture the viscous cross-flow during the waterflood. It is known that stable waterflood calculations are more challenging than unstable cases for streamline simulation for exactly this reason, and the current calculations are no exception. The heterogeneity tends to create more

channelized flow, and the OP streamline simulation curve approaches the reference solution with even fewer pressure updates.

3.4.4 2D, Homogeneous Cross-Section

The previous case study showed the impact of capillarity and the dependence of the results on the solution technique (OS or OP). We now repeat the calculation in a 2D cross-section to examine the impact of gravity. To simplify the analysis of the results, this calculation is performed in a homogeneous cross-section, Figure 3.19. We inject water at a fixed flow rate in the top layer of the model.

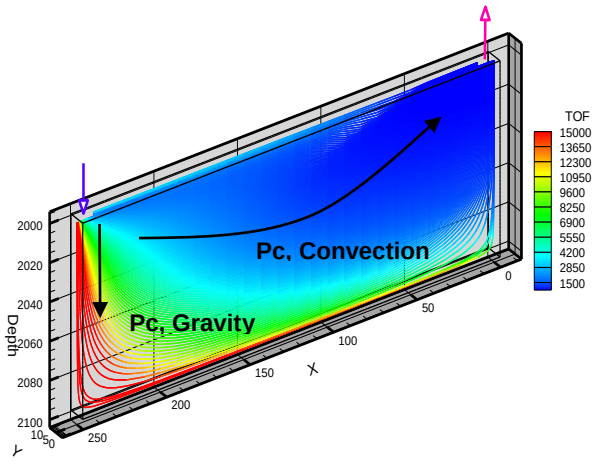

Figure 3.19: Water saturation distribution along streamlines for the 2D Cross-sectional case.

Production is from a single perforation, also at the top layer of the model. This geometry is selected to accentuate the differences between convection, gravity and capillarity. The gravity will drag the injected water to the bottom of the reservoir while

convection tries to transport water directly from injector to producer. The capillarity will tend to disperse water throughout the entire reservoir.

The results are shown in Figure 3.20, all calculated using an orthogonal projection. In Figure 3.20a, only convection is included. In Figure 3.20b we see the impact of convection and capillarity, and in Figure 3.20c we see the additional impact due to gravity. These calculations are for a strongly water-wet capillary pressure curve. Figures 3.21b and 3.21c show the earlier progression of the waterflood to the producer than does Figure 3.21a. Figure 3.21c shows the additional impact of vertical segregation on the flow. The impact of gravity is even stronger in the transverse corrector step, shown in Figure 3.21b since the streamlines are largely horizontal.

Figure 3.21 includes the results of commercial simulation as a reference solution, and also conventional operator splitting. The outlet water saturation is plotted in Figure 3.22. Even with 100 pressure recalculations, the operator splitting method remains too diffuse and does not converge to the commercial solution. In contrast the solution from orthogonal projection is close to the reference case.

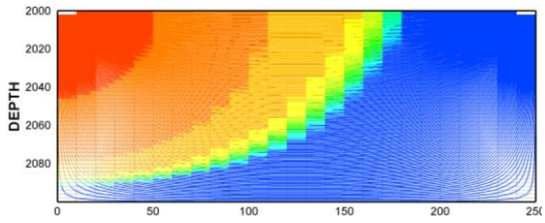

(a) OP, convection only

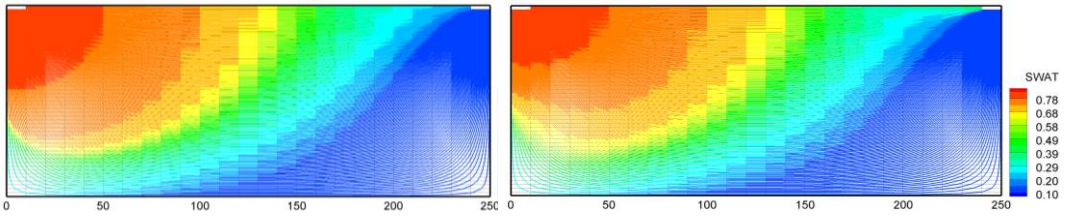

(b) OP, convection + Pc **(c) OP, convection + Pc + gravity**

Figure 3.20: Water saturation distribution using orthogonal projection along streamlines for the 2D Cross-sectional case.(a) Convective flow only (b) Capillarity + Convection flow (c) Gravity + Capillarity + Convective flow.

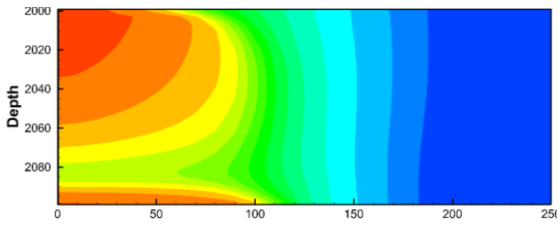

(a) Commercial simulator

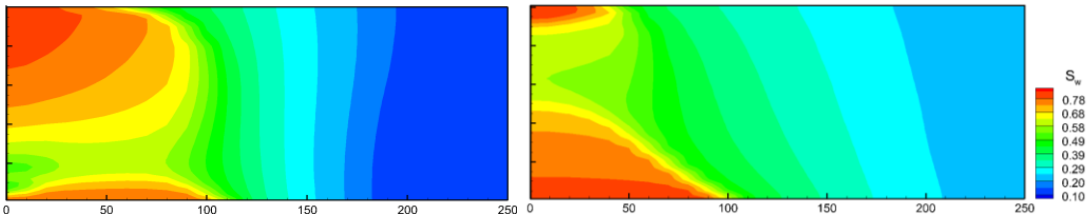

(b) Proposed method **(c) Operator split**

Figure 3.21: Water saturation distribution of cross-sectional model; (a) Commercial simulation (b) Orthogonal projection after including the transverse corrections (c) Operator splitting after including the transverse corrections.

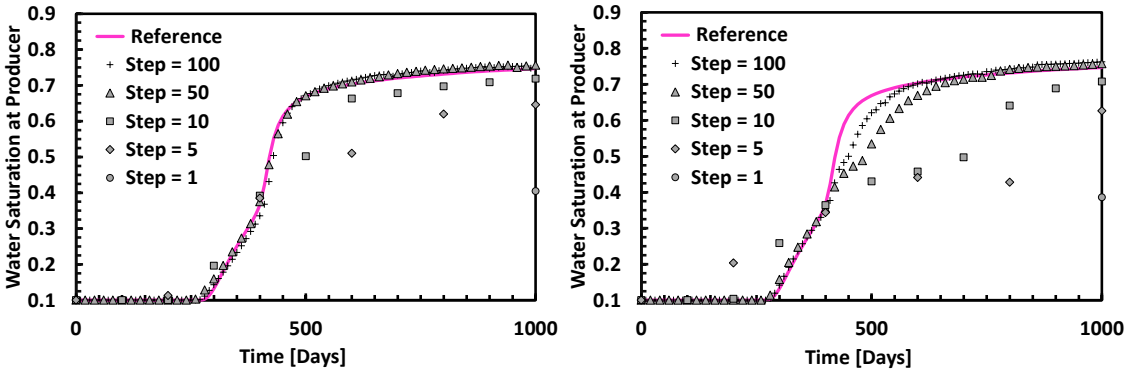

(a) Orthogonal projection **(b) Operator split**

Figure 3.22: Water saturation at the producer grid block versus time for the vertical cross-sectional model with 5 different frequencies of pressure recalculation. The pink curve (reference) is from the finite difference calculation. The gray lines show the solution at a given frequency of pressure recalculations (1, 5, 10, 50 and 100 recalculations). (a) Operator projection (b) Operator split.

3.4.5 3D SPE10 Comparative Model

As a final example, the orthogonal projection method is tested using the top zone (40 layers) of the SPE 10 model (Christie and Blunt 2001). The model is simulated as a five spot with 4 vertical producers and 1 central injector. The wells are fully completed in all layers. The top zone of SPE10 consists of sheet sands and both gravity and capillarity are significant. We inject 0.5 PVI over a 3 year period. An example of the streamline distribution is shown in Figure 3.23a.

Rock properties (porosity and permeability) and the streamline distribution obtained from the pressure solution are shown in Figure 3.23. The surface plot of the porosity and permeability shown in Figure 3.23b and 3.23c are relatively higher region in the reservoir. Figure 3.24 shows the water saturation distribution derived from the commercial simulator, orthogonal projection and operator splitting method. The OP and OS method results are calculated using only a single pressure solution. Although there are differences between the commercial simulator solution and OP, the OS solutions are again too diffusive and show significant departure from the commercial finite different simulator.

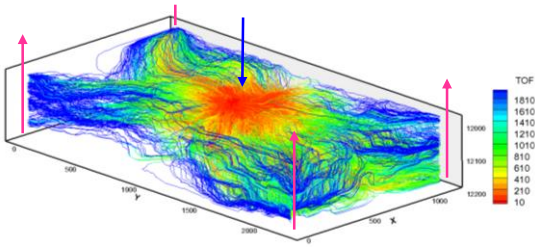

(a) Streamline distribution

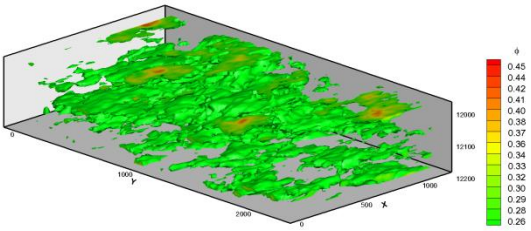

(b) Porosity (above 25%)

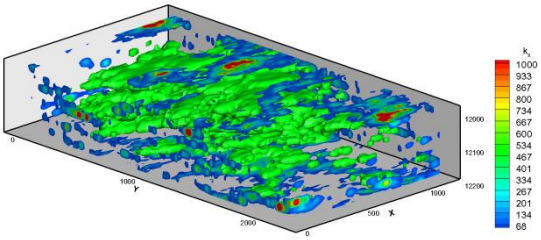

(c) Horizontal permeability (above 500mD)

Figure 3.23: Reservoir properties and streamline distribution of the SPE 10 model.

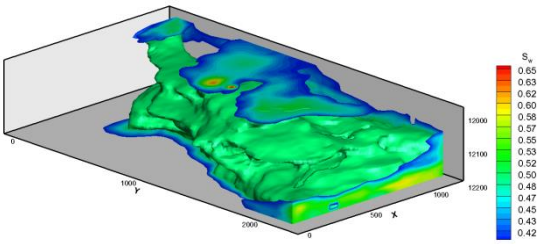

(a) Commercial simulation

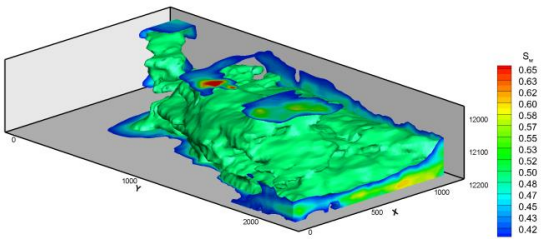

(b) Orthogonal projection

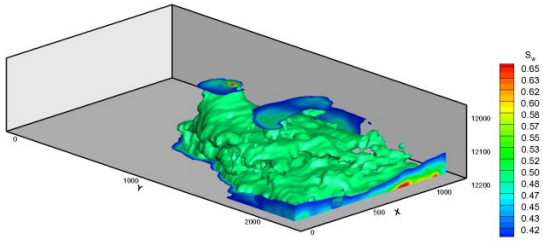

(c) Operator split

Figure 3.24: Water saturation distribution derived using the SPE10 model (single pressure calculation, 0.5 PVI).

3.5 General 3phase Multicomponent Formulation

The model is extended into the general multicomponent system. The solution of the pressure is first calculated by Appendix A. Once the system pressure is obtained, the velocity field can be calculated by Darcy's law. The mole fraction and saturation is solved based on specified boundary conditions and the pressure field. The solution procedure by the OS method is shown in Appendix B. To derive component transport equation, removing the sink/source term from the governing equation, we get mole fraction equation as

$$\frac{\partial}{\partial t}\left(\phi \sum_{j=ogw} y_{ij}\rho_j S_j\right) = -\nabla \bullet \sum_{j=ogw} y_{ij}\rho_j \vec{u}_j \quad \cdots\cdots\cdots\cdots\cdots\cdots\cdots\cdots\cdots\cdots \quad (3.16)$$

We supply the capillary pressure as a function of saturation between phase *j* and *m*, $p_{cjm} = \left(p_j - p_m\right)$ and define the density difference by $\Delta\rho_{jm}^m = \rho_j^m - \rho_m^m$ and total velocity as $\vec{u}_t = \vec{u}_w + \vec{u}_o + \vec{u}_g$. This allows rewriting the right hand side of Eq. 3.16 with convection, gravity and capillarity term as

$$\phi\frac{\partial}{\partial t}\sum_{j=ogw} y_{ij}\rho_j S_j = -\nabla \bullet \sum_{j=ogw} F_j y_{ij}\rho_j \vec{u}_t - \sum_{j=ogw} \nabla \bullet \vec{\vec{k}} \bullet y_{ij}\rho_j F_j \sum_{m=ogw, m\neq j} \lambda_m \left(\nabla p_{cjm} + \Delta\rho_{jm}^m g \nabla D\right)$$

$$\cdots\cdots\cdots\cdots\cdots\cdots\cdots\cdots\cdots\cdots\cdots\cdots\cdots\cdots\cdots\cdots\cdots\cdots\cdots\cdots\cdots\cdots \quad (3.17)$$

The conventional operator splitting method decouples Eq. 3.17 by physical mechanisms. Our objective here is to decouple equation in terms of fluxes parallel and transverse to the total velocity. Introducing fractional flow, the flow equation for each phase becomes

$$\vec{u}_j = F_j \cdot \vec{u}_t + F_j \sum_{m=ogw, m\neq j} \lambda_m \vec{\vec{k}} \bullet \left(\nabla p_{cjm} + \Delta\rho^m_{jm} g \nabla D\right) = f_j \vec{u}_t + \vec{u}_{j\perp} \quad \cdots\cdots\cdots \quad (3.18)$$

where f_j is a total fractional flow of phase j and contains gravity and capillary fluxes parallel to the total velocity. To apply in multicomponent systems, the molar fractional flow is derived as follows.

$$f_i = \sum_{j=owg} F_j y_{ij} \rho_j + \sum_{j=owg} \frac{\vec{u}_t}{u_t^2} \bullet \vec{\vec{k}} \bullet y_{ij} \rho_j F_j \sum_{m=ogw, m\neq j} \lambda_m \left(\nabla p_{cjm} + \Delta\rho^m_{jm} g \nabla D\right) \quad \cdot \quad (3.19)$$

This equation includes convective flux as well as capillary and gravity driven contributions to the fractional flow of component i in all the phases. Using this equation, the saturation/molar density is solved explicitly along each streamline.

The divergence of grid block i is calculated as follows

$$\nabla \bullet \vec{u}_t = \left(\sum_{face} q_i + q_w \right) / V_i = c \quad \cdots\cdots\cdots\cdots\cdots\cdots\cdots\cdots\cdots\cdots\cdots\cdots \quad (3.20)$$

where V_i, q_i and q_w are grid block volume, flow in/out from the grid block surface and well flow rate at reservoir condition, respectively. The effective density conserves mass in the streamline formulation (Cheng *et al.* 2006). All of the operator splitting formulations utilize the time-of-flight as a spatial coordinate, although the details of the implementation can be different for each case. Using Eqs. 3.17-19 and the time-of-flight operator in Eq. 3.19, the transport equation along the streamline can be written as follows:

$$\frac{\partial}{\partial t} m_i + \frac{\partial}{\partial \tau} f_i^{sl} = -\omega_i \quad \cdots\cdots\cdots\cdots\cdots\cdots\cdots\cdots\cdots\cdots\cdots\cdots \quad (3.21)$$

where f_i^{sl} is a total molar fractional flow along the streamline coordinate. The terms in the above equation are defined as follows:

$$m_i = \sum_{j=ogw} y_{ij}\rho_j S_j$$

$$f_i^{sl} = \sum_{j=owg} F_j y_{ij}\rho_j + \sum_{j=owg} \frac{k}{u_t^2}\, y_{ij}\rho_j\, F_j \sum_{m=ogwm\neq j} \lambda_m \frac{\partial}{\partial \tau}\left(p_{c,jm} + \Delta\rho_{jm}^m\, gD\right), \quad \omega_i = \phi^{-1}\, f_i^{sl} c \quad \cdots. \quad (3.22)$$

This is the one dimensional saturation/mole density equation expressed using the time-of-flight as the spatial coordinate. Unlike conventional operator splitting method, our proposed orthogonal projection includes more of the physics of flow in its 1D flow equation. Given the velocity field obtained from the solution of Eq. A.5, we transform the fractional flow using time-of-flight as a spatial coordinate. We approximate the spatial derivative of the capillary pressure along the time-of-flight coordinate using effective permeability in the direction of the convective flow. The gravity term depends upon the vertical permeability and depth changes along the streamline $\vec{u}_t \bullet \vec{\vec{k}} \bullet \nabla D = (\vec{u}_t \bullet \nabla D)\left(\nabla D \bullet \vec{\vec{k}} \bullet \nabla D \right) = k_v \cdot (\vec{u}_t \bullet \nabla D)$.

For the corrector term, the same approach of Eqs. 3.14 can be applied in for compositional streamline based simulation. As discussed before, OS with anti-diffusive correction has difficulties in the concave envelope construction for compositional models. The OS with anti-diffusive correction includes both longitudinal and transverse flux terms in the corrector step. In contrast, the OP includes only the transverse flux in

its corrector step. From Eq. 3.17 we have phase flux parallel and transverse to the total velocity. Thus, the molar balance equation across streamlines can be written as

$$\phi \frac{\partial m_i}{\partial t} = -\vec{\nabla}\Gamma_i$$
$$\Gamma_i = \sum_{j=ogw} \left(\vec{\vec{I}} - \hat{u}_t \hat{u}_t \right) \bullet \vec{\vec{k}} \bullet y_{ij} \rho_j F_j \sum_{m=ogw, m \neq j} \lambda_m \left(\nabla p_{cjm} + \Delta \rho_{jm}^m g \nabla D \right) \quad \cdots\cdots\cdots \quad (3.23)$$

The gravity and capillarity terms across streamline are solved using the initial conditions given by the solution of Eq. 3.22. The OP has a smaller magnitude of the corrector term compared with the conventional OS approach, thus allowing for larger time steps.

3.5.1 Time Step Selection

The selection of the time step for pressure and component transport equation determines to a large extent the efficiency of the simulation and also the stability and accuracy of the solution. A smaller time step for pressure update and larger time step for the saturation equation is ideal to maximize accuracy of the solution in an IMPES method; however, this approach will lose the advantages of the streamline based simulation. Plenty of literature can be found for time step selection of the IMPES method in black oil (Todd and Longstaff 1972, Aziz and Settari 1979, Osako, Datta-Gupta, and King 2004, Hurtado, Maliska, and Slivfa 2006) and multicomponent (Coats 2003a) simulation. For the time step selection with mole fraction/saturation equation, we utilize the guidelines provided by Coats (2003b). In terms of time step to update the pressure, the heuristic approaches are available to consider the stability problems because of

explicit treatment of primary variables (Todd and Longstaff 1972, Aziz and Settari 1979).

As discussed before, the stability issues of IMPES method can be minimized using an iterative IMPES method. Thus, we need to constrain the changes of the streamline trajectory during a single step by limiting phase flux changes and pore volume injected (PVI) during the time step. To start with, the initial time step is calculated by the following equation.

$$t_p^{init} = PV_{res} / \sum \left| Q_{well}^{rb} \right| \cdot \beta \quad \cdots\cdots\cdots\cdots\cdots\cdots\cdots\cdots\cdots\cdots\cdots\cdots\cdots\cdots\cdots\cdots \quad (3.24)$$

where β controls the pore volume injected. Once the initial time step is calculated, the next time step is chosen according to the maximum allowable changes of the phase flux as follows:

$$\gamma_\alpha = \sum_{grid} \left(\sum_{face} \left(\left| Q_{ijk,\alpha}^{n+1} - Q_{ijk,\alpha}^{n} \right| \right) / V_{ijk} \right) \quad \cdots\cdots\cdots\cdots\cdots\cdots\cdots\cdots\cdots\cdots\cdots\cdots \quad (3.25)$$
$$t_p^{n+1} = \min(t_p^n \cdot PV / \max(\gamma_\alpha) \cdot \beta, t_p^{init})$$

where the constraint of upper/lower bounds per time step is fixed by $0.85 < PV/\max(\gamma_\alpha) < 1.15$. This approach reduces the time step size as the movement of a phase flux increases, and vice versa. Similar expressions can be found in the literature using the total velocity field (Hurtado, Maliska, and Slivfa 2006). The use of the phase flux tends to choose smaller time step compared to the one with the velocity based equation.

3.5.2 Discretization and Implementation

The overall process is the same as for conventional streamline simulation except that capillarity and gravity terms are introduced along the streamlines. Let's now review and expand upon each step in the workflow.

- Solve the pressure equation, Eq. A.5 using finite difference method and calculate velocity on a 3D spatial grid. Pressure is calculated implicitly using Newton-Raphson iteration. Convergence tolerance is set as 1.E-2 of the maximum difference of pressure between iterations. After convergence, the total velocity field is obtained from the total of the phase fluxes computed using Darcy's law.
- Trace streamlines using the total velocity and resample fluid and rock properties, and saturation, along streamlines. Velocity and permeability are mapped according to geometrical information and the directions of the streamline.
- Calculate the component and saturation propagation along streamlines using Eq. 3.22. An explicit calculation is performed at a CFL number of 0.8 along each streamline. For the cases considered, this also keeps us lower a diffusion number of 0.5 for the capillary corrections. The equations can be effectively solved because of convection dominance.
- Resample saturation onto the 3D spatial grid. After resampling, we calculate the transverse flux due to capillarity and gravity using Eq. 3.23. This step simply consists of a spatial redistribution of saturation. We again use an explicit method to solve for saturation although one could replace this with a fully implicit calculation for improved stability.

- Steps 1 through 4 are repeated for pressure updates. The pressure update time steps are selected to minimize the error due to the change in total velocity due to mobility or changing well rates. This requirement is identical for any streamline simulator.

3.5.3 3-phse J-function Capillarity

Before applying model to multicomponent systems, the model is first tested on 3phase black oil system. Figure 3.25 shows a schematic view of 1D coreflood case. The overall simulation case study is same as the one conducted by Chapter II except the capillary is given as J-function with PVT, rock properties given by Appendix F. Here the 3 cases are conducted: IMPES approach with OS, iterative IMPES approach with OS and iterative IMPES with OP.

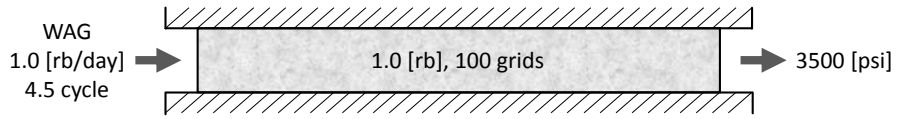

Figure 3.25: 1D injection schematic view used simulation with J-function capillarity.

Through the simulation, the boundary condition is assigned as reservoir volume rate constraint of gas or water, and fixed pressure is given by right side. Unlike previous oil-water scenario, the WAG injection case is a highly nonlinear problem the iterative IMPES method is required to obtain the correct solution. Figure 26(a) and (b) show the result of normal IMPES and iterative IMPES method, calculated by operator splitting

approach. The solid red line in the figure shows the reference solution, which obtained by a commercial simulator by using equivalent PVT and initial/boundary condition with 10000 pressure recalculations. The result of normal IMPES approach does not converges to the reference solution even 10000 pressure recalculation. This problem was seen in previous chapter. It is expected that the solution improves with iterative IMPES method. Figure 26(b) shows that the results are improved. However, the solution is sensitive to the time step length. The reason here is because of operator splitting approach to calculate capillarity. It requires around 1000 pressure recalculation to obtain reference solution.

Now the iterative IMPES is conducted with OP, shown in Figure 2.26(c). Here the effect is significant that solution with 100 shows good agreement with reference solution. This result can be seen in oil production rate shown in Figure 3.27.

The results of saturation distribution and pressures are shown in Figs. 3.28-30. Figs. 3.28 and 29 are the solutions obtained by operator splitting approach with IMPES and iterative IMPES method, respectively. As the number of time step decreases, then the differences with the reference solution increases by operator splitting approach, especially pressure distribution. The result of orthogonal projection is shown in Figure 30. Now the solution converges to the reference solution, even with 10 pressure recalculation.

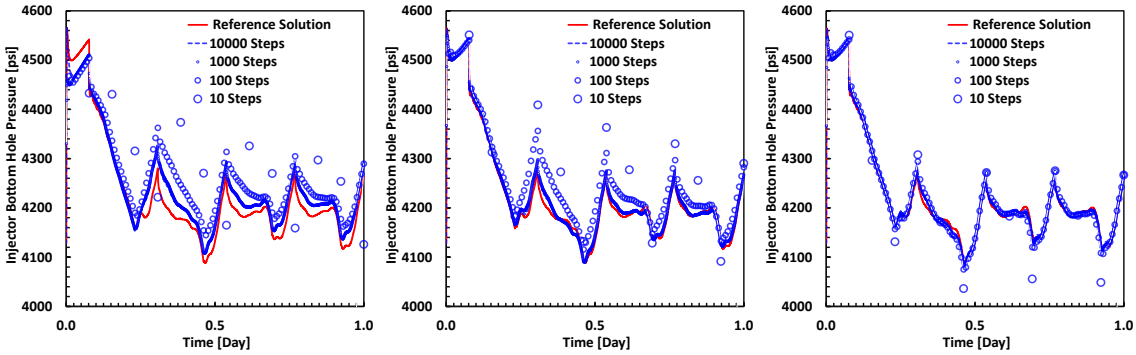

(a) IMPES with OS (b) Iterative IMPES with OS (c) Iterative IMPES with OP

Figure 3.26: History of injection bottom hole pressure by standard IMPES with OS (left), iterative IMPES with OS (middle), Iterative IMPES with OP (right).

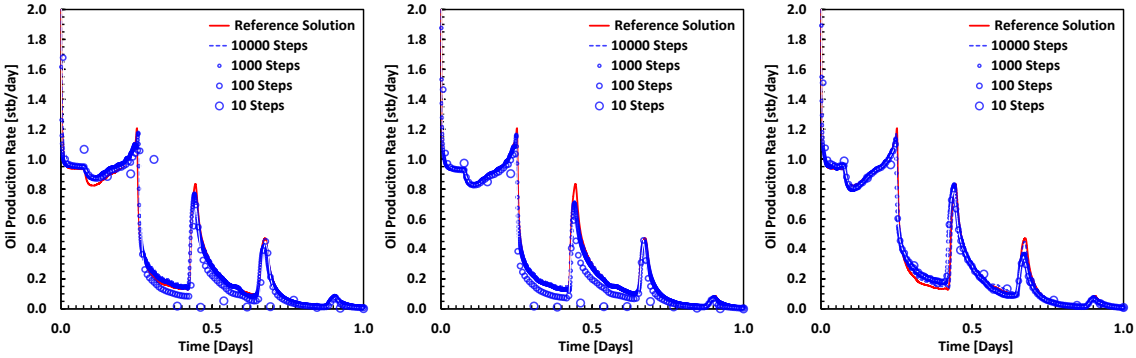

(a) IMPES with OS (b) Iterative IMPES with OS (c) Iterative IMPES with OP

Figure 3.27: History of oil production rate by standard IMPES with OS (left), iterative IMPES with OS (middle), Iterative IMPES with OP (right).

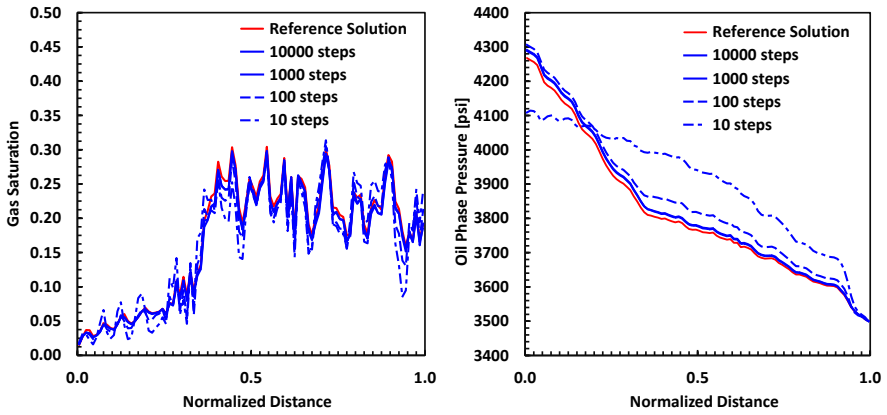

Figure 3.28: Gas saturation distribution (left) and pressure distribution (right) by normal IMPES operator splitting method with different time stepping.

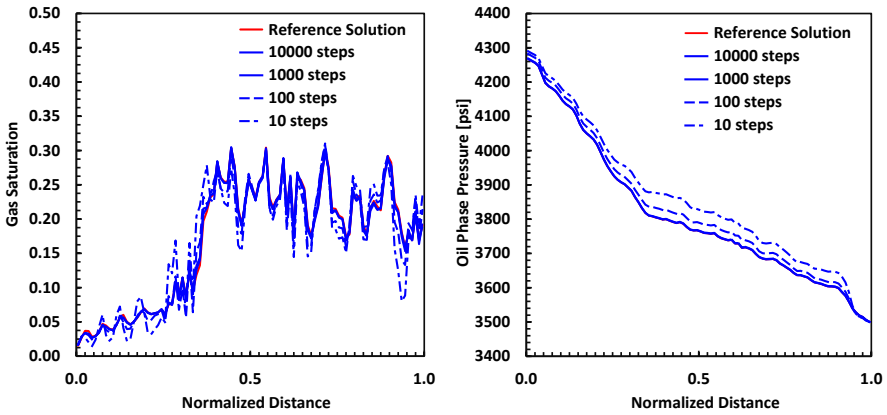

Figure 3.29: Gas saturation distribution (left) and pressure distribution (right) by iterative IMPES operator splitting method with different time stepping.

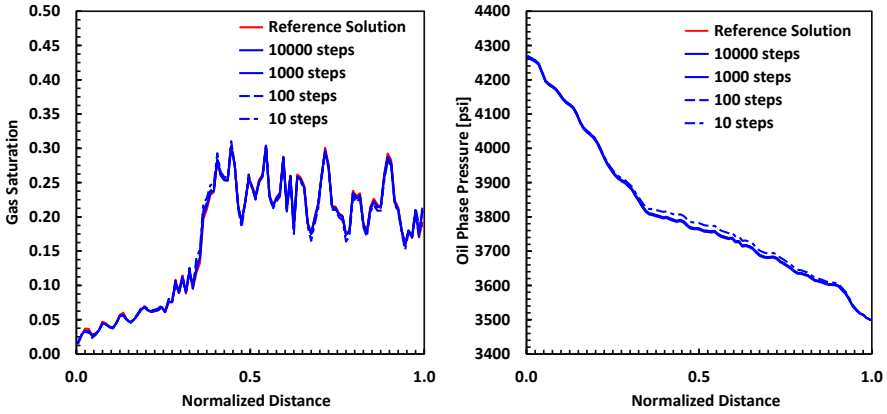

Figure 3.30: Gas saturation distribution (left) and pressure distribution (right) by iterative IMPES orthogonal projection method with different time stepping.

3.5.4 3-phase Multicomponent System

Our proposed model is tested using a series of test problems in 1-D, 2-D and a 3-D field case. The parameters used in these numerical experiments are given in Table F.1-3, including PVT, rock properties and initial conditions. A total of 7 hydrocarbon components and 1 water component are used for all numerical experiments. The initial composition of the field is given in Table F.2 and injection composition is either pure H_2O or 97% CO_2 with 3% of C1, C3. The initial pressure and temperatures are set as 2000 psi, 212 F˚ for the all the synthetic examples. For the purpose of comparisons with commercial simulator, the total mole fraction is normalized after excluding water component from the output of production profile and mole fraction distribution.

The 1D case demonstrates the sensitivity of the solution with respect to time stepping of OP and conventional operator splitting method for oil-gas 2 phase and oil-water-gas 3 phase cases. In 2D case we have applied our method in areal and cross-sectional models using proposed time stepping method and the solution is compared with a commercial finite difference compositional simulator. All the cases are tested for CO_2 injection and the solubility to the water phase is neglected in the synthetic example. The proposed model is also tested in Goldsmith field with CO_2 flooding to see the applicability of the approach for practical field situations.

1D Homogeneous Model

The reservoir permeability, initial porosity and surface tension are shown in Table F.3. The capillary pressure curves used in the simulation are shown in Appendix F, Figure F.2.1-2. The left boundary is set at a constant rate of 1.0 rb/day and a constant pressure of 2000 psi is specified on the right side boundary. The reservoir volume is 1.0 bbl at initial porosity, and CO_2 injection is conducted for 0.25 days. Thus, the total injection is 0.25 PVI.

The sensitivity study of time stepping of pressure equation and 1D saturation equation is conducted using relative permeability and capillary pressure curves given in Figure F.4-5. Figure 3.31 shows the gas saturation distribution and total mole fraction provided by OS and OP with a single pressure update. The parameter here is the frequency of streamline to grid mapping. The mapping is tested for 1,2,4,8,16,32 and 64 times for OS, and a single time for OP. As shown in Figure 3.31, the solution of the OS converges to OP with increasing mapping frequency between streamline and grid. This result concludes that the solution of OP is independent of mapping frequency, while OS introduces augmented dispersion of mole fraction and saturation without any anti-diffusive treatment.

Figure 3.32 shows the comparisons of OP with a commercial simulator. Again gas saturation distribution and total mole fraction of CO_2 are compared. Note that Fully-Implicit method (FIM) is used for the commercial simulator to correctly take into account capillary effects while the streamline-based method is an IMPES approach. The equation used in commercial simulator (Schlumberger 2012b) has differences in

sink/source treatment and the capillarity equation. Thus, the objective here is to verify that our solution is within reasonable agreement rather than exact agreement. The results of OP show good agreement with the one obtained by commercial simulator. In addition, the effect of frequency of the pressure update is not significant in this example. This result supports the strength of the iterative IMPES approach because it takes into account the non-linearity of PVT and mobility through an iterative process between pressure and saturation equation.

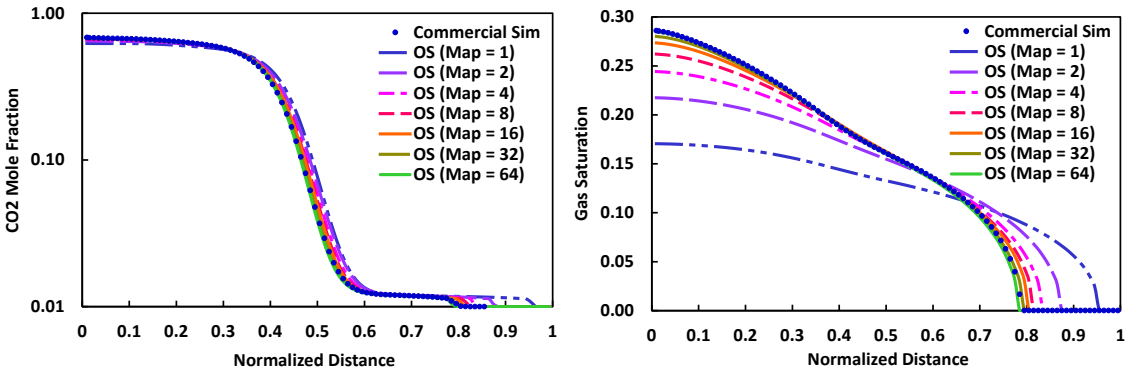

(a) CO_2 mole fraction **(b) Gas saturation**

Figure 3.31: CO_2 mole fraction and gas saturation distribution at 0.25 PVI for the 1D horizontal model. The solution is compared by OS with multiple mapping of saturation equation between streamline and grid (1,2,4,8,16,32,64) and OP with single mapping.

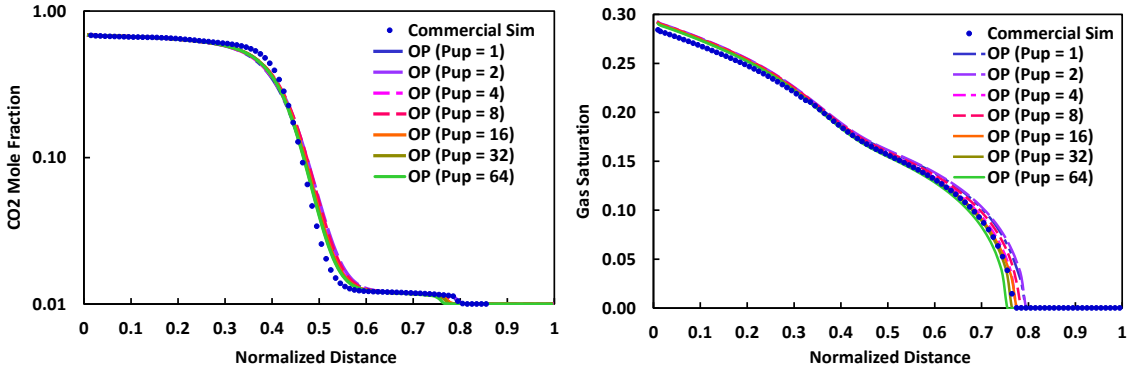

(a) CO_2 mole fraction **(b) Gas saturation**

Figure 3.32: CO_2 mole fraction and gas saturation distribution at 0.25 PVI for the 1D horizontal model. The solution is compared by OP with pressure updating of (1,2,4,8,16,32,64) times by solid lines, the commercial simulator is shown in dotted line.

The same numerical experiment is conducted with an initial water saturation of 50%. The three-phase relative permeability is calculated by the Stone's 2nd equation. The results are shown in Figure 3.33 and 3.34. The results of OP, OS and commercial simulator lead to same conclusions as in the 2-phase oil-gas cases. The model is also tested with OP using the proposed optimal time stepping method and the hydrocarbon mole fraction and water saturation distribution are compared with commercial simulator as shown in Figure 3.35. The proposed optimal time step method provides good agreement for this 1D 3-phase case.

Next, the simulation model is tested with different rock properties. The 3-different wettability cases (Oil Wet: OWET, Water Wet: WWET and mixed wet: MWET) have three different exponents in the relative permeability and capillary pressure equation and are designed after the literature (Di Carlo, Sahni, and Blunt 2000, Hustad 2002). The

numerical experiments showed that the gas front propagation is very sensitive to the exponents. A more diffused propagation of the gas front is generated with smaller exponents of relative permeability and capillary pressure equation while the shape of the gas front is similar for the OWET, WWET and MWET case.

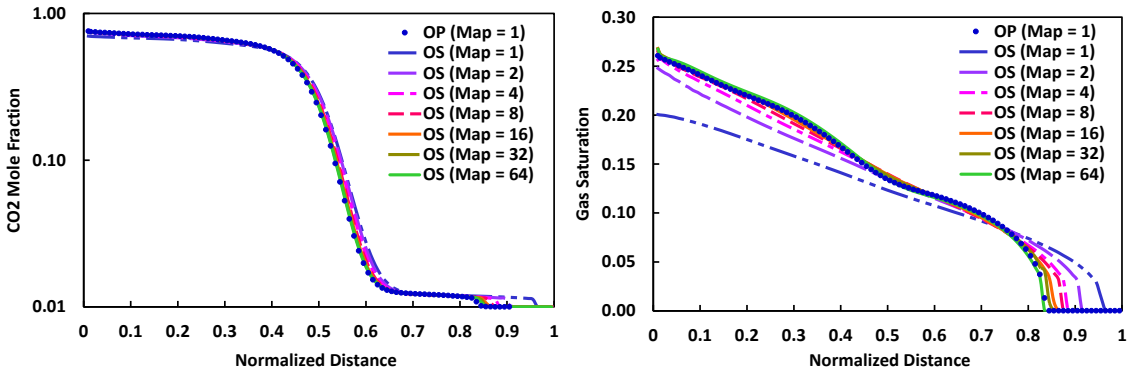

(a) CO_2 mole fraction **(b) Gas saturation**

Figure 3.33: CO_2 mole fraction and gas saturation distribution at 0.20 PVI for the 1D horizontal model. The solution is compared by OS with multiple mapping of saturation equation between streamline and grid (1,2,4,8,16,32,64) and OP with single mapping.

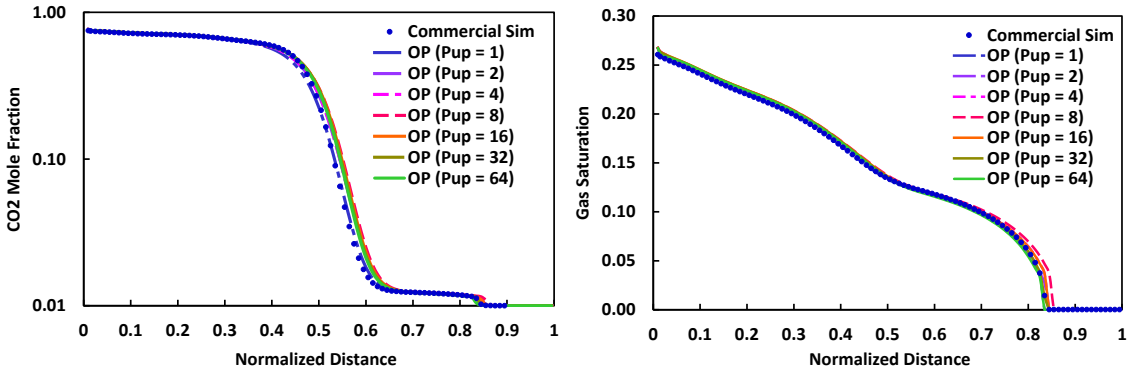

(a) CO_2 mole fraction **(b) Gas saturation**

Figure 3.34: CO_2 mole fraction and gas saturation distribution at 0.20 PVI for the 1D horizontal model. The solution is compared by OP with pressure updating of (1,2,4,8,16,32,64) times by solid line, the commercial simulator is shown in dotted line.

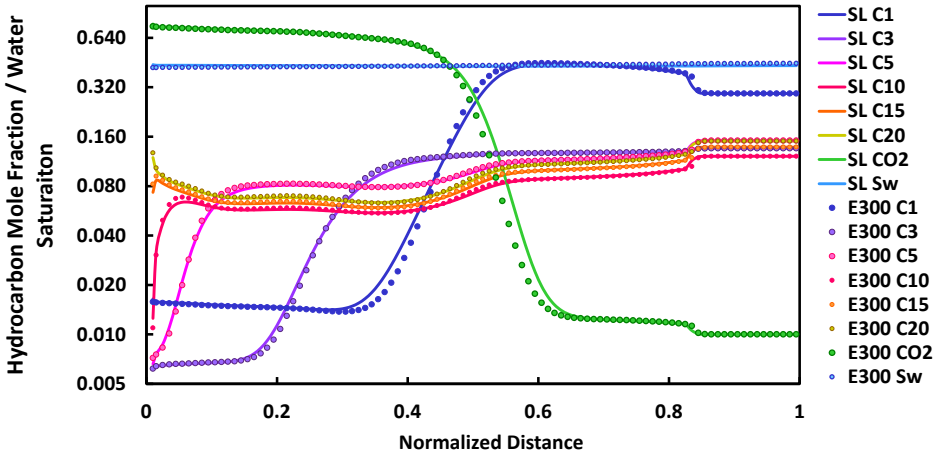

Figure 3.35: Comparisons of hydrocarbon mole fraction and water saturation at 0.2 PVI, by commercial simulator and OP with optimal time stepping. Solid line by OP and dotted by commercial simulator.

2D Areal and Cross-section

The simulation model is tested in 2D areal and cross-sectional cases with water-wet rock properties (Appendix F, Figure F.4a). The other properties such as component critical parameters are summarized in Table F.2-3. The injector is constrained by the reservoir volume of CO_2 injection rate and the producer by bottom-hole flowing pressure. Figure 3.36 shows the CO_2 mole fraction along streamlines obtained by convection only (Figure 3.36a) and with capillarity by OP (Figure 36b) using a single large time step. The final saturation distribution after adding the corrector term on the grid is shown in Figure 3.37. In the 2D areal model most of the capillary driven flow is considered to be along streamline as shown in Figure 3.36a and thus, the difference of the final mole fraction after the corrector step is small as in Figure 3.37b.

The model is also tested with a cross-section case with kv/kh = 0.1. A pressure of 2000 psi is assigned at the top of the reservoir and oil/water and gas/oil contact is set to be outside of the domain. The first test is the comparisons of CO_2 mole fraction with convection only and inclusion of capillary and gravity via OP. The result showed that the inclusion of capillarity and gravity along streamline is quite effective and the buoyancy effect of CO_2 component is captured along streamline, shown in Figure 3.38. The final result of CO_2 mole fraction is shown in Figure 3.39b and the result of commercial simulator, Figure 3.39a shows the same trend. The production mole fraction of areal and cross section case is shown in Figure 3.40 and 3.41, respectively. To compute production profile, the optimal time stepping method is used for OP. For each pressure recalculation, there is a single predictor step followed by a single corrector step. The

agreement between OP and the commercial simulator is quite satisfactory. The agreement of the production profile is also satisfactory in cross section case shown in shown as Figure 3.41.

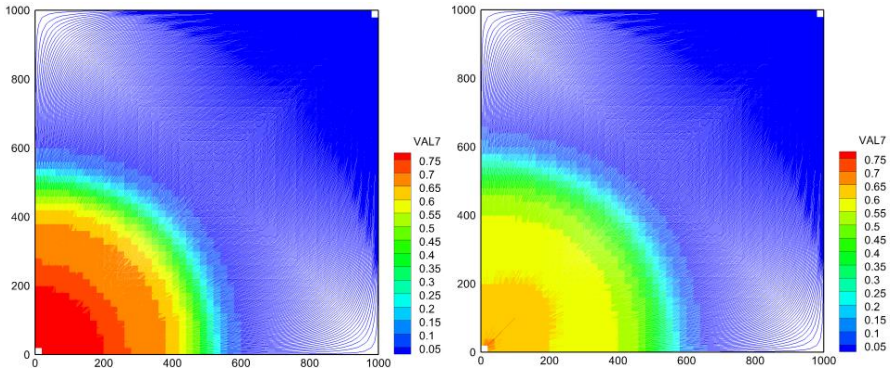

(a) OP, Convection only **(b) OP, Convection + Capillarity**

Figure 3.36: Homogeneous reservoir CO_2 mole fraction distribution of 10000 days obtained from: (a) Along streamline, convection only, single step (b) Along streamline, convection with capillarity effect, single step.

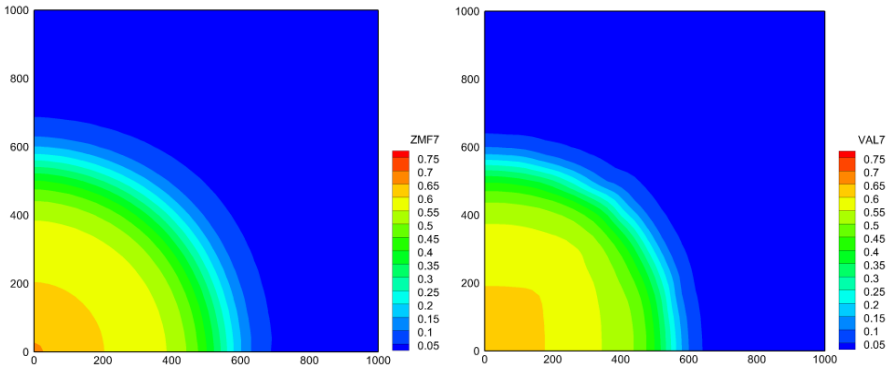

(a) Commercial simulator **(b) Streamline-based method**

Figure 3.37: Homogeneous reservoir CO_2 mole fraction distribution at 10000 days obtained from: (a) Commercial Simulator, default time stepping (b) Orthogonal projection, single step.

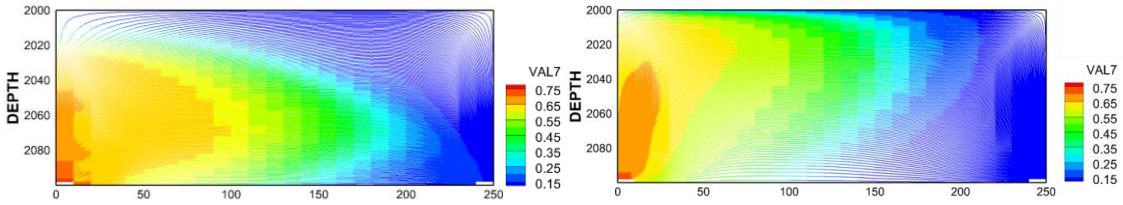

(a) OP, Convection only **(b) OP, Convection + Capillarity + Gravity**

Figure 3.38: CO_2 mole fraction distribution using orthogonal projection along streamlines for the 2D cross-sectional case.(a) Convective flow only (b) Gravity + Capillarity + Convective flow.

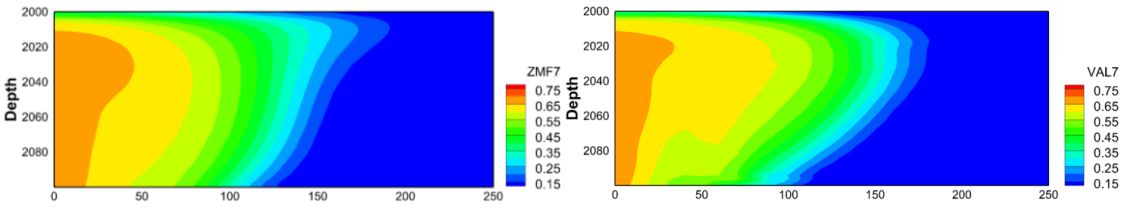

(a) Commercial simulator **(b) OP, after transverse correction**

Figure 3.39: CO_2 mole fraction distribution of cross-sectional model; (a) Commercial simulator (b) Orthogonal projection after including the transverse corrections on grids.

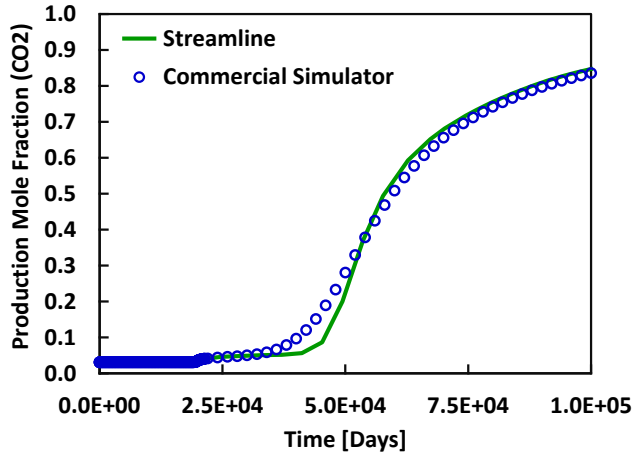

Figure 3.40: Production mole fraction of CO_2 by streamline-based orthogonal projection and commercial simulator: Areal homogeneous case.

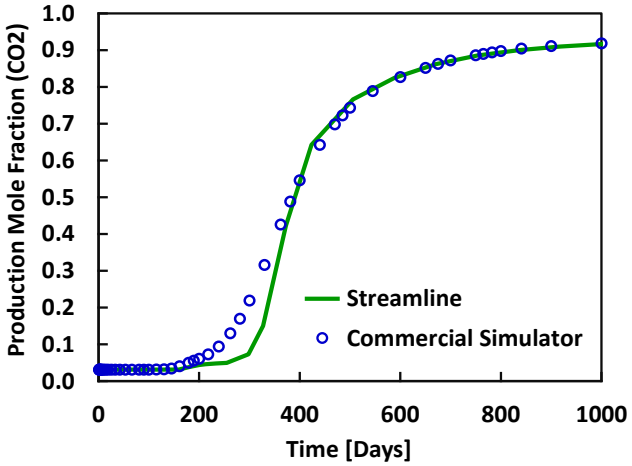

Figure 3.41: Production mole fraction of CO_2 by streamline-based orthogonal projection and commercial simulator: Cross section homogeneous case.

2D Cross-section with Heterogeneity

We repeat the CO_2 injection in a heterogeneous cross-section case. The heterogeneity is given by the permeability distribution ranging from 0.1 to 1000 mD, respectively. The vertical permeability is assigned to be *kv/kh* = 0.1 while capillary pressure is calculated using horizontal permeability with the Leverett J-Function. Figure 3.42 shows the streamline distribution with time-of-flight contours. The results of C1 distribution are shown in Figure 3.43 for the commercial simulator and streamline model. The high concentration region is observed around the periphery of the injected CO_2. The streamline-based approach shows a sharper front in C1 distribution. The production concentration of CO_2 shows a jump at breakthrough. The J-function provides strong capillarity at low permeability region and it causes fingering of the propagation of CO_2 in water-wet condition.

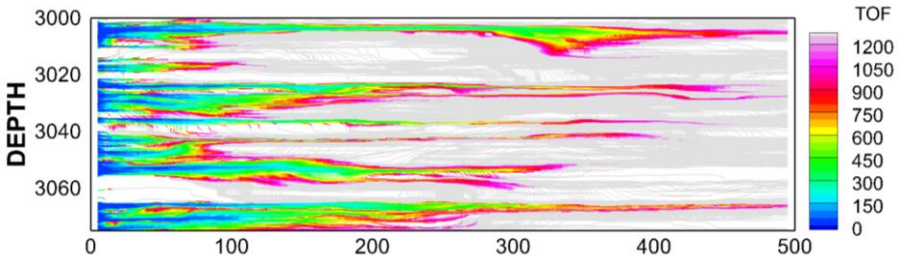

Figure 3.42: Streamline and time-of-flight by cross-section heterogeneous model.

The production mole fraction is shown in Figure 3.44. The time stepping of this case study including 2D areal and cross-sectional case is summarized in Table 3.3. The reservoir parameters used for the synthetic study is summarized in Table 3.4. The result

indicates that the time stepping of OP could be 2 times larger for the areal and cross-sectional cases. The production profiles are correctly captured with the PVI criteria, β = 0.01 in Eq. 3.25.

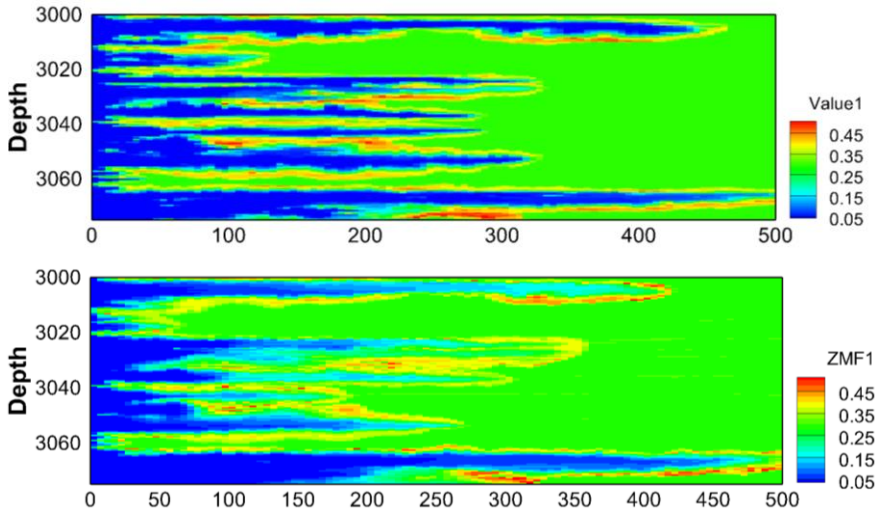

Figure 3.43: C1 mole fraction distribution of OP (top) and commercial simulator (bottom).

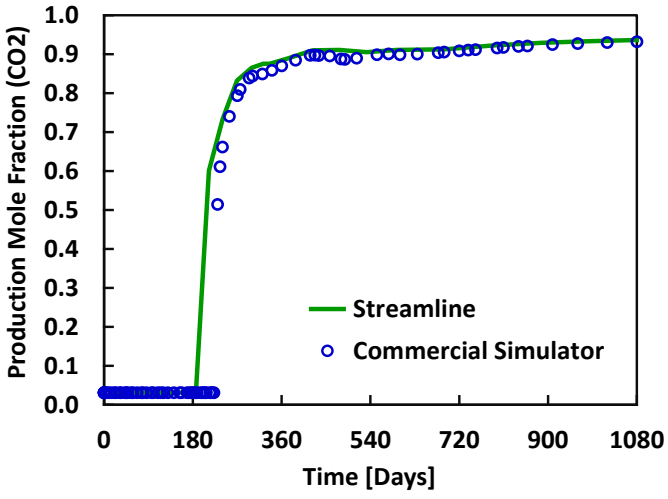

Figure 3.44: Production mole fraction of CO_2 by proposed method and commercial simulator.

Table 3.3: Time step used for simulation study			
Simulation Case	Commercial Simulator (E300 Default, FIM)	Streamline Simulation	Coefficient β in Eq. (3.25)
1D Oil-Gas	2500 (given)	1-64	-
1D Oil-Gas-Water	2000 (given)	1-64	-
2D Areal	473	37	0.01
2D Cross-Section	51	23	0.01
2D Cross-Section Heterogeneous	86	25	0.01
Goldsmith Field	383	120	-

Table 3.4: Parameters used to define Relperm and default capillary curve				
Simulation Case	Mobile Phase Existence	Porosity	Permeability [mD]	Surface Tension [dynes/cm]
1D Oil-Gas	Oil Gas	0.1	157.868	8.606
1D Oil-Gas-Water	Oil Water Gas	0.1	157.868	8.606
2D Areal	Oil Gas	0.15	100.0	5.592
2D Cross-Section	Oil Gas	0.1	100 (kv/kh=0.1)	5.0
2D Cross-Section Heterogeneous	Oil Water Gas	0.1	0.1-1000 (kv/kh=0.1)	5.0
Goldsmith Field	Oil Water Gas	0.05-0.15	0-1000 (kv/kh=0.1)	0.1

Application to the Goldsmith Field Case

We applied the streamline-based compositional model to a field case to demonstrate its practical feasibility. The asset is the Goldsmith field in San Andreas unit, a dolomite formation in West Texas shown in Figure 3.45. The simulation is performed first with waterflood for 20 years based on the historical injection and production rates, and then Water-Alternation-Gas (WAG) process is simulated using both the streamline and the

commercial finite-difference simulator. The reservoir permeability is shown in Figure 3.46 with example of streamline snapshot. The initial composition of the reservoir is not available and thus, the composition in Table F.3 is used. The composition is adjusted to have fluid viscosity and density close to the initial black-oil model.

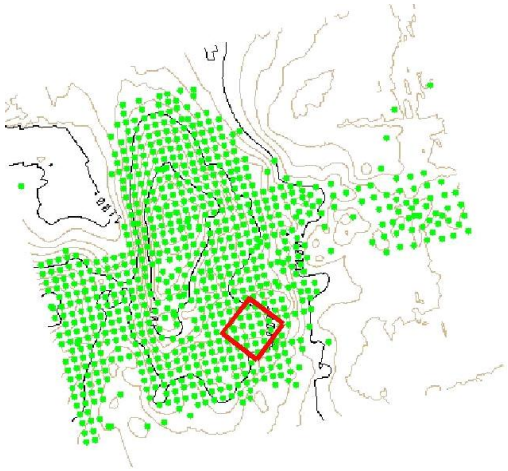

Figure 3.45: CO_2 pilot project site, Goldsmith field.

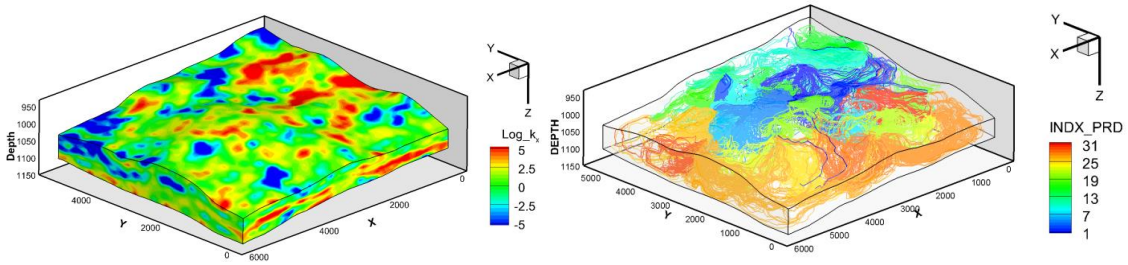

(a) Permeability (Log scale) **(b) Streamline distribution**

Figure 3.46: Reservoir properties and streamline distribution of the Goldsmith field.

After 20 years of waterflood, the WAG injection is performed for 10 years with every ¼ years of water-gas injection cycle. The injection volume of water and CO_2 is set

to be same as in the end of the historical data with a maximum injection pressure constraint. The production history of the simulation is shown in Figs 3.47-49. The production history of CO_2 concentration captures the same trend as in the commercial simulator with 3 times larger time step for the streamline-based OP method when compared with the commercial fully implicit simulation. In addition,

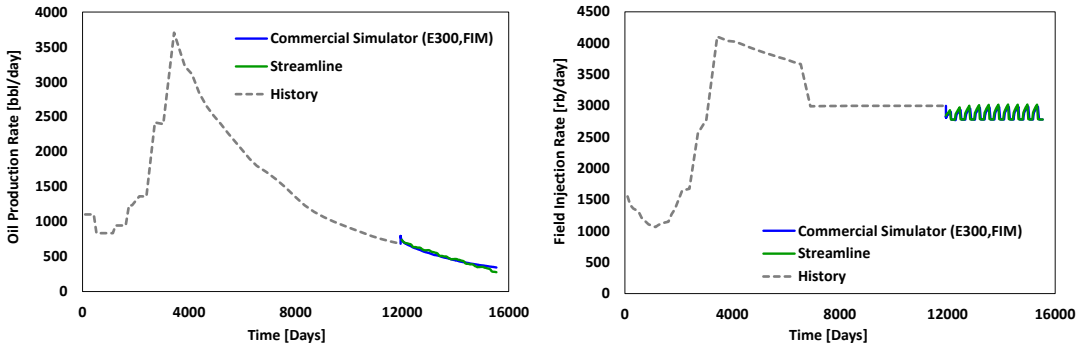

(a) Field total oil production rate **(b) Field total injection**

Figure 3.47: Production and injection profile of history and WAG process.

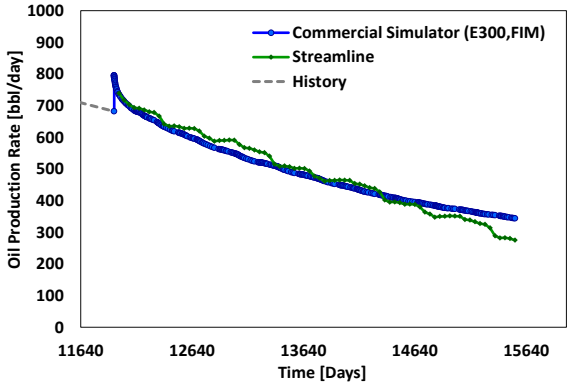

Figure 3.48: Comparisons of field oil production total during WAG period.

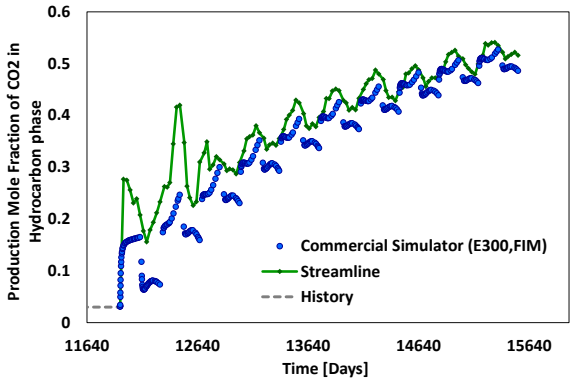

Figure 3.49: Production profile of WAG process, total mole fraction of CO_2 in hydrocarbon phase.

Figure 3.50 shows the streamline distribution with the contours of capillary-related parameters. With streamline distribution, we can now examine the interactions of fluid transport with capillary and buoyancy forces caused by the reservoir property variations and saturation distribution.

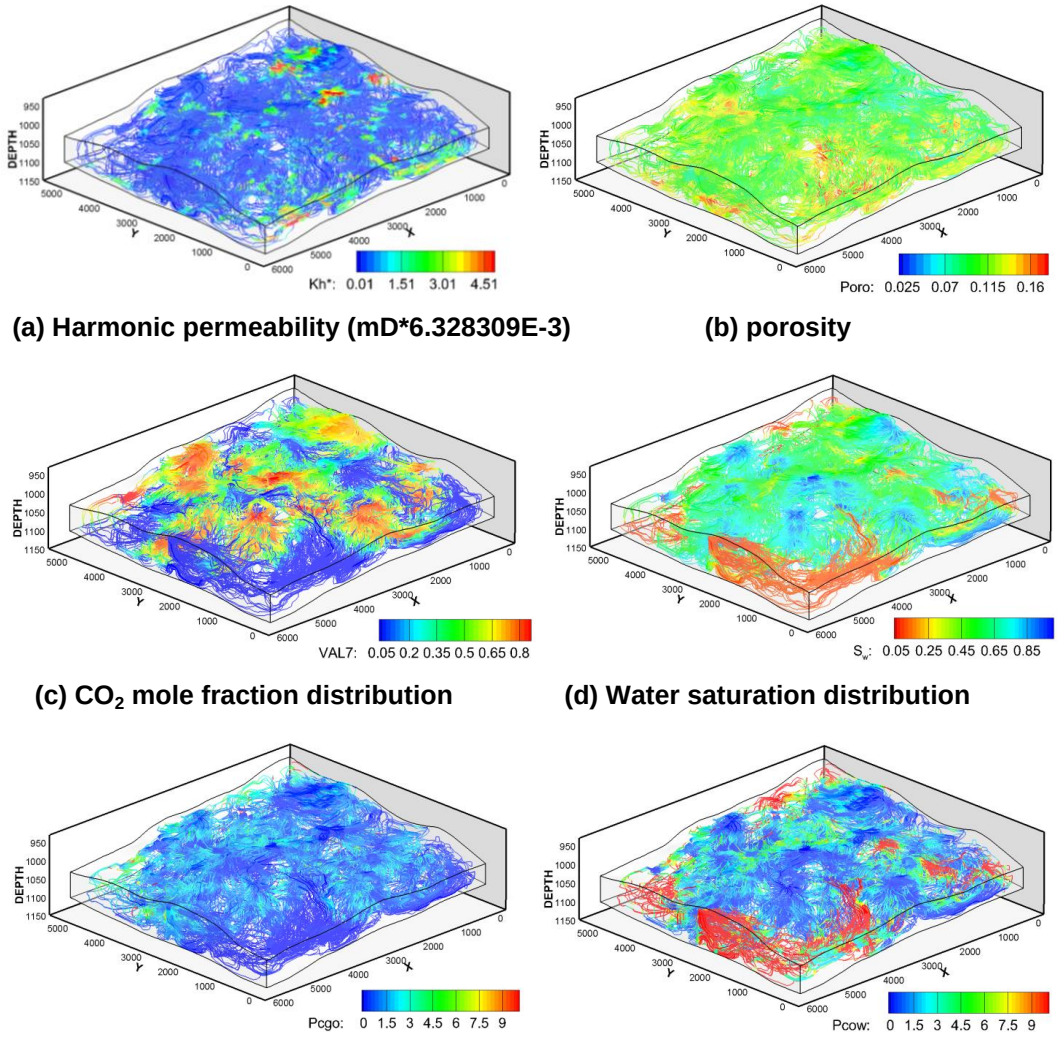

(a) Harmonic permeability (mD*6.328309E-3) **(b) porosity**

(c) CO_2 mole fraction distribution **(d) Water saturation distribution**

(e) Capillary pressure of oil-gas phase **(f) Capillary pressure of oil-water phase**

Figure 3.50: Streamline distribution with contours of capillarity-related properties.

3.6 Chapter Conclusions

A new orthogonal projection (OP) method to incorporate capillarity and gravity in streamline-based compositional simulation has been presented and its effectiveness is demonstrated with three phase black oil and fully compositional simulation. The proposed approach enables us to take larger time step compared with conventional operator splitting (OS) approaches and more importantly, bypasses the need for an anti-diffusive correction in operator splitting treatments. We confirmed the advantages of the OP approach compared to the OS through a series of 1D and 2D synthetic examples and a 3D field-scale CO_2 WAG injection case. For the 1D case with oil-gas 2phase and oil-water-gas 3 phase problems, our results showed good agreement with a commercial finite-difference simulator.

The solution with OP and a single streamline-grid mapping showed the same result as with multiple mapping of the OS without anti-diffusive treatment. The three-phase capillary model is also tested with various wettability cases and the results were consistent with the one obtained from a commercial simulator. For the 2D areal and 2D-cross-section examples with homogeneous and heterogeneous permeability fields, the proposed OP showed good agreement with the commercial simulator both in terms of component distribution and production history with larger time steps. The proposed method was also applied to a field-scale case to examine its practical feasibility.

The volumetric production and the mole concentration history capture the same trend as in the commercial simulator, again with approximately 3 times larger time step.

The streamline distribution seems to effectively capture the reservoir fluid dynamics and the interaction of convective, capillarity and gravity forces.

CHAPTER IV

APPLICATION OF STREAMLINE-BASED RESERVOIR SIMULATOR FOR HISTORY-MATCHING PROBLEMS

4.1 Summary

This chapter summarizes an application of the developed simulator to the history matching problem. The streamline based history matching has three main advantages. First, it is fast because of analytical ways of sensitivity calculation. Second, streamline based method enables updating of high resolution geological models. Third, the approach can be applied using post processing from simulation results and can be applicable to any available simulator. Here we first discuss conventional techniques about streamline-based data integration and then propose an improved approach.

4.2 Streamline-based History Matching

Up to the previous chapter, we discussed ways to forecast production history based on a given static reservoir model. These static data (or, called *a priori* data) typically comes from geostatistical methods (Caers, Avseth, and Mukerji 2001, Hansen *et al.* 2006, Remy, Boucher, and Wu 2009) derived from well log or core analysis (API 1960, Timur 1968). The history matching is the process to integrate static data with dynamic (*a posteriori*) data, which is production history, well test results or time-lapse seismic measurement data. Typically the history matching is the process to minimize production history and calculated simulation results as

$$\min\left\{\sum_{data}\left(d_{obs}-d_{cal}\right)^2\right\} \quad \cdots\cdots\cdots\cdots\cdots\cdots\cdots\cdots\cdots\cdots\cdots\cdots\cdots\cdots\cdots\cdots \quad (4.1)$$

In order to achieve this, several methods are available. They are mainly categorized by manual, deterministic (Yang and Watson 1988, Vega, Rojas, and Datta-Gupta 2004, Hoffman *et al.* 2006) and stochastic method (Hastings 1970, Granville, Krivanek, and Rasson 1994). The other category is gradient or non-gradient approach. The stochastic method is typically a non-gradient method because it tries to search all of the solution space by the evolutionary algorithm, Monte-Carlo method or geosatistical method such as Ensemble Kalman Filter (Aanonsen *et al.* 2009, Tanaka *et al.* 2010) or smoother (Chen and Oliver 2012). These methods generally require multiple initial static models and update to find the global minimum of the solution space. There is hybrid method available such as SPSA (Sen *et al.* 1995), which calculate gradient but objective function is stochastic. The other approach is to conduct deterministic and stochastic inversion sequentially to calibrate global parameter by stochastic algorithm such as oil-water contact, fault permeability or fluid PVT properties, then calibrate local permeability or porosity by deterministic approach (Yin *et al.* 2010). There are more literatures available for these inversion algorithms (Oliver, Reynolds, and Liu 2008) and here we review mainly the deterministic method.

The deterministic approach, or often called a gradient based approach is a method to find local or global minimum from a given single initial static data. The gradient method uses sensitivity of static data *m* to the production data *d* as

$$\mathbf{G} = \frac{\partial \mathbf{d}}{\partial \mathbf{m}} \quad \cdots\cdots\cdots\cdots\cdots\cdots\cdots\cdots\cdots\cdots\cdots\cdots\cdots\cdots\cdots\cdots\cdots\cdots \quad (4.2)$$

where **G** is the sensitivity matrix of the production data with respect to the reservoir parameter **m**, such as porosity or permeability. There is quite a bit of prior work to calculate sensitivity matrix efficiently. One example is the perturbation method and it requires *n+1* simulation with given *n* static parameters. If static parameter is permeability field, the simulation needs to be conducted (number of discretized grid +1) and thus, it is computationally expensive to update individual cell property (Dogru and Seinfeld 1981). The gradzone method is a practical method of the perturbation method (Brun, Gosselin, and Barker 2004) because this approach samples static data and calculate parameter sensitivity sparsely and uses interpolation to extend sparse sensitivity to entire field. The gradient simulator or adjoint method (Dogru and Seinfeld 1981, Wu and Datta-Gupta 2002, Zhang *et al.* 2006, Daoud and Velasquez. 2006) is effective compared with perturbation method, because it requires one forward simulation and another system of adjoint equation. Thus, the computational cost is less than 2 simulations. However, this approach requires a system of linear equation which is a discretized form of the flow equation and its derivative with respect to model parameters. Because of these reasons, it has difficulties in applicability unless the reservoir simulator can generate derivative of the discretized flow equation with respect to the static parameters.

Compared with these deterministic approach, the streamline-based method has advantages in terms of computational efficiency and applicability (Datta-Gupta and King

2007). The main advantage of the streamline-based method is that it is able to calculate parameter sensitivity with a single simulation with post processing of the simulation results. The calculated sensitivity is comparable to the sensitivities that are computed from adjoint method which requires to construct adjoint equation and solve it. Also streamline-based flow simulation has computational advantages as discussed in the previous chapter. It is possible to calculate parameter sensitivity from commercial simulator using streamline-based approach, because it can be calculated from the flux field and given static data. These are the main reason that streamline-based approach is often called an Assisted History Matching (Wang and Kovscek 2000, Milliken, Emanuel, and Chakravarty 2001, Datta-Gupta and King 2007), because streamline method can help history matching from the finite difference method using flux field.

4.2.1 Streamline and Parameter Sensitivity

The streamline based history matching starts from tracing of streamline from the given static and dynamic conditions as we discussed in Chapter II, and then finding time-of-flight sensitivity. It is important to note that the streamline trajectories and time-of-flight implicitly characterize the underlying heterogeneity of the field relevant to flow and transport. The relationship between time-of-flight and static parameter is introduced first by Vasco, Seongsik, and Datta-Gupta (1999) correlating Darcy's law with time-of-flight as

$$\tau = \int_s \frac{\phi(\xi)}{\lambda_t(\xi)k(\xi)|\Delta p(\xi)|} d\xi \quad \cdots\cdots\cdots\cdots\cdots\cdots\cdots\cdots\cdots\cdots\cdots\cdots\cdots\cdots\cdots\cdots \quad (4.3)$$

Note that this equation is used for sensitivity calculation and gravity term is not included. From the above equation, we can find the derivative of the reservoir parameter, porosity or permeability with respect to time-of-flight of node *i*, $\Delta\tau_i$, as

$$\frac{\partial \Delta \tau_i}{\partial k_i} = -\int_s \frac{\phi}{\lambda_t k^2 |\Delta p|} d\xi = -\int_s \frac{\tau}{k} d\xi = -\frac{\Delta \tau_i}{k_i} \quad \cdots\cdots\cdots\cdots\cdots\cdots\cdots\cdots \quad (4.4)$$

This relation is valid with the existence of the gravity. The time-of-flight is calculated by Eq. 2.59, not the Eq. 4.3, however. Alternatively, parameter sensitivity can be calculated using the same procedure shown as Stenerud and Lie (2004). This equation is based on Dykstra-Persons assumptions, whereby change of permeability affects only along 1D streamline space. Because most of the history matching process is under uncertainty and rigorous sensitivity calculation is not often required and it is quite useful to calculate parameter sensitivity such as porosity, mobility or flow rate by this simple formulation.

To extend the time-of-flight sensitivity to production data integration, production sensitivity is calculated, such as sensitivity of injection fluid arrival time to producer with respect to reservoir property. This is first exploited by Vasco, Seongsik, and Datta-Gupta (1999) for tracer inversion problem and seismic ray tracing algorithm by introducing a 'diffusive' time-of-flight based upon an asymptotic solution of the diffusion equation for integration of transient pressure data. He, Yoon, and Datta-Gupta (2002) extended the method for two phase convective flow problem. Based on two phase saturation transport equation, the shift of the saturation δS at producer with perturbation of reservoir static parameter δm is given as

$$\delta S(\tau,t)=\frac{\partial S}{\partial t}\delta t+\frac{\partial S}{\partial \tau}\frac{\partial \tau}{\partial m}\delta m=0 \quad \cdots\cdots (4.5)$$

This yields the following functional dependency between arrival time of water saturation and static parameter as

$$\frac{\delta t}{\delta m}=-\left(\frac{\partial S}{\partial t}\right)^{-1}\frac{\partial S}{\partial \tau}\frac{\partial \tau}{\partial m} \quad \cdots\cdots (4.6)$$

The self-similar condition of the Riemann problem or Buckley-Leverett theorem (Juanes and Patzek 2004) relates saturation change by the function of time and time-of-flight referred to the fractional flow derivative by

$$\frac{\partial f_\alpha}{\partial S_\alpha}=-\frac{\partial S_\alpha}{\partial t}\left(\frac{\partial S_\alpha}{\partial \tau}\right)^{-1} \quad \cdots\cdots (4.7)$$

Rearranging Eqs. 2.6-7, we have arrival time sensitivity of reservoir static property as

$$\frac{\delta t}{\delta m}=-\left(\frac{\partial f_\alpha}{\partial S_\alpha}\right)^{-1}\frac{\partial \tau}{\partial m} \quad \cdots\cdots (4.8)$$

This equation indicate that the sensitivity of the breakthrough time of a given static property *m* is a function of the speed of the phase flow of the front, $f_\alpha'^{-1}$ at the well and time-of-flight sensitivity along streamlines. When the problem is tracer injection in single phase system, the speed of the component is unity without physical diffusion or numerical dispersion of the component. Therefore, the sensitivity of the travel time of the tracer response is equivalent to the time-of-flight sensitivity.

The travel time sensitivity is used to find the shift time of the breakthrough information. If the amplitude matching of the observation and calculation data is required, it is also possible to derive production data sensitivity by the streamline method. This can be applied by taking derivative of the production data by chain rule as

$$\frac{\delta f_\alpha}{\delta m} = \frac{df_\alpha}{dS_\alpha}\frac{\partial S_\alpha}{\partial \tau}\frac{\partial \tau}{\partial m} \quad \cdots\cdots (4.9)$$

where $\frac{\partial S_\alpha}{\partial \tau}$ is calculated numerically along streamline. Here, an appropriate average is required to find $f_\alpha'^{-1}$ for Eq. 4.8 and $\frac{\partial S_\alpha}{\partial \tau}$ in Eq. 4.7. For both travel time and amplitude inversion, the 10% of total nodes along streamline are used to evaluate the average to find the numerical gradient.

4.2.2 Amplitude, Travel-time and Generalized Travel Time Inversion

As given in Eq. 4.1, the objective of the inverse problem is to minimize the misfit function. With a given number of observation data point through the time, N_d, and the number of wells, N_w, the production data misfit is represented as

$$R = \sum_{j=N_w}\sum_{i=N_d}\left(d_{obs}^{j}(t_i) - d_{cal}^{j}(t_i)\right)^2 \quad \cdots\cdots (4.10)$$

where the typical production data are water cut or tracer response which are measured periodically at individual wells. The approach to minimize the objective function through all the observed points and simulation results and defined as amplitude inversion, as shown in Eq. 4.10. The “travel-time inversion”, instead, attempts to match single reference time such as water breakthrough point or peak response of the tracer

response. The amplitude matching is more general in terms of reduction of the objective function, because the travel time inversion is to reduce the objective function at a single point while amplitude matching can cover all the data points. However, travel-time based approach is often used because the amplitude inversion is highly nonlinear and has difficulties to reduce objective function with large amount of wells and data points (Cheng *et al.* 2006).

An alternative approach to combine the advantages of the amplitude and travel time inversion is the Generalized Travel-Time Inversion (GTTI) method (He, Yoon, and Datta-Gupta 2002). The novelty of this method is to reduce the travel time inversion as well as the amplitude of the data. The objective is thus to find a optimal time shift $\Delta\tilde{t}$ which provides good agreement with arbitrary number of observed and calculated data points. In other words, the objective of the GTTI is to maximize the coefficient of determination of observed and calculated data points, defined as

$$R^2\left(\Delta\tilde{t}\right)=\frac{\sum_{i=N_d}\left(d_{obs}\left(t_i\right)-d_{cal}\left(t_i+\Delta\tilde{t}\right)\right)^2}{\sum_{i=N_d}\left(d_{obs}\left(t_i\right)-\bar{d}_{obs}\right)^2} \quad \cdots\cdots\cdots\cdots\cdots\cdots\cdots\cdots \quad (4.11)$$

The generalized travel time inversion retains the desirable properties of the travel-time inversion and at the same time accomplishes amplitude matching of the production data. It is important to note that the computation of the optimal travel-time shift does not require any additional flow simulation. It is carried out as post-processing of the data at each well after the production response is computed.

The sensitivity of the GTTI method is also found by travel time inversion shown in Eq. 4.8. Consider a small perturbation in reservoir properties, δm and the shift of the production response in time by δt. In a example of oil-water problem, Eq. 4.8 describe that change of the static parameter δm cause the time shift of the production response at every data point of well after arrival of the shock front saturation, $S_{a,shock}$ which can be found by the Buckley-Leverett theorem and the fractional flow. We then have the following relationship for the observed times

$$\delta t = \left[\frac{\partial t_i}{\partial \mathbf{m}}\right]^T \delta \mathbf{m} \quad \cdots\cdots\cdots\cdots\cdots\cdots\cdots\cdots\cdots\cdots\cdots\cdots\cdots\cdots\cdots\cdots \quad (4.12)$$

Summing Eq. 4.12 over all the data points, we can arrive at the following simple expression for the sensitivity of the travel-time shift with reservoir static parameter **m** as

$$\frac{\delta \tilde{t}}{\delta \mathbf{m}} = -\left(\sum_{i=data} \frac{1}{\Delta t_i}\right) \sum_{i=data} \Delta t_i \frac{\partial t_i}{\partial \mathbf{m}} \ , \ \frac{\partial t_i}{\partial \mathbf{m}} = \Delta t_i = 0 \ \forall \ S_\alpha < S_{\alpha,shock} \quad \cdots\cdots\cdots \quad (4.13)$$

Thus the generalized travel time sensitivity is nothing but the weighted sum of the travel time sensitivity with respect to the time step after break through saturation. The negative sign in the equation reflects the sign convention adopted for defining the generalized travel-time shift.

4.2.3 Pressure Drop Sensitivity

In the previous work of the streamline-based history matching, the objective function is the production flow rate and pressure data is treated separately. Vasco, Seongsik, and Datta-Gupta (1999) use 'Diffusive time-of-flight' as a prior process to match the transient pressure behavior. Their approach calibrates pressure data as a prior step and

assumes that these pressures are maintained through streamline-based Assisted History Matching (Alhuthali, Oyerinde, and Datta-Gupta 2007). However, pressure data shifts during the AHM process and thus iteration process is required to integrate both pressure and production rate. Wang and Kovscek (2000) use effective property idea to calibrate pressure data without using sensitivity calculation. Their approach is to tune permeability along streamline to match the observed data. Here the new approach is proposed to integrate pressure data by calculating analytical sensitivity of the pressure drop along streamlines with respect to reservoir parameters.

The streamlines are traced using pressure gradient generated by injector or producer. Normally, pressure is solved on 3D grid space as we discussed in Appendix A and B. However, it is also possible to construct pressure equation along streamline assuming that there is no interaction outside of the 1D coordinate. The overall idea is to construct pressure equation along streamline with the given boundary condition and take a derivative with respect to reservoir static properties.

In Continuous Space

To describe the concept of pressure drop sensitivity along streamline, we first find the derivative of pressure drop with respect to permeability on 1D homogeneous field. Assuming Darcy's equation can be applied along streamline, the pressure gradient is estimated as

$$\nabla p_{sl} = \int_s \left(-\frac{q_{sl}}{\lambda_t(\xi) k(\xi) A(\xi)} + \rho(\xi) g \nabla D(\xi) \right) d\zeta \quad \cdots\cdots\cdots\cdots\cdots\cdots\cdots \quad (4.14)$$

We assume that along the streamline trajectories, the total mobility does not change because of small perturbations in permeability. Knowing that the change of the reservoir static properties causes the change of the flux and pressure drop, Eq. 4.14 is expressed as

$$\frac{\Delta p_{sl}}{q_{sl}} = \frac{1}{q_{sl}}\left(-\frac{q_{sl}L}{\lambda_t kA} + \rho g \Delta D \right) \quad \cdots\cdots\cdots\cdots\cdots\cdots\cdots\cdots\cdots\cdots\cdots\cdots \quad (4.15)$$

where the parameters are function of location but it is omitted to avoid cumbersome expressions through the derivation process. The flow rate along a streamline is assumed constant through the injector to producer. Again the functional derivative of Eq. 4.15 involves change of pressure drop and flux by permeability, as

$$\delta\left(\frac{\Delta p_{sl}}{q_{sl}} \right) = \frac{1}{q_{sl}} \frac{\partial}{\partial k}\left[-\frac{q_{sl}L}{\lambda_t kA} + \rho g \Delta D \right] \delta k \quad \cdots\cdots\cdots\cdots\cdots\cdots\cdots\cdots\cdots\cdots \quad (4.16)$$

where both Δp_{sl} and q_{sl} can be a function of permeability and thus, the differentiation of the left side of the Eq. 4.16 becomes

$$\delta\left(\frac{\Delta p_{sl}}{q_{sl}} \right) = \frac{1}{q_{sl}} \delta \Delta p_{sl} - \frac{\Delta p_{sl}}{q_{sl}^2} \delta q_{sl} \quad \cdots\cdots\cdots\cdots\cdots\cdots\cdots\cdots\cdots\cdots\cdots\cdots \quad (4.17)$$

The right side of the Eq. 4.16, the partial derivative of the permeability with respect to pressure drop is simplified as follows

$$\frac{\partial}{\partial k}\left(-\frac{q_{sl}L}{\lambda_t kA} + \rho g \Delta D \right) \cong -\frac{q_{sl}L}{\lambda_t k^2 A} = \frac{\Delta p_{sl} - \rho g \Delta D}{k} \quad \cdots\cdots\cdots\cdots\cdots\cdots\cdots\cdots \quad (4.18)$$

Apply Eqs. 4.17-18 to Eq. 4.16, we get

$$\frac{1}{q_{sl}} \delta \Delta p_{sl} - \frac{\Delta p_{sl}}{q_{sl}^2} \delta q_{sl} = \left(\frac{\Delta p_{sl} - \rho g \Delta D}{k} \right) \delta k \quad \cdots\cdots\cdots\cdots\cdots\cdots\cdots\cdots\cdots\cdots \quad (4.19)$$

The equation is general which defines the change of the pressure drop and flux by change of permeability at a specific location, *s*. For the application along streamline, the boundary condition is fixed either flow rate or pressure. The boundary condition depends upon the constraint of the well connected by streamline. If the boundary condition is fixed rate, $\delta q_{sl} = 0$ and we get pressure drop sensitivity with respect to permeability. Define specific grid *i* and penetrated streamline coordinate by *i,in* and *i,out*, the pressure drop sensitivity is calculate a follows

$$\frac{\delta \Delta p_{sl}}{\delta k} = \frac{\Delta p_{sl} - \rho g \Delta D}{k} \quad \cdots\cdots\cdots\cdots\cdots\cdots\cdots\cdots\cdots\cdots\cdots\cdots\cdots\cdots \quad (4.20)$$

The boundary condition of the fixed pressure condition, $\delta p_{sl} = 0$ and we get

$$\frac{\delta q_{sl}}{\delta k} = -\frac{q_{sl}}{\Delta p_{sl}} \frac{\Delta p_{sl} - \rho g \Delta D}{k} \quad \cdots\cdots\cdots\cdots\cdots\cdots\cdots\cdots\cdots\cdots\cdots\cdots\cdots\cdots \quad (4.21)$$

The most of the application uses Eq. 4.19 because flow rate is often known for history matching problem, and rate constraint well is used for reservoir simulation.

Extension to the Discretized Space

The Eq. 4.19 is the pressure drop sensitivity at arbitrary location *i*. In order to extend the sensitivity to pressure drop sensitivity of the well with discretized space, the following treatment is conducted. Recall the general pressure equation for black oil and compositional model are described as follows

$$\phi c_t \frac{\partial p_o}{\partial t} + \nabla \bullet \vec{u}_t = Q_t \quad \cdots\cdots\cdots\cdots\cdots\cdots\cdots\cdots\cdots\cdots\cdots\cdots\cdots\cdots \quad (4.22)$$

Assume this equation can be applied to streamlines with given boundary conditions. Then, the objective here is to find pressure sensitivity with respect to reservoir permeability. The equation involves permeability in Eq. 4.22 in transfer and sink/source, $\nabla \bullet \vec{u}_t$ and Q_t, thus the accumulation term can be ignored. First, consider the velocity as follows

$$\vec{u}_t = -\sum_{\alpha=owg} \lambda_\alpha \vec{\vec{k}} \bullet \nabla\left(p_\alpha + \overline{\rho}_\alpha g D\right) \quad \cdots\cdots\cdots\cdots\cdots\cdots\cdots\cdots\cdots\cdots\cdots\cdots \quad (4.23)$$

The pressure drop here is evaluated along streamlines. The pressure drop between wells connected by streamline is calculated by taking summation from start to end point of the node as $\sum_{i=node} \Delta p_i$. Then, the sensitivity of the pressure drop with respect to permeability of grid block *i* is calculated as follows.

$$\frac{\partial \Delta p_{well}}{\partial k_i} = \frac{\partial}{\partial k_i}\left(\Delta p_1 + \Delta p_2 + ...\Delta p_i + ...\Delta p_n\right) \approx \frac{\partial \Delta p_i}{\partial k_i} \quad \cdots\cdots\cdots\cdots\cdots\cdots\cdots \quad (4.24)$$

Where Δp_i is pressure drop along streamline which passing through the grid block *i* with permeability, k_i. Then using Eq. 4.23, we construct an equation of pressure drop Δp_i along streamline and take a derivative with respect to permeability to find pressure sensitivity. To achieve this, Eq. 4.23 is transformed using properties along streamlines as

$$q_t = -\lambda_t A\left(\frac{L_i + L_{i+1}}{L_i k_i^{-1} + L_{i+1} k_{i+1}^{-1}}\right)\frac{\left(p_i - p_{i+1} - \overline{\rho}_i g\left(D_i - D_{i+1}\right)\right)}{L_i + L_{i+1}} \quad \cdots\cdots\cdots\cdots\cdots \quad (4.25)$$

All the term in the equation is displayed on Figure 4.1. Let $L_i + L_{i+1} = L_{i+1/2}$ and define effective permeability along streamline, $k_{i+}^{eff} = \dfrac{L_i + L_{i+1}}{L_i k_i^{-1} + L_{i+1} k_{i+1}^{-1}}$, the equation can be rearranged as follows

$$p_i - p_{i+1} = -\frac{q_t}{\lambda_t}\frac{L_{i+1/2}}{A k_{i+}^{eff}} + \rho_i g\left(D_i - D_{i+1}\right) \quad \cdots\cdots\cdots\cdots\cdots\cdots\cdots\cdots\cdots\cdots \quad (4.26)$$

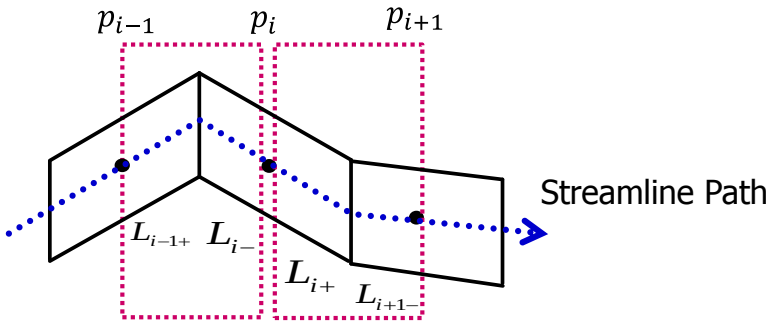

Figure 4.1: Streamline trajectory in corner point geometry.

Now the pressure drop sensitivity of grid block *i* is calculated using half cell pressure drop between neighboring grid blocks. This is because the pressure drop is defined as differences between neighboring cell center and change of permeability at *i* grid will affect its neighbor grids. In order to find the half cell pressure drop, half cell transmissibility and depth change is calculated along streamline. With half cell transmissibility, we can weight the intercell pressure drop to get target half cell pressure drop as

$$\left(p_i - p_{i+1/2}\right) = \frac{q_t L_{i+1/2}}{\lambda_t A_{i+}} \frac{1}{k_{eff,i+}} \left(\frac{T_{i+1/2}^{-1}}{T_{i+1/2}^{-1} + T_{i+1-1/2}^{-1}} \right) + \bar{\rho}_i g\left(D_i - D_{i+1}\right) \left(\frac{L_{i+}}{L_{i+} + L_{i+1-}} \right) \cdot \quad (4.27)$$

Now the equation for half cell pressure drop is obtained. The parameters used in this equation are illustrated in Figure 4.2. Also, the half cell pressure drop is highlighted by blue break line.

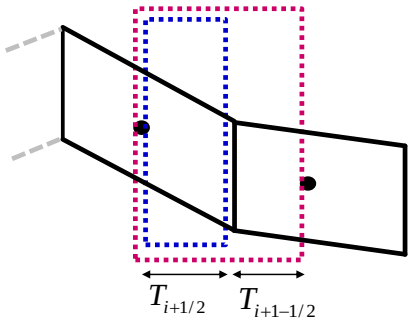

Figure 4.2: 2D corner point grid with half cell transmissibility.

The sensitivity of the half cell pressure drop, p_i - $p_{i+1/2}$ with respect to reservoir permeability, k_i, is calculated by taking the derivative of Eq. 4.27, as

$$\frac{\partial \Delta p_{i+}^{sl}}{\partial k_i} = \frac{q_{sl,i}^{eff} L_{i+1/2}}{\lambda_{t,i} A_{sl}^{eff}} \left[\frac{L_{i+}\left(k_{i+1} L_i \left(k_{i+1} L_{i+} + 2 k_i L_{i+1-}\right) + L_{i+1} L_{i+1-} k_i^{\,2}\right)}{k_i^{\,2}\left(L_i + L_{i+1}\right)\left(L_{i+} k_{i+1} + L_{i+1-} k_i\right)^2} \right] \quad \cdots\cdots \quad (4.28)$$

where q_{sl}^{eff} and A_{sl}^{eff} are effective rate and area along streamline, and for compressible fluid, these values are no longer constant along streamline and thus

$$q_{sl,i}^{eff} = \frac{q_{sl,0}}{\rho_{eff}} \quad \cdots\cdots \quad (4.29)$$

$$A_{sl}^{eff} = \frac{V_{sl}^{eff}}{L_{i+1}} = \frac{q_{sl,i}^{eff} \Delta \tau_i}{\phi_i L_{i+1}} \quad \cdots\cdots \quad (4.30)$$

Then we take a derivative of pressure drop p_i - $p_{i+1/2}$ with respect to reservoir permeability, k_i, as

$$\frac{\partial \Delta p_{i+}}{\partial k_i} = \left(\sum_{Nsl,w} \frac{q_{sl}}{\rho_{eff}} \right)^{-1} \frac{q_{sl}}{\rho_{eff}} \sum_{N_{sl,ip}} \left(\frac{\partial \Delta p_{i+}^{sl}}{\partial k_i} - \frac{\left(p_{bhp} - p_i \right)}{k_i} \right) \quad \cdots\cdots\cdots\cdots\cdots\cdots\cdots\cdots \quad (4.31)$$

The sink/source term $(p_{bhp}\text{-}p_i)/k_i$ is non zero at the launch point and end node (first and last node including cell with sink/source) for the treatment of the pressure drop of the sink source, which is derived by differentiating Peaceman's equation.

The $N_{sl,w}$ is the number of the streamlines launched from injector or producer. This is unknown variable until all the streamlines are traced. However, this requires to save all the sensitivity along streamline to give weight by the number of streamlines and thus we use alternative equation as follows.

$$N_{sl,p} = N_{sl} \frac{q_p}{\sum q_p} \quad \cdots\cdots\cdots\cdots\cdots\cdots\cdots\cdots\cdots\cdots\cdots\cdots\cdots\cdots\cdots\cdots \quad (4.32)$$
$$N_{sl,i} = N_{sl} \frac{q_i}{\sum q_i}$$

The N_{sl} is the total streamlines (initial total streamlines assigned by input). This method avoids the use of effective density in Eq. 4.31 because weight is correctly evaluated as follows

$$\frac{\partial \Delta p_{i+}}{\partial k_i} = \frac{1}{N_{sl,w}} \sum_{N_{sl,iip}} \left(\frac{\partial \Delta p_{i+}^{sl}}{\partial k_i} - \frac{\left(p_{bhp} - p_i \right)}{k_i} \right) \quad \cdots\cdots\cdots\cdots\cdots\cdots\cdots\cdots \quad (4.33)$$

4.2.4 Bottom Hole Pressure Sensitivity

The Eq. 4.33 is applicable only if one of the side connected by streamline is pressure constrained well. If pressure constraint is given in one side, the pressure drop sensitivity is equivalent to the bottom hole pressure sensitivity. This can be derived for example for the injector as rate constraint and the producer constrained by bottom hole pressure. Then $\frac{\partial p_{bhp}^{prd}\big|_{bhp}}{\partial k_i} = 0$ and following formula is satisfied.

$$\frac{\partial \Delta p_{well}}{\partial k_i} = \frac{\partial\left(p_{bhp}^{inj}\big|_{rate} - p_{bhp}^{prd}\big|_{bhp}\right)}{\partial k_i} = \frac{\partial p_{bhp}^{inj}}{\partial k_i} \approx \frac{\partial \Delta p_i}{\partial k_i} \quad \cdots\cdots\cdots\cdots\cdots\cdots\cdots \quad (4.34)$$

However, for practical applications of history matching problems, the well constraint may be given as rate and thus assumption made for bottom hole pressure sensitivity is no longer applicable. To apply for rate constraint case for injector and producer, we use the following equation to estimate rate-rate constraint sensitivity from rate-bhp constraint sensitivity as

$$\left.\frac{\partial p_{bhp}^{inj}}{\partial k_i}\right|_{\substack{rate \\ \leftrightarrow rate}} = \left.\frac{\partial p_{bhp}^{inj}}{\partial k_i}\right|_{\substack{rate \\ \leftrightarrow bhp}} \frac{\tau_i}{\tau_{end}} \quad \cdots\cdots\cdots\cdots\cdots\cdots\cdots\cdots\cdots\cdots\cdots\cdots\cdots \quad (4.35)$$

where τ_{end} stand for the end note time-of-flight at producer or injector. Once the bottom hole pressure sensitivity is calculated, we construct a sensitivity matrix. Here, we use the same approach as in generalized travel time inversion whereby our objective function is the sum of the difference of bottom hole pressure through the time

$$\frac{\delta\tilde{p}_{bhp}}{\delta\mathbf{m}} = -\left(\sum_{i=data}\Delta t_i\right)\sum_{i=data}\Delta t_i\frac{\delta p_{bhp}}{\delta\mathbf{m}} \quad \cdots\cdots \quad (4.36)$$

where $\delta\tilde{p}_{bhp}$ is a difference between calculated pressure and observation data averaged over all the observed points. As we make an objective function of GTTI by the shift of the time, pressure is also integrated in the same manner so that we are able to reduce the size of the minimization equations and run high resolution inverse problem.

4.2.5 Objective Function Minimization Formulation

As mentioned before, the objective function of this study is the production data (e.g. water-cut, GOR) and bottom hole pressure misfit for the rate constrained wells. The minimization formulation is shown below

$$O(\Delta\mathbf{m}) = \min\left\{ \left\|\delta\mathbf{d}_{wct} - \mathbf{G}_{wct}\delta\mathbf{m}\right\| + \left\|\delta\mathbf{d}_{bhp} - \mathbf{G}_{bhp}\delta\mathbf{m}\right\| + \beta_1\left\|\mathbf{I}\delta\mathbf{m}\right\| + \beta_2\left\|\mathbf{L}\delta\mathbf{m}\right\| \right\} \quad \cdots \quad (4.37)$$

again $\delta\mathbf{d}$ is the data misfit of water cut and bottom hole pressure between the observation and simulated response, and **G** is the sensitivity matrix containing the sensitivities of the corresponding data with respect to reservoir parameters. An iterative sparse matrix solver, LSQR (Paige and Saunders 1982), is used for solving the system of the equation. Because the original minimization equations often lead to unstable solution, the additional regularization term is added to improve both convergence and final solution. Here **L** and β_2 describe the correlation matrix described by stencil to the non-diagonal term. It is possible to smooth the solution by adding symmetric stencil, or give some prior information as a covariance like matrix. The term with β_1 ensures the difference between the prior and final model is minimized. This prevents large changes and

maintains geologic realism by preserving major features of the prior model during the model calibration process. The final matrix for LSQR algorithm is then described as follows

$$\begin{bmatrix} \mathbf{G}_{wct} \\ \mathbf{G}_{bhp} \\ \beta_1 \mathbf{I} \\ \beta_2 \mathbf{L} \end{bmatrix} [\Delta \mathbf{m}] = \begin{bmatrix} \delta \mathbf{d}_{wct} \\ \delta \mathbf{d}_{bhp} \\ 0 \\ 0 \end{bmatrix} \quad \cdots\cdots\cdots\cdots\cdots\cdots\cdots\cdots\cdots\cdots\cdots\cdots\cdots\cdots\cdots\cdots \quad (4.38)$$

Once the update of the static variable is calculated by Eq. 4.38, then the parameters are updated and again the flow simulation is conducted. The history-matching process is going to continue until the residual reaches certain tolerance or given maximum iteration number.

4.3 Verification of Pressure Sensitivity

The model is tested by synthetic case to verify the proposed pressure sensitivity equation. Because the model is applicable for multiphase corner point geometry, all the cases are tested based on 3phase water and gas injection problem with capillary and gravity. Here, however, in order to ignore the complexity due to capillary effects to bottom hole pressure, the capillary and surface tension is not given. The tested geometry is 1D corner point and 2D areal model. The permeability is given as a heterogeneous field. The PVT properties of oil, water and gas phase are shown in Appendix. F. The rock table is given by Figure F.2 in Appendix F with the water wet condition.

4.3.1 1D 3Phase Problem

The first test of sensitivity verification is conducted with 1D corner point geometry. The geometry has zigzag shape with uphill trend with vertical direction shown in Figure 4.3 below. Three cases of different boundary conditions are tested: Single producer at center, single injector at center, and rate constraint of both injector and producer located at the edge of the model.

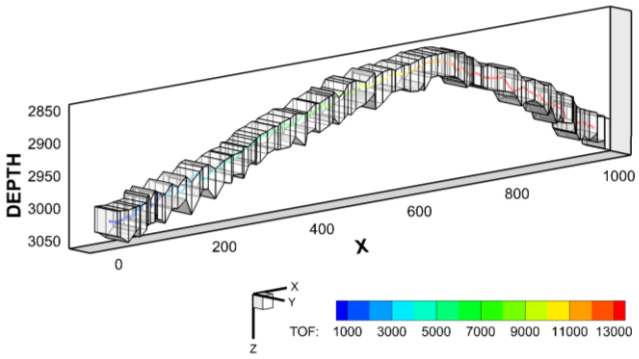

Figure 4.3: Corner point geometry and streamlines.

The permeability is given as heterogeneous, ranging from 10 to 1000 mD and randomly distributed. The initial condition, PVT properties and other parameters are summarized in Table 4.1.

Table 4.1: Reservoir parameters for 1D corner point model used for verification of pressure sensitivity

Parameter Name	Value
Grid dimension	(nx,ny,nz) = (100,1,1)
Grid geometry	Figure 4.3
Porosity	1.0
Permeability	10-1000 [md]
Pore compressibility	4.0E-6[psi^{-1}]
ρ_o, ρ_w, ρ_g (surface)	30.0,60.0,0.01 [lb/cft]
B_w,μ_w,c_w	1.0,1.0,1.0E-6 [psi^{-1}]
Oil, Gas PVT properties	Appendix F
Rel-Perm function	Appendix F, water-wet model
Surface tension	1.0 [dyne/cm]
Equilibrium condition	3000 [psi] at 3000 [ft] OWC = 3050, GOC = 1000 [ft]
Initial R_s,p_b	0.6 [Mscf/stb], 3000 [psi]
Injector	Gas, 100 [Mscf/day]
Producer	Liquid, 100 [bbl/day]
Wellbore diameter	1.0
Simulation time	10 [days]

The analytical sensitivity calculated by proposed method is verified by adjoint based method implemented in a commercial simulator (Schlumberger 2012b). The perturbation method is tested to see the accuracy, however, we observed that the adjoint based method is much more efficient in terms of computational efficiency and accuracy of the results. The perturbation method is sensitive to the magnitude of the perturbation of static value and not reliable to find accurate parameter sensitivity.

Case1: Single Producer

The first case is the demonstration by a single producer well problem. The well is located at the center of the 1D corner point geometry model. The production constraint is given by surface rate of 100 bbl/day, 10 days of the simulation period. This production schedule creates drainage radius that reaches to the boundary of the 1D field. The reservoir is above the bubble point pressure throughout the production period and thus it is 3 components 2phase oil water problem. Figure 4.4 shows the pressure sensitivity calculated by the adjoint gradient method and analytical method proposed by this study.

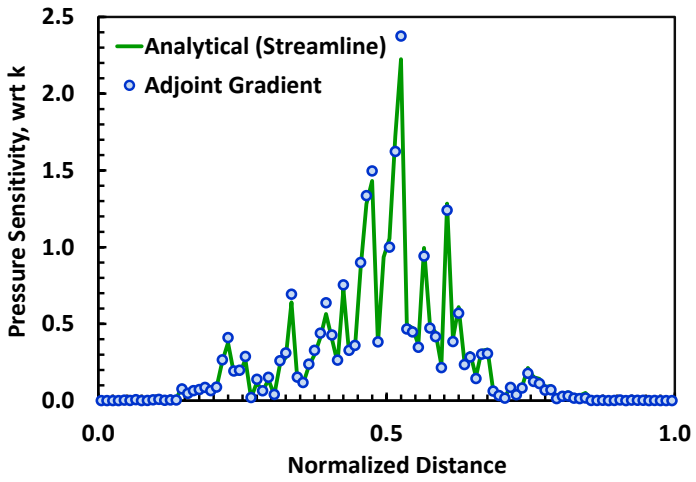

Figure 4.4: Bottom hole pressure sensitivity of the producer, green solid line by proposed analytical method, blue dot by the adjoint gradient solution.

The single well problem uses Eq. 4.31 to find the pressure sensitivity. This is because the bottom hole pressure sensitivity of single well problem is equivalent to pressure drop sensitivity as we go through by Eq. 4.2. Thus, whenever streamline is terminated at stagnant cell or bottom hole pressure constraint well, Eq. 4.31 is used.

As shown in Figure. 4.4, the sensitivity of the single production problem showed positive sensitivity to the field. The match is good and thus proposed pressure drop sensitivity equation could capture heterogeneous geometry and reservoir permeability correctly.

Case2: Gas Injector

The second case is the equivalent model with case 1 but well is controlled as gas injection. Again the simulation is 10 days with surface rate of 100 bbl/day. Because of gas injection, free gas phase appears near the injector. The result of the sensitivity is shown in Figure 4.5 below.

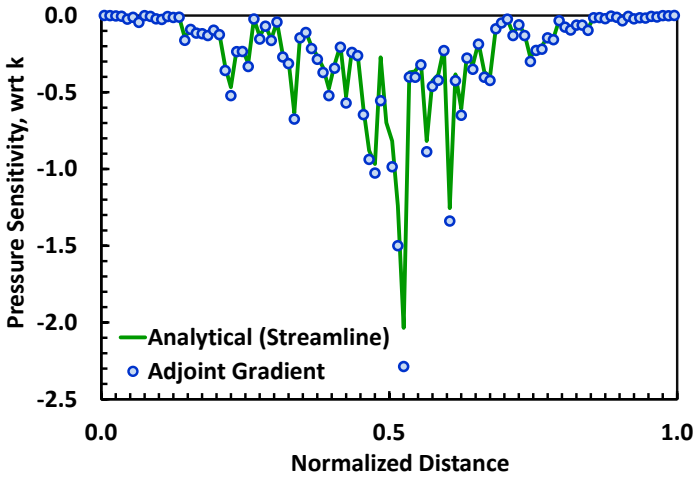

Figure 4.5: Bottom hole pressure sensitivity of the injector, green solid line by proposed analytical method, blue dot by the adjoint gradient solution.

Again Eq. 4.31 is used to calculate pressure drop sensitivity. The result of the sensitivity is ok, however, there is a slight difference between adjoint method and proposed approach around the injector. This difference is caused by additional gas phase

appeared around the well. The injected gas is going to dissolve oil phase and this high accumulation is the possible reason. However, considering the history matching is always conducted under uncertainty, this difference is not a problem for the practical application.

Case3: Gas Injector and Producer

The demonstration continues with 1D corner point field with injector and producer. The well constraint is given as rate for both wells. The sensitivity is calculated for both injection and production well, using Eq. 4.35. This equation is always used when the start and end point of the streamline is both rate constrained.

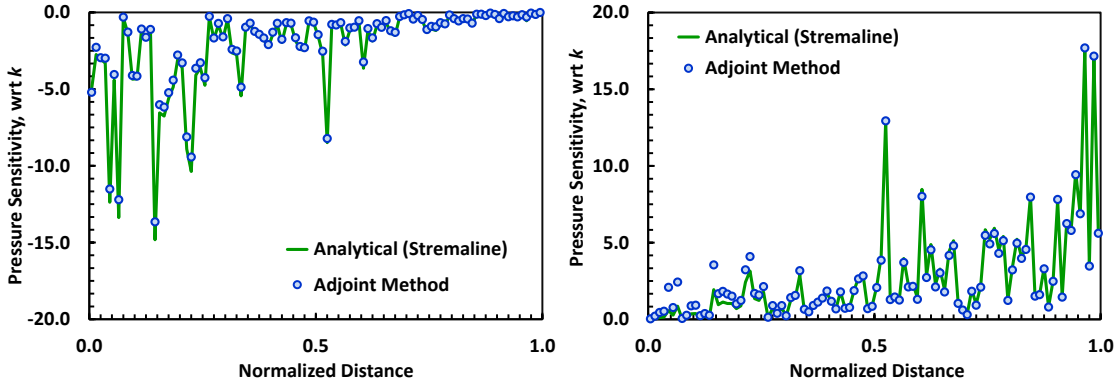

Figure 4.6: Bottom hole pressure sensitivity of injector (left) and producer (right), green solid line by proposed analytical method, blue dot by the adjoint gradient solution.

Figure. 4.6 shows the result of the bottom hole pressure sensitivity for both injector and producer. As shown in the figure, the sensitivity of the rate constraint well pair decays as distance increases from the source point. The time-of-flight weighted equation could capture this behavior very well except small differences that can be seen around

the injector. The reason here can be same as the previous case, which result in high accumulation (high divergence) due to gas injector. Literature of the Generalized Pulse Spectrum Method (Tang and Chen 1985) has analogous situation with our approach and this method includes the accumulation term for the sensitivity of the permeability. Thus, as we ignored accumulation term through the derivation of pressure sensitivity, this might be the cause of this difference. Again, however, the effect is not significant.

4.3.2 Multiwell, Multidimension, Multiphase Problem

The model is tested by 2D areal heterogeneous, quarter five spot problem. Here again all the well is constrained by surface rate. Also, all the parameters assigned for PVT and reservoir condition is same as the one used in Chapter II except initial permeability and boundary condition. The permeability is ranging from 1-10000 mD with relatively high permeability trend in diagonal shown in Figure 4.7. The initial condition etc. are summarized in Table 4.2.

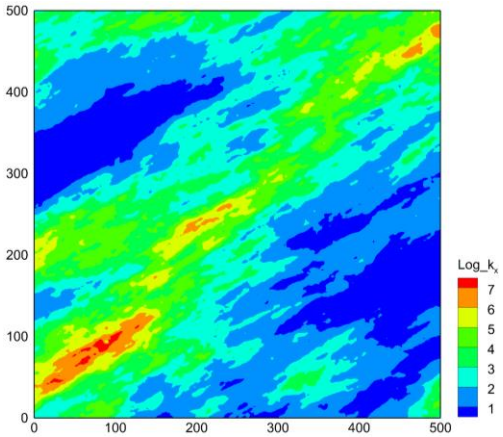

Figure 4.7: Permeability distribution tested for sensitivity analysis.

Figs. 4.8 and 4.9 are the result of the pressure sensitivity comparisons with adjoint method and the proposed approach. The pressure sensitivity of injector is shown in Figure 4.8. The result shows that the negative sensitivity with respect to reservoir permeability, and the trend of magnitude is related to permeability field shown in Figure 4.7. The result from adjoint based method and proposed model shows very good agreement. The difference of the sensitivity is observed in pressure sensitivity of producer well, shown in Figure 4.9. There is both positive and negative region in adjoint based method in adjoint based method, however, only positive region can be found in proposed method. This is because pressure sensitive is calculated only along streamline and thus the negative region is not evaluated in proposed method.

Table 4.2: Reservoir parameters for 2D quarter five spot model for sensitivity verification

Parameter Name	Value
Grid dimension	(nx,ny,nz) = (250,250,1)
Grid length	dx=dy=dz = 2.0 [ft]
porosity	0.1
Permeability	1-1000 [md]
Pore Compressibility	1.0E-8[psi^{-1}]
B_w, μ_w, c_w	1.0,1.0,1.0E-8[psi^{-1}]
B_o, μ_o, c_o	1.2,2.0,1.0E-6[psi^{-1}]
Rel-Perm function	Appendix F, water-wet model
Top depth	3000 [ft]
Surface tension	1.0 [dyne/cm]
Equilibrium condition	3000 [psi] at 3000 [ft] OWC = 3200
Injector	Gas, 2.0 [bbl/day]
Producer (4 well)	Liquid, 0.5[bbl/day]
Wellbore diameter	0.25
Simulation time	0.1 [days]

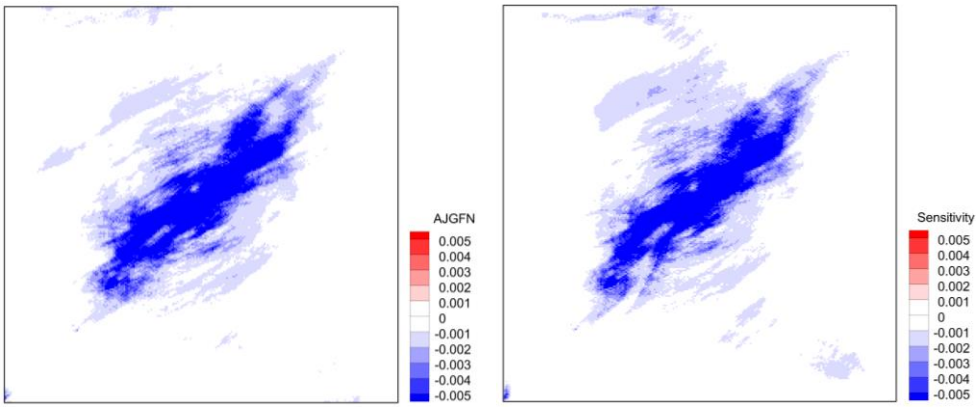

Figure 4.8: Injector pressure sensitivity derived by the adjoint method (left) and proposed approach (right).

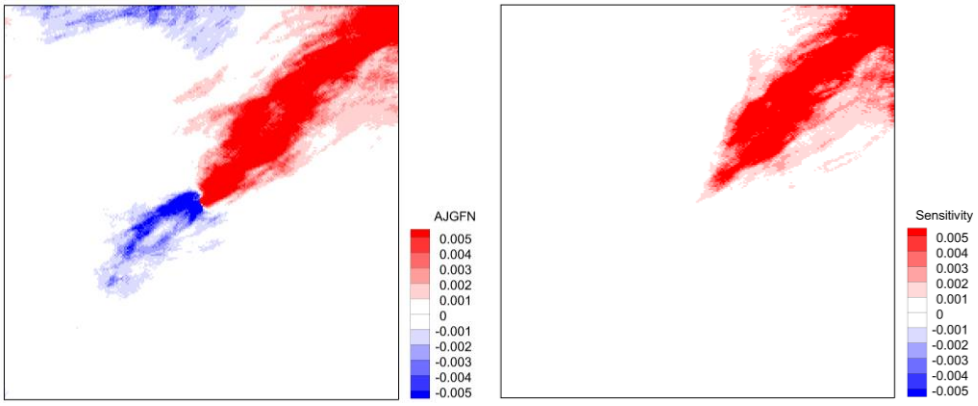

Figure 4.9: Producer bottom hole pressure sensitivity of producer well compared with the adjoint gradient method (left) and proposed approach (right).

4.4 History Matching Applications

4.4.1 1-Dimensional Space

First demonstration of history matching is conducted on a 1D reservoir gas flooding model, shown in Figure 4.10. The objective here is to match the bottom hole pressure and water breakthrough time by calibrating reservoir permeability. In general, 1D core flood model does not change the velocity of the fluid by change of permeability. In other words, streamline-based water-cut sensitivity cannot apply for 1D scenario because the formulation is founded by convection equation. In this scenario, matching of pressure will adjust the compression of rock and fluid, and we could match the pressure as well as breakthrough of water.

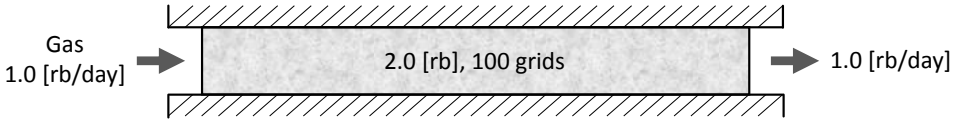

Figure 4.10. 1D core flood example used for pressure sensitivity and history-matching

The results of production profile from reference and initial model is shown in Figs. 4.11-12. The reference history is generated by permeability given in page 199 Figure 4.14 ranging linearly from 250 to 50mD from left to right side of the field. The initial permeability is given as 500mD shown as a gray brake line. The capillarity is given as J-function and initial saturation depends on permeability field. Thus, there are large differences of initial water saturation between reference and initial model. Because of

water wet wettability, the lower permeability has strong water capillary pressure and thus initial model has a lower average water saturation.

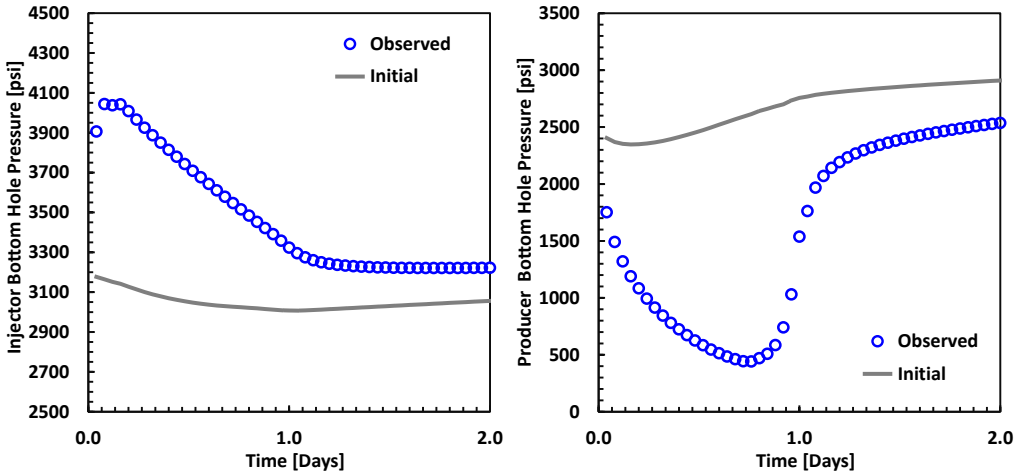

Figure 4.11. Bottom hole pressure history of initial model (gray break line) and observed model (blue circle). Left figure by injector and right by producer.

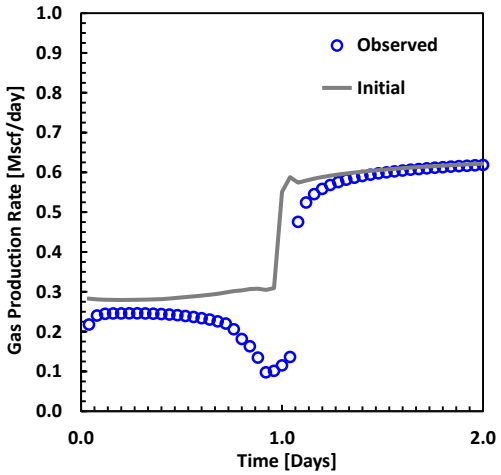

Figure 4.12. Gas production history of initial model by gray break line and observed model by blue circle.

The boundary condition is given as fixed rate for both injector and producer at 1 rb/day, and inject 2.0 PVI of the reservoir. It is expected that matching of injector and producer BHP will match reservoir average pressure.

The change of the permeability field adjusts the accumulation of fluid and initial water saturation towards the reference model, and gives correction to gas breakthrough time. The sensitivity is calculated for every time step as shown in Figure 4.13 by blue lines, and the red line show the normalized sensitivity through the simulation. The bottom hole pressure data is integrated using pressure sensitivity. Ten iterations were required to match reference history data and the result is shown Figs. 4.14-15.

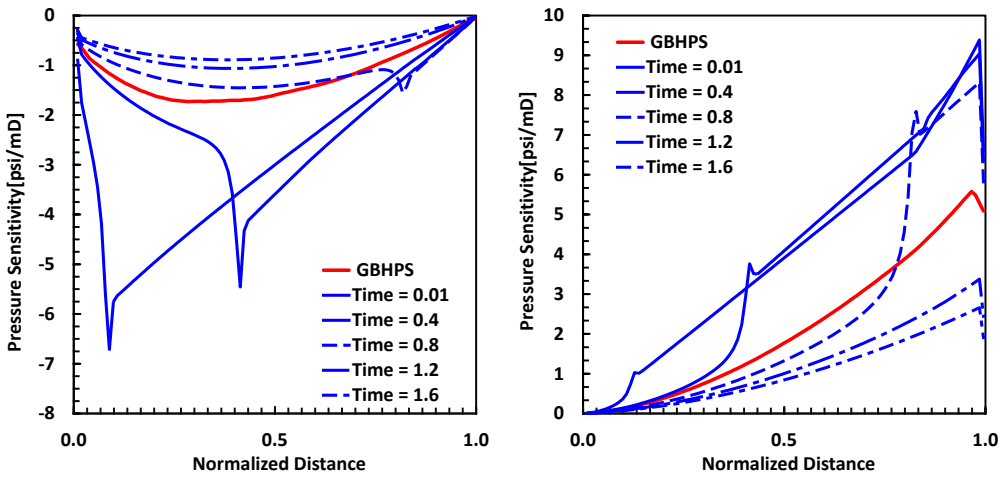

Figure 4.13: Pressure sensitivity with different time (0.01,0.4,0.8,1.2 and 1.6 days), shown as break blue line. The normalized sensitivity of bottom hole pressure by redline. Left figure by injector and right by producer sensitivity.

The result showed that initial permeability reduces as the iteration goes. It started with 500 mD shown as gray line in Figure 4.14, and it matches roughly to the reference

model after 3 iterations. The reduction of the objective function can be seen in Figure 4.15. Here, the objective function is bottom hole pressure, however, phase flow rate of the production well is also displayed.

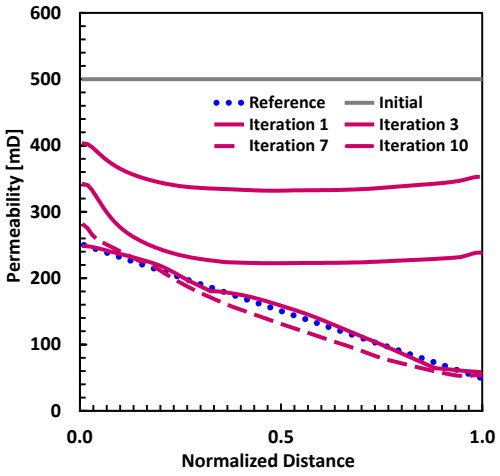

Figure 4.14: Initial and reference permeability (gray, blue), red lines for permeability through iteration of history matching.

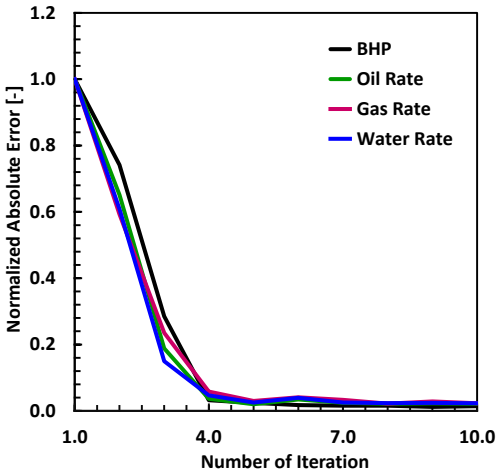

Figure 4.15: Normalized error of the objective function: Bottom hole pressure and phase flow rate.

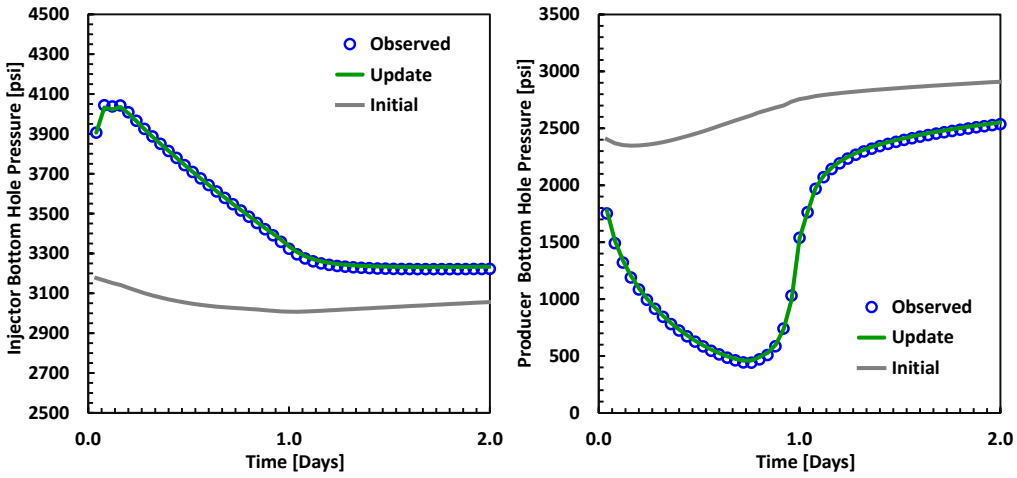

Figure 4.16: Bottom hole pressure history of initial model (gray break line) and observed model (blue circle) left: Injector, right: producer.

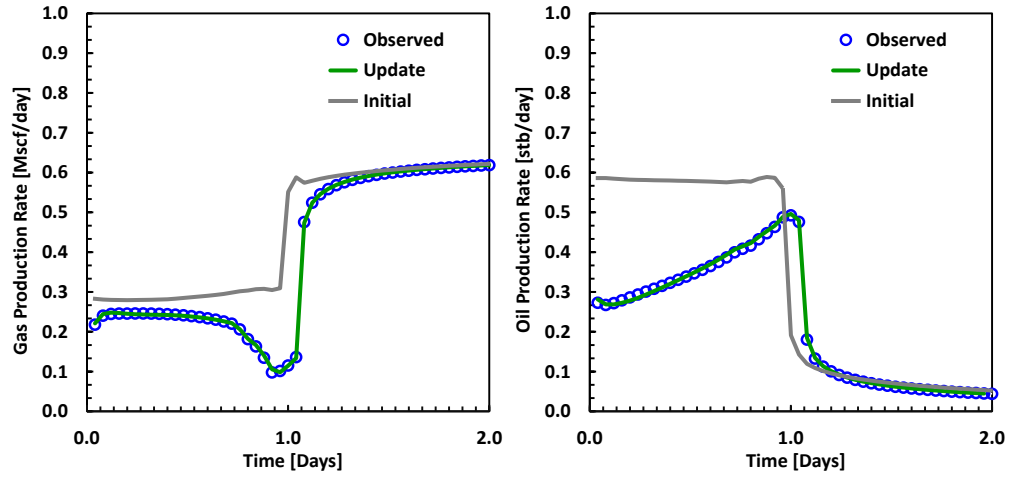

Figure 4.17: Gas production rate and (left) and observed model (right), initial as gray, observed by circle and update by green.

Figs. 4.16-17 shows the result of final production profile before and after history matching. As we seen in reduction of objective function, the agreement of production profile is quite satisfactory.

4.4.2 2D Five-Spot Synthetic Case

The second example of history matching is a synthetic 2-D areal model. The reservoir is discretized by 251 cells for both *x* and *y* direction, with a five-spot well configuration: one injector in the center and 4 producers at the corners. Both injector and producers are constrained by the historical (constant) reservoir flow rates. The rock and fluid properties and the simulation specifications are summarized in Appendix F, except gas and solution gas phase does not appear throughout the simulation.

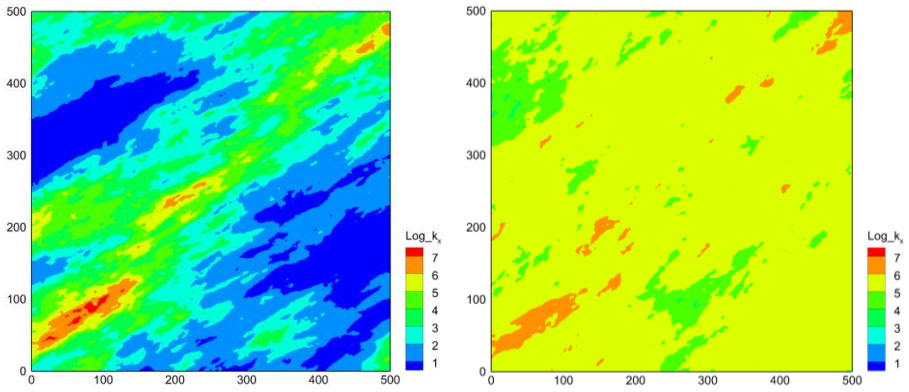

Figure 4.18: Reference permeability (left) and initial permeability distribution (right).

The reference permeability model is equivalent to the one used for the verification of the pressure sensitivity. The initial permeability model is shown in Figure 4.18. It is also generated by sequential Gaussian simulation but with different geostatistical parameters from the reference model except for well grid permeability. The observation data or objective function of this case is to minimize water cut at 4 producer and bottom hole pressure of all the wells.

Here, a 2-step matching is conducted. The first step is to use 100 days of historical data for the history-matching. It is often the problem that the conventional streamline-based history matching is not applicable when the breakthrough data is not available as either observation data or simulation data. It is a common situation at the beginning of the production period. Because of these reasons, we first demonstrate the applicability of the novel streamline-based pressure and water cut history matching for the first 100 days of the observation data, shown in Figure 4.19.

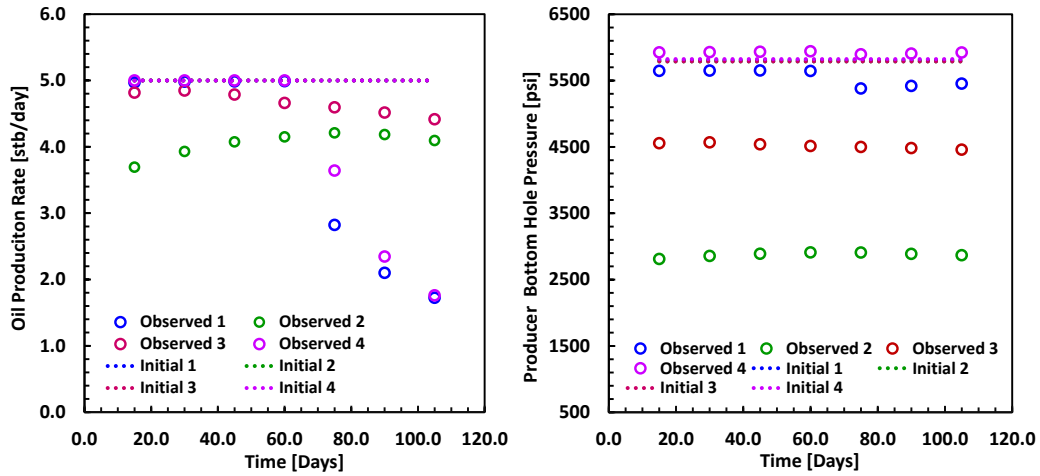

Figure 4.19: Oil production rate (left) and production BHP pressure (right). Circle by observed data and dotted lines generated by initial permeability field.

The initial data shows no clear breakthrough through 100 days. Without breakthrough data, generalized travel time inversion cannot be applied because it is not possible to calculate correlation coefficient between observed and calculated points. However, it is clear that bottom hole pressure has clear differences between calculated data and observed data and thus, the approach can be used to match these pressures.

Figure 4.20 shows the normalized absolute error between observed data and calculated data. The objective function is bottom hole pressure and water cut. As we expected from calculation data, it is not able to match water cut due to the limitation of the data. However, total error of the bottom hole pressure reduces 80% after 7 to 10 iteration and thus new approach could take into account pressure data at the early stage of the production.

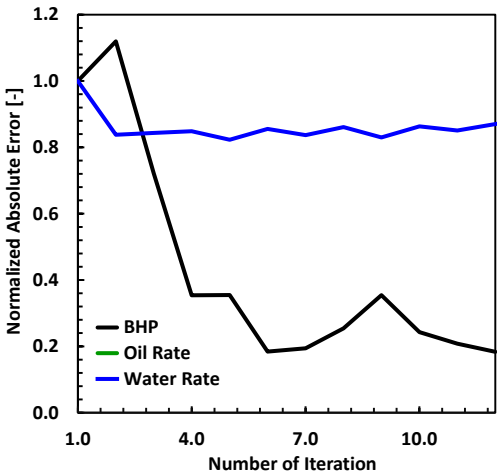

Figure 4.20: Normalized error of the objective function through iteration, use of 100 days of observed data.

The match of the pressure data can be seen in both producer and injector bottom hole pressure. Figure 4.21 shows the history of the producer both oil production rate and bottom hole pressure. The match of the pressure is good, however, there is not clear improvement in the oil production rate.

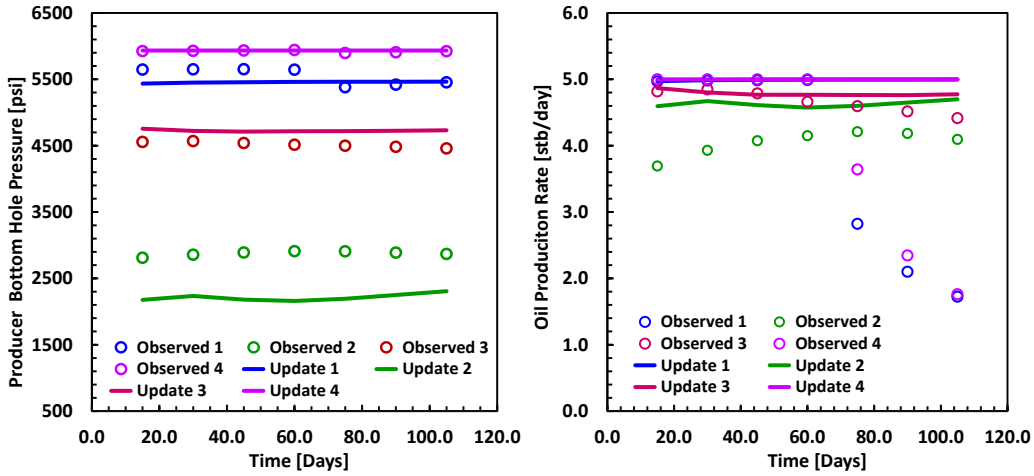

Figure 4.21: Final calculated and observed data of 4 producers: production bottom hole pressure (left), oil production rate (right).

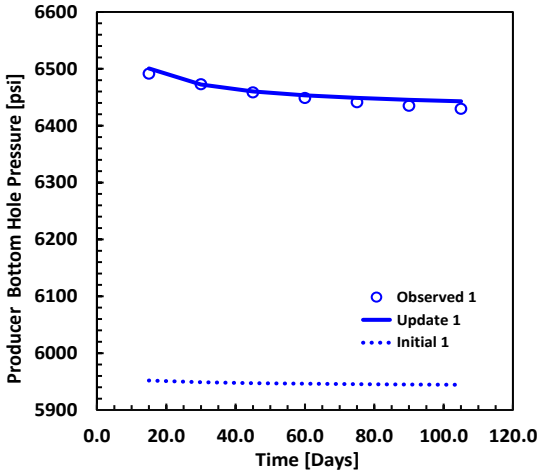

Figure 4.22: Final calculated and observed data of injector BHP.

Figure 4.22 shows the bottom hole pressure of the injector, after pressure matching. As it is shown in the figure, the original bottom hole pressure is approximately 6500 psi, however, the initial model shows less than 6000 psi. In order to integrate these data, the permeability needs to be reduced around the injector, or entire field so that the viscous pressure drop increases and then the injector bottom hole pressure will follow the history. This trend is clearly shown in the final result of the permeability field, shown in Figure 4.23. The result is a final permeability field after history matching of 100 days. The reduction of the permeability field is observed around injector and its corresponding producers. Using proposed streamline-based pressure and rate integration method, it is able to describe the reservoir.

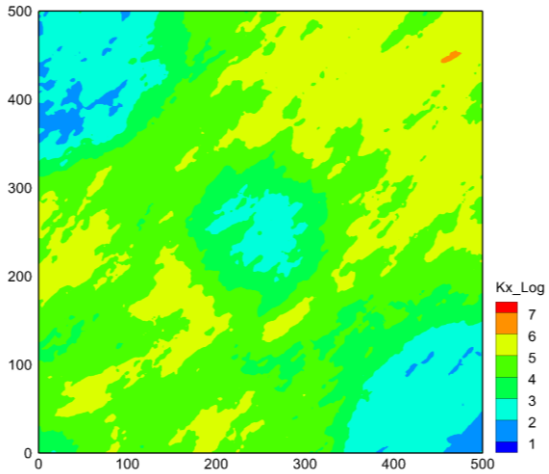

Figure 4.23: Final permeability after history-match of early production period.

Then the model is tested in the same permeability field but have all the historical data. Now the available data is for 600 days, and the clear production data is observed.

In order to make the problem consistent, the initial permeability shown in Figure 4.18 is used to generate initial production profile shown in Figure 4.24. Then both GTTI and pressure data integration is conducted simultaneously for the history matching. The reduction of the objective function is shown below.

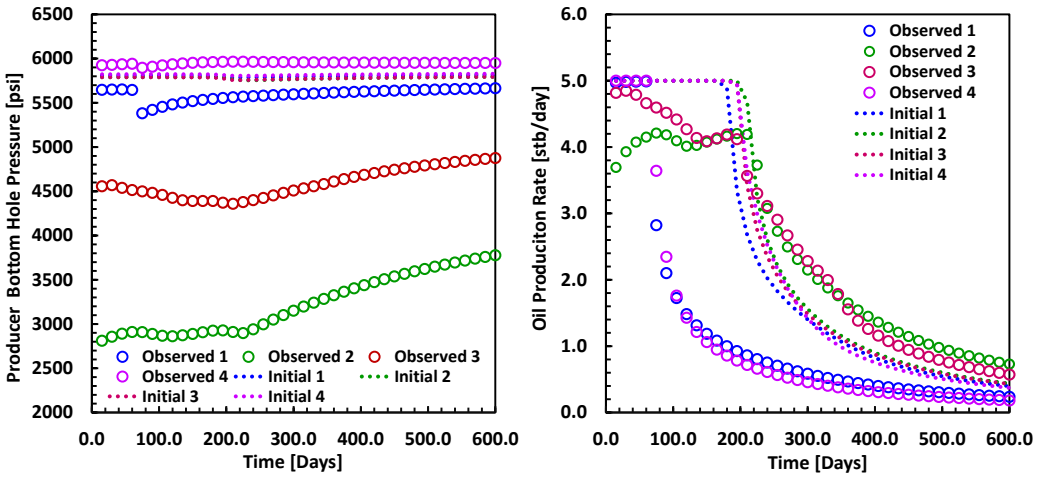

Figure 4.24: Initial and observed data of 4 producers: production bottom hole pressure (left), oil production rate (right).

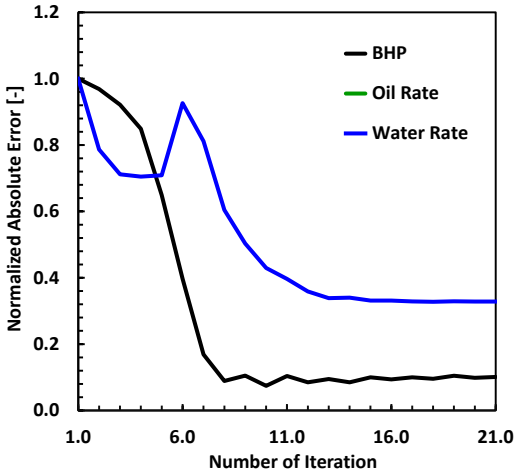

Figure 4.25: Normalized error of the objective function through iteration by 2D case.

The reduction of objective function is shown in Figure 4.25. The final model responses shows good agreement with the one generated by the reference permeability model for both bottom hole pressure and water cut data as shown in Figure 4.26.

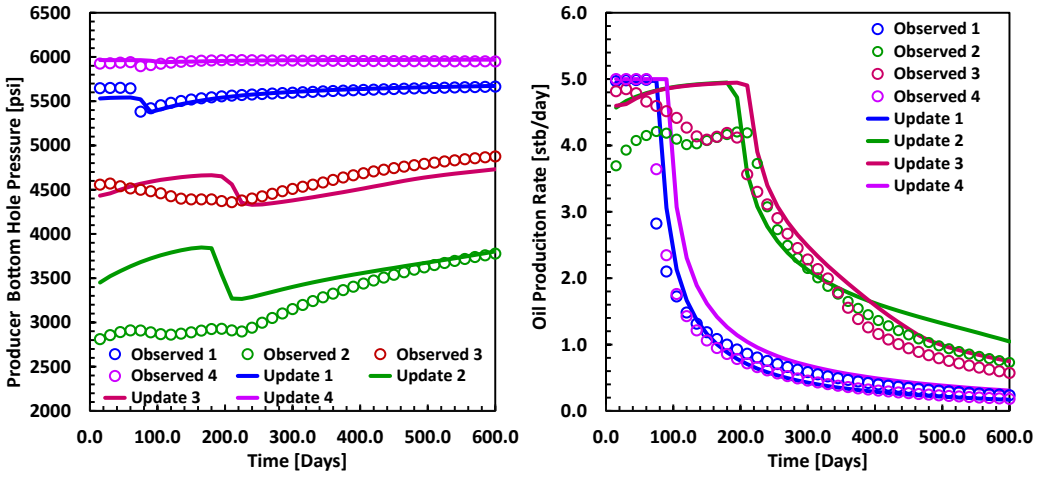

Figure 4.26: Final calculated and observed data of 4 producers: production bottom hole pressure (left), oil production rate (right).

Here the bottom hole history of the injector is not shown and it showed as good match as shown in Figure 4.22. The final permeability model updates by the inversion process are displayed in Figure 4.27. The left side of Figure 4.27 shows the final permeability distribution and right side shows the changes required from initial model, respectively.

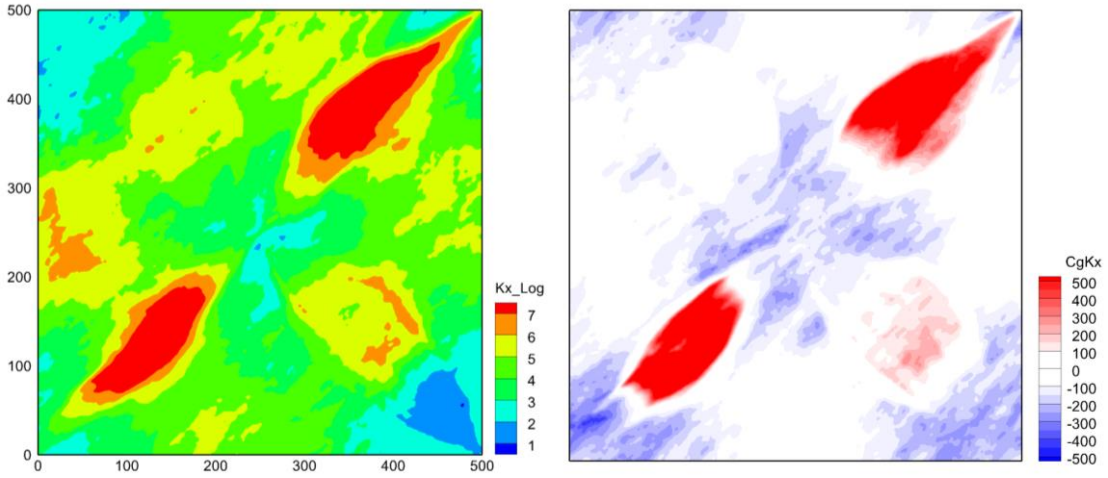

Figure 4.27: Permeability after history-match (left) and changes required (right).

These results confirm that the consistent integration of the high permeability region shown in the reference model. Although the prior model of this history matching does not have any high or low permeability field, the history matching process creates a clear contrast and they are consistent with the reference model. Additional information is required to generate consistent results shown in the reference model, such as seismic data, while use of pressure clearly provides more information compared with the conventional streamlined based approach.

4.4.3 The Brugge Benchmark Case

The history matching approach is tested in the Brugge field case. The Brugge field case was designed for a SPE benchmark project to test the combined use of history matching and waterflooding optimization methods in a closed-loop workflow (Peters *et al.* 2009). The structure of the Brugge field consists of an east/west elongated half-dome with a large boundary fault at its northern edge and one internal fault with a modest throw as shown in Figure 4.28.

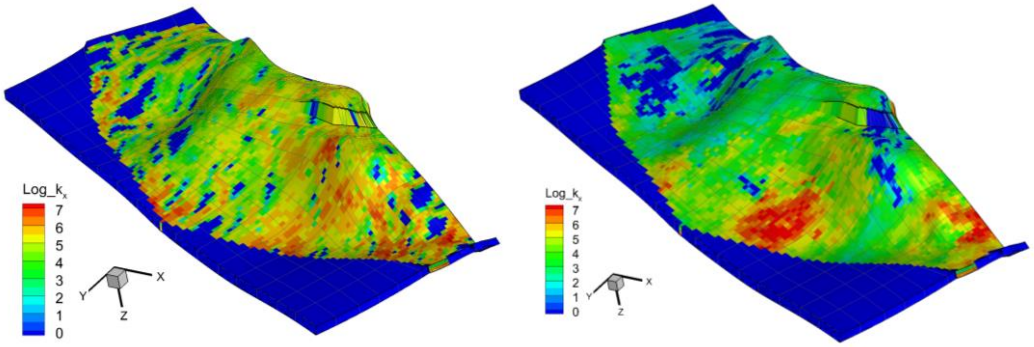

Figure 4.28: Reference permeability (left) and initial permeability distribution (right) used for Brugge history-matching scenario.

The dimensions of the field are roughly 10 km × 3 km. The reservoir model contains more than 40,000 active grid cells, 20 producers located top of the reservoir and 10 infill water injectors located in the periphery of the oil-water contact. A total of 104 realizations were generated by four different classes of geologic parameters: (1) facies association, (2) facies modeling, (3) porosity, and (4) permeability. The detailed descriptions of the realization construction can be found in Peters *et al.* (2009). The prior

and reference model is selected from the realization 1 and 77, shown in Figure 4.28. Production data are given in the form of water and oil rates, and also bottom hole pressure at each of the 20 producers for the 10 years of production. The reservoir is an under the saturated oil reservoir

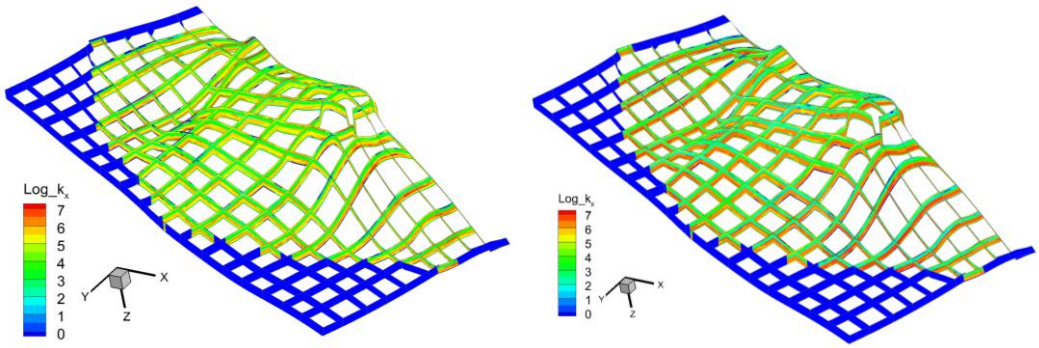

Figure 4.29: Reference permeability (left) and initial permeability distribution (right) with cross-section view.

The reservoir has total 9 layers (i.e., formations called the Scheld, Maas, Wall, and Schie), and each layer has a discontinuous permeability distribution. In general, the first two layers and middle 3 layers have high permeability. As shown in Figure 4.29, the cross-section plot identifies the high permeability region on the bottom and low permeability on a top of the field. In general, the reference model has low permeability. Thus, it is expected that the history matching reduces the permeability of the high permeability layer as well as creating the high permeability channel to describe facies like connection shown in reference permeability in Figure 4.28.

Here again the history matching is conducted with 2 different scenarios: first scenario uses water-cut as objective, second scenario uses both water cut and pressure of the all of the wells including injector and producer. Total 100 iterations are conducted for the history matching. The result of the change of the permeability is shown in Figure 4.30. As expected by visual comparisons of reference and initial permeability distribution shown in Figure 4.29, the pressure and water cut matching reduced permeability at the middle of the reservoir. In contrast, the one with water-cut matching does not decrease permeability in field scale.

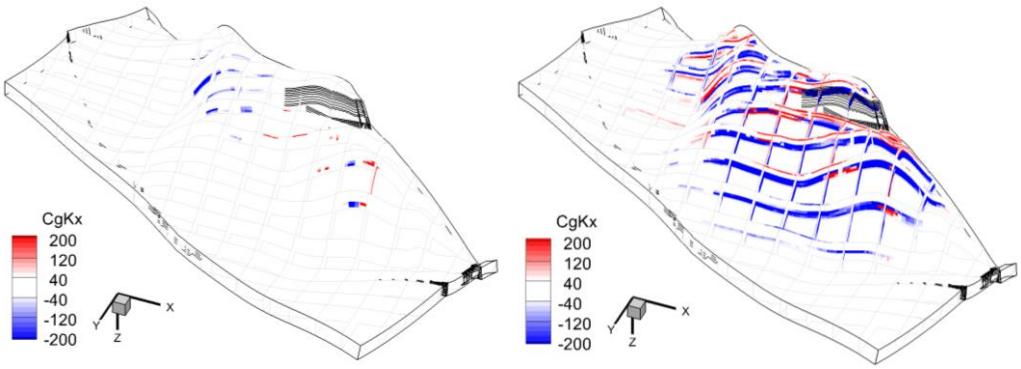

Figure 4.30: The change of the permeability after history-matching of water cut data (left) history-matching of both water-cut and bottom hole pressure (right).

The reduction of the objective function is shown in Figs 4.31-32. Figure 4.31 shows the objective function of bottom hole pressure through the iteration process of the history matching, for total 30 wells including injector and producer. As seen in the figure, the objective function decreases for all the wells including injector and producers. The blue

line in a figure shows the average error of the bottom hole pressure of all the wells. The result shows that after 50 iterations, the 90 % of the pressure error is decreased by average.

Figure 4.32 shows the objective function of water-cut through the iteration of the history matching for total 20 producers. Although the objective function decreases for all the wells, the reduction of the average water-cut error is around 50%. One possible reason for this result may be the quality of the prior data. The prior permeability distribution is based on Gaussian distribution, however, the reference data has a clear channel in several layers.

The quality of the history matching is improved by the use of the pressure data. It clearly captured the average change of the permeability to match the bottom hole pressure. In order to improve the result, additional information is needed such as seismic information to take into account for the change of the saturation and pressure through the time. The Brugge benchmark model continues to production optimization problem in next chapter.

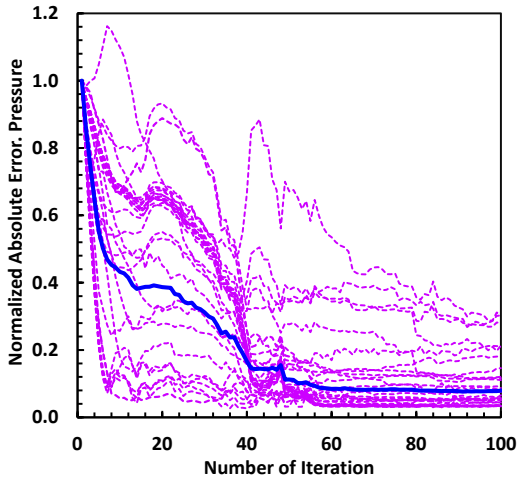

Figure 4.31: The normalized objective function of bottom hole pressure with respect to iteration, break purple lines by individual well, blue line by mean of the all wells.

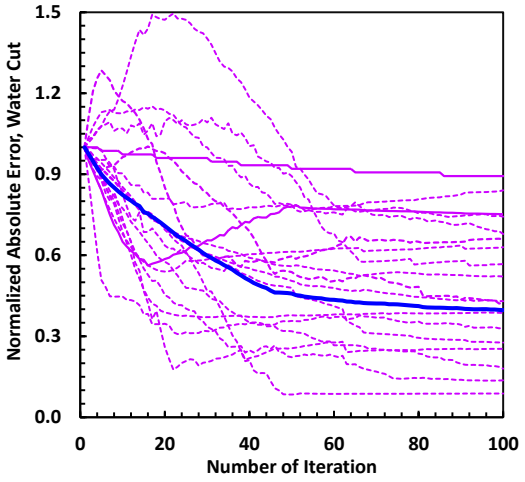

Figure 4.32: The normalized objective function of water cut with respect to iteration, break purple lines by individual well, blue line by mean of the all wells.

4.4.4 A Multimillion Cell, Multiwell Case

As mentioned before, the biggest advantages of the streamline-based history matching is the computational efficiency. With GTTI and average pressure matching technique, it is able to conduct a history matching with multimillion grid cells with multiple well problems. To demonstrate this, the history matching of water-cut and MDT pressures with 6 years of history is performed on multimillion cell problem. Total 9 producers and 2 injector in the field. In addition, each of the injector well has 30 points of measured pressure data. Thus, the matching parameter is 9 water cut data with 60 points of injector MDT pressure with multiple observation time. Because the grid has over 3 million cells, conducting amplitude matching with conventional method requires huge amount of computer resources. With streamline-based simulation and inverse modeling, it is possible to conduct history matching of million grids problem even with laptop computer, although it requires 10 GBytes of memory.

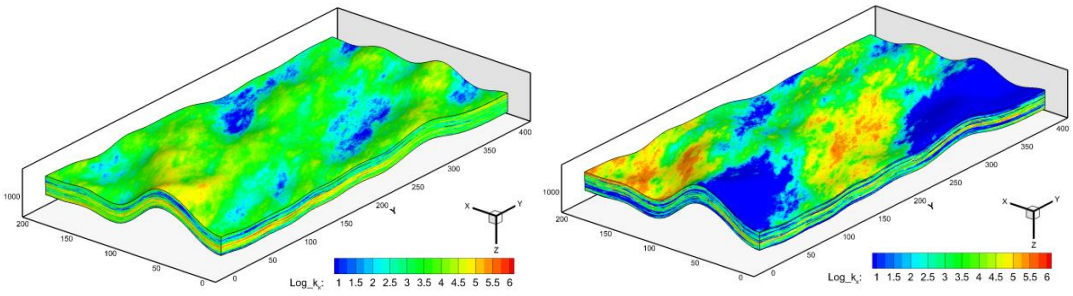

Figure 4.33: Reference permeability (left) and initial permeability distribution (right) for 3D multiwall synthetic scenario.

Figure 4.33 shows the permeability of initial and reference model for this history matching problem. Both permeability distributions are generated by the unconditional Sequential Gaussian simulation. The mean of the permeability of the model is approximately 10 mD, while each layer has a distinct trend of the permeability.

First, the forward simulation is conducted by reference permeability field. Using the simulation results of reference permeability as the observed data, the history matching is conducted starting from initial permeability. The simulation model is oil-water 2phase system without capillarity. Again the objective function is water-cut of 9 producers and MDT pressure of the injection well by every perforation location. Figure 4.34 shows the objective function of both water cut and pressure, through the 100 times of the iteration.

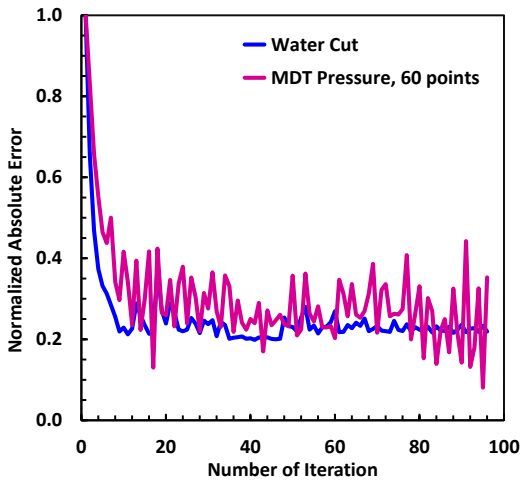

Figure 4.34: The reduction of the normalized RMSE of the objective function: Red by pressure and blue by water cut response.

As shown in Figure 4.34, the objective function decreases rapidly around the first 20 iterations, and then it gets flat. The objective function of pressure data has fluctuated

while still decreases monotonically as a trend. Through this history matched process, it is able to decrease around 70% of mismatch for both water cut and pressure data. The required change of the permeability field is shown in Figure 4.35. Often times, the permeability is upscaled to conduct history matching of the million grid cells, however, the proposed method is able to conduct by original resolution.

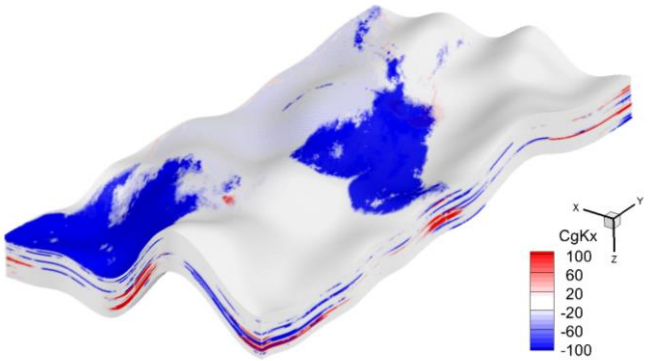

Figure 4.35: Change of the permeability made after the history matching process.

Again the blue and red region shows the decrease and increase of the permeability. The change of the permeability can be seen in entire reservoir. We observed that the pressure information calibrate the permeability near the injector and water cut information create high/low permeability region by inter well.

Figure 4.36 shows the MDT pressure of 2 injectors. The blue circle shows the observed pressure, and gray dot line shows the pressure response from the initial permeability field. Again, every perforation point of the injector well has the observed point, total 30 points per well. The observed point shows the high pressure at the middle-top of the field. In other word, there are low permeability layers exists in the reference

model while it was not modeled correctly in a prior model. The green line shows the results after history matching. The result shows good agreement with bottom of the reservoir. In addition, it creates low permeability region at the top of the field attain close match with the observed data.

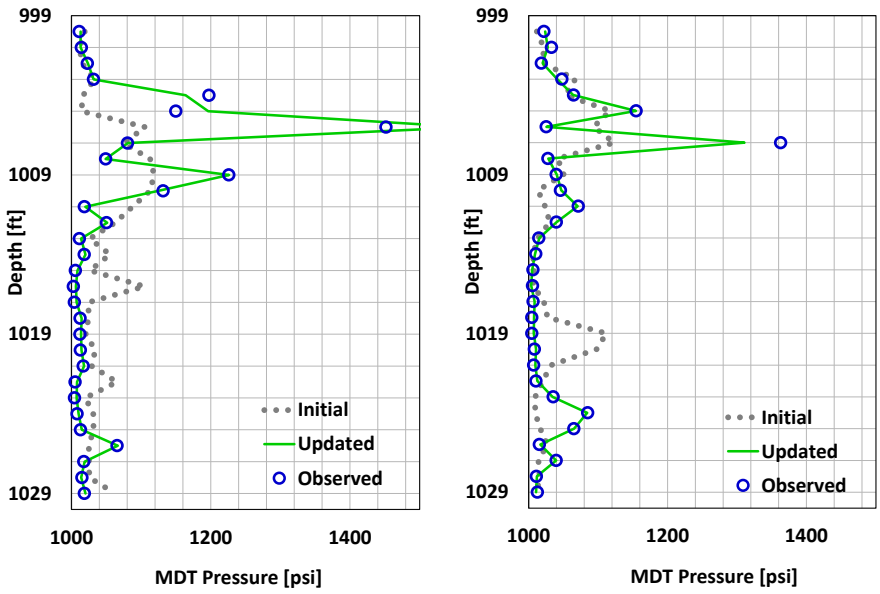

Figure 4.36: The MDT pressure data of two injectors. Displayed by initial model as gray dot, observed point as blue circle and updated response by green.

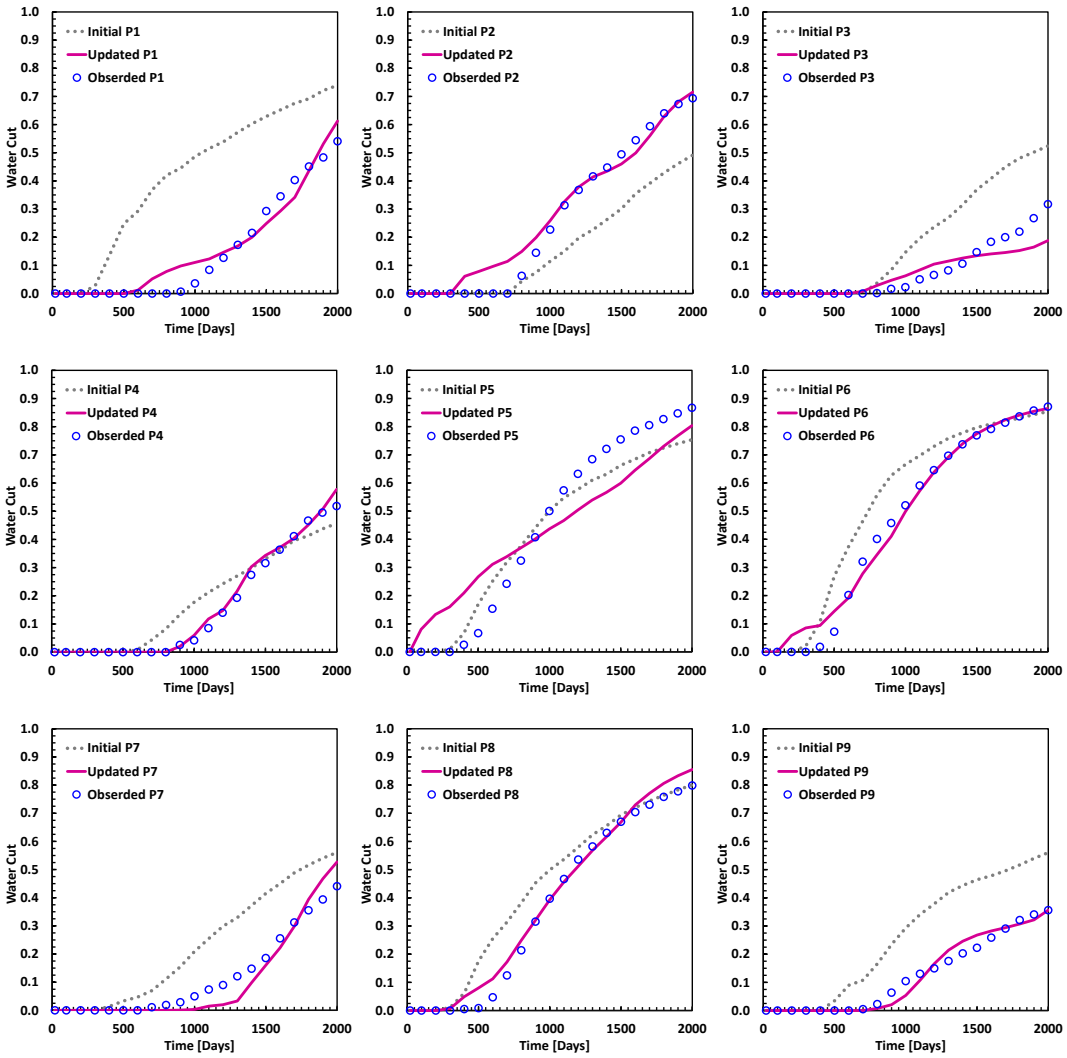

Figure 4.37: The production water-cut of initial (gray dot), observed point (blue circle) and updated response of all the producers.

Figure 4.37 shows the water-cut response of individual well, compared with initial, reference and updated results, respectively. As shown in figure, some of the wells have similar responses from the prior model. The clear differences can be seen by P1, P3 and

P9 for example. The GTTI inversion successfully reduces both breakthrough and the magnitude of the response. Some of the well, P5 for instance showed the increase of the error compared with initial data while overall shape is kept.

The reservoir parameters used for this case study is summarized in Table 4.3.

Table 4.3: Reservoir parameters for 3D multimillion multiwell history matching demonstration

Parameter Name	Value
Grid dimension	(nx,ny,nz) = (200,400,30)
Grid length	(dx,dy,dz) = (1.0,1.0,0.2)
porosity	0.35
Permeability	Figure 4.33
Pore compressibility	1.0E-10 [psi^{-1}]
B_w,μ_w,c_w	1.0,1.0,1.0E-10 [psi^{-1}]
B_o,μ_o,c_o	1.0,1.0,1.0E-10 [psi^{-1}]
Rel-Perm function	$K_{rw} = S_w^2, k_{ro} = S_o^2$
Initial saturation	1.0-S_{wc}
ρ_o, ρ_w	40.0,60.0 [lb/cft]

4.5 Chapter Conclusions

In this chapter, we have presented an efficient history matching approach that integrates the bottom hole pressure and well production data. Although our approach relies on streamline-based sensitivity calculations to relate pressure and saturation responses to the reservoir parameters, it can be applied with either streamline simulators or conventional finite difference simulators. We demonstrated the effectiveness of our proposed approach through synthetic and the Brugge benchmark applications. The conclusions from this chapter are summarized below.

- We have proposed a novel methodology for streamline-based analytic approaches to compute bottom hole pressure sensitivity with respect to the permeability.
- Our numerical examples validate the proposed sensitivity calculations for the saturation and pressure drop by comparison with adjoint based sensitivity.
- The Brugge benchmark with pressure matching shows improvement of the model calibration compared with the conventional water-cut based history matching. However, the pressure data is the single point of the well and it does not improve the model by individual layer. The calibration of the permeability can be seen by the average change through the formations. As discussed in the multimillion cell case in Figure 4.36, the MDT type pressure data contribute more to describe the reservoir. It is very important to measure the pressure by several points of the well.
- The multimillion cell problem is tested and the effectiveness of the proposed approach is demonstrated.

- Inclusion of the geologic uncertainty is future work. One possible approach is to update the ensemble of realizations, such as Brugge synthetic case.

CHAPTER V

APPLICATION OF THE STREAMLINE-BASED RESERVOIR SIMULATOR FOR RATE ALLOCATION OPTIMIZATION

5.1 Chapter Summary

This chapter summarizes an application of the newly developed streamline simulator to the production rate optimization problem of secondary waterflooding process. Streamline-based rate allocation optimization has shown its power and utility for the waterflooding application. The main concept of the streamline-based rate optimization technique is that it evaluates and ranks the injector and producer performance by streamline trajectories and time-of-flight information. We first visit the previous study and states advantages of the current streamline-based rate allocation optimization algorithm and its limitation. Then we propose an improved approach that aims to optimize field Net Present Value (NPV). Then we present several numerical examples including Brugge benchmark case. The performance of the presented approach is evaluated by comparing the result with previous work and the presented approach. The presented approach showed the best performance in terms of NPV in all the tested cases.

5.2 Streamline-based Rate Allocation Optimization

The waterflooding optimization is a nonlinear optimization problem under multiple constraints. There are several techniques available to solve this problem, and they are mainly categorized as a gradient based method (Hiriart-Urruty and Lemarechal 1996, Suwartadi 2012, Wang 2003) or non-gradient based method (Spall 2005). The concept is

similar as history-matching problem discussed in the previous chapter, except the objective function needs to be maximized under multiple constraints. The gradient based method calculate parameter sensitivity first by perturbation method, adjoint method, or ensemble based method with multiple realization (Chen, Oliver, and Zhang 2010). The solution of the gradient optimization method often stuck at local minima as number of control variable increases, and thus the additional treatment is required such as combine with non-gradient approach (Cetin, Burdick, and Barhen 1993)

The non-gradient approach, or stochastic approach is able to find the global optimum point (Spall 2005) by searching all the solution space. Because the number of simulation increase exponentially as number of control variable increases (Harding, Radcliffe, and King 1996), it is difficult to apply for rate allocation optimization. To avoid this, the upscaling of geological model and/or proxy construction is often applied (Schlumberger 2012a).

The use of streamline information for optimization problem is proved to be effective (Alhuthali, Oyerinde, and Datta-Gupta 2007, Thiele and Batycky 2003) compared with previously stated method. Because streamline captures the convective flow between wells with special and time information from its distribution and time-of-flight as shown in Figure 5.1, it is able to evaluate and rank the well. Several literatures can be found for the application of the rate allocation problem. Of these available methods, two main approaches establish the foundation of the idea of streamline-based rate allocation method. The first approach is to find optimal injection rate using well allocation factor, developed by (Thiele and Batycky 2003). The second approach is to equalize the

average travel time to the producer, (Alhuthali, Oyerinde, and Datta-Gupta 2007). Both approaches use streamline information to increase the oil production total by reallocating injector or producer flow rate. The main difference is that the first approach is derivative free, but the second approach calculates the analytical derivative to minimize an objective function. The objective of this section is to clarify streamline-based rate allocation method by going through previous studies and state the pros and cons.

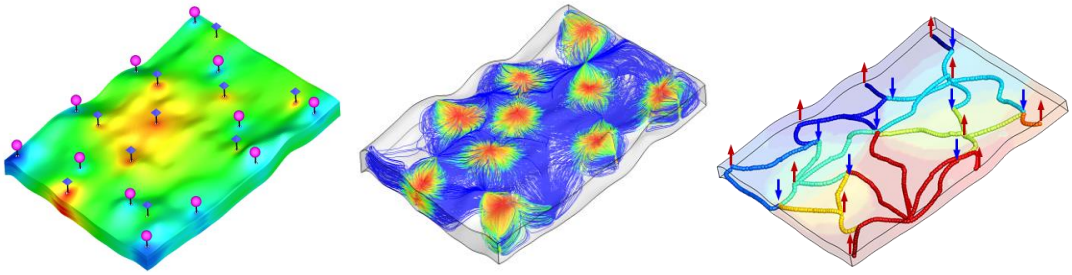

Figure 5.1: 3D geometry with well location and streamlines, connection map.

Although many papers and field applications can be found about the use of the streamline for optimization problem, the basic concept is same. The objective is to 'equalize' streamline properties to improve the oil rate. For instance, equalize offset production oil rate (Thiele and Batycky 2003), equalize travel time (Alhuthali, Oyerinde, and Datta-Gupta 2007), or reduce the variance of the travel time (Park and Datta-Gupta 2011) etc.

The base of the streamline-based rate allocation method lies in flow diagnostic generated by streamlines parameters. Once streamlines are traced between wells, the time-of-flight is calculated based on velocity and flux field. In addition to time-of-flight,

it is able to map dynamic reservoir properties along streamlines such as phase saturation and mobility. These information provides quantitative information of the reservoir such as heterogeneity or sweep efficiency between wells. They are quite useful for the reservoir management, which conventional finite difference simulator does not supply. Here we go through two approaches about the streamline-based rate allocation algorithm in detail and state its applicability and limitation.

5.2.1 Use of Well Allocation Factors

The first approach is the use of well allocation factors presented by (Thiele and Batycky 2003). In short, this approach tries to find the higher field total oil production rate by controlling the injection water rate or total production rate, based on the 'allocation factor'. The allocation factor is an offset production rate of the well pair. Then, they define the injection efficiency that is the offset oil production of the injection-production well pair. It can be said that the efficiency by the well allocation factor is nothing but the oil cut between well pair. The streamlines simulation carries water from injector to producer by Eq. 3.22 as shown in Figure 5.2, and each individual streamline provides an individual breakthrough time of injection fluid to the producer.

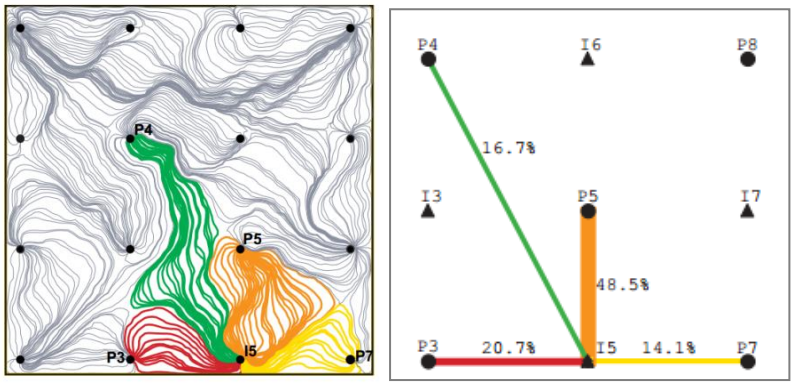

Figure 5.2: Streamline distribution and well allocation factor.

Figure 5.2 shows that the streamlines colored by well pairs starting from injector I5 to connected producers. With this information, it is able to identify the region where the injector or producer sweeps the reservoir. Define rate of the each streamline by q_l, the injection efficiency based on well allocation factor is calculated as

$$e_{ip} = \frac{\text{offset oil production rate of producer } i}{\text{water injection rate of injector } i \text{ to producer } p} = \frac{\sum_l^{Nsl} q_{ip,l} F_{o,l}^{end}}{\sum_l^{Nsl} q_{ip,l}} \quad \cdots\cdots \quad (5.1)$$

where the subscript *ip* stands for the connection IDs of injector and producer pair and *l* stands for individual streamline. The fractional flow of oil in the equation is evaluated at the end node of the streamlines. This means that the $q_{ip,l} F_{o,l}^{end}$ in Eq. 5.1 is the oil rate of the streamline at the producer under the assumption of an incompressible system. Using well allocation factor, it is able to define oil cut, say efficiency, of the well pair. In Figure 5.2, for instance, the efficiency of the I5-P7 is around 50% and I5-P4 has less than 20%. The objective of the proposed method by (Thiele and Batycky 2003) is to

conduct preferential injection of production by using these well allocation factor as an efficiency.

We show the process of the injection rate optimization as an example here. Once streamlines are traced after running single step of the reservoir simulation and well allocation factors are computed, update water injection rate of the individual injection well as

$$q_{ip}^{n+1} = \left(1 + w_{ip}\right) q_{ip}^{n} \times r \quad \cdots\cdots\cdots\cdots\cdots\cdots\cdots\cdots\cdots\cdots\cdots\cdots\cdots\cdots\cdots\cdots \quad (5.2)$$

where w is the weight factor calculated by well allocation factor and r is the factor to give constraint of the total amount of injection water. Assuming that initial total injection rate is the total available water in a field, the constraint r is calculated as follows

$$r = \frac{\sum_{i}^{Ninj} q_i^n}{\sum_{ip}^{Nip} \left(1 + w_{ip}\right) q_{ip}^n} \quad \cdots\cdots\cdots\cdots\cdots\cdots\cdots\cdots\cdots\cdots\cdots\cdots\cdots\cdots\cdots\cdots \quad (5.3)$$

again the w is the factor to determine the reallocation of the injection rate, as follows.

$$w_i = \begin{cases} \min\left[w_{\max}, w_{\max} \left(\dfrac{e_i - \bar{e}}{\bar{e} - e_{\min}} \right)^{\alpha} \right], & if\ e_i \geq \bar{e} \\ \min\left[w_{\min}, w_{\min} \left(\dfrac{\bar{e} - e_i}{\bar{e} - e_{\min}} \right)^{\alpha} \right], & if\ e_i \leq \bar{e} \end{cases} \quad \cdots\cdots\cdots\cdots\cdots\cdots\cdots\cdots\cdots\cdots \quad (5.4)$$

The exponent α and constraint values $w_{max,min}$, $e_{max,min}$ control the degree of reallocation from the deviation of the average efficiency of the field. The average efficiency $\bar{e}$ in Eq. 5.4 is calculated as

$$\bar{e} = \frac{\sum_i^{Nprd}\sum_l^{Nsl} q_{p,l}^{oil}}{\sum_i^{Ninj}\sum_l^{Nsl} q_{i,l}^{wat}} \cong \frac{\sum_p^{Nprd} q_p^{oil}}{\sum_i^{Ninj} q_i^{wat}} = \frac{q_{field,prd}^{oil}}{q_{field,inj}^{wat}} \quad \cdots\cdots\cdots\cdots\cdots\cdots\cdots\cdots \quad (5.5)$$

After calculating efficiency of the all injector-producer pairs and its field average, the water injection rate is updated using Eq. 5.2 and the weight function, Eq. 5.4. The weight function can be depicted in Figure 5.3. In a short, this equation tries to reduce the injection rate if the offset production is less than average, or vice versa. In other words, the equation tries to equalize oil cut of all the injection-production pair of the field. This is heuristic approach and does not require setting up any objective function to maximize the oil production rate; It is expected that increasing the rate of low water cut well pair instead of higher water cut well is going to increase oil production rate in a field.

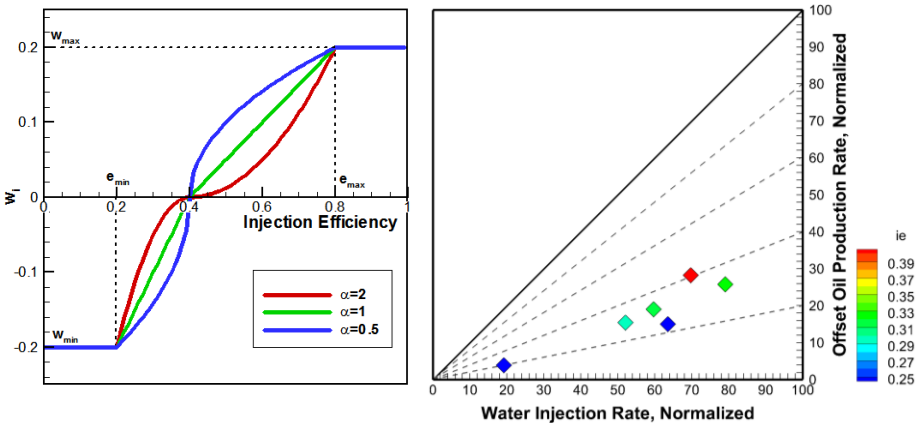

Figure 5.3: The weight function (left) and injection-production efficiency (right).

The final injector rate of the next time level is then calculated by summing all the injector producer pair rate as

$$q_i^{n+1} = \sum_{ip}^{Nip,i} q_{ip}^{n+1} \quad \cdots\cdots\cdots\cdots\cdots\cdots\cdots\cdots\cdots\cdots\cdots\cdots\cdots\cdots\cdots\cdots \quad (5.6)$$

The rate allocation optimization method based on well allocation factor is summarized as follows. The approach optimizes oil production rate under constraint of total injection or production rate of the field. The update of the well rate is conducted single time or can be several times. The optimal solution is the matching of all the efficiency of the well pair, which is expected to produce a maximum oil production rate. The limitation of this approach is that it requires clear breakthrough information to propose new injection rate. If the water-cut has non-smooth profile, the proposed injection rate will follow it and some smoothing factor is required to generate realistic operation profile. The change of the factors shown in Eq. 5.4 might avoid this, however, it requires several times of trial and error process.

5.2.2 Equalize Arrival Time

The objective of this approach is to maximize sweep efficiency by equalizing the arrival time of the water front of the producer by controlling the flow rate of the individual well. The objective function is to minimize following equation

$$\mathbf{G}\delta\mathbf{q} = \mathbf{R} \quad \cdots\cdots\cdots\cdots\cdots\cdots\cdots\cdots\cdots\cdots\cdots\cdots\cdots\cdots\cdots\cdots \quad (5.7)$$

where **R** is a residual vector $R_{ip} = t_m - t_{ip}$. The arrival time of t_m and t_{ip} are the mean of the field average (arithmetic mean) break thorough time and individual well pair breakthrough time, respectively. They are approximated using the average value of the bundle of streamline time-of-flight at well and the Buckley-Leverett solution for the general multiphase problem. The matrix **G** is the partial derivative of the residual vector

with respect to well flow rate. The dimension of the matrix **G** is $N_{prd}\times N_{inj}$ that is the number of possible connections of injector and producer. Assume t_m is constant by change of local well rate, the sensitivity is calculated by the partial derivative of connection time, t_{ip}. If the control variable is injection rate, the sensitivity coefficient is calculated as follows

$$G_{ip} = -\frac{\partial t_{ip}}{\partial q_i} \approx -\frac{\partial \tau_{ip}}{\partial q_i} = -\frac{\partial \tau_{ip}}{\partial q_{sl}}\frac{\partial q_{sl}}{\partial q_i} \approx -\frac{1}{N_{sl,i}}\frac{1}{N_{sl,ip}}\frac{\partial}{\partial q_{sl}}\sum_{sl}^{Nsl,ip}\tau_{sl} \quad \cdots\cdots\cdots \quad (5.8)$$
$$= \frac{1}{N_{sl,i}}\frac{1}{N_{sl,ip}}\sum_{sl}^{Nsl,ip}\frac{\tau_{sl}}{q_{sl}}$$

where t_{ip}, τ_{ip} are the actual mean break through time and average time of light at the well pairs. Here we assume that $t_{ip} = \tau_{ip}$ such as tracer response without diffusion. The partial derivative of the streamline rate with respect to injection rate, $\partial q_{sl}/\partial q_i$ is approximated by the number of streamlines launched form the well *i*. The partial derivative of time-of-flight at producer by change of flow along streamlines, $\frac{\partial \tau_{sl}}{\partial q_{sl}}$, is approximated by $-\frac{\tau_{sl}}{q_{sl}}$ based on Darcy's law (Alhuthali, Oyerinde, and Datta-Gupta 2007). The equation is applicable to the incompressible single component system. The compressible multiphase problem requires multiplication by speed of the phase α by $F_\alpha'^{-1}$ and effective density to evaluate streamline flux at producer. The equation becomes

$$G_{ip} \approx \frac{1}{q_i}\sum_{sl}^{Nsl,ip}\frac{q_{sl}}{\rho_{eff}}\frac{\partial \tau_{sl}}{\partial q_{sl}}\cdot\left.\frac{\partial F_\alpha}{\partial S_\alpha}\right|_{prd}^{-1} \quad \cdots\cdots\cdots\cdots\cdots\cdots\cdots\cdots\cdots\cdots \quad (5.9)$$

The effect of capillary and gravity can be applied by use of total fractional flow, f_α, Eq. 3.12. However, the previous work indicates that the approximate equation shown in Eq. 5. 7 can be applied to the practical problem (Alhuthali, Oyerinde, and Datta-Gupta 2007, Ekkawong 2013) and rigorous sensitivity calculation is not necessary.

The change of the flow rate of the well is calculated by Eq. 5. 7, which minimizes the arrival time difference of each connection of well to the field average, as follows.

$$\begin{bmatrix} \mathbf{G} \\ \mathbf{I} \end{bmatrix} \delta\mathbf{q} = \begin{bmatrix} \mathbf{R} \\ 0 \end{bmatrix} \quad \cdots\cdots\cdots\cdots\cdots\cdots\cdots\cdots\cdots\cdots\cdots\cdots\cdots\cdots\cdots\cdots \quad (5.10)$$

where identity matrix $\mathbf{I}$ is introduced to give a constraint of a total change of well rate to be zero. This constraint is required if field injection/production constraint is given. The equation is over determined and if an iterative solver is used, extra normalization is required, as follows.

$$q_i^{new} = q_i^{old} + \left(\Delta q_i^{lsqr} - \Delta \bar{q}_i^{lsqr}\right) \quad \cdots\cdots\cdots\cdots\cdots\cdots\cdots\cdots\cdots\cdots\cdots\cdots\cdots\cdots \quad (5.11)$$

Al-Huthali proposed to minimize the objective function of squared equation by Sequential Quadric Programming (SQP) to attain quadratic convergence with constrained optimization. The SQP based method gives faster convergence under constraint and suitable for optimization/minimization problem rather than Eq. 5.10 with Hessian matrix described detail in Alhuthali, Oyerinde, and Datta-Gupta (2007).

The rate allocation of equalizes arrival time approach is summarized as follows. The objective is to equalize the arrival time of the injector-producer well pair. The arrival time is the function of the mobility and thus the rate allocation factor changes

dynamically. The method is purely function of frontal propagation of the injection fluid and thus the best performance is obtained if reservoir is saturated by oil. For the application of the non-uniform scenario, penalized factor needs to be included in the model, for instance, give weight factor for high water-cut well etc. (Ekkawong 2013)

5.3 Streamline-based NPV Optimization

A new approach is proposed here to optimize field NPV by rate allocation for both injector and producer well. The objective is to keep the advantages of the streamline-based approach: gradient free, and ability to update with post processing from the results of simulator. In addition, the new approach avoids the limitations as stated in the previous approach. In addition to avoiding limitations of previous streamline work, the method directly improves NPV and thus it is able to avoid factors to modify by every case study.

5.3.1 Generalized Derivative-Free Optimization by Streamline

First, we define the pore volume along streamline. It is discussed in Chapter II in Eq. 2.41 that streamline is a line but has an associated volume. In general, for compressible flow system, the pore volume along a streamline is calculated as follows.

$$PV_{sl} = \int_0^s A(\xi)\phi(\xi)d\xi = \int_0^s \frac{q_{sl}\phi(\xi)}{\rho_{eff}(\xi)u_t(\xi)}d\xi = \sum_i^{node} \frac{q_{sl}}{\rho_{eff,i}}\Delta\tau_i \quad \cdots\cdots\cdots\cdots \quad (5.12)$$

where ρ_{eff} is effective density, which varies along streamline in compressible system. In an example of injection well with closed boundary, pore volume is large at launching point because effective density is defined as 1.0 but it disappears at the stagnation point because the effective density goes to infinity. As we know the pore volume along a

streamline, it is able to find the 'value' and NPV along streamline. The 'value' is calculated as:

$$\Lambda_{sl} = q_{sl} \sum_{node} \frac{1}{\rho_{eff}} \sum_{\alpha=og} \left(S_\alpha b_\alpha R_\alpha \right) \quad \cdots\cdots\cdots\cdots\cdots\cdots\cdots\cdots\cdots\cdots\cdots\cdots \quad (5.13)$$

where R_α stands for the price of fluid in per unit volume, b_α is the inverse of the formation volume factor. The equation is nothing but multiplying the hydrocarbon volume with price along streamline. The 'value' is always positive for practical application under positive price of the hydrocarbon. Then NPV along streamline is calculated as

$$r_{sl} = q_{sl} \sum_{node} \frac{\Delta\tau}{\rho_{eff}} \sum_{\alpha=owg} \left(S_\alpha b_\alpha R_\alpha \right) \cdot \left(1+d\right)^{-\tau_{node} \cdot f_\alpha^{-1}/365} \notin \tau_{node} > t_{rsm} \quad \cdots\cdots\cdots\cdots \quad (5.14)$$

where R_α stands for the price of the fluid per unit volume, t_{rsm} is the remaining reservoir life time or contract period, and d is the discount rate. The term $\left(1+d\right)^{-\tau_{node} \cdot f_\alpha^{-1}/365}$ gives discount factor of volume along streamline by time to arrive at producer. The derivative of the fractional flow is used to find the speed of the component. Fractional flow is evaluated based on the Buckley-Leverett theorem, e.g. breakthrough saturation is the maximum speed. The Pressure is averaged to find the viscosity, in order to find average speed at node i to the producer. Using these values, the efficiency of the individual streamline is evaluated as

$$e_{ip,NPV} = \frac{r_{ip}}{\Lambda_{ip}} = \sum_{sl}^{Nsl,ip} \frac{r_{sl}}{\Lambda_{sl}} \quad \cdots\cdots\cdots\cdots\cdots\cdots\cdots\cdots\cdots\cdots\cdots\cdots\cdots\cdots \quad (5.15)$$

Here we can define the efficiency of other terminology that is related to previous works. Define the ratio of the travel time as follows.

$$e_{ip,EqA} = \frac{\tau_{ip}}{\tau_{fm}} = \frac{N_{sl,ip}^{-1} \sum_{sl}^{Nsl,ip} \tau_{sl}}{N_{sl}^{-1} \sum_{sl}^{Nsl} \tau_{sl}} \quad \cdots\cdots\cdots\cdots\cdots\cdots\cdots\cdots\cdots\cdots\cdots\cdots \quad (5.16)$$

The allocation factor is also evaluated as follows.

$$e_{ip,WAF} = \frac{Q_{o,ip}}{Q_{t,ip}} = \sum_{sl}^{Nsl,ip} \frac{q_{sl}}{\rho_{eff}} \frac{b_w q_{sl}^w}{\left(b_w q_{sl}^w + b_o q_{sl}^o\right)} = \sum_{sl}^{Nsl,ip} \frac{q_{sl} F_{w,sl}}{\rho_{eff}} \quad \cdots\cdots\cdots\cdots\cdots\cdots \quad (5.17)$$

The factors defined through Eqs. 5.15-17 has similarities in previous streamline work, $e_{ip,EqA}$ as in equalizing arrival time and $e_{ip,WAF}$ as in optimization based upon well allocation factor. The objective of their approach has analogous to equalize these factors. As shown in these equations, these variables use only the end point information along streamline except NPV-based method. This is the main reason that their approach has limitation in applicability, such as it does not work before the breakthrough for WAFs, or, EqAT could not improve recovery after breakthrough. In contrast, the proposed NPV-based efficiency integrates all the information along streamline with the discount rate. This is the reason the proposed approach has the ability to optimize NPV even before breakthrough or after.

As discussed before, use of NPV based factor is robust compared with previous work of streamline-based optimization. In some situation, however, the objective function is not NPV but oil production rate or balancing saturation front propagation. One example is that if an operator needs to maximize oil production rate at short period

of time regardless of NPV, well allocation factor will satisfy this objective. Considering these cases, define the 'integrated efficiency' as follows.

$$e_{ip} = \left(\frac{\tilde{r}_{ip}}{\tilde{\Lambda}_{ip}} \right)^{\alpha} \cdot \left(\frac{\tau_{ip}}{\tau_{fm}} \right)^{\beta} \cdot \left(\frac{Q_{o,ip}}{Q_{t,ip}} \right)^{\gamma} \quad \cdots\cdots\cdots\cdots\cdots\cdots\cdots\cdots\cdots\cdots\cdots\cdots \quad (5.18)$$

where α, β and γ stands for the weight to the each objective. The NPV and 'value' are normalized by $\tilde{r}_{ip} = r_{ip} \cdot 100 / \max(\Lambda)$ and $\tilde{\Lambda} = \Lambda_{ip} \cdot 100 / \max(\Lambda)$. In the above situation, for instance, the optimization of the oil production in a short time period is done by (α,β,γ) = (0,0,1). In the general case, (α,β,γ) = (1,0,0) because the objective of the rate allocation problem is to maximize NPV. The factor of arrival time, β, is to equalize the arrival time of the injection fluid, however, this can be used to reduce the change of the well rate through the operation. For instance, (α,β,γ) = (1,0.25,0) will reduce the change of the well rate per time step compared to (α,β,γ) = (1,0,0).

5.3.2 Workflow

The workflow of the proposed optimization method is described by using following multiwell example, shown in Figure 5.4. For the simplicity, the workflow is demonstrated by the single injector (Injector-4) and connected producers.

The first process is the tracing of streamlines. This step can be omitted by use of streamline simulation because all the parameters can be calculated through simulation process. When the conventional finite difference simulator is used, streamline tracing is necessary by post processing of the simulation results. The colored streamlines in Figure

5.4 shows the connected lines started from Injector-4 to producers. As shown in the figure below, streamlines clearly identify the flow patterns.

Then the Eq. 5.3 is evaluated using streamlines traced in the field. The required parameters are the all the dynamic data and time-of-flight along underline grids. To evaluate the coefficient of equalized arrival time shown in Eq. 5.17, the average time-of-flight of well pair is calculated by a simple arithmetic average of bundle of streamlines at the end node of the well pair. The coefficient of the well allocation factor in Eq. 5.18 is also evaluated by the saturation and fractional flow at the end node of the streamline. The NPV use all the information along the streamline to evaluate the value of the fluid with associated connection well pair. The demonstration here is evaluated by (α,β,γ = 1.0,0,0) in Eq. 5.18 to set NPV as an objective function.

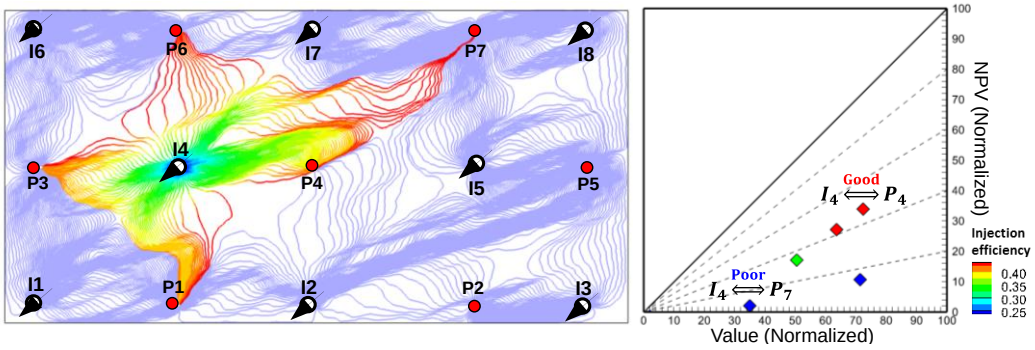

Figure 5.4: The streamline distribution highlighted by injector I4 and flow diagnostics.

After calculating the 'value' and NPV along streamline using Eq. 5.13 and 5.14, the normalize value $\tilde{r}_{ip} = r_{ip} \cdot 100 / \max(\Lambda)$ and $\tilde{\Lambda} = \Lambda_{ip} \cdot 100 / \max(\Lambda)$ can be displayed by Figure 5.4. The example shown here is the producers which have a connection by

streamline launched from Injector-4. Each point shown in Figure 5.4 as diamond shape is connection efficiency based on NPV, colored by red and blue as high and low efficiency by relative scale. The figure shows that as the point moves to the right, then the amount of hydrocarbon is high and as a point moves up, then the hydrocarbon can be recovered and will contribute high NPV. As displayed in the figure, the connection of I4-P4 has a value of 40% where I4-P7 has less than 10% in relative scale. Using this NPV flow diagnostic plot, the desirable connection rate is updated to increase NPV by reallocating injection or production rate. Based on this concept, the actual procedure is as follows.

First, because the well-pair efficiency can be ranging between 1.0 to negative value, transform data to the mean of 1.0 and range of σ as follows

$$\hat{e}_{ip} = \sigma\left(\frac{e_{ip} - e_{\min}}{e_{\max} - e_{\min}}\right) + 1.0 \quad \cdots\cdots\cdots\cdots\cdots\cdots\cdots\cdots\cdots\cdots\cdots\cdots\cdots\cdots \quad (5.19)$$

Now the transformed data indicates that when the efficiency is more than 1.0, it is worth increasing flow rate to improve NPV. In contrast, if the efficiency lowers 1.0, the contribution is small or connection is not efficient relative to the field average. Note that this transformation is used only for update of the well rate. In the example in Figure 5.5, the points shown by blue color is going to be less than 1.0 and the red points is going to be more than 1.0. Using these parameters, update connection rate as follows.

$$\begin{cases} \Delta e_{ip} = \hat{e}_{ip} - 1 \\ \hat{q}_{ip}^{n+1} = \left(1 + \Delta e_{ip}\right) q_{ip}^{n} \end{cases} \quad \cdots\cdots\cdots\cdots\cdots\cdots\cdots\cdots\cdots\cdots\cdots\cdots\cdots\cdots \quad (5.20)$$

Once flow rate of the well pair is updates, the individual well rate is evaluated using Eqs. 5.3 to 5.6 for instance. Then, the simulation is conducted a gain and diagnostic plot is updated. For the diagnostic plot, it is better shown by efficiency before transformed by Eq. 5.19. Figure 5.5 shows the NPV diagnostic plot generated by the example case of before and after the update of the well rate. As shown in the Figure, the reallocation is conducted to equalize the well pair NPV. It is clear that after update of well rate by Eq. 5.20, the variance of the point is clearly reduced shown in left plot of Figure 5.5. In addition, it can be observed that the average of the relative NPV increased after update of the well. The example figure shows around 40% of the profitability after reallocation of the flow rate, which is much higher than the one before the update.

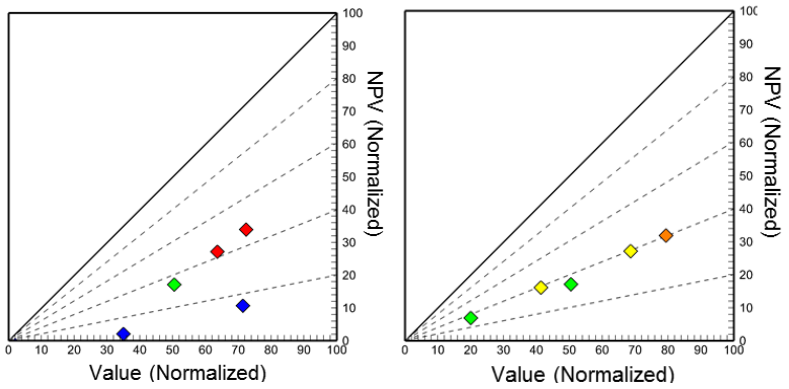

Figure 5.5: The flow diagnostic plot, before update (left) and after update (right).

The result of the Eq. 5.20 is the well pair and individual well rates calculated by this process but ignores the constraint of the well. The optimization under constraint is a difficult problem when the optimization process is carried out as a post processing of the simulator. One option here is to control the constraint by simulator side. Most of the

simulator allows having a primary and secondary constraint per well or group. This constraint will prevent the unrealistic well control. However, it is always better that the optimization algorithm itself handle constraint of the well to avoid proposing unrealistic rate. To achieve that, we follow the additional process below.

When the individual well is either upper or lower constraint of the rate or pressure, then the connection rate related to that well needs to be kept, as

$$\hat{q}_{ip}^{n+1} = \begin{cases} q_{ip}^{n}, \text{if } q_i > q_{i,const} \\ Eq.5.20, else \end{cases} \quad \cdots\cdots\cdots\cdots\cdots\cdots\cdots\cdots\cdots\cdots\cdots\cdots \quad (5.21)$$

Then consider field available water or gas rate. In this study, the maximum available water is assumed to be assigned as an input data, or initial injection/production total. If the available water is the summation of the initial injection total, the well rate is updated by

$$q_{ip}^{n+1} = \hat{q}_{ip}^{n+1} \cdot \frac{\sum_{i}^{Ninj} q_i^n}{\sum_{ip}^{Nip} \left(1 + \Delta e_{ip}\right) q_{ip}^n} \quad \cdots\cdots\cdots\cdots\cdots\cdots\cdots\cdots\cdots\cdots\cdots\cdots \quad (5.22)$$

Eq. 5.22 rescales the injector (or producer) rate to make sure that the total rate is not exceeds maximum constraint. Note that the rescale is conducted the well which is not at the constraint either rate or pressure.

The total injection rate is updated during to the optimization process. First, if the total injection rate is constrained by q_{tmi}, check following conditions during the update

$$q_i^{n+1} = q_i^{n+1} \cdot \frac{q_{tmi}}{\sum_{i}^{Ninj} q_i^{n+1}} \ \ if \ \ q_{tmi} < \sum_{i}^{Ninj} q_i^{n+1} \quad \cdots\cdots\cdots\cdots\cdots\cdots\cdots\cdots\cdots\cdots \quad (5.23)$$

Because the injection rate often decrease the NPV, the total injection rate is also updated based on injection efficiency. The update is conducted only if all the well pair efficiency or negative, or positive. In other words, if most of the efficiency has negative but there is a single well which has positive NPV, we do reallocate individual well rate, however, keep total injection rate. Only if all the well pair NPV is negative, we do reduce the total injection rate as

$$\begin{cases} q_{tmi}^{n+1} = q_{tmi}^{n} \cdot \alpha \\ \alpha < 1 \, if \;\; \forall e_{ip}, e_{ip} < 0 \\ \alpha > 1 \, if \;\; \forall e_{ip}, e_{ip} > 0 \end{cases} \quad \cdots\cdots\cdots\cdots\cdots\cdots\cdots\cdots\cdots\cdots\cdots\cdots\cdots\cdots\cdots\cdots \quad (5.24)$$

The updated total constraint is used in Eq. 5.23.

The update of flow rate is conducted iteratively until change of the flow rate gets small, or iteration reaches maximum number.

5.4 Application

The developed model is tested by series of synthetic example including Brugge bench mark scenario. The general parameters used for rate allocation optimization is shown in Table 5.1 below.

Table 5.1: Parameters used for rate allocation optimization

Parameter Name	Value
Relative oil price	1.0 [$/bbl]
Relative water price (Produced)	-0.2 [$/bbl]
Relative water price (Injected)	-0.2 [$/bbl]
Relative gas price	0.0 [$/bbl]
e_{min},e_{max},w_{min},w_{max},α (For WAFs)	0.0,1.0 , -0.1,0.1,2.0
Amount of SL use (For EqAT)	80%
α,β,γ (For SLNPV)	1.0,0.2,0.0

5.4.1 1D Example

The First demonstration is 1-dimensional 2-phase incompressible, piston-like displacement problem. Figure 5.6 shows the schematic view of the reservoir and wells. The injector is located at the each side of the reservoir and the producer is located at the left side. The producer is given as pressure constraint and thus, the control variable is the water injection rate of the wells located at the side of the reservoir. The constraint is specified as total available water rate by 20bbl/day.

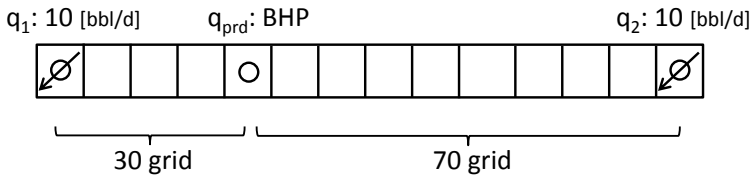

Figure 5.6: Schematic view of 1D example for rate allocation optimization of ideal scenario.

Here the four different scenarios are tested: (a) the uniform injection scenario, (b) the optimization by WAFs (c) the optimization by EqAT (d) the optimization by SLNPV. In order to evaluate NPV, the oil and water relative price is given by 1.0 and -0.2. The discount rate is 10%. The recovery factor and NPV are compared. Simulation period is 800 days and rate control is conducted every 30 days.

The result of the NPV and recovery factor is shown in Figure 5.7 with all the tested optimization scenario including uniform injection scenario. The uniform injection scenario is shown by gray color and other method shows the best performance for both NPV and recovery factor.

Now we go through the result in detail how each optimization scenario worked for this 1D scenario.

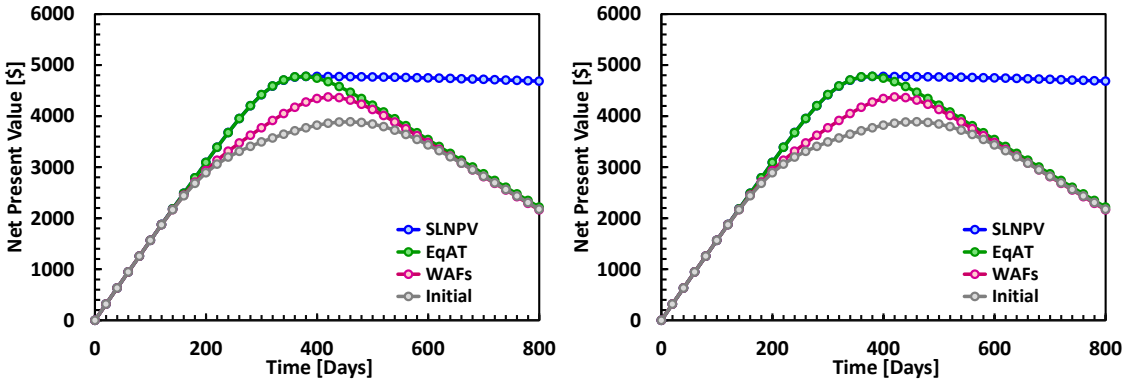

Figure 5.7: Net Present Value (left) and recovery factor (right) by 1D scenario.

The optimal injection rate at the initial condition can be calculated analytically. Because this problem is piston-like displacement on 1D domain, thus the optimal injection rate is 30% of available water to q1 and 70% to q2. This injection scenario will have equivalent breakthrough time at the producer. As shown in Figure 5.7, the result of SLNPV and EqAT shows this trend. Meanwhile, the result of WAF does not change the injection rate at the beginning. This is because there is no breakthrough at producer and then WAF-based optimization cannot evaluate the efficiency of the well at the beginning of the production period. The rate change of WAF start around 100 days, however, it is too late to catch up with the optimal solution. Thus, the best solution can be obtained either SLNPV or EqAT method. The main difference between these two methods is that the SLNPV start reducing the injection rate to maintain the NPV. This is because the efficiency gets negative and reducing of the total injection is the only choice to maintain

the NPV. This is the main reason that the NPV history shown in Figure 5.8 showed clear differences between SLNPV and WAF. The proposed method can detect when the NPV start decreasing and try to keep NPV positive by reducing total injection rates.

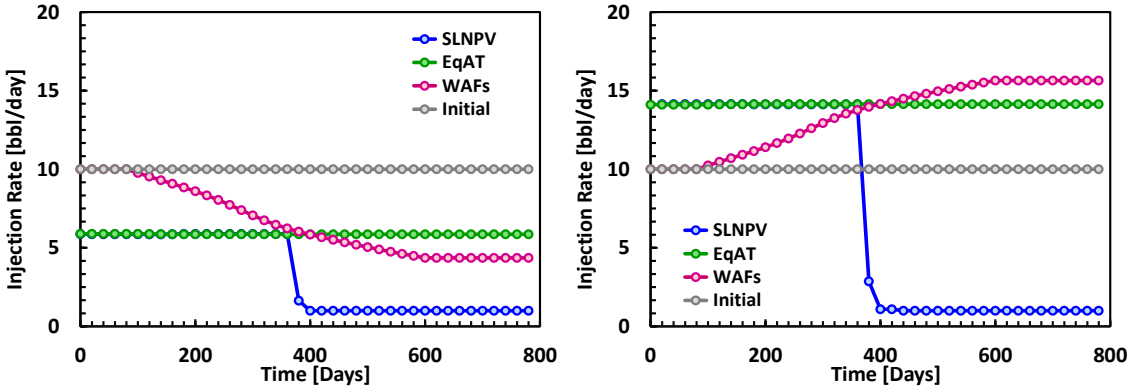

Figure 5.8: Injection rate history of left side of the well (left) and the right side of the well (right) by 1D scenario.

5.4.2 2D Quarter Five Spot Example

The model is tested in a 2D areal quarter five spot case. Again the fluid PVT is 2-phase incompressible, piston-like displacement problem and no capillarity between phases. The injector is the constant rate of 100 bbl/day. The initial rate of the 4 injection well well is assigned by 25 bbl/day for each. Figure 5.9 shows the well name and its location. The objective of this problem is to reallocate the injector well, I1 to I4 to improve the recovery factor or NPV.

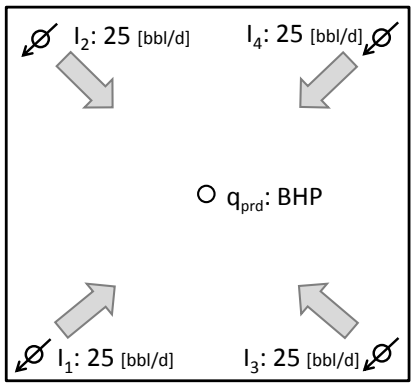

Figure 5.9: The schematic view of quarter five spot configuration used for rate allocation optimization.

Figure 5.10 (a,b) shows the permeability and porosity distribution. The model is heterogeneous both permeability and porosity with high permeability channel running diagonal from Injector-1 to Injector-4. The initial saturation is given as 5.10c. The saturation distribution also given as heterogeneous at initial condition. As shown in Figure 5.10, the high oil saturation at the left side of the field. The preferable allocation strategy of injection water should be higher at the I1 and I2 because of high oil

saturation around the well at the beginning. The I1 seems the best well because of high permeability, porosity as well as oil saturation. Again the 4 different strategy is tested for the rate allocation optimization; the uniform injection, WAFs, EqAT and SLNPV. The oil price and water price is same as previous case, 1.0 and -0.2 with discount rate of 10%.

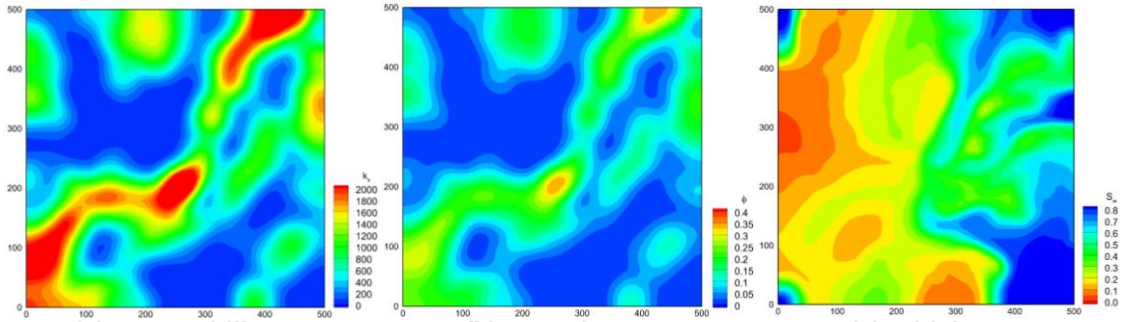

Figure 5.10: The permeability, porosity distribution and initial oil saturation.

Figure 5.11 shows the injection strategy of the four different scenarios after optimized process. Again the control variable is 4 well, field water injection rate of 100 bbl/day. The uniform injection scenario is allocated by 25 bbl/day for all the cases. Figure 5.11b shows the injection scenario of the EqAT. Because of the piston like displacement with unit mobility of oil and water phase, it is steady state for through the simulation. The steady state condition keeps streamline distribution and time-of-flight constant, so the injection rate does not change through the simulation. In EqAT, the I3 showed the reduction of the injection rate while other wells are increasing the rate.

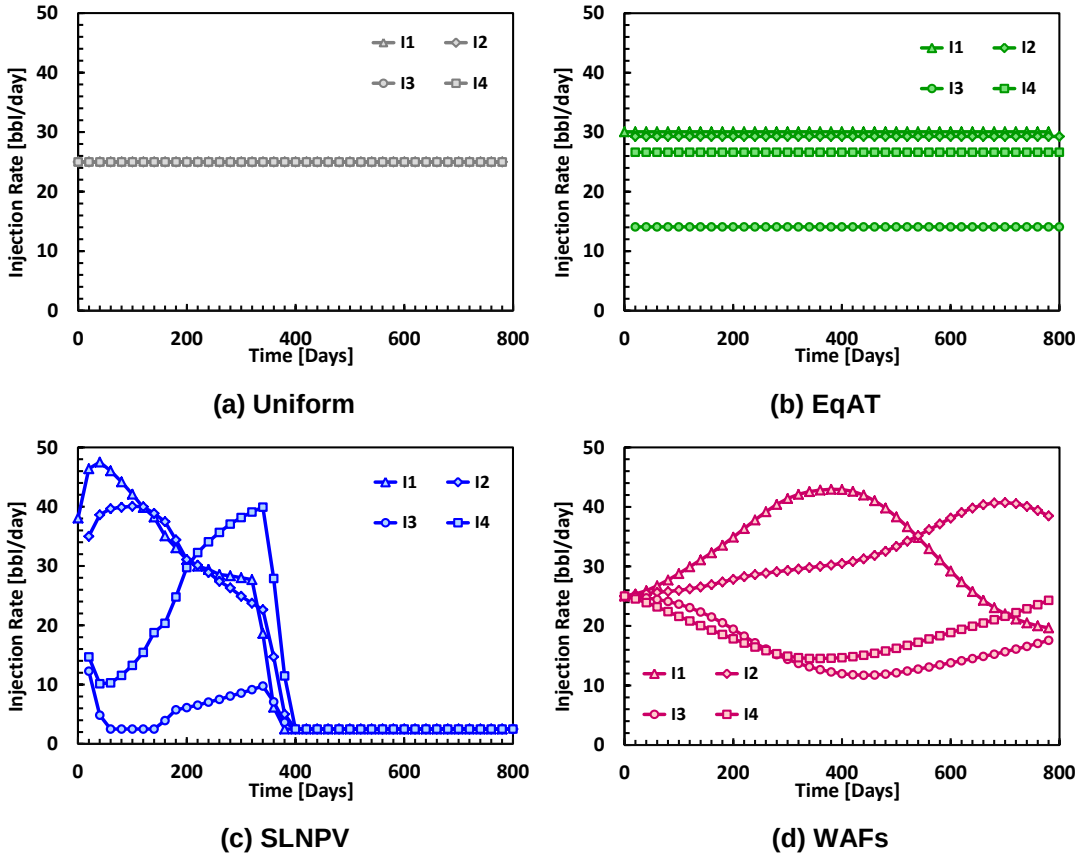

Figure 5.11: The history of the injection rate of four strategies: (a) uniform injection (b) EqAT (c) SLNPV (d) WAFs.

Figure 5.11c shows the result from SLNPV. The result clearly shows the high injection of I1 and I2, which have the high oil saturation around the injector. In contrast, the rate of I3 and I4 is small, especially I3 shows the minimum injection rate until 100 days. The other point in SLNPV is that it starts reducing injection rate of the all the well, and after 400 days, all the wells are at the minimum rate.

Figure 5.11d shows the result of the WAFs. The initial injection rate is same as the uniform. This is because the initial saturation around the producer does not have clear differences between 4 injectors. In addition, finite difference simulations cause

numerical dispersion and saturation mapping error. These numerical dispersion causes smeared saturation with the course simulation model which makes it difficult to distinguish well allocation factor. However, as simulation goes, it shows the same trend with the strategy with SLNPV.

Figure 5.12 shows the comparisons of the NPV and recovery factor. It is clear that the SLNPV shows the highest NPV through the simulation. The saturation distribution also verifies that the oil saturation distribution is much less in SLNPV at the middle of the simulation, in Figure 5.13

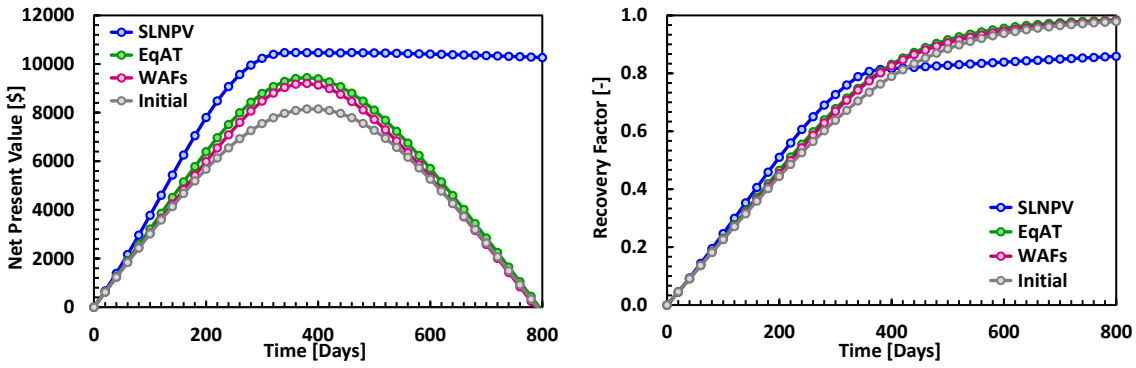

Figure 5.12: Net present value (left) and recovery factor (right) by 2D quarter five spot.

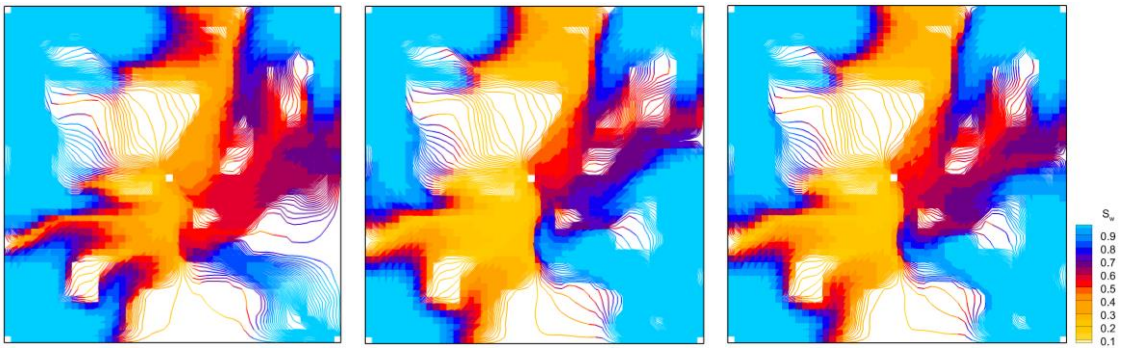

Figure 5.13: The streamline distribution of SLNPV (left), EqAT (middle) and WAFs (right). The color is by water saturation.

5.4.3 2D Areal Multiwell Problem

The model is now tested in a multiwell 2D case. The example here is a 3 phase water flooding. The fluid PVT data and rock table is given by Appendix F. constraint here is total available water by 1010 rb/day so as production total by 1000 rb/day. Total 8 injectors and 7 producers placed by 5 spot configurations shown in Figure 5.14. The control variable here is all the injector and producer, reallocate all the wells under given constraint of total available injection rate and available processing production rate.

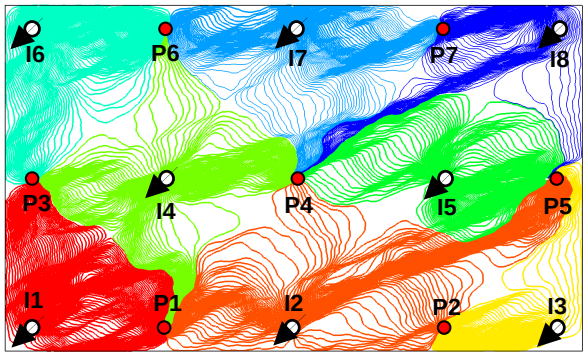

Figure 5.14: The well configuration and streamline distribution by the uniform injection scenario.

Figure 5.14 also shows well placement pattern and streamline distribution by uniform injection scenario. The streamline is highly heterogeneous and some of the cell does not have streamlines.

The permeability field and initial saturation are given in Figs. 5.15-16. The saturation distribution also given as heterogeneous, it assumes that high permeability region has been swept away at starting condition. The porosity has the same distribution

as permeability field, with an average value of 0.15. Now the problem is difficult, one might guess high injection and production by low permeability region, however, it will cause large drawdown and will generate free gas phase. The price of oil, gas and water is 1.0,0.0 and -0.2 and thus the appearance of free gas will reduce the total NPV.

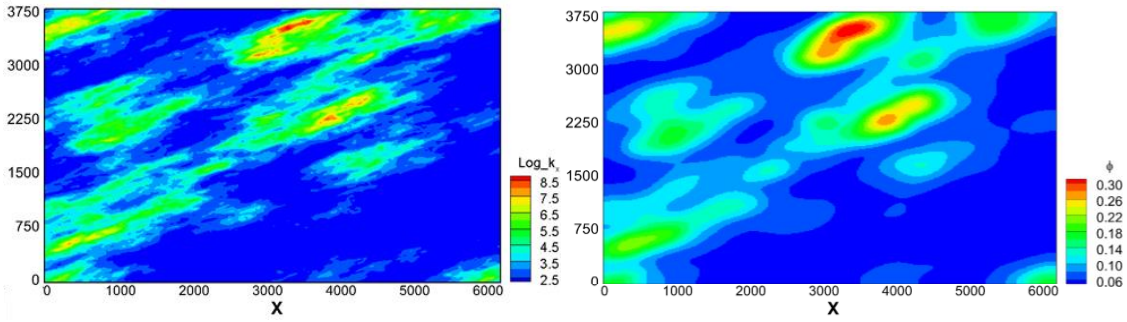

Figure 5.15: The permeability and porosity field used for multiwell optimization scenario.

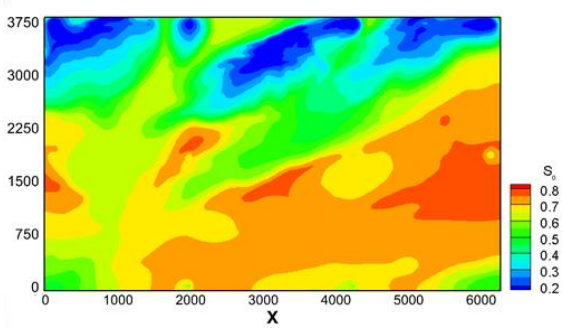

Figure 5.16: The initial oil saturation distribution.

Again the four scenarios are tested: uniform injection, use of Well Allocation Factors (WAFs), Equalize arrival time (EqAT) and developed NPV based method (SLNPV). First, the diagnostic plot is analyzed at the first step of the simulation. Figure 5.17 shows the diagnostic plot by all the injector and producer pair. Some of the well

pair has up to 50% of the profitability, while there are several points around 10%. The mean of the profitability was 30%. The SLNPV algorithm optimizes NPV using this diagnostic plot. The right side of Figure 5.17 shows the optimized distribution after reallocation. As shown in the figure, the reallocation reduces the scattered distribution. The reason it does not fully equalize the data point is because of nonlinearity. With multiple connections with 3 phase problem, it is not possible to equalize efficiency of the all of the well pair. However, the range of the distribution is lessened and the average of the efficiency increased around 10%.

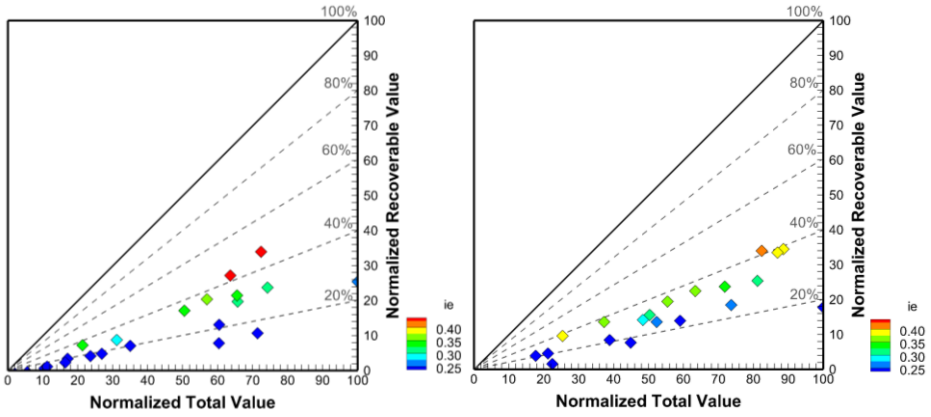

Figure 5.17: The flow diagnostic plot of uniform injection scenario (left) update after SLNPV (right).

The streamline and water saturation is then investigated to see the effect of the streamline-based NPV optimization. Figure 5.18 shows the streamline distribution by uniform injection scenario and after update by SLNPV. This is the result after 100 days, however, the difference is clear. The top of the region had high water saturation at the

beginning, and thus the flux around these regions was reduced. Instead, faster water propagation can be observed at the lower part of the reservoir.

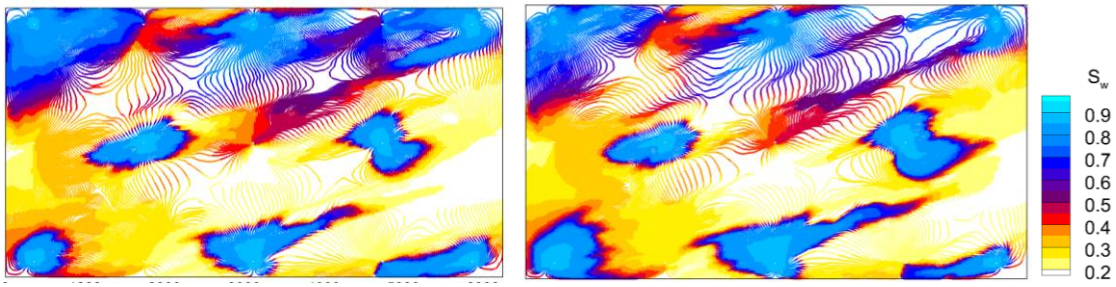

Figure 5.18: Streamline distribution contoured by water saturation (left) uniform injection (right) SLNPV.

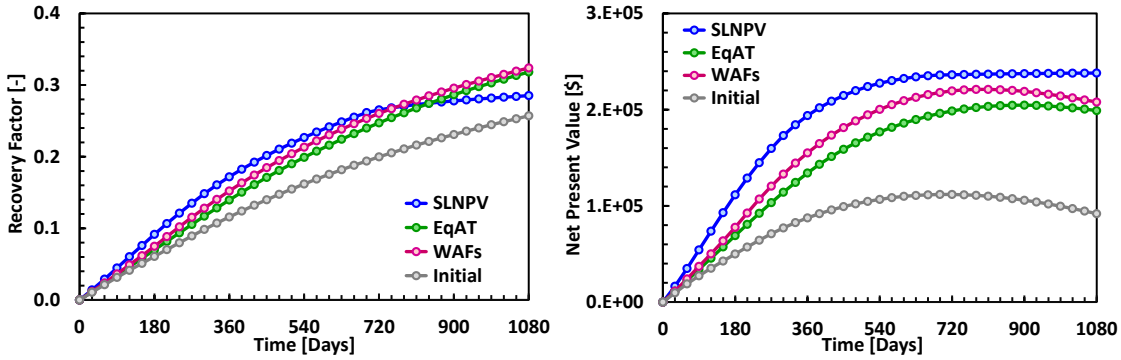

Figure 5.19: Net present value (left) and recovery factor (right) by 2D multiwall case.

The result of recovery factor and NPV is plotted by Figure 5.19, for all the 4 cases. A comparisons of the recovery factor shows that the best recovery is obtained by EqAT. We found that EqAT shows better performance compared with piston like displacement case. This is because EqAT dynamically reallocate injector and producer rate to sweep lower mobility of oil. The result of WAFs also increased both NPV and recovery factor

compared with an initial uniform scenario, however, the improvement is less than EqAT and SLNPV. The best result is obtained by SLNPV, because it clearly shows faster recovery of oil and highest NPV at the end of the simulation.

The well and reservoir parameters used for this multiwall case study is summarized in Table 5.2 below.

Table 5.2: Reservoir parameters for 2D multiwell optimization scenario

Parameter Name	Value
Grid dimension	(nx,ny,nz) = (250,250,1)
Grid length	(dx,dy,dz) = (25,15,8)
Porosity	Figure 5.15
Permeability	Figure 5.15
Pore compressibility	3.6E-6 [psi^{-1}]
B_w, μ_w, c_w	1.0031,0.65,1.0E-6 [psi^{-1}]
B_o, μ_o, c_o	1.15,2.50,1.0E-6 [psi^{-1}]
Rel-Perm function	Appendix F, water-wet model
Initial pressure	1550 [psi]
Initial saturation	Figure 5.16
8 injector control (Uniform scenario)	RESV, 125.0 [bbl/day]
7 producer control (Uniform scenario)	RESV, 142.85 [bbl/day]
Simulation time	1080 [days]

5.4.4 The Brugge Benchmark Case

In this section, we demonstrate the application of our proposed optimization approach with the benchmark Brugge field (Peters *et al.* 2009). The Brugge field model was presented at SPE Applied Technology Workshop (ATW) for the purpose of evaluating various production optimization methods. The reservoir is designed by a North sea Brent-type field. The field includes 20 vertical producers completed in the top 8 layers and 10 peripheral water injectors completed in all layers. The demonstration here is conducted by the same reservoir model demonstrated by the Chapter II. Figure 5.20 shows the initial oil saturation with injection and production well location.

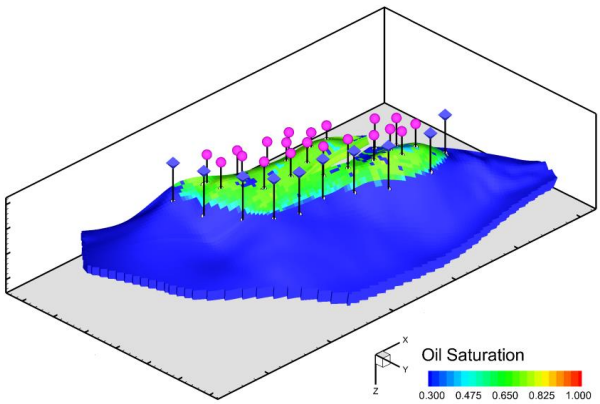

Figure 5.20: The well location and initial oil saturation distribution by Brugge benchmark study.

The reservoir and simulation parameters of Brugge optimization problem is summarized in Table 5.3. In this study, the optimization is conducted by through the 20 years of waterflood. The interval of the rate reallocation is 4 months. Same as previous

case, the four different scenario is conducted and including uniform injection scenario. The constraints used in this benchmark scenario are as follows:

- Maximum available water in a field: 20100 RB/day
- Maximum allowable production/injection rate per well: 6000 RB/day
- Maximum injector bottom hole pressure: 6000 psi
- Minimum producer bottom hole pressure: 500 psi

Table 5.3: Reservoir parameters for optimization of Brugge benchmark scenario

Parameter Name	Value
Grid dimension	(nx,ny,nz) = (139,48,9)
Permeability	Figure. 2.44 (a)
Porosity	Figure. 2.44 (b)
Net to Gross Ratio	Figure. 2.44 (c)
Rock table	Figure. 2.44 (d)
Pore compressibility	3.5E-6[psi^{-1}]
B_w, c_w, μ_w	1.0[rb/stb], 3.E-6[psi^{-1}] 0.32 [cp]
B_o, μ_o (mean of table)	0.98[rb/stb], 1.25 [cp]
Surface density (ρ_o,ρ_w)	56,62.6 [lb/cft]
10 injector control (Uniform)	2010 [rb/day]
20 producer control (Uniform)	1000 [rb/day]
Simulation time	7200 [day]
Interval of rate update	140.0 [day]

All the constraints shown above are included both simulator side and optimization process. For example, the simulator constrains pressure by 6000 psi as secondary constraint and once pressure exceeds during Newton-Raphson process, it switch to bottom hole pressure constraint (will revive as rate constraint by next time step). Then, optimizer checks whether the well is pressure or rate constraint, and update the well rate

only if the well is rate constraint. All the four approaches use same handling of the constraint for the purpose of consistency. The result of recovery factor and NPV is plotted by Figure 5.21, for all the four cases.

The best result is obtained by SLNPV for both recovery factor and NPV. Compared with base uniform injection scenario, SLNPV increased around 30% of recovery factor and NPV. In contrast, the improvement of the EqAT and WAFs is around 15%. Figure 5.22 shows the proposed rate of both injector and producer through 10 years of the forecasting. The large change of the injection and production rate allocation can be observed after 10 to15 years. Also, the algorithm correctly handles individual well constraint. Figs. 5.23-24 show the streamline distributions of uniform injection scenario and optimized scenario provided by SLNPV. It is clear that the density of the streamlines are higher at the top of the reservoir after optimization by SLNPV. This is reasonable result because oil saturation is higher at the top of the reservoir at the initial condition. The optimized scenario sweep less aquifer region but conducting preferential injection and production at high oil saturation.

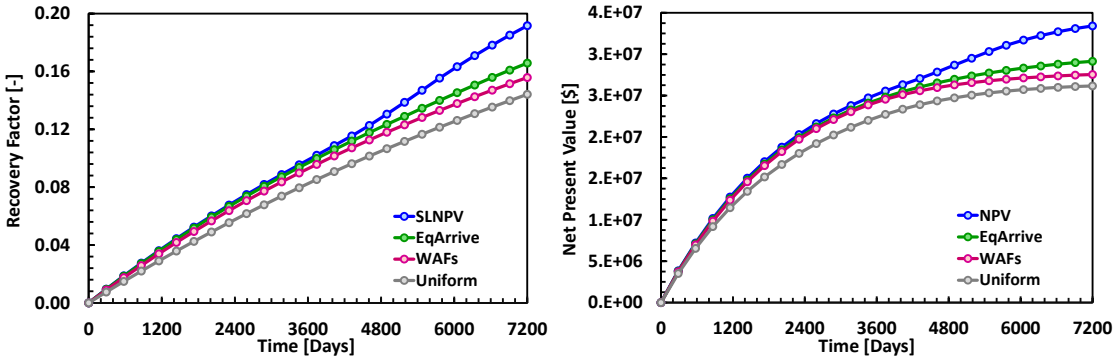

Figure 5.21: The results of recovery factor (left) and NPV (right) by Brugge benchmark example.

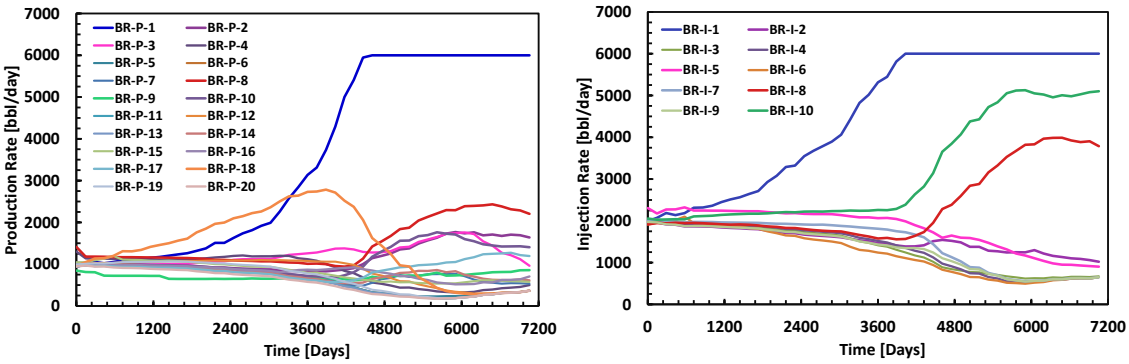

Figure 5.22: The history of the total flow rate of all the injector (left) and producer (right).

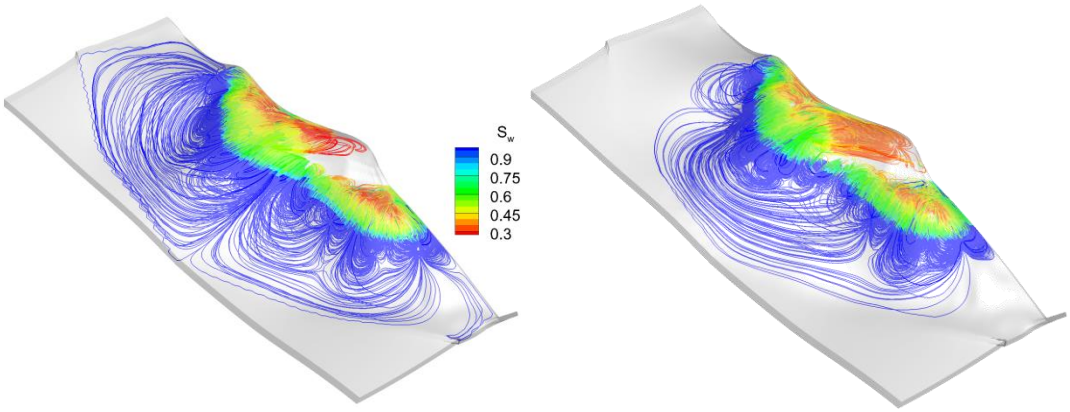

Figure 5.23: The streamline distribution before optimized (left) and after optimized (right), contoured by time-of-flight at 10 year.

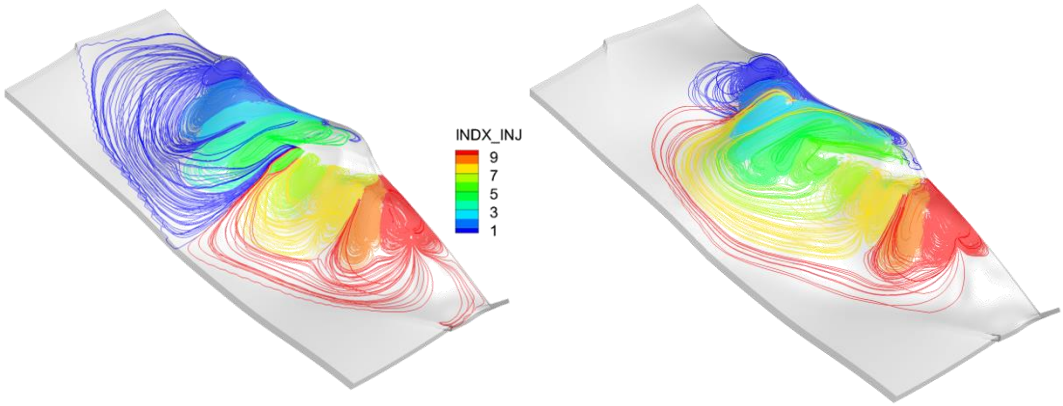

Figure 5.24: The streamline distribution before optimized (left) and after optimized (right), contoured by injector IDs at 10 year.

Optimization Under Uncertainty: Brugge Example

We demonstrate the application of our approach using multiple realizations to address the geologic uncertainty of Brugge benchmark scenario. The Brugge example has 104 realizations of permeability, porosity, net to gross ratio, saturation table and initial oil saturation. The realization contains the model generated by sequential Gaussian simulation, collocated simulation and multipoint geostatistics simulation. Because the streamline simulation and optimization process is quick and it is able to evaluate all the realization in short time. The SLNPV is tested for all the 104 cases in addition to the uniform injection scenario. The result is shown in Figure 5.25.

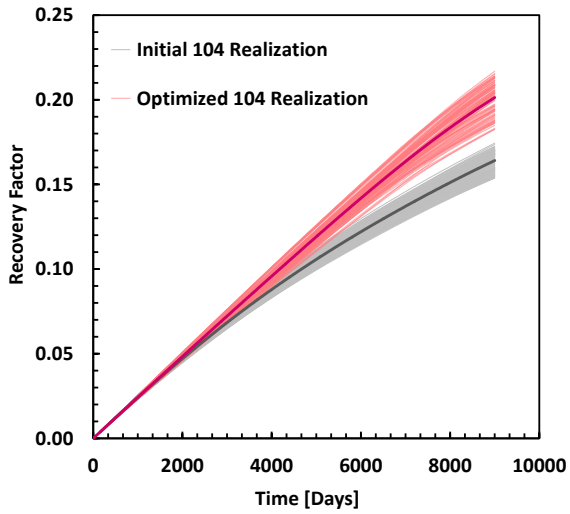

Figure 5.25: The recovery factor of the 104 realizations of the Brugge benchmark case: gray by uniform injection scenario, red by update by SLNPV. The thick line shows the mean of the recovery.

The recovery factor generated from 104 realizations has a wide range of the distribution, starting from pessimistic to optimistic results. Normally, the objective of the

optimization under uncertainty is to provide the well rate to improve mean of the recovery factor or NPV. This study focuses on the evaluation of the distribution of the recovery factor and identifying profitable well by average sense.

The average well rate from multiple realizations can be a representative to capture geologic uncertainty from multiple outcomes, shown in Figs. 5.25-27. This information will help decision making process of the future strategy of the asset. In Brugge example, it is able to identify high and low profitable wells shown in Figs. 5.26-27 under uncertainty of the permeability, porosity and initial oil saturation distribution etc.

The well locations of the high performance wells shown in Figs. 5.26 and 5.27 is shown in Figure 5.28. The 2 injectors (Inj-9 and Inj-1) and 2 producers (Prd-1 andPrd-7) is shown with permeability field, indicating that production well at the top of the reservoir surrounded by fault (P-1) and one before the fault (P-7) should increase the rate to improve NPV. Also high injection rate is preferred to the south and north side (both side of the *x* direction). This result is reasonable considering geological structure and oil-water contact.

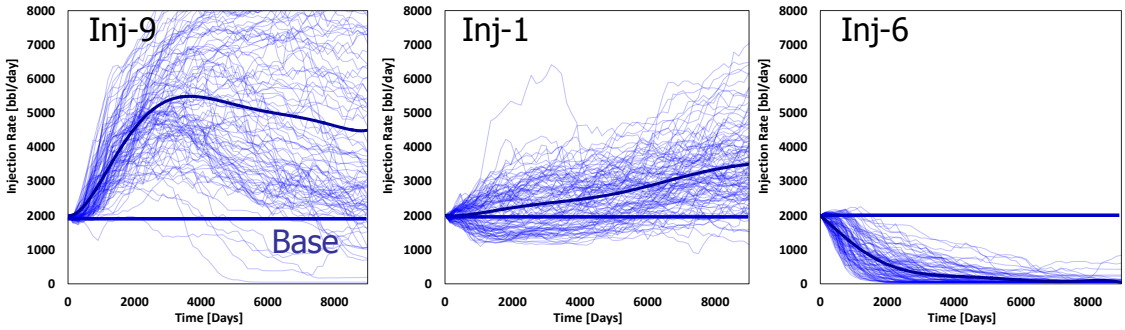

Figure 5.26: The example of proposed injection rate history: High profitable injector (left) profitable injector (middle), low profitable injector (right).

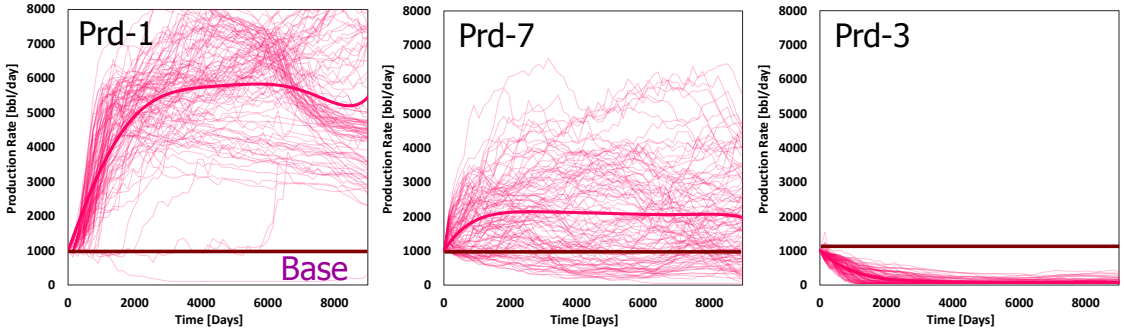

Figure 5.27: The example of proposed production rate history: High profitable producer (left) profitable producer (middle), low profitable producer (right).

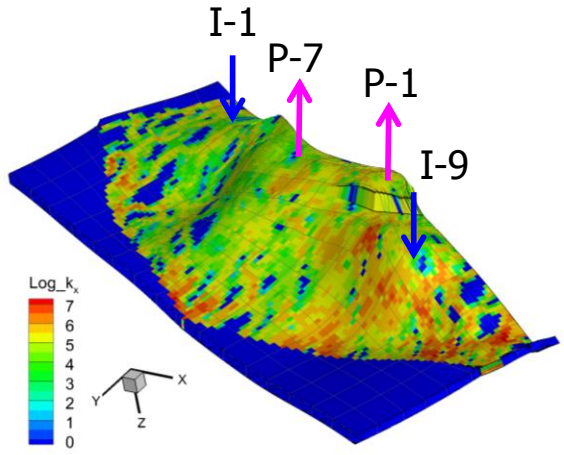

Figure 5.28: The location of the profitable wells: 2 injectors and 2 producers contribute to improve recovery factor and NPV.

5.5 Chapter Conclusions

In this chapter, we included the concept of the NPV optimization by calculating pseudo-NPV along streamlines. The pseudo-NPV uses the phase volume and price in addition to the discount rate using travel time to the producer. By integrating individual streamlines into well pair bundle, the relative contribution is measured for the use in the rate allocation. This cannot be done with conventional finite difference methods

- Streamlines provide compartment of the field where injector-producer pairs sweep the hydrocarbon. Based on this, we proposed a new approach to diagnose NPV of well pair to find the relative contribution to the field NPV.
- The new approach is derivative free and the well rate is updated by a single simulation run.
- The algorithm is flexible to choose different objective function similar to previous streamline work, such as travel-time (Alhuthali, Oyerinde, and Datta-Gupta 2007) or oil production rate (Thiele and Batycky 2003). It is possible to provide a multi objective by giving the selected weight factor, changing it through the simulation time.
- The model is validated by 1D and 2D synthetic piston-like displacement. The proposed approach could obtain possible best scenario under provided constraints.
- The robustness and practical feasibility of proposed approach have been demonstrated using the multiwell example including Brugge benchmark case.

CHAPTER VI

CONCLUSIONS AND RECOMMENDATIONS

6.1 Conclusions

This study summarized the development and application of a comprehensive streamline-based reservoir simulator and improvements in computational efficiency. The improved simulator is demonstrated by CO_2 EOR, history matching and rate allocation optimization problem.

For the streamline-based reservoir simulation, we introduced a new approach to incorporate capillary and gravity effects via orthogonal projection method. It is verified that our proposed formulation is less sensitive to the selection of time step size and improves computational efficiency. The model is extended from 3 phase black oil to multicomponent compositional cases.

The simulator is applied to history matching and rate allocation problem. The previous work of streamline-based history matching and optimization method has been reviewed and limitations are stated. We proposed a new approach to avoid these limitations, and demonstrated that the proposed approach improves the previous approach, for instance, incorporates pressure information, or improves NPV by a new flow diagnostic method.

The summary of the all the works and findings are listed below

- A streamline-based 3D 3-phase multicomponent model was developed with effect of compressibility and gravity by operator splitting technique Implicit and explicit saturation solvers were also implemented and solutions were examined.
- Streamline simulation with iterative IMPES was developed, which is a sequential iterative approach for pressure and saturation calculations. In a tested case of WAG injection scenario, the results of the iterative IMPES method showed significant improvement of the solution.
- A new orthogonal projection method to incorporate capillarity and gravity in streamline-based compositional simulation has been presented. The proposed approach enables us to take a larger time step compared with conventional operator splitting approaches and more importantly, bypasses the need for an anti-diffusive correction in operator splitting treatments.
- We have proposed a novel methodology for streamline-based analytic approaches to compute bottom hole pressure sensitivity with respect to the permeability. Our numerical examples validate the proposed sensitivity calculations for the saturation and pressure drop by comparison with adjoint based sensitivity. The formulation is tested with the Brugge benchmark case with pressure matching. The results showed improvement of the model calibration compared with the conventional water-cut based history matching.
- The streamlines provide compartment of the field where injector-producer pairs sweep the hydrocarbon. Based on this, we proposed a new approach to diagnose NPV of well pairs to find the relative contribution to the overall field NPV. The

algorithm is flexible to choose different objective function such as travel-time or oil production rate. The robustness and practical feasibility of proposed approach have been demonstrated using a multiwell example including the Brugge benchmark case.

6.2 Recommendations, Future Work

There are several recommendations that can be drawn from this study.

- The modeling of the non-neighbor connection is the further work for the application of the Brugge benchmark model. The algorithm needs to be developed to detect which grids have a connection between faults and tracing algorithm needs to be implemented.
- The developed history matching and optimization method needs to be applied for a real field scale model to examine the benefits and the limitations of the method.
- The sensitivity calculation with gas injection scenario showed differences from adjoint gradient methods. The main cause of this difference is due to solution gas effect. The formulation needs to be revisited to take into account more physics.
- Pressure matching will help history matching with a gas injection scenario, especially compositional simulation. To achieve that, the travel time matching of the primary injection component might be appropriate and formulation needs to be constructed from the component tracking method (Orr 2007), or numerical sensitivity can be calculated by differentiating Eq. 3.22. For instance, matching of CO_2 injection can be done by calculating sensitivity by taking the analytical

derivative of total mole fraction, as shown in Figure 6.1. And the sensitivity of the travel time can be calculated by Eq. 6.1.

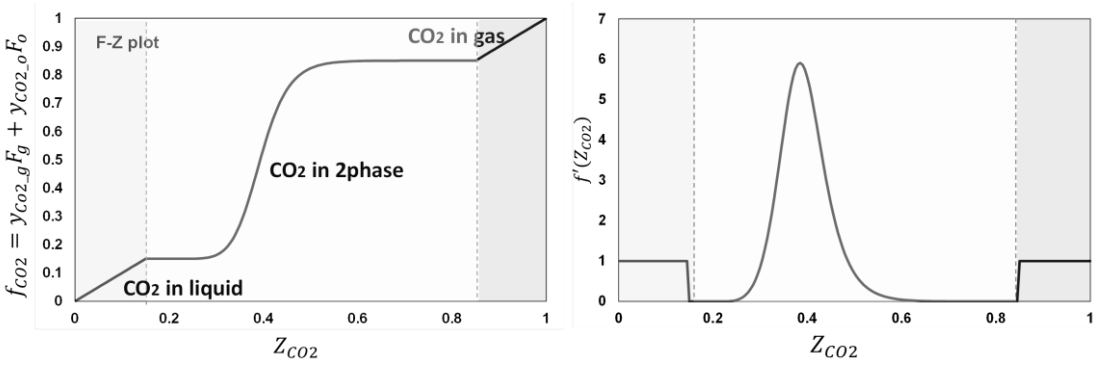

Figure 6.1: The example of the fractional flow of total mole fraction of CO_2 and its derivative.

$$\frac{\partial t_{co2}}{\partial k_i} = \frac{1}{f'(Z_{co2})}\frac{\Delta\tau}{\Delta k_i} \quad \cdots\cdots\cdots\cdots\cdots\cdots\cdots\cdots\cdots\cdots\cdots\cdots\cdots\cdots\cdots\cdots \quad (6.1)$$

$$\frac{\partial r_{sl}}{\partial q_{sl}} = \frac{\partial r_{sl}}{\partial \tau_{sl}}\frac{\partial \tau_{sl}}{\partial q_{sl}}$$

$$\frac{\partial r_{sl}}{\partial \tau_{sl}} = \frac{\partial}{\partial \tau_{sl}}\left(q_{sl}\sum_{node}\frac{\Delta\tau}{\rho_{eff}}\sum_{\alpha=owg}\left(S_\alpha b_\alpha R_\alpha\right)\cdot\left(1+d\right)^{-\tau_{node}f_\alpha'^{-1}/365}\right) \quad \cdots\cdots\cdots\cdots \quad (6.2)$$

$$\approx \sum_{node}\frac{q_{sl}}{\rho_{eff}}\sum_{\alpha=owg}\left(S_\alpha b_\alpha R_\alpha\right)\cdot\left(1+d\right)^{-\tau_{node}f_\alpha'^{-1}/365}$$

- The NPV based optimization works robustly and provided the best solution compared with previous works. However the result is not the best solution for the field case study. The objective function based method might be the appropriate way to find the best solution. For that, formulation is required to calculate the

analytical sensitivity of the NPV. One possible way is to take the derivative of the following NPV equation, with respect to flow rate, for instance

NOMENCLATURE

A	=	area, ft^2
b_α	=	reciprocal of formation volume factor of phase α, $\alpha = o$ or w
b_g	=	reciprocal of gas formation volume factor, *Mscf/bbl*
B_α	=	formation volume factor of phase α, $\alpha = o$ or w, *bbl/STB*
B_g	=	gas formation volume factor, *bbl/scf*
c	=	divergence of the velocity field, $c = \nabla \bullet u_t$
c_α	=	compressibility of phase α, psi^{-1}
c_r	=	rock compressibility, psi^{-1}
c_t	=	total compressibility $c_r+S_oc_o+S_wc_w+S_gc_g$, psi^{-1}
$c_{\mu\alpha}$	=	viscosibility of phase α, psi^{-1}
C	=	coordinates of the corner point nodes, *ft*
d	=	observed or calculated data
D	=	depth, *ft*
e_{ip}	=	efficiency between injector *i* to producer p, dimensionless
F_α	=	convective fractional flow of phase α, $\alpha = o,g,w$ dimensionless
F_i	=	convective fractional flow of component *i*, dimensionless
$f_{\alpha,i}$	=	total fractional flow of phase α or component *i*, dimensionless
f_{ki}	=	fugacity of component i in phase, *psi*
g	=	gravity acceleration constant, ft/day^2
G	=	parameter sensitivity matrix

H_i	=	Henry's constant, *mol/psi/ft*^{3}
I	=	identify matrix
k	=	absolute permeability (tensor), *mD*
$k_{r\alpha}$	=	relative permeability of phase α, dimensionless
k_H	=	well effective isotropic permeability, *ft*^{2}
$K_{i\alpha}$	=	equilibrium ratio of component *i* in phase α
L	=	length, *ft*
m	=	reservoir static property
m_i	=	molar density of component *i*, *lb-mol/ ft*^{3}
m_{wi}	=	molecular weight of component *i*, *g/mol*
n_c	=	number of component, dimensionless
n_w	=	number of well, dimensionless
n_i	=	number of injector, dimensionless
n_p	=	number of producer, dimensionless
n_{wk}	=	number of perforation of single well, dimensionless
n_d	=	number of data observed or calculated, dimensionless
N_c	=	Courant number, dimensionless
N_{sl}	=	number of streamlines traced
p_b	=	bubble-point pressure, *psi*
p_α	=	pressure of phase α, *psi*
p_{bhp}	=	bottom hole pressure, *psi*
p_{cjm}	=	capillary pressure between phase *j* and *m*, *psi*

q_i = molar rate of component *i*, *lb-mol/ day*

$q_{\alpha i}$ = molar rate of component *i* in phase *j* , *lb-mol /day*

Q_α = volumetric rate of phase α at surface condition, *bbl/day*

r_{eq} = effective radius of well, *ft*

r_{ip} = net present value between injector *i* to producer *p*, dollars

r_w = well radius, *ft*

R_s = solution gas/oil ratio, *Mscf/STB*

s = skin factor

S_α = saturation of phase α, dimensionless

t = time, day

T = temperature of the system, *kelvin*

T_{i+-} = intercell transmissibility of grid *i*, *bbl.md.ft^2/cp/psi*

Ψ_{i+-} = intercell transmissibility of geometric part, *bbl.md.ft^2/cp/psi*

u_α = velocity of phase α, *ft/day*

v_α = interstitial velocity of phase α, *ft/day*

V = volume, ft^3

y_{ij} = phase mole fraction of component *i* in phase *j*, dimensionless

z_i = mole fraction of component *i*, dimensionless

z_α = compressibility factor of phase α, $\alpha = L,V$

z = elevation, *ft*

υ_α = phase fraction, $\alpha = L,V,W$, dimensionless

ρ_α	=	molar density of phase α, *lb-mol/ ft*^{3}
$\rho^m{}_\alpha$	=	mass density of phase α, *lb/ ft*^{3}
ϕ	=	porosity, dimensionless
λ_α	=	relative phase mobility of phase , α , *cp*$^{-1}$
μ_α	=	viscosity of phase, *cp*
τ	=	time-of-flight, *day*
Λ_{ip}	=	NPV between injector *i* to producer *p*, dimensionless
Γ	=	capillarity and gravity flux
η	=	net to gross ratio, dimensionless
ψ,χ	=	bi-streamfunctions
ξ	=	streamline trajectory
μ_α	=	viscosity of phase α, *cp*

REFERENCES

Aanonsen, S. I., Nævdal, G., Oliver, D. S., Reynolds, A. C. and Vallès, B. 2009. The Ensemble Kalman Filter in Reservoir Engineering--a Review: *SPE Journal* 14 (03): 393-412, doi: 10.2118/117274-PA.

Agarwal, B. and Blunt, M. J. 2001. Full-Physics, Streamline-Based Method for History Matching Performance Data of a North Sea Field: Paper SPE-66388-MS Presented at the SPE Reservoir Simulation Symposium, 11-14 February, Houston, Texas, U.S.A., doi: 10.2118/66388-MS.

Akamine, K., Tanaka, S. and Arihara, N. 2009. A Streamline-Based 3-Phase Equlibrium Compositional Model with Adaptive Implicit Method: *Journal of Japanese Association of Petoleum Technology*: 74 (3): 211-114.

Al-Harbi, M. H., Cheng, H., He, Z. and Datta-Gupta, A. 2005. Streamline-Based Production Data Integration in Naturally Fractured Reservoirs: *SPE Journal* 10 (04): 426-439, doi: 10.2118/89914-PA.

Alhuthali, A., Oyerinde, A. and Datta-Gupta, A. 2007. Optimal Waterflood Management Using Rate Control: *SPE Journal* 10 (05): 539-551, doi: 10.2118/102478-PA.

Ammer, J. R., Brummert, A. C. and Sams, W. N. 1991. *Miscible Applied Simulation Techniques for Energy Recovery*, Morgantown Energy Technology Center. Morgantown, West Virginia, U.S.A.

Anders, J. L., Rossberg, R. S., Dube, A. T., Engel, H. R. and Andrews, D. 2008. Well Integrity Operations at Prudhoe Bay, Alaska: *SPE Journal* 23 (02): 280-286, doi: 10.2118/102524-PA.

Andrianov, N., Bratvedt, K. and Myasnikov, A. 2007. Implicit 1-D Transport Solvers For a Streamline Simulator For Fractured Reservoirs: Paper SPE-107471-MS Presented at the EUROPEC/EAGE Conference and Exhibition, 11-14 June, London, U.K. doi: 10.2118/107471-MS.

Anterion, F., Eymard, R. and Karcher, B. 1989. Use of Parameter Gradients for Reservoir History Matching: Paper SPE-18433-MS Presented at the SPE Symposium on Reservoir Simulation, 6-8 February, Houston, Texas, U.S.A., doi: 10.2118/18433-MS.

API. 1960. *API Recommended Practice for Core-analysis Procedure*, American Petroleum Institute. Washington D.C., U.S.A.

Atan, S., Kazemi, H. and Caldwell, D. H. 2006. Efficient Parallel Computing Using Multiscale Multimesh Reservoir Simulation: Paper SPE-103101-MS Presented at the SPE Annual Technical Conference and Exhibition, 24-27 September, San Antonio, Texas, U.S.A., doi: 10.2118/103101-MS.

Au, A. D. K., Behie, G. A., Rubin, B. and Vinsome, P. K. 1980. Techniques For Fully Implicit Reservoir Simulation: Paper SPE-9302-MS Presented at the SPE Annual Technical Conference and Exhibition, 21-24 September, Dallas, Texas, U.S.A., doi: 10.2118/9302-MS.

Aziz, K. and Settari, A. 1979. *Petroleum Reservoir Simulation*, Applied Science Publishers Ltd. London, U.K.

Baker, L. E., Pierce, A. C. and Luks, K. D. 1982. Gibbs Energy Analysis of Phase Equilibria: *SPE Journal* 22 (05): 731-742, doi: 10.2118/9806-PA.

Batycky, R. P., Blunt, M. J. and Thiele, M. R. 1997. A 3D Field-Scale Streamline-Based Reservoir Simulator: *SPE Journal* 12 (04): 246-254, doi: 10.2118/36726-PA.

Berenblyum, R. A., Shapiro, A. A., Jessen, K., Stenby, E. H. and Orr, F. M. 2003. Black Oil Streamline Simulator With Capillary Effects: Paper SPE-84037-MS Presented at the SPE Annual Technical Conference and Exhibition, 5-8 October, Denver, Colorado, U.S.A., doi: 10.2118/84037-MS.

Blunt, M. J. and Christie, M. A. 1994. Theory of Viscous Fingering in Two Phase, Three Component Flow: *SPE Journal* 2 (02): 52-60, doi: 10.2118/22613-PA.

Bommer, P. l. M. and Schechter, R. S. 1979. Mathematical Modeling of In-Situ Uranium Leaching: *SPE Journal* 19 (06): 393-400, doi: 10.2118/7533-PA.

Bratvedt, F., Bratvedt, K., Buchholz, C. F., Holden, L., Holden, H. and Risebro, N. H. 1992. A New Front-Tracking Method for Reservoir Simulation: *SPE Journal* 7 (01): 107-116, doi: 10.2118/19805-PA.

Bratvedt, F., Gimse, T., and Tegnander, C. 1996. Streamline Computations For Porous Media Flow Including Gravity: *Transport Porous Media* 25 (1): 63-78, doi: 10.1007/BF00141262.

Brodie, J. A., Jhaveri, B. S., Moulds, T. P. and Mellemstrand Hetland, S. 2012. Review of Gas Injection Projects in BP: Paper SPE-154008-MS Presented at the SPE

Improved Oil Recovery Symposium, 14-18 April, Tulsa, Oklahoma, U.S.A., doi: 10.2118/154008-MS.

Brown, M., Ozkan, E., Raghavan, R. and Kazemi, H. 2011. Practical Solutions for Pressure-Transient Responses of Fractured Horizontal Wells in Unconventional Shale Reservoirs: *SPE Journal* 14 (06): 663-676, doi: 10.2118/125043-PA.

Brun, B., Gosselin, O. and Barker, J. W. 2004. Use of Prior Information in Gradient-Based History Matching: *SPE Journal* 9 (01): 67-78, doi: 10.2118/87680-PA.

Caers, J., Avseth, P. and Mukerji, T. 2001. Geostatistical Integration of Rock Physics, Seismic Amplitudes and Geological Models in North-Sea Turbidite Systems: Paper SPE-71321-MS Presented at the SPE Annual Technical Conference and Exhibition, September, New Orleans, Louisiana, U.S.A., doi: 10.2118/71321-MS.

Cetin, B. C., Burdick, J. W. and Barhen, J. 1993. Global Descent Replaces Gradient Descent to Avoid Local Minima Problem in Learning With Artificial Neural Networks: *Neural Networks* 2: 836-842, doi: 10.1109/ICNN.1993.298667.

Chavent, G., Dupuy, M. and Lemmonier, P. 1975. History Matching by Use of Optimal Theory: *SPE Journal* 15 (01): 74-86, doi: 10.2118/4627-PA.

Chen, Y. and Oliver, D. S. 2012. Ensemble Randomized Maximum Likelihood Method as an Iterative Ensemble Smoother: *Mathematical Geosciences* 44 (1): 1-26, doi: 10.1007/s11004-011-9376-z.

Chen, Y., Oliver, D. S. and Zhang, D. 2010. Efficient Ensemble-Based Closed-Loop Production Optimization: *SPE Journal* 13 (06): 884-892, doi: 10.2118/112873-PA.

Cheng, H., Osako, I., Datta-Gupta, A. and King, M. J. 2006. A Rigorous Compressible Streamline Formulation for Two and Three-Phase Black-Oil Simulation: *SPE Journal* 11 (04): 407-417, doi: 10.2118/96866-PA.

Christie, M. A. and Blunt, M. J. 2001. Tenth SPE Comparative Solution Project: A Comparison of Upscaling Techniques: Paper SPE-66599-MS Presented at the SPE Reservoir Simulation Symposium, 11-14 February, Houston, Texas, U.S.A., doi: 10.2118/66599-MS.

Coats, K. H. 1980. An Equation of State Compositional Model: *SPE Journal* 20 (05): 363-376, doi: 10.2118/8284-PA.

Coats, K. H. 2000. A Note on IMPES and Some IMPES-Based Simulation Models: *SPE Journal* 5 (03): 245-251, doi: 10.2118/65092-PA.

Coats, K. H. 2003a. IMPES Stability: Selection of Stable Timesteps: *SPE Journal* 8 (02): 181-187, doi: 10.2118/84924-PA.

Coats, K. H. 2003b. IMPES Stability: The CFL Limit: *SPE Journal* 8 (03): 291-297, doi: 10.2118/85956-PA.

Computer Modeling Group. 2012. *CMG-WinProp Phase-Behaviour and Fluid Property Program Version 2012*, Computer Modeling Group Ltd. Calgary, Alberta, Canada.

Cordes, C. and Kinzelbach, W. 1992. Continuous Groundwater Velocity Fields and Path Lines in Linear, Bilinear, and Rrilinear Finite Elements: *Water Resources Research* 28 (11): 2903-2911, doi: 10.1029/92WR01686.

Corey, A. T. 1954. The Interrelation Between Gas and Oil Relative Permeabilities: *Producers Monthly* 19: 38-41.

Crane, M., Bratvedt, F., Bratvedt, K., Childs, P. and Olufsen, R. 2000. A Fully Compositional Streamline Simulator: Paper SPE-63156-MS Presented at the SPE Annual Technical Conference and Exhibition, 1-4 October, Dallas, Texas, U.S.A., doi: 10.2118/63156-MS.

Daoud, A. M. and Velasquez, L. V. 2006. 3D Field-Scale Automatic History Matching Using Adjoint Sensitivities and Generalized Travel Time Inversion: Paper SPE-101779-MS Presented at the SPE Annual Technical Conference and Exhibition, 24-27 September, San Antonio, Texas, U.S.A., doi: 10.2118/101779-MS.

Datta-Gupta, A. 2000. Streamline Simulation: A Technology Update (includes associated papers 71204 and 71764): *SPE Journal* 52 (12): 68-84, doi: 10.2118/65604-JPT.

Datta-Gupta, A. and King, M. J. 1995. A Semianalytic Approach to Tracer Flow Modeling in Heterogeneous Permeable Media: *Advances in Water Resources* 18 (1): 9-24, doi: 10.1016/0309-1708(94)00021-V.

Datta-Gupta, A. and King, M. J. 2007. *Streamline Simulation: Theory and Practice*, SPE Textbook series Vol. 11., Society of Petroleum Engineers. Richardson, Texas, U.S.A.

Di Carlo, D. A., Sahni, A., Blunt, M. J. 2000. Three-Phase Relative permeability of Water-Wet, Oil-Wet and Mixed-Wet Sandpacks: *SPE Journal* 5 (01): 82-91, doi: 10.2118/60767-PA.

Di Donato, G., Huang, W. and Blunt, M. J. 2003. Streamline-Based Dual Porosity Simulation of Fractured Reservoirs: Paper SPE-84036-MS Presented at the SPE Annual Technical Conference and Exhibition, 5-8 October, Denver, Colorado, U.S.A., doi: 10.2118/84036-MS.

Dogru, A. H. and Seinfeld, J. H. 1981. Comparison of Sensitivity Coefficient Calculation Methods in Automatic History Matching (includes associated paper 10873): *SPE Journal* 21 (05): 551-557, doi: 10.2118/8251-PA.

Dontchev, A. L. and Rockafellar, R. T. 2010. Newton's Method for Generalized Equations: A Sequential Implicit Function Theorem: *Mathematical Programming* 123 (1): 139-159, doi: 10.1007/s10107-009-0322-5.

Ekkawong, P. 2013. Multiobjective Design and Optimization of Polymer Flood Performance. M.S. Thesis, Texas A&M University, College Station, Texas, U.S.A.

Ertekin, T., Abou-Kassem, J. H. and King, G. R. 2001. *Basic Applied Reservoir Simulation*, SPE Textbook Series Vol. 7., Society of Petroleum Engineers. Richardson, Texas, U.S.A

Fagin, R. G. and Stewart, C. H. 1966. A New Approach to the Two-Dimensional Multiphase Reservoir Simulator: *SPE Journal* 6 (02): 175-182, doi: 10.2118/1188-PA.

Fanchi, J. R. 1987. *Phase Transitions in Black Oil Reservoir Simulation*, Society of Petroleum Engineers. Richardson, Texas, U.S.A.

Fang, D. K. 1986. Solution of Numerical Problems Related to Gas Phase Appearance Or Disappearance in Impes Black Oil Or Pseudo Miscible Simulation: Paper PETSOC-86-37-72 Presented at the Annual Technical Meeting, June 8-11, Calgary, Alberta, Canada. doi: 10.2118/86-37-72.

Ferreira, L. E. A., Descant, F. J., Delshad, M., Pope, G.A. and Sepehrnoori, K. 1992. A Single-well Tracer Test to Estimate Wettability: Paper SPE24136 Presented at the SPE/DOE 8th Symposium on Enhanced Oil Recovery, April 22-24, Calgary, Tulsa, Oklahoma, U.S.A. doi: 10.2118/24136-MS.

Firoozabadi, A. and Pan, H. 2002. Fast and Robust Algorithm for Compositional Modeling: Part I - Stability Analysis Testing: *SPE Journal* 7 (01): 78-89, doi: 10.2118/77299-PA.

Granville, V., Krivanek, M. and Rasson, J. P. 1994. Simulated Annealing: A Proof of Convergence: *Pattern Analysis and Machine Intelligence, IEEE Transactions on* 16 (6): 652-656, doi: 10.1109/34.295910.

Hansen, T. M., Journel, A. G., Tarantola, A. and Mosegaard, K. 2006. Linear Inverse Gaussian Theory and Geostatistics: *Geophysics* 71 (6): 101-111, doi: 10.1190/1.2345195.

Harding, T. J., Radcliffe, N. J. and King, P. R. 1996. Optimisation of Production Strategies using Stochastic Search Methods: Paper SPE-35518-MS Presented at the European 3-D Reservoir Modelling Conference, 16-17 April, Stavanger, Norway. doi: 10.2118/35518-MS.

Hastings, W. K. 1970. Monte Carlo Sampling Methods Using Markov Chains and Their Applications: *Biometrika* 57 (1): 97-109, doi: 10.1093/biomet/57.1.97.

He, Z., Yoon, S. and Datta-Gupta, A. 2002. Streamline-Based Production Data Integration With Gravity and Changing Field Conditions: *SPE Journal* 7 (04): 423-436, doi: 10.2118/81208-PA.

Herning, E. and Zipperer, L. 1936. Calculation of the Viscosity of Technical Gas Mixtures From the Viscosity of the Individual Gases: *Gas-und Wasserfach* 79: 49-54, 69-73.

Higgins, R. V. and Leighton, A. J. 1962. A Computer Method to Calculate Two-Phase Flow in Any Irregularly Bounded Porous Medium: *Journal of Petroleum Technology* 14 (06): 679-683, doi: 10.2118/243-PA.

Higham, N. 2002. *Accuracy and Stability of Numerical Algorithms*. Applied Mathematics, Society for Industrial and Applied Mathematics. Philadelphia, U.S.A.

Hiriart-Urruty, J. B. and Lemarechal, C. 1996. *Convex Analysis and Minimization Algorithms I: Part 1: Fundamentals*. Grundlehren der mathematischen Wissenschaften, Springer. Heidelberg, Berlin.

Hoffman, B. T., Caers, J. K., Wen, X. and Strebelle, S. B. 2006. A Practical Data Integration Approach to History Matching: Application to a Deepwater Reservoir: *SPE Journal* 11 (04): 464-479, doi: 10.2118/95557-PA.

Holden, H., Karlsen, K. H. and Lie, K.-A. 2000. Operator Splitting Methods for Degenerate Convection–diffusion Equations II: Numerical Examples With Emphasis on Reservoir Simulation and Sedimentation: *Computational Geosciences* 4 (4): 287-322, doi: 10.1023/A:1011582819188.

Hurtado, F. S. V., Maliska, C. R. and Slivfa, A.F.C. 2006. A Variable Timestep Strategy for Accelerating The IMPES Solution Algorithm in Reservoir Simulation: Proceeding of the XXVII Iberian Latin American Congress on Computational Methods in Engineering, 3-6 September, Belém, Brazil.

Hustad, O. S. 2002. A Coupled Model for Three-Phase Capillary Pressure and Relative Permeability: *SPE Journal* 7 (01): 59-69, doi: 10.2118/74705-PA.

Iino, A. and Arihara, N. 2007. Use of Streamline Simulation for Waterflood Management in Naturally Fractured Reservoirs: Paper SPE-108685-MS Presented at the International Oil Conference and Exhibition in Mexico, 27-30 June, Veracruz, Mexico. doi: 10.2118/108685-MS.

Iino, A., Arihara, N. and Okatsu, K. 2006. Tracer Flow Simulation for Characterization of Naturally Fractured Reservoirs by Streamline Method: Paper SPE-100183-MS Presented at the SPE Europec/EAGE Annual Conference and Exhibition, 12-15 June, Vienna, Austria. doi: 10.2118/100183-MS.

Ingebrigtsen, L., Bratvedt, F. and Berge, J. 1999. A Streamline Based Approach to Solution of Three-Phase Flow: Paper SPE-51904-MS Presented at the SPE Reservoir Simulation Symposium, 14-17 February, Houston, Texas, U.S.A., doi: 10.2118/51904-MS.

Jessen, K. and Orr, F. M. 2004. Gravity Segregation and Compositional Streamline Simulation: Paper SPE-89448-MS Presented at the SPE/DOE Symposium on Improved Oil Recovery, 17-21 April, Tulsa, Oklahoma, U.S.A., doi: 10.2118/89448-MS.

Jimenez, E., Datta-Gupta, A. and King, M. J. 2010. Full-Field Streamline Tracing in Complex Faulted Systems With Non-Neighbor Connections: *SPE Journal* 15 (01): 7-17, doi: 10.2118/113425-PA.

Juanes, R. and Patzek, T. W. 2004. Analytical Solution to the Riemann Problem of Three-Phase Flow in Porous Media: *Transport in Porous Media* 55 (1): 47-70, doi: 10.1023/B:TIPM.0000007316.43871.1e.

Karlsen, K. H., Lie, K.-A., Natvig, J. R., Nordhaug, H. F. and Dahle, H. K. 2001. Operator Splitting Methods For Systems of Convection-diffusion Equations: Nonlinear Error Mechanisms and Correction Strategies: *Journal of Computational Physics* 173 (2): 636–663, doi: 10.1006/jcph.2001.6901.

Karlsen, K. H. and Espedal M. S. 2007. Numerical Solution of Reservoir Flow Models Based on Large Time Step Operator Splitting Algorithms: *Filtration in Porous Media and Industrial Application* 1734: 9-77, doi: 10.1007/BFb0103975.

King, M. J. and Dunayevsky, V. A. 1989. Why Waterflood Works: A Linearized Stability Analysis: Paper SPE-19648-MS Presented at the SPE Annual Technical Conference and Exhibition, 8-11 October, San Antonio, Texas, U.S.A., doi: 10.2118/19648-MS.

King, M. J., Osako, I. and Datta-Gupta, A. 2005. A Predictor–corrector Formulation for Rigorous Streamline Simulation: *International Journal for Numerical Methods in Fluids* 47 (8-9): 739-758, doi: 10.1002/fld.913.

Nedelcheva, D. K. 2012. A Sequential Implicit Function Theorem For Iterative Solution of Generalized Equation Involving Point-based Approximation: *Rendiconti del Circolo Matematico di Palermo* 61 (1): 65-78, doi: 10.1007/s12215-011-0073-z.

Kozlova, A., Bratvedt, F., Bratvedt, K. and Myasnikov, A. 2006. A Three-Phase Compressible Dual-Porosity Model for Streamline Simulation: Paper SPE-102549-MS Presented at the SPE Annual Technical Conference and Exhibition, 24-27 September, San Antonio, Texas, U.S.A., doi: 10.2118/102549-MS.

Kulkarni, K. N., Datta-Gupta, A. and Vasco, D. W. 2001. A Streamline Approach for Integrating Transient Pressure Data Into High-Resolution Reservoir Models: *SPE Journal* 6 (03): 273-282, doi: 10.2118/74135-PA.

Lake, L. W., Johnston, J. R. and Stegemeier, G. L. 1981. Simulation and Performance Prediction of a Large-Scale Surfactant/Polymer Project: *SPE Journal* 21 (06): 731-739, doi: 10.2118/7471-PA.

Lax, P. and Wendroff, B. 1960. Systems of Conservation Laws: *Communications on Pure and Applied Mathematics* 13 (2): 217-237, doi: 10.1002/cpa.3160130205.

LeBlanc, J. L. and Caudle, B. H. 1971. A Streamline Model for Secondary Recovery: *SPE Journal* 11 (01): 7-12, doi: 10.2118/2865-PA.

Leverett, M. C. 1941. Capillary Behavior in Porous Solids: *Transactions of the AIME* 142 (01): 152-169, doi: 10.2118/941152-G.

Li, R., Reynolds, A. C. and Oliver, D. S. 2003. Sensitivity Coefficients for Three-Phase Flow History Matching: *Journal of Canadian Petroleum Technology* 42 (04): 70-77, doi: 10.2118/03-04-04.

Li, Y. K. and Nghiem, L. X. 1986. Phase Equilibria of Oil, Gas and Water/Brine Mixtures from a Cubic Equation of State and Henry's Law: *Canadian Journal of Chemical Engineering* 64 (3): 486–496, doi: 10.1002/cjce.5450640319

Lohrenz, J., Bray, B. G. and Clark, C. R. 1964. Calculating Viscosities of Reservoir Fluids From Their Compositions: *Journal of Petroleum Technology* 16 (10): 1,171-1,176, doi: 10.2118/915-PA.

Lu, B., Alshaalan, T. and Wheeler, M. F. 2007. Iteratively Coupled Reservoir Simulation for Multiphase Flow: Paper SPE-110114-MS Presented at the SPE Annual Technical Conference and Exhibition, 11-14 November, Anaheim, California, U.S.A., doi: 10.2118/110114-MS.

MacDonald, R. C. 1970. Methods for Numerical Simulation of Water and Gas Coning: *SPE Journal* 10 (04): 425-436, doi: 10.2118/2796-PA.

Milliken, W. J., Emanuel, A. S. and Chakravarty, A. 2001. Applications of 3D Streamline Simulation to Assist History Matching: *SPE Journal* 4 (06): 502-508, doi: 10.2118/74712-PA.

Moreno, J., Kazemi, H. and Gilman, J. R. 2004. Streamline Simulation of Countercurrent Water-Oil and Gas-Oil Flow in Naturally Fractured Dual-Porosity Reservoirs: Paper SPE-89880-MS Presented at the SPE Annual Technical Conference and Exhibition, 26-29 September, Houston, Texas, U.S.A., doi: 10.2118/89880-MS.

Muskat, M. and Wyckoff, R. D. 1934. A Theoretical Analysis of Waterflooding Networks: *Transactions of the AIME* 107 (01): 62-76, doi: 10.2118/934062-G.

Muskat, M. and Wyckoff, R. D. 1937. *The Flow of Homogeneous Fluids Through Porous Media*, McGraw-Hill. New York, U.S.A.

Nghiem, L. X., Fong, D. K. and Aziz, K. 1981. Compositional Modeling With an Equation of State (includes associated papers 10894 and 10903): *SPE Journal* 21 (06): 687-698, doi: 10.2118/9306-PA.

Oliver, D. S., Reynolds, A. C. and Liu, N. 2008. *Inverse Theory for Petroleum Reservoir Characterization and History Matching*, Cambridge University Press, Cambridge, U.K.

Osako, I., Datta-Gupta, A. and King, M.J. 2004. Timestep Selection During Streamline Simulation Through Transverse Flux Correction: *SPE Journal* 9 (04), 450-464. doi: 10.2118/79688-PA.

Orr, F. M. 2007. *Theory of Gas Injection Processes*, Tie-Line Publications. Holte, Denmark.

Paige, C. C. and Saunders, M. A. 1982. LSQR: An Algorithm for Sparse Linear Equations and Sparse Least Squares: *ACM Transactions on Mathematical Software (TOMS)* 8 (1): 43-71, doi: 10.1145/355984.355989.

Park, H. and Datta-Gupta, A. 2011. Reservoir Management Using Streamline-based Flood Efficiency Maps and Application to Rate Optimization: Paper SPE-144580-MS Presented at the SPE Western North American Region Meeting, 7-11 May, Anchorage, Alaska, U.S.A., doi: 10.2118/144580-MS.

Parsons, R. W. 1972. Directional Permeability Effects in Developed and Unconfined Five-Spots: *Journal of Petroleum Technology* 24 (04): 487-494, doi: 10.2118/3368-PA.

Peaceman, D. W. 1983. Interpretation of Well-Block Pressures in Numerical Reservoir Simulation With Nonsquare Grid Blocks and Anisotropic Permeability: *SPE Journal* 23 (03): 531-543, doi: 10.2118/10528-PA.

Peng, D. Y. and Robinson, D. B. 1976. A New Two-Constant Equation of State: *Industrial and Engineering Chemistry* 15 (1): 59-64, doi: 10.1021/i160057a011.

Peters, L., Arts, R., Brouwer, G. and Geel, C. 2009. Results of the Brugge Benchmark Study for Flooding Optimisation and History Matching: Paper SPE-119094-MS Presented at the SPE Reservoir Simulation Symposium, 2-4 February, The Woodlands, Texas, U.S.A., doi: 10.2118/119094-MS.

Pollock, D. W. 1988. Semianalytical Computation of Path Lines for Finite-Difference Models: *Ground Water* 26 (6): 743-750, doi: 10.1111/j.1745-6584.1988.tb00425.x.

Ponting, D. K. 1998. Hybrid Streamline Methods: Paper SPE-39756-MS Presented at the SPE Asia Pacific Conference on Integrated Modelling for Asset Management, 23-24 March, Kuala Lumpur, Malaysia. doi: 10.2118/39756-MS.

Prevost, M., Edwards, M. G. and Blunt, M. J. 2002. Streamline Tracing on Curvilinear Structured and Unstructured Grids: *SPE Journal* 7 (02): 139-148, doi: 10.2118/78663-PA.

Bird, R. B., Stewart, W. E., Lightfoot, E. N. 1960. *Transport Phenomena*, John Wiley & Sons. New York, U.S.A.

Remy, N., Boucher, A. and Wu, J. 2009. *Applied Geostatistics with SGeMS: A User's Guide*, Cambridge University Press. Cambridge, U.K.

Rodriguez, P. G., Segura, M. K. and Moreno, F. J. M. 2003. Streamline Methodology Using an Efficient Operator Splitting for Accurate Modelling of Capillary and Gravity Effects: Paper SPE-79693-MS Presented at the SPE Reservoir Simulation Symposium, 3-5 February, Houston, Texas, U.S.A., doi: 10.2118/79693-MS.

Saad, Y. 2003. *Iterative Methods for Sparse Linear Systems: Second Edition*, Society for Industrial and Applied Mathematics. Philadelphia, U.S.A.

Sahni, I. and Horne, R. N. 2005. Multiresolution Wavelet Analysis for Improved Reservoir Description: *SPE Journal* 9 (01): 53-69, doi: 10.2118/87820-PA.

Schlumberger. 2012a. *MEPO for Petrel User Manual*, Schlumberger. Houston, Texas, U.S.A.

Schlumberger. 2012b. *ECLIPSE Technical Descriptions and Manuals*, Schlumberger. Houston, Texas, U.S.A.

Sen, M. K., Datta-Gupta, A., Stoffa, P. L., Lake, L. W. and Pope, G. A. 1995. Stochastic Reservoir Modeling Using Simulated Annealing and Genetic Algorithm: *SPE Journal* 10 (01): 49-56, doi: 10.2118/24754-PA.

Spall, J. C. 2005. *Introduction to Stochastic Search and Optimization: Estimation, Simulation, and Control*. Wiley Series in Discrete Mathematics and Optimization, John Wiley & Sons. New York, U.S.A.

Stenerud, V. R., Kippe, V., Lie, K.-A. and Datta-Gupta, A. 2008. Adaptive Multiscale Streamline Simulation and Inversion for High-Resolution Geomodels: *SPE Journal* 13 (01): 99-111, doi: 10.2118/106228-PA.

Stenerud, V. R. and Lie, K.-A. 2004. *Streamline-Based History-Matching: A Review*. SINTEF. Oslo, Norway.

Stiel, L. I. and Thodos, G. 1961. The Viscosities of Nonpolar Gases at Normal Pressures: *AIChE Journal* 7 (4): 611–615, doi: 10.1002/aic.690070416.

Stoll, W. M., al Shureqi, H., Finol, J., Al-Harthy, Said A. A., Oyemade, S. N., De Kruijf, A., Van Wunnik, J., Arkesteijn, F., Bouwmeester, R. *et al.* 2011. Alkaline/Surfactant/Polymer Flood: From the Laboratory to the Field: *SPE Journal* 14 (06): 702-712, doi: 10.2118/129164-PA.

Stüben, K. 1999. *Algebraic Multigrid (AMG): An Introduction with Applications; Updated Version of GMD Report No 53, March 1999*. GMD-Report, GMD-Forschungszentrum Informationstechnik. Augustin, Germany.

Suwartadi, E. 2012. Gradient-based Methods for Production Optimization of Oil Reservoirs. Ph.D Thesis, Norwegian University of Science and Technology, TrondhePEim, Norway.

Tanaka, M., Tanaka, S., Arihara, N. and Okabe, H. 2010. Estimation of Fracture Effective Permeability by Upscaling Using Ensemble Kalman Filter: Paper SPE-134396-MS Presented at the SPE Asia Pacific Oil and Gas Conference and Exhibition, 18-20 October, Brisbane, Queensland, Australia. doi: 10.2118/134396-MS.

Tanaka, S., Arihara, N. and Al-Marhoun, M. A. 2010a. Effects of Oil Compressibility on Production Performance of Fractured Reservoirs Evaluated by Streamline Dual-Porosity Simulation: Paper SPE-130397-MS Presented at the SPE EUROPEC/EAGE Annual Conference and Exhibition, 14-17 June, Barcelona, Spain. doi: 10.2118/130397-MS.

Tanaka, S., Arihara, N. and Al-Marhoun, M. A. 2010b. Evaluation of Oil Compressibility Effects on Pressure Maintenance in Naturally Fractured Reservoirs Using Streamline Simulation: Paper SPE-131716-MS Presented at the International Oil and Gas Conference and Exhibition in China, 8-10 June, Beijing, China. doi: 10.2118/131716-MS.

Tanaka, S., Datta-Gupta, A. and King, M. J. 2013. A Novel Approach for Incorporation of Capillarity and Gravity Into Streamline Simulation Using Orthogonal Projection: Paper SPE-163640-MS Presented at the SPE Reservoir Simulation Symposium, 18-20 February, The Woodlands, Texas, U.S.A., doi: 10.2118/163640-MS.

Tanaka, S., Datta-Gupta, A. and King, M. J. 2014. Compositional Streamline Simulation of CO2 Injection Accounting for Gravity and Capillary Effects Using Orthogonal Projection: Paper SPE-169066-MS Presented at the SPE Improved Oil Recovery Symposium, 12-16 April, Tulsa, Oklahoma, U.S.A., doi: 10.2118/169066-MS.

Tang, Y. N. and Chen, Y. M. 1985. *Application of GPST Algorithm To History Matching of Single-Phase Simulator Models*, Society of Petroleum Engineers. Richardson, Texas, U.S.A.

Thiele, M. R. and Batycky, R. P. 2003. Water Injection Optimization Using a Streamline-Based Workflow: Paper SPE-84080-MS Presented at the SPE Annual Technical Conference and Exhibition, 5-8 October, Denver, Colorado, U.S.A., doi: 10.2118/84080-MS.

Timur, A. 1968. An Investigation of Permeability, Porosity, Residual Water Saturation Relationships For Sandstone Reservoirs: *The Log Analyst* 9 (04), doi: SPWLA-1968-vIXn4a2.

Todd, M. R. and Longstaff, W. J. 1972. The Development, Testing, and Application of a Numerical Simulator for Predicting Miscible Flood Performance: *SPE Journal* 24 (7): 874-882, doi: 10.2118/3484-PA

Vasco, D. W., Seongsik, Y. and Datta-Gupta, A. 1999. Integrating Dynamic Data Into High-Resolution Reservoir Models Using Streamline-Based Analytic Sensitivity Coefficients: *SPE Journal* 4 (04): 389-399, doi: 10.2118/59253-PA.

Vega, L., Rojas, D. and Datta-Gupta, A. 2004. Scalability of the Deterministic and Bayesian Approaches to Production-Data Integration Into Reservoir Models: *SPE Journal* 9 (03): 330-338, doi: 10.2118/88961-PA.

Wang, P. 2003. Development and Application of Production Optimization Techniques for Petroleum Fields. Ph.D Thesis, Stanford University, Palo Alto, California, U.S.A.

Wang, Y. and Kovscek, A. R. 2000. Streamline Approach for History Matching Production Data: Paper SPE-58350-PA Presented at the SPE/DOE Improved Oil

Recovery Symposium, 3-5 April, Tulsa, Oklahoma, U.S.A., doi: 10.2118/58350-PA.

Watanabe, S., Han, J., Datta-Gupta, A. and King, M. J. 2013. Streamline-Based Time Lapse Seismic Data Integration Incorporating Pressure and Saturation Effects: Paper SPE-166395-MS Presented at the SPE Annual Technical Conference and Exhibition, 30 September-2 October, New Orleans, Louisiana, U.S.A. doi: 10.2118/166395-MS.

Wen, X., Deutsch, C. V. and Cullick, A. S. 1998. Integrating Pressure and Fractional Flow Data in Reservoir Modeling With Fast Streamline-Based Inverse Method: Paper SPE-48971-MS Presented at the SPE Annual Technical Conference and Exhibition, 27-30 September, New Orleans, Louisiana, U.S.A., doi: 10.2118/48971-MS.

Wu, Z. and Datta-Gupta, A. 2002. Rapid History Matching Using a Generalized Travel-Time Inversion Method: *SPE Journal* 07 (2): 113-122, doi: 10.2118/78359-PA.

Yang, P. H. and Watson, A. T. 1988. Automatic History Matching With Variable-Metric Methods: *SPE Journal* 3 (03): 995-1,001, doi: 10.2118/16977-PA.

Yin, J., Park, H., Datta-Gupta, A. and Choudhary, M. K. 2010. A Hierarchical Streamline-Assisted History Matching Approach With Global and Local Parameter Updates: Paper SPE-132642-MS Presented at the SPE Western Regional Meeting, 27-29 May, Anaheim, California, U.S.A., doi: 10.2118/132642-MS.

Zhang, F., Skjervheim, J. A., Reynolds, A. C. and Oliver, D. S. 2006. Automatic History Matching in a Bayesian Framework, Example Applications: Paper SPE-84461-MS Presented at the SPE Annual Technical Conference and Exhibition, 24-27 September, San Antonio, Texas, U.S.A., doi: 10.2118/84461-MS.

Zhang, Y., King, M. J. and Datta-Gupta, A. 2012. Robust Streamline Tracing Using Inter-cell Fluxes in Locally Refined And Unstructured Grids: *Water Resources Research* 48 (6): W06521, doi: 10.1029/2011WR011396.

APPENDIX A

DISCRITIZATION OF PRESSURE EQUATIONS

A-1 Derivation of Pressure Equation: Compositional Model

In the streamline based simulation, pressure field is first solved on the grids by grid-based finite difference method. A variable is implicit if it is evaluated at the current time level *n+1*, and it is explicit if it is evaluated at the previous time level *n*. Though the study done in main chapter, pressure is always treated as implicit because the final equation has elliptic nature and explicit treatment is not practical to find a solution in terms of computational aspect.

The brief description of the derivation of the pressure equation is made here. In general black oil system, IMPES method is used to find the pressure implicitly while saturation by explicit method. For the compositional model, the primary variable is a component and thus it is sometimes referred as IMPECS (Implicit Pressure Explicit Saturation) method, while we call it IMPES for the consistency with the main document. To find the pressure equation for compositional simulation, we start from governing equation of the general multicomponent model as shown below.

$$\sum_{j=owg}\left[\frac{\partial}{\partial t}\left(\phi y_{ij}\rho_j S_j\right)+\nabla\bullet\left(y_{ij}\rho_j\vec{u}_j\right)-y_{ij}\tilde{q}_{ij}\right]=0 \quad \cdots\cdots\cdots\cdots\cdots\cdots\cdots\cdots \quad (A.1)$$

Here the mole fraction in phase is treated explicitly through pressure time step. This simplifies accumulation term by summing composition in Eq. A.1 and mole fraction y_{ij}

is eliminated. Through this step the molar volume is assumed to be same by between phases. Then the material balance equation of each phase becomes:

$$\frac{\partial}{\partial t}\left(\phi\rho_j S_j\right)+\nabla\bullet\left(\rho_j\vec{u}_j\right)-\tilde{q}_j=0 \quad \cdots\cdots\cdots\cdots\cdots\cdots\cdots\cdots\cdots\cdots \quad \text{(A.2)}$$

The time dependent accumulation term shown in left hand side of the Eq. A.2 is discretized as follows

$$\begin{aligned}\frac{\partial}{\partial t}\left(\phi\sum_{j=ogw}\rho_j S_j\right)&=\frac{\partial p}{\partial t}\frac{\partial}{\partial p}\left(\phi\sum_{j=ogw}\rho_j S_j\right)\\&=\frac{\partial p}{\partial t}\left(\frac{\partial\phi}{\partial p}\sum_{j=ogw}\rho_j S_j+\phi\sum_{j=ogw}\frac{\partial\rho_j}{\partial p}S_j\right) \quad \cdots\cdots\cdots\cdots \quad \text{(A.3)}\\&=\phi\left(\frac{1}{\phi}\frac{\partial\phi}{\partial p}\sum_{j=ogw}\rho_j S_j+\sum_{j=ogw}\frac{\partial\rho_j}{\partial p}S_j\right)\end{aligned}$$

Because phase density is the function of the pressure and velocity is the vector, the divergence term $\nabla\bullet\left(\rho_j\vec{u}_j\right)$ is discretized as follows.

$$\phi\left(\frac{1}{\phi}\frac{\partial\phi}{\partial p}+\frac{1}{\rho_j}\frac{\partial\rho_j}{\partial p}S_j\right)\frac{\partial p}{\partial t}+\frac{1}{\rho_j}\frac{\partial\rho_j}{\partial p}\vec{u}_j\cdot\nabla p_o+\nabla\bullet\vec{u}_j-\frac{1}{\rho_j}\tilde{q}_j=0 \quad \cdots\cdots \quad \text{(A.4)}$$

Furthermore, use the expression of the compressibility of the phase as c_j and the equation becomes

$$\phi\left(c_r+c_j S_j\right)\frac{\partial p}{\partial t}+c_j\vec{u}_j\cdot\nabla p_o+\nabla\bullet\vec{u}_j-Q_j=0 \quad \cdots\cdots\cdots\cdots\cdots\cdots\cdots \quad \text{(A.5)}$$

where c_j is phase compressibility calculated by taking derivative of the molar density with respect to pressure, as $c_j=\frac{1}{p_o}-\frac{1}{z_j}\frac{dz_j}{dp_o}$ for oil and gas phase. The water phase

compressibility is assumed by constant number for the all the application made in the main chapters. By summing above equation by all the phases and we get pressure equation as follows:

$$\phi c_t \frac{\partial p_o}{\partial t} + \nabla p_o \sum_{j=ogw} c_j \vec{u}_j + \nabla \bullet \sum_{j=ogw} \vec{u}_j - \sum_{j=ogw} Q_j = 0 \quad \cdots\cdots\cdots\cdots\cdots\cdots \quad (A.6)$$

Then define the molar rate and volumetric rate of the well. The molar flow rate of component *i* into or out of a well is expressed as follows:

$$\tilde{q}_i = \sum_{\alpha=owg} \tilde{q}_{i\alpha} = \sum_{\alpha=owg} y_{i\alpha} \rho_\alpha Q_\alpha \quad \cdots\cdots\cdots\cdots\cdots\cdots\cdots\cdots\cdots\cdots \quad (A.7)$$

where $\tilde{q}_i$, $\tilde{q}_{ij}$ and Q_α stands for the total molar rate of component *i* and molar rate of component *i* in phase α, volumetric flow rate of phase α, respectively. The production or injection rate at a well is controlled either by the rate itself or with bottom-hole pressure. As the compositions and volumes of the fluid vary as pressure and temperature changes, phase equilibrium calculations are required at both reservoir and surface conditions. The detail of the treatment of the sink/source is described later.

A-2 Derivation of Pressure Equation: Black Oil Model

The derivation of the pressure equation for black oil is same as compositional model, however, the detail is discussed here using black oil volume balance equation. First, based on the black oil system described by (Aziz and Settari 1979)**,** the flow equation of each phase can be formed as

$$\nabla \bullet \left(b_o \vec{u}_o\right) + Q_o = \frac{\partial}{\partial t}\left(\phi\, b_o S_o\right) \quad \cdots\cdots\cdots\cdots \quad \text{(A.8)}$$

$$\nabla \bullet \left(b_w \vec{u}_w\right) + Q_w = \frac{\partial}{\partial t}\left(\phi\, b_w S_w\right) \quad \cdots\cdots\cdots\cdots \quad \text{(A.9)}$$

$$\nabla \bullet \left(b_g \vec{u}_g + R_s b_o \vec{u}_o\right) + Q_g = \frac{\partial}{\partial t}\left(\phi\, b_g S_g + \phi R_s b_o S_o\right) \quad \cdots\cdots\cdots\cdots \quad \text{(A 10)}$$

Define accumulation term and transfer term as R_a and F_a, for a = oil, water and gas phase, respectively. The equation becomes

$$F_\alpha + Q_\alpha = R_\alpha \quad \cdots\cdots\cdots\cdots \quad \text{(A.11)}$$

In the IMPES method, the saturation derivative with respect to time must be eliminated in order to linearize system of pressure equation. Multiplying $(b_g\text{-}b_oR_s)/(b_ob_g)$ to Eq. A.8 and $1/b_w$ to Eq. A.9 and $1/b_g$ to Eq. A.10. Then use the expression of transfer term and accumulation by Eq. A.11 with sink source of the free gas at the surface by $Q_{gg} = Q_g\text{-}R_sQ_o$ and we get

$$\left(\frac{b_g - b_o R_s}{b_o b_g}\right) F_o + \frac{F_w}{b_w} + \frac{F_g}{b_g} + q_o + q_w + q_{gg} = \left(\frac{b_g - b_o R_s}{b_o b_g}\right) R_o + \frac{R_w}{b_w} + \frac{R_g}{b_g} \quad \cdot \quad \text{(A.12)}$$

Rearrange the equation of transfer term by divergence theorem and we have

$$\left(\frac{b_g - b_o R_s}{b_o b_g}\right) F_o + \frac{F_w}{b_w} + \frac{F_g}{b_g} = \nabla \bullet \sum_{\alpha=ogw} \vec{u}_\alpha + \sum_{\alpha=owg} \frac{\vec{u}_\alpha}{b_\alpha} \nabla b_\alpha + \frac{b_o}{b_g} \vec{u}_o \nabla R_s \quad \cdots\cdots \quad \text{(A.13)}$$

Again the formation volume factor is a function of the pressure and thus it is calculated as $\nabla b_\alpha = \frac{1}{b_\alpha} \frac{\partial b_\alpha}{\partial p_o} \frac{\partial p_o}{\partial p_x} = c_\alpha \nabla p_o$. Then the transfer term of the Eq. A.13 is approximated as follows

$$\nabla \bullet \vec{u}_t + \sum_{\alpha=owg} \frac{\vec{u}_\alpha}{b_\alpha} \nabla b_\alpha + \frac{b_o}{b_g} u_o \nabla R_s \approx \nabla \bullet \sum_{\alpha=ogw} \vec{u}_\alpha + \sum_{\alpha=owg} c_\alpha \vec{u}_\alpha \nabla p_o \quad \cdots\cdots\cdots \quad \text{(A.14)}$$

The formulation cannot be applied if the formulation volume factors are calculated by upstream weighting. This approach will not create higher order term. The time derivative is taken from the accumulation term using the chain rule, such that

$$R_o = \phi\, b_o \frac{\partial S_o}{\partial t} + \left(S_o b_o \frac{\partial \phi}{\partial p_o} + S_o \phi \frac{\partial b_o}{\partial p_o} \right) \frac{\partial p_o}{\partial t} \quad \cdots\cdots\cdots\cdots\cdots\cdots\cdots\cdots \quad \text{(A.15)}$$

$$R_w = \phi\, b_w \frac{\partial S_w}{\partial t} + \left(S_w b_w \frac{\partial \phi}{\partial p_o} + S_w \phi \frac{\partial b_w}{\partial p_o} \right) \frac{\partial p_f}{\partial t} \quad \cdots\cdots\cdots\cdots\cdots\cdots\cdots\cdots \quad \text{(A.16)}$$

$$R_g = \phi\, b_g \frac{\partial S_g}{\partial t} + \left(S_g b_g \frac{\partial \phi}{\partial p_o} + S_g \phi \frac{\partial b_g}{\partial p_o} \right) \frac{\partial p_o}{\partial t}$$

$$+ \phi\, b_o R_s \frac{\partial S_o}{\partial t} + \left(b_o S_o R_s \frac{\partial \phi}{\partial p_o} + \phi\, b_o S_o \frac{\partial R_s}{\partial p_o} + S_o \phi\, R_s \frac{\partial b_o}{\partial p_o} \right) \frac{\partial p_o}{\partial t} \quad \cdots\cdots\cdots\cdots \quad \text{(A.17)}$$

The equation can be simplified using a saturation constraint equation, $S_o + S_w + S_g = 1$. The derivative of the phase constraint equation with respect to time becomes as follows.

$$\frac{\partial S_g}{\partial t} = -\frac{\partial S_o}{\partial t} - \frac{\partial S_w}{\partial t} \quad \cdots\cdots \quad \text{(A. 18)}$$

Applying the above equation into Eq. (A.17) to eliminate gas saturation derivative with respect to time,

$$R_g = \left(\phi b_o R_s - \phi b_g\right)\frac{\partial S_o}{\partial t} - \phi\, b_g \frac{\partial S_w}{\partial t} + \left(S_g b_g \frac{\partial \phi}{\partial p_o} + S_g \phi \frac{\partial b_g}{\partial p_o} \right.$$

$$\left. + b_o S_o R_s \frac{\partial \phi}{\partial p_o} + \phi b_o S_o \frac{\partial R_s}{\partial p_o} + S_o \phi R_s \frac{\partial b_o}{\partial p_o} \right)\frac{\partial p_o}{\partial t} \quad \cdots\cdots \quad \text{(A.19)}$$

Repeat same process to the oil and water phase, R_o and R_w. Again multiplying $(b_g - b_o R_s)/(b_o b_g)$ to Eq. A.8 and $1/b_w$ to Eq. A.9 and $1/b_g$ to Eq. A.10 as we did in Eq. A.12 which gives the accumulation term as follows.

$$\left(\frac{b_g - b_o R_s}{b_o b_g}\right)R_o = -\phi\left(\frac{b_o}{b_g}R_s - 1\right)\frac{\partial S_o}{\partial t} + \left(-\frac{b_o}{b_g}S_o R_s \frac{\partial \phi}{\partial p_o} + S_o \frac{\partial \phi}{\partial p_o} - \left(\frac{b_o}{b_g}\phi\, S_o R_s - \phi\, S_o\right)\frac{1}{b_o}\frac{\partial b_o}{\partial p_o}\right)\frac{\partial p_o}{\partial t}$$

$\cdots\cdots$ (A.20)

$$\frac{R_w}{b_w} = \phi\frac{\partial S_w}{\partial t} + \left(S_w \frac{\partial \phi}{\partial p_o} + S_w \phi \frac{1}{b_w}\frac{\partial b_w}{\partial p_o}\right)\frac{\partial p_o}{\partial t} \quad \cdots\cdots \quad \text{(A.21)}$$

$$\frac{R_g}{b_g} = \phi\left(\frac{b_o}{b_g}R_s - 1\right)\frac{\partial S_o}{\partial t} - \phi\frac{\partial S_w}{\partial t} + \left(S_g \frac{\partial \phi}{\partial p_o} + S_g \phi \frac{1}{b_g}\frac{\partial b_g}{\partial p_o}\right)\frac{\partial p_o}{\partial t}$$

$$+\left(\frac{b_o}{b_g}S_o R_s \frac{\partial \phi}{\partial p_o} + S_o \phi \frac{b_o}{b_g}\frac{\partial R_s}{\partial p_o} + S_o \phi\, R_s \frac{b_o}{b_g}\frac{1}{b_o}\frac{\partial b_o}{\partial p_o}\right)\frac{\partial p_o}{\partial t} \cdots\cdots \quad \text{(A.22)}$$

Sum up Eqs. (A.20-22) to eliminate the time derivatives of saturation

$$\left(\frac{b_g - b_o R_s}{b_o b_g}\right) R_o + \frac{R_w}{b_w} + \frac{R_g}{b_g} = \left[\left(S_o + S_w + S_g\right) \frac{\partial \phi}{\partial p_o} + \frac{S_g \phi}{b_g} \frac{\partial b_g}{\partial p_o} \right.$$

$$\left. + \phi S_o \left(\frac{b_o}{b_g} \frac{\partial R_s}{\partial p_o} + \frac{1}{b_o} \frac{\partial b_o}{\partial p_o} \right) + \phi S_w \left(\frac{1}{b_w} \frac{\partial b_w}{\partial p_o} \right) \right] \frac{\partial p_o}{\partial t} \quad \cdots\cdots\cdots\cdots\cdots\cdots\cdots\cdots \quad \text{(A.23)}$$

The right hand side of Eq. A.23 represents fluid and rock compaction with respect to pressure; referred as black oil compressibility, and each phase compressibility can be calculated using formation volume factor by $c_\alpha = \frac{1}{b_\alpha} \frac{\partial b_\alpha}{\partial p_o}$ except oil phase we have

$$c_o = \frac{1}{b_o} \frac{\partial b_o}{\partial p} + \frac{b_o}{b_g} \frac{\partial R_s}{\partial p_o} \quad \cdots\cdots\cdots\cdots\cdots\cdots\cdots\cdots\cdots\cdots\cdots\cdots\cdots\cdots \quad \text{(A.24)}$$

Here again the total compressibility is calculated as $c_t = c_r + S_o c_o + S_w c_w + S_g c_g$. The effect of capillary pressure in the accumulation term is simplified, for instance,

$$\left(\frac{b_g - b_o R_s}{b_o b_g}\right) R_o + \frac{R_w}{b_w} + \frac{R_g}{b_g} = \phi c_t \frac{\partial p}{\partial t} \quad \cdots\cdots\cdots\cdots\cdots\cdots\cdots\cdots\cdots\cdots\cdots\cdots \quad \text{(A.25)}$$

$$\nabla \bullet \vec{u}_t + \sum_{\alpha = owg} c_\alpha \vec{u}_\alpha \nabla p_o + q_o + q_w + q_{gg} - \phi c_t \frac{\partial p_o}{\partial t} = 0 \quad \cdots\cdots\cdots\cdots\cdots\cdots \quad \text{(A.26)}$$

As we see in Eq. A.7 and A.26, the formulation of pressure equation is same as compositional model. During the derivation of the equation, some assumptions are made and discussed here. First, when the gas PVT table is given as measured gas pressure, then the effect of the capillary pressure needs to be included to derivative of the PVT property with respect to pressure. In the model here, we assume that the gradient of the

PVT with respect to pressure is not the significant function of the capillary and then calculate as follows.

$$\frac{\partial b_g}{\partial p_o} = \frac{\partial b_g}{\partial p_o}\left(\frac{\partial p_o}{\partial t} + \frac{\partial p_{cgo}}{\partial t}\right) \approx \frac{\partial b_g}{\partial p_g} \quad \cdots\cdots \quad \text{(A.27)}$$

where p_g is explicitly updated from the oil pressure and gas saturation. It is applicable for water property as well. Other assumptions are made for the treatment of the solution gas in the accumulation term, as follows.

$$\frac{\partial R_s}{\partial t} = \frac{\partial R_s}{\partial p_o}\frac{\partial p_o}{\partial t} \quad \cdots\cdots \quad \text{(A.28)}$$

This equation implies that the change of the R_s is linear regardless through the time step. In most of the gas injection application, this assumption is not accurate because Rs changes nonlinearly as the component of the gas moves. Thus, the standard IMPES approach will generate large material balance error due to this assumption. In order to prevent this problem, we use not Eq. A.26 but use Eq. A.12 where the accumulation term is calculated as an

$$\frac{\partial}{\partial t}\left(\phi\, b_g S_g + \phi R_s b_o S_o\right) = \frac{1}{\Delta t}\left[\left(\phi\, b_g S_g + \phi R_s b_o S_o\right)^{n+1} - \left(\phi\, b_g S_g + \phi R_s b_o S_o\right)^{n}\right] \quad \text{(A.29)}$$

where oil and water phases are evaluated with same discretization. Here $R_s^{n+1} = R_s^n$ in standard IMPES approach and thus this treatment will provide the same result with Eq. A.26 if all the compressibility is constant. In Iterative IMPES method, however, this equation takes care the material balance correctly and improves the results.

A-3 Discretization of Pressure Equation by Space

We then consider the discretization in space $\nabla \bullet \vec{u}_t$ in Eqs. A.7 and A.26. The governing flow equation can be solved with the finite difference approximation with appropriate numerical technique. We introduce numerical discretization by the two point grid-centered approximation method of arbitrary shape of corner point geometry for the convective term. First, we have a corner pint of eight nodes from C1 to C8 shiwn in Figure A.1 as follows.

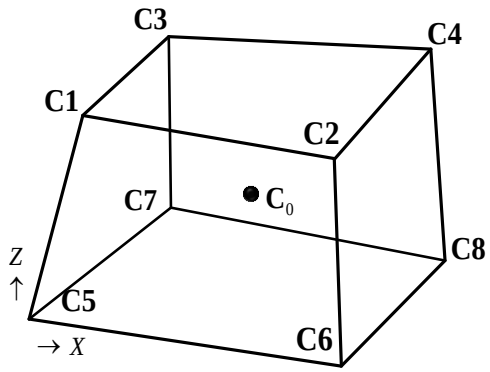

Figure A.1: Corner point geometry and assigned nodes.

Each of the coordinate have coordinate of x,y,z, respectively, and eight corners are described as $\mathbf{C}i=(x_i,y_i,z_i)$ form i=1 to 8. The centroid is shown as $\mathbf{C}_0$ in the above picture. If coordinate information is given as other format, we transform data appropriately, as described in (Schlumberger 2012b)

First, we relate actual coordinate system of $\mathbf{C}i=(x_i,y_i,z_i)$ with unit volume space $\mathbf{U}i=(\alpha_i,\beta_i,\gamma_i)$ as follows.

$$\mathbf{C} = \mathbf{P}_1\alpha + \mathbf{P}_2\beta + \mathbf{P}_3\gamma + \mathbf{P}_4\alpha\beta + \mathbf{P}_5\beta\gamma + \mathbf{P}_6\alpha\gamma + \mathbf{P}_7\alpha\beta\gamma + \mathbf{P}_8 \quad \cdots\cdots\cdots\cdots\cdots \quad (A.30)$$

where,

$$\begin{bmatrix} \mathbf{P}_1 \\ \mathbf{P}_2 \\ \mathbf{P}_3 \\ \mathbf{P}_4 \\ \mathbf{P}_5 \\ \mathbf{P}_6 \\ \mathbf{P}_7 \\ \mathbf{P}_8 \end{bmatrix} = \begin{bmatrix} \mathbf{C}_2 - \mathbf{C}_1 \\ \mathbf{C}_3 - \mathbf{C}_1 \\ \mathbf{C}_5 - \mathbf{C}_1 \\ \mathbf{C}_1 + \mathbf{C}_4 - \mathbf{C}_2 - \mathbf{C}_3 \\ \mathbf{C}_1 + \mathbf{C}_7 - \mathbf{C}_3 - \mathbf{C}_5 \\ \mathbf{C}_1 + \mathbf{C}_6 - \mathbf{C}_2 - \mathbf{C}_5 \\ \mathbf{C}_2 + \mathbf{C}_3 + \mathbf{C}_5 + \mathbf{C}_8 - (\mathbf{C}_1 + \mathbf{C}_4 + \mathbf{C}_6 + \mathbf{C}_7) \\ \mathbf{C}_1 \end{bmatrix} \quad \cdots\cdots\cdots\cdots\cdots\cdots \quad (A.31)$$

Our objective here is to find grid property such as volume, area, distance or the centroid of the grid to descretize corner point geometry from coordinate information. Define grid block volume, V_i, and length between connection, $L_{i,j}$ equivalent connection is, A_{ij} and elevation of the centroid, $z_{i,j}$.as shown in the Figure A.2 shown below.

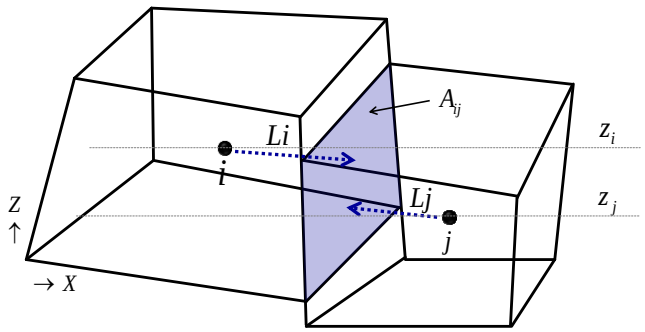

Figure A.2: Corner point grids and properties between grid *i* and *j*.

The bulk volume of the grid block is obtained by integrating unit space of (α,β,γ) from 0 to 1 and relates actual bulk volume by using Jacobian of the point **P**. The Jacobian of the corner point grid is calculated as

$$J(a,\beta,\gamma)=\frac{\partial \mathbf{P}(x,y,z)}{\partial \mathbf{U}(a,\beta,\gamma)}=\begin{vmatrix} \frac{\partial x}{\partial a} & \frac{\partial x}{\partial \beta} & \frac{\partial x}{\partial \gamma} \\ \frac{\partial y}{\partial a} & \frac{\partial y}{\partial \beta} & \frac{\partial y}{\partial \gamma} \\ \frac{\partial z}{\partial a} & \frac{\partial z}{\partial \beta} & \frac{\partial z}{\partial \gamma} \end{vmatrix} \quad \cdots\cdots\cdots\cdots\cdots\cdots\cdots\cdots \quad (A.32)$$

Note that the Jacobian is always set to zero if it is negative. The each component of the Jacobian is also calculated as

$$\begin{aligned} \frac{\partial \mathbf{P}}{\partial \alpha} &= \mathbf{P}_1+\mathbf{P}_4\beta+\mathbf{P}_6\gamma+\mathbf{P}_7\beta\gamma \\ \frac{\partial \mathbf{P}}{\partial \beta} &= \mathbf{P}_2+\mathbf{P}_4\alpha+\mathbf{P}_5\gamma+\mathbf{P}_7\alpha\gamma \\ \frac{\partial \mathbf{P}}{\partial \gamma} &= \mathbf{P}_3+\mathbf{P}_5\beta+\mathbf{P}_6\alpha+\mathbf{P}_7\beta\alpha \end{aligned} \quad \cdots\cdots\cdots\cdots\cdots\cdots\cdots\cdots\cdots\cdots\cdots\cdots\cdots\cdots \quad (A.33)$$

Using partial derivatives of each component in Jacobian, the grid volume is calculated by the triple integral over the unit cube.

$$V_i=\int_{\gamma=0}^{1}\int_{\beta=0}^{1}\int_{\alpha=0}^{1} J(\alpha,\beta,\gamma)d\alpha d\beta d\gamma=\sum_{k=1}^{2}\sum_{j=1}^{2}\sum_{i=1}^{2} w_i w_j w_k J(\alpha_i,\beta_j,\gamma_k) \quad \cdots\cdots\cdots \quad (A.34)$$

The 2-point polynomial integral is used for summing the Jacobian over unit cube. The weight is given as w_1=w_2=0.5, with points by x_1=0.5·(1-1/√3), x_2=0.5 (1+1/√3) for $\alpha_i,\beta_j,\gamma_k$ to calculate the Jacobian, which given in different form

$$J(\alpha_i,\beta_j,\gamma_k)=\frac{\partial x}{\partial \alpha_i}\cdot\left(\frac{\partial y}{\partial \beta_j}\frac{\partial z}{\partial \gamma_k}-\frac{\partial z}{\partial \beta_j}\frac{\partial y}{\partial \gamma_k}\right) \quad \cdots\cdots \quad (A.35)$$
$$-\frac{\partial y}{\partial \alpha_i}\cdot\left(\frac{\partial x}{\partial \beta_j}\frac{\partial z}{\partial \gamma_k}-\frac{\partial z}{\partial \beta}\frac{\partial x}{\partial \gamma_k}\right)-\frac{\partial z}{\partial \alpha_i}\cdot\left(\frac{\partial y}{\partial \beta_j}\frac{\partial y}{\partial \gamma_k}-\frac{\partial y}{\partial \beta_j}\frac{\partial x}{\partial \gamma_k}\right)$$

Next, define contact area A facing towards grid block j as $A_{i+,}$ and area of grid block j facing towards grid block i, A_{j-}. The corner point grid has 6 surface to have connections to neighboring grid. The contact area between i and j is calculated again by

$$A_{i+}=\int_{\gamma=0}^{1}\int_{\beta=0}^{1}J(1,\beta,\gamma)d\beta d\gamma=\sum_{k=1}^{2}\sum_{j=1}^{2}\sum_{i=1}^{2}w_i w_j w_k J(1,\beta_j,\gamma_k) \quad \cdots\cdots\cdots\cdots \quad (A.36)$$

Again the Jacobian is calculated as

$$J(1,\beta_j,\gamma_k)=\frac{\partial y}{\partial \beta_j}\frac{\partial z}{\partial \gamma_k}-\frac{\partial z}{\partial \beta_j}\frac{\partial y}{\partial \gamma_k} \quad \cdots\cdots\cdots\cdots\cdots\cdots\cdots\cdots\cdots\cdots \quad (A.37)$$

The face area can be calculated same manner for A_{i-} by a = 0, with varying β, γ. This calculation is repeated to find contact area of 6 direction.

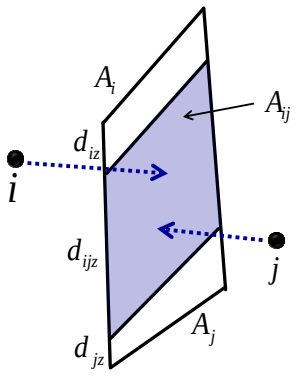

Figure A.3: The evaluation of intersecting area between corner point grids.

The contact area between grids is not necessary to overlap, as shown in Figure A.3. In order to deal with this situation, we calculate equivalent overlap area A_{ij} as

$$\mathbf{D} = \left(\frac{d_{ijl}}{d_{il} + d_{jl} + d_{ijl}} \right); l = z, y \quad \cdots\cdots\cdots\cdots\cdots\cdots\cdots\cdots\cdots\cdots\cdots\cdots \quad \text{(A.38)}$$

$$A_{ij} = \|\mathbf{D}\| \cdot \left(\frac{A_i + A_j}{2} \right) \quad \cdots\cdots\cdots\cdots\cdots\cdots\cdots\cdots\cdots\cdots\cdots\cdots \quad \text{(A.39)}$$

The partial length of the z direction overlaps area d_{ijz} is calculated from coordinate information. This is an example for Figure A.3 and will be repeated for y direction to find **D** in Eq. A.35. The length which does not overlap is shown as d_{il} and **D** approaches to unity as d_{il} decreases.

The last component we need to find is the length and elevation of the grid center. The length between grid is calculated by the length of grid centroid projected to the face center to the connection, shown as L_i and L_j in Figure A.2. To find an example of L_i, we calculate centroid of grid $\mathbf{C}_0$ and face center $\mathbf{C}_{i+}$ as

$$\begin{aligned} \mathbf{C}_0 &= \int_{\gamma=0}^{1} \int_{\beta=0}^{1} \int_{\alpha=0}^{1} \mathbf{P}(x,y,z) J(\alpha,\beta,\gamma) d\alpha d\beta d\gamma \approx \frac{1}{8} \sum_i \mathbf{C}_i \\ \mathbf{C}_{i+} &= \int_{\gamma=0}^{1} \int_{\beta=0}^{1} \int_{\alpha=0}^{1} \mathbf{P}(x,y,z) J(\alpha,\beta,\gamma) d\alpha d\beta d\gamma \approx \frac{1}{4} \left(\mathbf{C}_2 + \mathbf{C}_4 + \mathbf{C}_6 + \mathbf{C}_8 \right) \end{aligned} \quad \cdots \quad \text{(A.40)}$$

The length from centroid to face center is calculated as

$$L_{i+} = \|\mathbf{C}_0 - \mathbf{C}_{i+}\| \quad \cdots\cdots\cdots\cdots\cdots\cdots\cdots\cdots\cdots\cdots\cdots\cdots \quad \text{(A.41)}$$

T length from centroid of j grid toward i grid is calculated as $L_{j-} = \|\mathbf{C}_0\text{-}\mathbf{C}_{j-}\|$ and total length between grid connection is $L = L_{i-}+L_{j-}$. The difference of an elevation between grid is also calculated as

$$\Delta D \approx \frac{1}{8}\left(\sum_l z_{i,l} - \sum_l z_{j,l}\right) \quad \cdots\cdots\cdots\cdots\cdots\cdots\cdots\cdots\cdots\cdots\cdots\cdots\cdots\cdots\cdots\cdots \quad (A.42)$$

Because we have distance from the centroid to each face and cross-sectional area, it is able to define half cell transmissibility such as

$$\mathbf{\Psi}_{half\pm} = c \cdot \eta \cdot \vec{\vec{\mathbf{k}}} \bullet \frac{\mathbf{A}_{\pm} \bullet \mathbf{L}_{i\pm}}{\mathbf{L}_{i\pm} \bullet \mathbf{L}_{i\pm}} \quad \cdots\cdots\cdots\cdots\cdots\cdots\cdots\cdots\cdots\cdots\cdots\cdots\cdots\cdots\cdots\cdots \quad (A.43)$$

where η is net gross ratio and it only effective for horizontal direction (=1.0 for vertical direction). Using half cell transmissibility, define the connection transmissibility as follows

$$\Psi = \Psi_m \left[\Psi_{half,i+}{}^{-1} + \Psi_{half,j-}{}^{-1}\right]^{-1} \quad \cdots\cdots\cdots\cdots\cdots\cdots\cdots\cdots\cdots\cdots\cdots\cdots\cdots\cdots\cdots\cdots \quad (A.44)$$

Then we introduce “Phase transmissibility” as follows. This transmissibility includes properties of the fluid, such as mobility or formation volume factor as

$$T_{o,i\pm 1/2} = \Psi\left(\frac{k_{ro,}}{\mu_o B_o}\right)_{i\pm 1/2} \quad \cdots\cdots\cdots\cdots\cdots\cdots\cdots\cdots\cdots\cdots\cdots\cdots\cdots\cdots\cdots\cdots \quad (A.45)$$

Because the transmissibility is defined between the grid boundaries, we need to define some averaged-boundary parameters which can hold geometric and fluid property information with respect to upstream or downstream information. In this study, any

parameter which is a function of saturation or pressure, such as $k_{r\alpha}$, μ_α ,B_α, is treated using the upstream value.

$$\text{If } \Phi_{\alpha,i} > \Phi_{\alpha,i\pm1} \text{ then, } \left(\frac{k_{r\alpha,}}{\mu_\alpha B_\alpha}\right)_{i\pm1/2} = \left(\frac{k_{r\alpha,}}{\mu_\alpha B_\alpha}\right)_i \quad \cdots\cdots\cdots\cdots\cdots\cdots\cdots \quad (A.46)$$

$$\text{If } \Phi_{\alpha,i} < \Phi_{\alpha,i\pm1} \text{ then, } \left(\frac{k_{r\alpha,}}{\mu_\alpha B_\alpha}\right)_{i\pm1/2} = \left(\frac{k_{r\alpha,}}{\mu_\alpha B_\alpha}\right)_{i\pm1} \quad \cdots\cdots\cdots\cdots\cdots\cdots\cdots \quad (A.47)$$

where α stand for oil, gas and water phase and Φ is for flow potential. The potential of the flow is calculated by pressure and the average density between the interface of the grid block as

$$\Phi_{\alpha,i} = p_{\alpha,i+1} - p_{\alpha,i} - \bar{\rho}_\alpha^m g\Delta D \quad \cdots\cdots\cdots\cdots\cdots\cdots\cdots\cdots\cdots\cdots\cdots\cdots \quad (A.48)$$

The saturation weighted average is used to find average density. The main reason of the use of the saturation weighted density is to prevent overestimation of the density caused by phase appearance or disappearance, especially compositional simulation

$$\bar{\rho}_\alpha^m = \frac{\left(S_\alpha \rho_\alpha^m\right)_i + \left(S_\alpha \rho_\alpha^m\right)_{i+1}}{S_{\alpha,i} + S_{\alpha,i+1} + \varepsilon} \quad \cdots\cdots\cdots\cdots\cdots\cdots\cdots\cdots\cdots\cdots\cdots\cdots \quad (A.49)$$

Applying the above definition into velocity term in Eq. (A.7) or (A.26), we get

$$\nabla \bullet \vec{u}_\alpha = \nabla \bullet \vec{\vec{k}} b_\alpha \lambda_\alpha \left(\nabla p_\alpha - \bar{\rho}_\alpha^m g \nabla D\right) = \sum_{i=cxn} T_{\alpha,i} \Phi_{\alpha,i} \quad \cdots\cdots\cdots\cdots\cdots\cdots \quad (A.50)$$

The equations can be discretized for *y*, *z* direction in the same manner. Thus, the summed-up form of the differential equation for *x,y* and *z* directions of oil phase becomes.

A-4 Treatment of Well

In the reservoir simulation, the idea of well appears as a boundary condition of sink/source terms in governing equation. Usually well pressures (well bottom-hole pressures or tubing head pressure) or injection/production rates (surface rate, reservoir rate or target phase rate) are defined at the center of the grid with a given diameter of the cylinder. In order to describe the relationship of production/injection volumetric rate pressures, we introduce Peaceman's (Peaceman 1983) model as.

$$Q_{\alpha,k} = T^{w}_{\alpha,k}(p_{bhp,k} - p_{o,i}) \quad \cdots\cdots\cdots\cdots\cdots\cdots\cdots\cdots\cdots\cdots\cdots\cdots\cdots\cdots \quad (A.51)$$

Here the capital T stands for well transmissibility, which contains well structure and geometric information with fluid property. Here, the superscript w, stands for well. $p_{bhp,k}$ is a given or calculated bottom hole pressure of arbitrary perforation location k and $p_{o,i}$ is a grid block oil phase pressure contacted at the well. Note that the effect of the capillary pressure is ignored for a sink source term. While the well model is quite complex and still has much room for discussions, we use Peaceman's formula in this model, which is defined by

$$T^{w}_{\alpha,k} = \frac{2\pi\lambda_{\alpha}k_{ew}\Delta z_{k}}{\ln\frac{r_{eq}}{r_{w}} + s} \quad \cdots\cdots\cdots\cdots\cdots\cdots\cdots\cdots\cdots\cdots\cdots\cdots\cdots\cdots \quad (A.52)$$

where r_{eq} stands for equivalent well block radius. To describe grid with non-square and anisotropic case

$$r_{eq} = 0.28\frac{\sqrt{\sqrt{k_y/k_x}(\Delta x)^2 + \sqrt{k_x/k_y}(\Delta y)^2}}{\sqrt[4]{k_y/k_x} + \sqrt[4]{k_x/k_y}} \quad \cdots\cdots\cdots\cdots\cdots\cdots\cdots\cdots \quad (A.53)$$

where the effective isotropic permeability, k_{ew}, is defined as

$$k_{ew} = \sqrt{k_x k_y} \quad \cdots\cdots\cdots\cdots\cdots\cdots\cdots\cdots\cdots\cdots\cdots\cdots\cdots\cdots\cdots\cdots \quad (A.54)$$

Peaceman's model is modified for corner point grid with arbitrary orientation. The Figure A.4 illustrates the possible well trajectory along the corner point geometry.

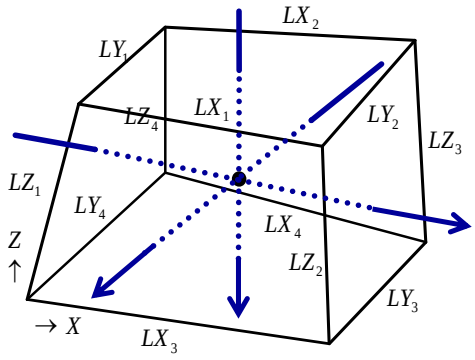

Figure A.4: Three pattern of well penetration direction of well model.

Suppose well is penetrated for x direction, then find penetration length by $\Delta z = \Delta L = (LX_1 + LX_1 + LX_3 + LX_4)/4$. Also, the k_{ew} and r_{eq} is calculated based on the direction of the well. The net gross ratio is considered effective permeability except z-direction, for example, $k_{ew} = \eta\sqrt{k_x k_y}$. For the motilities used in well transmissibility, we use upstream values for production and injection. For injection wells, we use total injected fluid mobility, λ_t. For production wells we use phase motilities in the well grid-block.

$$\lambda_t = \sum_{\alpha=owg} \frac{k_{r\alpha}}{\mu_\alpha} = \sum_{\alpha=owg} \lambda_\alpha \quad \cdots\cdots\cdots\cdots\cdots\cdots\cdots\cdots\cdots\cdots\cdots\cdots\cdots\cdots\cdots\cdots \quad (A.55)$$

The well equation can be calculated for each grid-block in which the well is completed. For a multilayer well, the well pressure can be replaced by the potential for the fluid at the elevation of the grid-centered nodes. Thus, we can calculate well pressure from the defined *k* layer pressure with the inter-well density gradient as

$$\Delta p_k^w = p_{bhp} + \gamma_k^w - p_{o,i} \quad \cdots\cdots\cdots\cdots\cdots\cdots\cdots\cdots\cdots\cdots\cdots\cdots\cdots\cdots\cdots\cdots \quad \text{(A.56)}$$

$$\gamma_k^w = \sum_{i=1}^{k} \frac{\sum_{\alpha=owg} F_{\alpha,i}\rho_{\alpha,i} + \sum_{\alpha=owg} F_{\alpha,i-1}\rho_{\alpha,i-1}}{2} g\left(D_i - D_{i-1}\right) \quad \cdots\cdots\cdots\cdots\cdots\cdots\cdots\cdots \quad \text{(A.57)}$$

where F_α is a phase fractional flow. Summing up the well flow equation with phase and layer, the governing flow equation can be derived as the following form

$$Q_t = \sum_{\alpha=owg} \sum_{k=1}^{n_{wk}} b_{\alpha,i} T_{\alpha,k}^w \Delta p_k^w + \sum_{k=1}^{n_{wk}} R_{s,i} b_{o,i} T_{o,k}^w \Delta p_k^w \quad \cdots\cdots\cdots\cdots\cdots\cdots\cdots\cdots\cdots\cdots \quad \text{(A.58)}$$

This equation becomes the boundary condition used in this model. If we specify the well rate Q_t, the well bottom hole pressure, p_{bhp}, becomes an unknown parameter. Otherwise Q_t becomes unknown if the well pressure is given.

A-5 Well of Multicomponent System

The compositional model use molar rate to define the surface volumetric rate by molar density and a component fraction of phase.

$$\tilde{q}_i = \sum_{\alpha=owg} \tilde{q}_{i\alpha} = \sum_{\alpha=owg} y_{i\alpha}\rho_\alpha Q_\alpha \quad \cdots\cdots\cdots\cdots\cdots\cdots\cdots\cdots\cdots\cdots\cdots\cdots \quad (A.59)$$

where $\tilde{q}_i$, $\tilde{q}_{ij}$ and Q_α stands for the total molar rate of component *i* and molar rate of component *i* in phase α, volumetric flow rate of phase α, respectively. The flow rate in a compositional model depends on pressure and temperature for both surface and reservoir condition. Thus, the flash calculation is conducted reservoir and surface condition to find the volumetric flow rate. The formulation implemented here is referred from (Nghiem, Fong, and Aziz 1981). Their model is modified and introduced below.

Production Well

Molar rate of the production well is calculated as

$$\tilde{q}_{i,k} = \sum_{\alpha=owg} T^w_{\alpha,k}\rho_{\alpha,k}y_{i\alpha,k}\Delta p^w_k \quad \cdots\cdots\cdots\cdots\cdots\cdots\cdots\cdots\cdots\cdots\cdots\cdots \quad (A.60)$$

The total mole fraction of layer *k*, $z_{ik}{}^w$, is calculated as

$$z^w_{i,k} = \frac{\sum_{\alpha=owg}\lambda_{\alpha,k}\rho_{\alpha,k}y_{i\alpha,k}}{\sum_{\alpha=owg}\lambda_{\alpha,k}\rho_{\alpha,k}} \quad \cdots\cdots\cdots\cdots\cdots\cdots\cdots\cdots\cdots\cdots\cdots\cdots \quad (A.61)$$

Using Eq. A.40, interface density is calculated by flash calculation to find the hydrostatic gradient of the well. The volumetric flow rate of perforation *k* at surface condition $Q_{j,k}$ is also calculated as

$$Q_{j,k} = \frac{\varsigma_k \sum_i^{n_c} \tilde{q}_{i,k}}{\rho_{j,k}^{sc}} \quad \cdots\cdots \quad (A.62)$$

where ς_k is phase fraction of layer *k* and $\rho_{j,k}{}^{sc}$ is the molar density of layer k at surface condition. The surface rate is calculated by Eq. A.62 with given bottom hole pressure data. When the well is given by rate constraint it is required to keep the material balance of well as

$$Q_j = \sum_{k=1}^{n_{kw}} Q_{j,k} \quad \cdots\cdots \quad (A.63)$$

Bottom hole pressure is calculated explicitly as

$$p_{bhp} = \frac{Q_j - \sum_{k=1}^{n_{kw}} \left[\frac{\varsigma_k}{\rho_{j,k}^{sc}} \left(\sum_{m=ogw} T_{j,k}^w \rho_{j,k} \right) \left(\gamma_k^w - p_{o,i} \right) \right]}{\sum_{k=1}^{n_{kw}} \left[\frac{\varsigma_k}{\rho_{j,k}^{sc}} \left(\sum_{j=ogw} T_{j,k}^w \rho_{j,k} \right) \right]} \quad \cdots\cdots \quad (A.64)$$

Injection Well

Normally the injection composition and phase flow rate is specified during simulation. The molar rate of layer *k* of the injector is calculated as

$$\tilde{q}_{ij,k} = T_{k,j}^w \rho_{j,k} y_{ij,k}^{in} \Delta p_k^w \quad \cdots\cdots \quad (A.65)$$

where total mobility is used to calculate infectivity as we discussed in black oil model. The hydrostatic pressure drop is calculated same as the producer. The molar rate and volumetric rate are calculated by Eq. A.62 if boundary condition is given by the bottom

hole pressure constraint. The rate constraint needs to keep the material balance of well with given surface rate Q_j as

$$Q_j \rho_j^{sc} = \sum_k^{n_{kw}} \sum_i^{n_c} \tilde{q}_{ij,k} \quad \cdots\cdots\cdots\cdots\cdots\cdots\cdots\cdots\cdots\cdots\cdots\cdots\cdots\cdots\cdots\cdots \quad \text{(A.66)}$$

The bottom hole pressure is calculated explicitly as

$$p_{bhp} = \frac{Q_j \rho_j^{sc} - \sum_{k=1}^{n_{kw}} T_{j,k}^w \rho_{j,k} \left(\gamma_k^w - p_{o,i} \right)}{\sum_{k=1}^{n_{kw}} T_{j,k}^w \rho_{j,k}} \quad \cdots\cdots\cdots\cdots\cdots\cdots\cdots\cdots\cdots\cdots \quad \text{(A.67)}$$

The bottom hole pressure calculated here is not the final solution because we solve equations by implicitly. Instead, it uses as initial guess of the Newton-Raphson process. Thus, the well molar balance equation and pressure is solved implicitly by the Newton-Raphson method as described in the black oil system.

A-6 Construction of the Jacobian Matrix

We now consider the solution of nonlinear set of equations. The pressure equations are discretized in an implicit manner and thus the primary unknown variables of pressure for next time level are distributed on each grid-block. Combining the discretized equations along for individual nodes, a set of matrix-form equations are derived. The matrix form is banded with 7 nonzero variables for the reservoir. We now introduce a method for solving the nonlinear set of equations by Newton's method. This is the known method for finding successively better approximations to the root of a real-valued function. Newton's method can often converge remarkably quickly, especially if the iteration begins sufficiently near the desired root.

The idea of the method is shown in Figure A.5: one starts with an initial guess at x_0 which is reasonably close to the true root, then the function *f(x)* is approximated by its tangent line with appropriate derivative of *f(x)*, and computes the *x*-intercept (x_1) of this tangent line. This *x*-intercept will typically be a better approximation to the function's root than the original guess, and the method can be iterated.

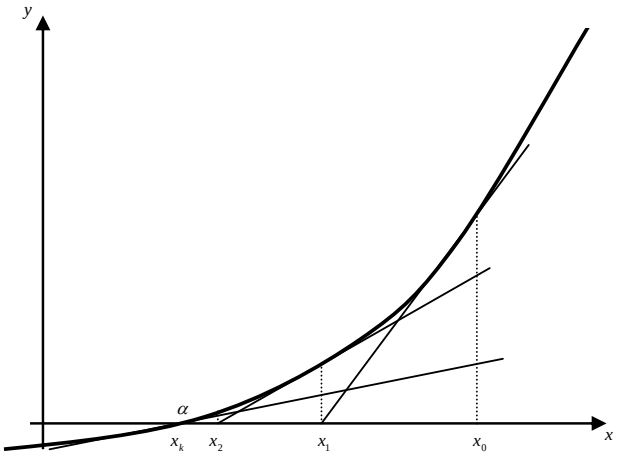

Figure A.5: An illustration of finding root of non-linear equation by Newton's method.

The continuous function, *f(x),* can be expanded in infinitely differentiable form with Taylor series at the initial guess, x_0 as

$$f(x) = f(x_0) + (x - x_0) f'(x_0) + (x - x_0)^2 f''(x_0) + (x - x_0)^3 f'''(x_0) + \cdots + \frac{1}{n!}(x - x_0)^n f^n(x_0) + \cdots$$

…… (A.68)

Considering the difference of *x* and x_0 is small, that is, the guessed point x_0 is located in the neighborhood of the root *x*, we can neglect the term after the second derivative. Thus, the Taylor series can be approximated by the following expression.

$$f(x) \cong f(x_0) + (x - x_0) f'(x_0) \quad \cdots\cdots \quad \text{(A.69)}$$

This approximation form gives

$$x_1 = x_0 - \frac{f(x_0)}{f'(x_0)} \quad \cdots\cdots \quad \text{(A.70)}$$

The above equation can clearly illustrate the idea of Figure A.5. The iterative general form is described as

$$x_{k+1} = x_k - \frac{f(x_k)}{f'(x_k)} \quad \cdots\cdots \quad \text{(A.71)}$$

Eq. A.71 is the called the Newton-Raphson formula for solving nonlinear equations of the form $f(x) = 0$. Thus starting with an initial guess, x_0, we can find the next guess, x_1, by using Eq. A.70. The iterative process is repeated until we find the root that we need.

$$\delta x_{k+1} = x_{k+1} - x_k \quad \cdots\cdots \quad \text{(A.72)}$$

Theoretically, we could execute an infinite number of iterations to find a perfect representation of the root of our function. However, this is not an efficient method for computational aspect, so we give tolerance criteria for convergence. Therefore, we assume that the process has completed accurately when differential of Eq. A.72 becomes less than a tolerance, ε, as.

$$\delta x_{k+1} < \varepsilon \quad \cdots\cdots \quad \text{(A.73)}$$

Regarding the derivative of the function, we can find the following approximation of functions $f'(x_k)$ using Eqs. A.72 and A.73 as

$$f'(x_k) = -\frac{f(x_k)}{\delta x_{k+1}} \quad \cdots\cdots \quad (A.74)$$

Multiplying δx_{k+1}, we get

$$f'(x_k)\delta x_{k+1} = -f(x_k) \quad \cdots\cdots \quad (A.75)$$

Newton's method is used to solve systems of non-linear equations, which amount to finding the roots of continuously differentiable functions. Here we define *F(x)* as a set of nonlinear equations which consist of *n* nonlinear equations with *n* variables.

$$\begin{aligned} F_1(x_1,.....x_n) &= 0 \\ F_2(x_1,.....x_n) &= 0 \\ &\vdots \\ F_n(x_1,.....x_n) &= 0 \end{aligned} \quad \cdots\cdots \quad (A.76)$$

Note that *F(x)* is expressed in vector notation. Applying the mapping definition to Eq. A.76, $x \in \mathbf{R}^n$ and F: $\mathbf{R}^n \rightarrow \mathbf{R}^n$ are defined as

$$F(x) = \begin{bmatrix} F_1(x_1,.....x_n) \\ F_2(x_1,.....x_n) \\ \vdots \\ F_n(x_1,.....x_n) \end{bmatrix} = 0 \quad \cdots\cdots \quad (A.77)$$

In the formulation given above, we have to multiply the derivative of the same size of Jacobian matrix $dF(x)$ to the left for linearization, that works as the approximation function used in Eq. A.75 as $f'(x_n)$.

$$dF(x)^{\nu}\begin{bmatrix}\delta x_1\\ \delta x_2\\ \vdots\\ \delta x_n\end{bmatrix}=-\begin{bmatrix}F_1\\ F_2\\ \vdots\\ F_n\end{bmatrix}^{\nu} \quad \cdots\cdots\cdots\cdots\cdots\cdots\cdots\cdots\cdots\cdots\cdots\cdots\cdots\cdots \quad \text{(A.78)}$$

where the superscript, v, indicates the iterative level. The Jacobian matrix, $dF(x)$, is composed of elements for each grid discretization. An element of an arbitrary block is expressed as follows.

$$dF(x_i)=\frac{\partial F_i}{\partial p_i} \quad \cdots\cdots\cdots\cdots\cdots\cdots\cdots\cdots\cdots\cdots\cdots\cdots\cdots\cdots \quad \text{(A.79)}$$

Also the differential, δx_i, and function F_i can be expressed as

$$\delta x_i=\delta p_{,i} \quad \cdots\cdots\cdots\cdots\cdots\cdots\cdots\cdots\cdots\cdots\cdots\cdots\cdots\cdots \quad \text{(A.80)}$$

$$F_i=F_i \quad \cdots\cdots\cdots\cdots\cdots\cdots\cdots\cdots\cdots\cdots\cdots\cdots\cdots\cdots \quad \text{(A.81)}$$

Considering the above expressions, we can obtain the final matrix form as shown in Eq. A.82 below

$$\begin{pmatrix}
a & b & & e & & f & & & & & & \\
c & a & b & & e & & f & & & & & \\
 & \cdot & \cdot & \cdot & & \cdot & & \cdot & & & & \\
\cdot & & \cdot & \cdot & \cdot & & \cdot & & \cdot & & & \\
 & \cdot & & \cdot & \cdot & \cdot & & \cdot & & \cdot & & \\
g & & d & & c & a & b & & e & & f & \\
 & g & & d & & c & a & b & & e & & f \\
 & & g & & d & & c & a & b & & e & \\
 & & & \cdot & & \cdot & & \cdot & \cdot & \cdot & & \cdot \\
 & & & & \cdot & & \cdot & & \cdot & \cdot & \cdot & \\
 & & & & & \cdot & & \cdot & & \cdot & \cdot & \cdot \\
 & & & & & & g & & d & & c & a & b \\
 & & & & & & & g & & d & & c & a
\end{pmatrix}
\begin{pmatrix}\delta p_{o,1}\\ \\ \\ \delta p_{o,i}\\ \\ \\ p_{o,nxyz}\end{pmatrix}
=-\begin{pmatrix}F_1\\ \\ \\ F_i\\ \\ \\ F_{nxyz}\end{pmatrix}
\quad \cdots\cdots\cdots\cdots \quad \text{(A.82)}$$

where the elements, a through g, expressed in Eq. A.82 are:

$$a = \frac{\partial F_i}{\partial p_{o,i}} \quad \cdots\cdots \quad \text{(A.83)}$$

$$b, c, d, e...x = \frac{\partial F_{b,c,d,e,...x}}{\partial p_{o,b,c,d,e,...x}} \quad \cdots\cdots \quad \text{(A.84)}$$

Define *a* as target *i* block and *b* to *x* as connections from *i* grid to neighbors. In box shape Cartesian grid, *x* is normally *g* (6 connection) by the 5 point scheme. In the 9 point scheme, it might increase up to 36 points by including diagonal connection. Some cases such as geometry with fault might introduce non-neighbor connection, while it is not modeled in this study.

Recall the Jacobian matrix, *dF*, shown in Eq. A.78 as the matrix form. In the matrix, *F* stands for the flow equations, and their derivatives with respect to grid pressure, *p*, were expressed as *a* through *g* for the related blocks. *F* is composed of transfer term, sink/source term, accumulation term. These terms can be expressed as the following formulation.

$$F_{trns,i} = \left(B_o - R_s B_g\right)_i \sum_{j=cxn} T_{o,j} \Phi_{o,j} + B_{w,i} \sum_{j=cxn} T_{w,j} \Phi_{w,j} + B_{g,i} \sum_{j=cxn} T_{g,j} \Phi_{g,j} + R_{s,oup} \sum_{j=cxn} T_{o,j} \Phi_{o,j} \quad \text{(A.85)}$$

$$F_{ss,i} = B_{o,i} Q_{o,i} + B_{w,i} Q_{w,i} + B_{g,i} Q_{gg,i} \quad \cdots\cdots \quad \text{(A.86)}$$

$$F_{acc,i} = -V_{b,i} \eta_i \phi_i^{n+1} c_{t,i}^{n+1} \frac{p_{o,i}^{n+1} - p_{o,i}^{n}}{\Delta t} \quad \cdots\cdots \quad \text{(A.87)}$$

$$F_{acc,i} = -\frac{V_{b,i} \eta_i}{\Delta t} \left[\left(B_o - R_s B_g\right)^{n+1} \left\{ \left(\phi\, b_o S_o\right)^{n+1} - \left(\phi\, b_o S_o\right)^{n} \right\} + B_w^{n+1} \left\{ \left(\phi\, b_o S_o\right)^{n+1} - \left(\phi\, b_o S_o\right)^{n} \right\} \right. \quad \text{(A.88)}$$
$$\left. + B_g^{n+1} \left\{ \left(\phi\, b_g S_g + \phi R_s b_o S_o\right)^{n+1} - \left(\phi\, b_g S_g + \phi R_s b_o S_o\right)^{n} \right\} \right]$$

where Eq. A.87 is used for conventional IMPES or first step if iterative IMPES approach. Iterative IMPES then use Eq. A.88 from the second iteration. First, the derivatives of transfer term with respect to pressure, can be derived as the following equations (Eq.A.85 - Eq. A.88)

$$\frac{\partial F_{trns,i}}{\partial p_{o,i}} = \left(B_o - R_s B_g\right)_i \left[\frac{\partial T_{o,cxn}}{\partial p_{o,i}} \left(p_{o,cxn} - p_{o,i}\right) + T_{o,cxn} + \left(\frac{\partial T_{o,cxn}}{\partial p_{o,i}} \bar{\rho}_o + T_{of,i-1/2} \frac{\partial \bar{\rho}_o}{\partial p_{o,i}} \right) g\left(z_{i,cxn} - z_i\right) \right]$$

$$+ B_{w,i} \left[\frac{\partial T_{w,cxn}}{\partial p_{o,i}} \left(p_{w,cxn} - p_{w,i}\right) + T_{w,cxn} + \left(\frac{\partial T_{w,cxn}}{\partial p_{o,i}} \bar{\rho}_w + T_{w,cxn} \frac{\partial \bar{\rho}_w}{\partial p_{o,i}} \right) g\left(z_{i,cxn} - z_i\right) \right]$$

$$+ B_{g,i} \left[\frac{\partial T_{g,cxn}}{\partial p_{o,i}} \left(p_{g,cxn} - p_{g,i}\right) + T_{g,cxn} + \left(\frac{\partial T_{g,cxn}}{\partial p_{o,cxn}} \bar{\rho}_{g,cxn} + T_{o,cxn} \frac{\partial \bar{\rho}_{g,cxn}}{\partial p_{o,cxn}} \right) g\left(z_{i,cxn} - z_i\right) \right.$$

$$+ \left(\frac{\partial R_{s,oup}}{\partial p_{o,i}} T_{o,cxn} + R_{s,oup} \frac{\partial T_{o,cxn}}{\partial p_{o,i}} \right) \cdot \left(p_{o,cxn} - p_{o,i}\right) + R_{s,oup} T_{o,cxn}$$

$$\left. + \left(\frac{\partial R_{s,oup}}{\partial p_{o,i}} \bar{\rho}_o T_{o,cxn} + R_{s,oup} \frac{\partial \bar{\rho}_o}{\partial p_o} T_{o,cxn} + R_{s,oup} \bar{\rho}_o \frac{\partial T_{o,cxn}}{\partial p_{o,cxn}} \right) g\left(z_{i,cxn} - z_i\right) \right] \quad \cdots\cdots\cdots\cdots$$

$\cdots\cdots\cdots\cdots$ (A.89)

The derivative of phase transmissibility, $T_{pf,\alpha\pm1/2}$, for α = oil, water and gas phase with respect to the oil phase pressure of the current grid block (p_o,$_i$) is calculated as follows.

$$\frac{\partial T_{\alpha,cxn}}{\partial p_{o,i}} = -\Psi_{i,cxn} \lambda_{\alpha,up} b_{\alpha,up} \left(\frac{1}{\mu_{\alpha,up}} \frac{\partial \mu_{\alpha,up}}{\partial p_{o,i}} - c_{\alpha,up} \right) \quad \cdots\cdots\cdots\cdots \quad \text{(A.90)}$$

where $\frac{\partial \mu_{\alpha,up}}{\partial p_{o,i}}$ and $c_{\alpha,up}$ becomes zero if upstream side is not located *i* grid block. In addition, often case the magnitude of $\frac{\partial T_{\alpha,cxn}}{\partial p_{o,i}}$ and $\frac{\partial \overline{\rho}_{\alpha}}{\partial p_{o,i}}$ is relatively small compared with the transmissibility $T_{\alpha,cxn}$ in Eq. A.89, and thus the derivative of the transfer term is simplified as follows.

$$\frac{\partial F_{trns,i}}{\partial p_{o,i}} = \left(B_o - R_s B_g\right)_i T_{o,cxn} + B_{w,i} T_{w,cxn} + B_{g,i} T_{g,cxn} + R_{s,oup} T_{o,cxn} \quad \cdots\cdots\cdots\cdots \quad (A.91)$$

This assumption may not produce rigorous gradient, however, when the formation volume factor and relative permeability is given as tables, this assumption provide much better convergence behavior. This is because $\frac{\partial \mu_{\alpha}}{\partial p_{o,i}}$ becomes discontinuous function between given table nodes and can avoid discontinuous gradient.

The partial differential form of the sink source term with respect to pressure can be calculated as follows.

$$\frac{\partial F_{ss,i}}{\partial p_{o,i}} = \sum_{\alpha=owg} \left[\frac{\partial \left(b_{\alpha,i} T^{w}_{\alpha,k}\right)}{\partial p_{o,i}} \Delta p^{w}_{k} - b_{\alpha,i} T^{w}_{\alpha,i} \right] \quad \cdots\cdots\cdots\cdots\cdots\cdots\cdots\cdots \quad (A.92)$$

The derivative of the producer well transmissibility of *j* phase is calculated as

$$\frac{\partial \left(b_{\alpha,i} T^{w,prd}_{\alpha,k}\right)}{\partial p_{o,i}} = -T^{w,prd}_{\alpha,k} \left(\frac{1}{\mu_{\alpha,i}} \frac{\partial \mu_{\alpha,i}}{\partial p_{o,i}} \right) - T^{w,prd}_{j,k} \left(\frac{1}{B_{\alpha,i}} \frac{\partial B_{\alpha,i}}{\partial p_{o,i}} \right) \quad \cdots\cdots\cdots\cdots \quad (A.93)$$

The injector use total mobility and thus the derivative is calculated as

$$\frac{\partial\left(b_{\alpha,i}T_{\alpha,k}^{w,inj}\right)}{\partial p_{o,i}} = -\frac{T_{j,k}^{w,inj}}{\lambda_{t,i}b_{\alpha,i}}\sum_{\alpha=owg}\left(k_{r\alpha,i}\frac{1}{\mu_{\alpha,i}^{2}}\frac{\partial\mu_{\alpha,i}}{\partial p_{o,i}}\right) - T_{\alpha,k}^{w,inj}\left(\frac{1}{B_{\alpha,i}}\frac{\partial B_{\alpha,i}}{\partial p_{o,i}}\right) \quad \cdots\cdots\cdots\cdots \quad (A.94)$$

Again these derivative also able to simplify to make because of the magnitude of $T_{\alpha,i}^{w}$ is much larger than $\frac{\partial T_{i,j}^{w,prd}}{\partial p_{o,i}}$ in Eq. A.92, and thus the equation is better simplified if the formation volume factor and viscosity are given as table input.

$$\frac{\partial F_{ss,i}}{\partial p_{o,i}} = -\sum_{\alpha=owg} b_{\alpha,i}T_{\alpha,k}^{w} \quad \cdots\cdots\cdots\cdots\cdots\cdots\cdots\cdots\cdots\cdots\cdots\cdots\cdots\cdots\cdots\cdots \quad (A.95)$$

The derivative of the linearized accumulation term is calculated by form as

$$\frac{\partial F_{acc,i}}{\partial p_{o,i}} = \frac{\partial}{\partial p_{o}^{n+1}}\left(-V_b\eta\phi^{n+1}c_t^{n+1}\frac{p_o^{n+1}-p_o^{n}}{\Delta t}\right) \approx -\frac{1}{\Delta t}V_b\eta\phi^{n+1}c_t^{n+1} \quad \cdots\cdots\cdots\cdots \quad (A.96)$$

Accumulation term uses a different equation with the iterative IMPES method because of the inaccuracy of the linearized form. Thus, we directly take a derivative of Eq. A.88 and the result is shown as

$$\frac{\partial F_{acc,i}}{\partial p_{o,i}} = \frac{\partial}{\partial p_{o,i}^{n+1}}\left[\left(\frac{b_g - b_o R_s}{b_o b_g}\right)R_o + \frac{R_w}{b_w} + \frac{R_g}{b_g}\right]$$

$$= \frac{V_b\eta}{\Delta t}\left(\frac{b_g - b_o R_s}{b_o b_g}\right)^{n+1}\left[S_o\left(\phi^{n+1}c_r^{n+1}b_o^{n} + \phi^{n}c_o^{n+1}b_o^{n+1}\right) + R_s S_o\left(\phi^{n+1}c_r^{n+1}b_o^{n} + \phi^{n}c_o^{n+1}b_o^{n+1}\right) + S_o\phi^{n+1}b_\alpha^{n+1}\frac{\partial R_s}{\partial p_o}\right]$$

$$+ B_w^{n+1}\left[S_w\left(\phi^{n+1}c_r^{n+1}b_w^{n} + \phi^{n}c_w^{n+1}b_w^{n+1}\right)\right] + B_g^{n+1}\left[S_g\left(\phi^{n+1}c_r^{n+1}b_g^{n} + \phi^{n}c_g^{n+1}b_g^{n+1}\right)\right] \quad \cdots \quad (A.97)$$

This equation is used after 2nd iteration of iterative IMPES approach. The compressibility of oil is calculated without solution gas term, such as $c_o = \frac{1}{B_o}\frac{\partial B_o}{\partial p_o}$. The

derivative of the accumulation term cannot simplified because the magnitude of the all the component is small.

Diagonal term of the matrix (*a* in Eq. A.84) is calculated using transfer equation, sink/source term and accumulation term as

$$a = -\sum_{j=cxn} \frac{\partial F_{trns,i}}{\partial p_{o,i}} + \frac{\partial F_{ss,i}}{\partial p_{o,i}} + \frac{\partial F_{acc,i}}{\partial p_{o,i}} \quad \cdots\cdots\cdots\cdots\cdots\cdots\cdots\cdots\cdots\cdots\cdots\cdots\cdots\cdots \quad \text{(A.98)}$$

The shape of the Jacobian matrix changes with given boundary condition of the well. When the primary variable of the well constraint is given as bottom hole pressure, the flow rate is calculated using grid block pressure with Peacemen's formula and does not affect the shape of the Jacobian. However, when surface flow rate or reservoir volume is given, additional boundary condition is required to find bottom hole pressure because Peaceman's formula and grid flow equation are both functions of pressure and it becomes under determinant problem. This treatment is not required if the boundary condition is given as mass rate, however, mass rate is not practical for use of the petroleum industry. Because of this reason, the bottom-hole pressure becomes primary variable and additional component is added to Jacobian matrix when boundary condition is given as rate constraint. Here we describe the way to add boundary condition from the given well rate.

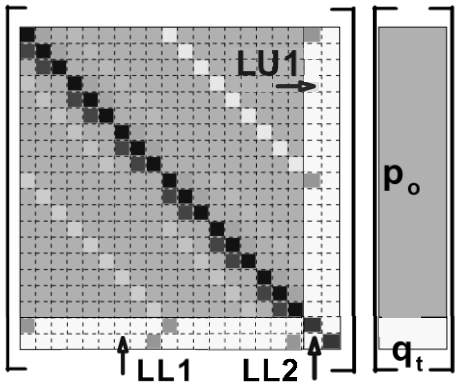

Figure A.6: An example of Jacobian matrix with well boundary conditions.

First, let well mass balance equation Eq. A.99 be R_{ss} as follows. R_{ss} must be zero if bottom-hole pressure satisfies to provide given volumetric flow rate.

$$R_{ss} = -\sum_{\alpha=owg}\sum_{k=1}^{n_{kw}} b_{\alpha,i} T^w_{\alpha,k} \Delta p^w_k + \sum_{k=1}^{n_{kw}} R_{s,i} b_{o,i} T^w_{o,k} \Delta p^w_k - Q_t = 0 \quad \cdots\cdots\cdots\cdots\cdots\cdots \quad (A.99)$$

The following boundary conditions, LU2, LL1, LL2, are added to the left hand side vector. The location of these compoennts are shown in Figure A.6, which is the derivative of the sink/source term with respect to grid and bottom hole pressure.

$$LU2 = \frac{\partial F_{ss}}{\partial p_{bhp}} \approx \sum_{\alpha=owg} \frac{\partial\left(b_{\alpha,i} T^w_{\alpha,k}\right)}{\partial p_{o,i}} \Delta p^w_k - \sum_{k=1}^{n_{kw}} \sum_{\alpha=owg} b_{\alpha,i} T^w_{\alpha,k} - \sum_{\alpha=owg} T^w_{o,k} b_{o,i} R_{s,i} \quad \cdots\cdots\cdots\cdots \quad (A.100)$$

$$\begin{aligned} LL1 = \frac{\partial R_{ss,k}}{\partial p_{o,i}} = & \sum_{\alpha=owg} \frac{\partial\left(b_{\alpha,i} T^w_{\alpha,k}\right)}{\partial p_{o,i}} \Delta p^w_k - \sum_{\alpha=owg} b_{\alpha,i} T^w_{\alpha,k} - T^w_{o,k} b_{o,i} R_{s,i} \\ & + \frac{\partial R_{s,i}}{\partial p_{o,i}} b_{o,i} T^w_{o,k} \Delta p^w_k + R_{s,i} \frac{\partial\left(b_{o,i} T^w_{o,k}\right)}{\partial p_{o,i}} \Delta p^w_k \end{aligned} \quad \cdots\cdots\cdots\cdots \quad (A.101)$$

$$LL2 = \frac{\partial R_{ss}}{\partial p_{bhp}} = \sum_{\alpha=owg}\sum_{k=1}^{n_{kw}} b_{\alpha,i} T^w_{\alpha,k} + \sum_{k=1}^{n_{kw}} R_{s,i} b_{o,i} T^w_{o,k} \quad \cdots\cdots\cdots\cdots\cdots\cdots\cdots\cdots \quad (A.102)$$

The production rate can be a phase target rate such as oil, water, gas or liquid rate. The phase target rate can be constrained by modifying Eq. A.99 as follows.

If the target oil rate is given, mass balance equation of the well becomes

$$R_{ss} + \sum_{\alpha=wg}\sum_{k=1}^{n_{kw}} b_{\alpha,i} T^{w}_{\alpha,k} \Delta p^{w}_{k} + \sum_{k=1}^{n_{kw}} R_{s,i} b_{o,i} T^{w}_{o,k} \Delta p^{w}_{k} + Q_{o}^{target} = 0 \quad \cdots\cdots\cdots\cdots\cdots\cdots \quad \text{(A.103)}$$

The water phase target as

$$R_{ss} + \sum_{\alpha=og}\sum_{k=1}^{n_{kw}} b_{\alpha,i} T^{w}_{\alpha,k} \Delta p^{w}_{k} + \sum_{k=1}^{n_{kw}} R_{s,i} b_{o,i} T^{w}_{o,k} \Delta p^{w}_{k} + Q_{w}^{target} = 0 \quad \cdots\cdots\cdots\cdots\cdots\cdots \quad \text{(A.104)}$$

The liquid phase target (sum of oil and water rate) as

$$R_{ss} + \sum_{k=1}^{n_{kw}} b_{\alpha,i} T^{w}_{g,k} \Delta p^{w}_{k} + \sum_{k=1}^{n_{kw}} R_{s,k} b_{o,i} T^{w}_{o,k} \Delta p^{w}_{k} + Q_{g}^{target} = 0 \quad \cdots\cdots\cdots\cdots\cdots\cdots \quad \text{(A.105)}$$

And gas rate

$$R_{ss} + \sum_{\alpha=ow}\sum_{k=1}^{n_{kw}} b_{\alpha,i} T^{w}_{\alpha,k} \Delta p^{w}_{k} + Q_{g}^{target} = 0 \quad \cdots\cdots\cdots\cdots\cdots\cdots\cdots\cdots \quad \text{(A.106)}$$

The Jacobian matrix for the compositional model is also calculated for multicomponent simulation. Again the pressure equation for multicomponent system is defined by Eq. A.6 as

$$\phi c_t \frac{\partial p_o}{\partial t} + \nabla p_o \sum_{j=ogw} c_j \vec{u}_j + \nabla \bullet \sum_{j=ogw} \vec{u}_j - \sum_{j=ogw} Q_j = 0$$

Then the derivative of the pressure with respect to pressure is calculated in the discretized form. Using transmissibility as shown in black oil model, the

$$F_{trns,i} = -\sum_{j=cxn}\sum_{\alpha=ogw}\left[T_{\alpha,j}\Phi_{\alpha,j} + T_{\alpha,j}\Phi_{\alpha,j}c_{j,up}\Delta p_{\alpha}\right] \quad \cdots\cdots \quad (A.107)$$

$$F_{acc,i} = -V_{b,i}\eta_i\phi_i^{n+1}c_{t,i}^{n+1}\frac{p_{o,i}^{n+1} - p_{o,i}^{n}}{\Delta t} \quad \cdots\cdots \quad (A.108)$$

$$F_{ss,p}^{p} = -\sum_{j=ogw}T_{w,k}\lambda_{j,k}\Delta p_k^{w} \quad \cdots\cdots \quad (A.109)$$

$$F_{ss,p}^{i} = -T_{w,k}\lambda_{t,k}^{n}\Delta p_k^{w} \quad \cdots\cdots \quad (A.110)$$

where Eqs. A.109-110 are producer and injector equations, respectively. The derivative can be taken same manner with black oil model. First, the derivatives of transfer and accumulation with respect to pressure, can be derived as the following equations

$$\begin{aligned}\frac{\partial F_{trns}}{\partial p_{k\pm1}^{n+1}} &= -\sum_{j=ogw}\left[T_{j,up} + \Delta p_{\alpha}c_{j,up}T_{j,up}\right] - \sum_{j=ogw}\left[\left(T_{j,up}\Phi_{\alpha,j}c_{j,up} + T_{j,up}\Phi_{\alpha,j}\right)\right] \\ &\approx -\sum_{j=ogw}T_{j,up}\end{aligned} \quad \cdots\cdots \quad (A.111)$$

$$\frac{\partial F_{acc}}{\partial p_k^{n+1}} = V_{b,i}\eta_i\phi_i^{n+1}c_{t,i}^{n+1}\frac{1}{\Delta t} \quad \cdots\cdots \quad (A.112)$$

Then the derivative of sink/source term is calculated. The derivative of grid block pressure and bottom hole pressure is required for pressure and rate boundary condition. The equation for producer well, we get

$$\frac{\partial F_{ss,p}^{p}}{\partial p_k^{n+1}} = \sum_{j=ogw}\left[T_{w,k}\lambda_{j,k} - T_{w,k}\frac{\partial\lambda_{j,k}^{n+1}}{\partial p_k^{n+1}}\Delta p_k^{w}\right] \quad \cdots\cdots \quad (A.113)$$

$$\frac{\partial F_{ss,p}^{\ p}}{\partial p_{bhp}^{n+1}} = -\sum_{j=o,g,w} T_{w,k}\lambda_{j,k} \quad \cdots\cdots\cdots\cdots\cdots\cdots\cdots\cdots\cdots\cdots\cdots\cdots\cdots\cdots\cdots\cdots \quad \text{(A.114)}$$

For injector well, we get

$$\frac{\partial F_{ss,i}^{\ i}}{\partial p_{k}^{n+1}} = -T_{w,k}\lambda_{t,k} - T_{w,k}\frac{\partial \lambda_{t,k}^{n+1}}{\partial p_{k}^{n+1}}\Delta p_{k}^{w} \quad \cdots\cdots\cdots\cdots\cdots\cdots\cdots\cdots\cdots\cdots\cdots\cdots\cdots\cdots\cdots\cdots \quad \text{(A.115)}$$

$$\frac{\partial F_{ss,i}^{\ i}}{\partial p_{bh}^{n+1}} = -T_{w,k}\lambda_{j} \quad \cdots\cdots\cdots\cdots\cdots\cdots\cdots\cdots\cdots\cdots\cdots\cdots\cdots\cdots\cdots\cdots\cdots\cdots\cdots\cdots\cdots\cdots \quad \text{(A.116)}$$

APPENDIX B

DISCRETIZATION OF THE SATURATION EQUATIONS ALONG STREAMLINE

1D TIME-OF-FLIGHT COORDINATE

B-1 Discretization of the Saturation Equation: Compositional Model

The derivation and discretization of the saturation/composition equation is discussed here. Removing the sink/source term from the governing equation, we get

$$\frac{\partial}{\partial t}\left(\phi \sum_{j=ogw} y_{ij}\rho_j S_j\right) = -\nabla \bullet \left(\sum_{j=ogw} y_{ij}\rho_j \vec{u}_j\right) \quad \cdots\cdots\cdots\cdots\cdots\cdots\cdots\cdots\cdots\cdots \quad \text{(B.1)}$$

Using the total Darcy velocity, Eq. B1 becomes

$$\phi \frac{\partial m_i}{\partial t} = -\nabla \bullet \left(f_i \vec{u}_t\right) - \nabla \bullet \Gamma_i \quad \cdots\cdots\cdots\cdots\cdots\cdots\cdots\cdots\cdots\cdots\cdots\cdots\cdots\cdots \quad \text{(B.2)}$$

where porosity, ϕ, is assumed constant during a pressure time-step, and m_i and F_i are the molar concentration of component *i* (moles of component *i* per unit volume of porous medium) and the molar flux of the each component *i*, respectively. The molar concentration and molar flux are obtained as follows. We use the factional flow "*f*" for the mass flux calculations, and the fractional flow of phase *j* is defined as

$$m_i = \sum_{j=1}^{n_p} y_{ij}\rho_j S_j \quad \cdots\cdots\cdots\cdots\cdots\cdots\cdots\cdots\cdots\cdots\cdots\cdots\cdots\cdots\cdots\cdots\cdots\cdots \quad \text{(B.3)}$$

$$f_i = \sum_{j=1}^{n_p} F_j y_{ij}\rho_j \quad \cdots\cdots\cdots\cdots\cdots\cdots\cdots\cdots\cdots\cdots\cdots\cdots\cdots\cdots\cdots\cdots\cdots\cdots \quad \text{(B.4)}$$

$$F_j = \frac{k_{rj}/\mu_j}{\sum_{k=1}^{n_p}(k_{rk}/\mu_k)} \quad \cdots\cdots\cdots\cdots \quad \text{(B.5)}$$

$$\Gamma_i = \sum_{j=ogw} \vec{\vec{k}} \bullet g y_{ij} \rho_j F_j \sum_{m=ogw, m\neq j} \lambda_m \left(\nabla p_{cjm} + \Delta\rho_{jm}^m g \nabla D\right) \quad \cdots\cdots\cdots\cdots \quad \text{(B.6)}$$

Eq. B.2 is expanded as

$$\phi \frac{\partial m_i}{\partial t} = -\vec{u}_t \cdot \nabla F_i - F_i \nabla \bullet \vec{u}_t - \nabla \bullet \Gamma_i \quad \cdots\cdots\cdots\cdots \quad \text{(B.7)}$$

Here we introduce time-of-flight. Differentiating Eq. B.7 with respect to *s*, we obtain

$$\left|u_t\right| \frac{\partial}{\partial s} \equiv \vec{u}_t \cdot \nabla = \phi \frac{\partial}{\partial \tau} \quad \cdots\cdots\cdots\cdots \quad \text{(B.8)}$$

Eq. B.7 becomes as follows:

$$\frac{\partial m_i}{\partial t} = -\frac{\partial f_i}{\partial \tau} - \frac{f_i}{\phi} \nabla \bullet \vec{u}_t - \frac{1}{\phi} \nabla \bullet \Gamma_i \quad \cdots\cdots\cdots\cdots \quad \text{(B.9)}$$

Then, using operator-splitting technique, the Eq. B.10 is divided into convection and gravity/capillarity flow as

$$\frac{\partial m_i}{\partial t} = -\frac{\partial F_i}{\partial \tau} - \frac{F_i}{\phi} \nabla \bullet \vec{u}_t$$

$$\frac{\partial m_i}{\partial t} = -\frac{1}{\phi} \nabla \bullet \Gamma_i \quad \cdots\cdots\cdots\cdots \quad \text{(B.10)}$$

The Eq. B.1 is solved with an explicit single point upstream method. The discretized form becomes as follows,

$$m_i^{n+1} = m_i^n - \frac{\Delta t_{1D}}{\Delta \tau_i}\left(f_{i+1}^{n+1} - f_i^{n+1}\right) - \frac{f_i}{\phi}\nabla \bullet \vec{u}_t \quad \cdots\cdots\cdots\cdots\cdots\cdots\cdots\cdots \quad \text{(B.11)}$$

where the subscript *s* denotes the node number along a streamline, setting the first node with well block properties. The properties of the well block node are well bottom-hole pressure, injection/production component and saturation.

Using Eq. B.12, the molar concentration of component *i*, m_i^n, is renewed for the next time-step level *n*+1. In the 1D numerical solver, flash calculations are required for each 1D small time step loop in order to update the molar flux and molar concentration. The renewed moles of component *i*, m_i^{n+1}, are used to renew the total mole fraction on streamline, z_i^{n+1}, as follows:

$$z_i^{n+1} = \frac{m_i^{n+1}}{\sum_c^{n_c} m_c^{n+1}} \quad \cdots\cdots\cdots\cdots\cdots\cdots\cdots\cdots\cdots\cdots\cdots\cdots\cdots\cdots\cdots\cdots \quad \text{(B.12)}$$

Conducting flash calculations with the renewed total mole fraction z_i^{n+1} and pressure p^{n+1}, component mole fractions of each phase, $y_{i,o}^{n+1}$, $y_{i,g}^{n+1}$, phase mole fractions, L^{n+1}, V^{n+1}, and phase mole densities, ρ_o^{n+1}, ρ_g^{n+1} are calculated. Then, the phase volumes are calculated as follows.

$$\begin{aligned} V_o &= \frac{L^{n+1}}{\rho_o^{n+1}} \\ V_g &= \frac{V^{n+1}}{\rho_g^{n+1}} \\ V_w &= W^n \times (1 + c_w \Delta p + 0.5 c_w{}^2 \Delta p^2), \Delta p = p_w - p_{ref} \end{aligned} \quad \cdots\cdots\cdots\cdots\cdots\cdots \quad \text{(B.13)}$$

where W^n denotes the water phase mole-fraction. In FrontSim the water phase is given as a "phase", and also compressibility and formation volume factors are given by PVT table. Hence, the volume of the water phase is calculated with the given compressibility data as shown above.

Using the phase volumes, phase saturations, S_o^{n+1}, S_g^{n+1}, S_w^{n+1}, are obtained as in Eq.B.14. Saturation and densities are updated to recalculate fractional flow for 1D small time-step loop. At the last step of the 1D solver, the solutions such as the mole fraction, saturation and volume information are then pulled back from the 1D grid onto the global grid.

$$\begin{aligned} S_o^{n+1} &= \frac{V_o}{(V_o + V_s) \times (1.0 - V_w)} \\ S_g^{n+1} &= \frac{V_g}{(V_o + V_g) \times (1.0 - V_w)} \\ S_w^{n+1} &= V_w \end{aligned} \quad \cdots\cdots\cdots\cdots\cdots\cdots\cdots\cdots\cdots\cdots\cdots\cdots\cdots\cdots \quad \text{(B.14)}$$

The mapping and mapping-back processes have important roles for streamline-based simulation. The re-flash calculations should be done on the global grid in order to minimize the molar material balance error. In this model, we conduct re-flash calculations not on the global grid but on the streamline to which the parameters were mapped from the global grid.

B-2 Discretization of Saturation Equation: Black Oil Model

The saturation equations of reservoir domain can be derived from the governing equation. Ignoring the sink/source term from Eqs. A.8-10, we get

$$\nabla \bullet \left(b_o \vec{u}_o\right) + \frac{\partial}{\partial t}\left(b_o \phi S_o\right) = 0 \quad \cdots\cdots\cdots\cdots \quad \text{(B.15)}$$

$$\nabla \bullet \left(b_w \vec{u}_w\right) + \frac{\partial}{\partial t}\left(b_w \phi S_w\right) = 0 \quad \cdots\cdots\cdots\cdots \quad \text{(B.16)}$$

$$\nabla \bullet \left(b_g \vec{u}_g + b_o R_s \vec{u}_o\right) + \frac{\partial}{\partial t}\left(b_g \phi S_g + b_o \phi R_s S_o\right) = 0 \quad \cdots\cdots\cdots\cdots \quad \text{(B.17)}$$

Using the total Darcy velocity and Eqs. B.15-17 with gravity and capillary effect by $\Gamma_\alpha = \vec{\vec{k}} \bullet F_\alpha \sum_{\alpha=ogw,\alpha\neq j} \lambda_m (\nabla p_{c\alpha m} + \Delta\rho_{\alpha m}) g \nabla D$, the saturation equation becomes as follows

$$\phi \frac{\partial}{\partial t}\left(b_o S_o\right) + \nabla \bullet \left(b_o F_o \vec{u}_t\right) + \nabla \bullet \left(b_o \Gamma_o\right) = 0 \quad \cdots\cdots\cdots\cdots \quad \text{(B.18)}$$

$$\phi \frac{\partial}{\partial t}\left(b_w S_w\right) + \nabla \bullet \left(b_w F_w \vec{u}_t\right) + \nabla \bullet \left(b_w \Gamma_w\right) = 0 \quad \cdots\cdots\cdots\cdots \quad \text{(B.19)}$$

$$\phi \frac{\partial}{\partial t}\left(b_g S_g + b_o R_s S_o\right) + \nabla \bullet \left(b_g F_g \vec{u}_t + b_o R_s F_o \vec{u}_t\right) + \nabla \bullet \left(b_g \Gamma_g + b_o R_s \Gamma_o\right) = 0 \quad \cdots\cdots \quad \text{(B.20)}$$

where porosity, ϕ, is assumed to be constant. The transverse flux vectors Γ_α are

$$\Gamma_o = \vec{\vec{k}} \bullet F_o \left[(p_o - p_w) + (p_o - p_g) + \left\{ \lambda_w (\rho_o - \rho_w) + \lambda_g (\rho_o - \rho_g) \right\} g \nabla D \right] \quad \cdots\cdots \quad \text{(B.21)}$$

$$\Gamma_w = \vec{\vec{k}} \bullet F_o \left[(p_w - p_o) + (p_w - p_g) + \left\{ \lambda_o (\rho_w - \rho_o) + \lambda_g (\rho_w - \rho_g) \right\} g \nabla D \right] \quad \cdots\cdots \quad \text{(B.22)}$$

$$\Gamma_g = \vec{\vec{k}} \bullet F_o \left[(p_g - p_o) + (p_g - p_w) + \left\{ \lambda_o (\rho_g - \rho_o) + \lambda_w (\rho_g - \rho_w) \right\} g \nabla D \right] \quad \cdots\cdots \quad \text{(B.23)}$$

The Eqs. 3.18-20 can be expanded by extracting divergence as:

$$\phi\frac{\partial}{\partial t}\left(b_o S_o\right)+b_o F_o\nabla\bullet\vec{u}_t+\vec{u}_t\cdot\nabla\left(b_o F_o\right)+\nabla\bullet\left(b_o\Gamma_o\right)=0 \quad \cdots\cdots \quad \text{(B.24)}$$

$$\phi\frac{\partial}{\partial t}\left(b_w S_w\right)+b_w F_w\nabla\bullet\vec{u}_t+\vec{u}_t\cdot\nabla\left(b_w F_w\right)+\nabla\bullet\left(b_w\Gamma_w\right)=0 \quad \cdots\cdots \quad \text{(B.25)}$$

$$\phi\frac{\partial}{\partial t}\left(b_g S_g+b_o R_s S_o\right)+\left(b_g F_g+b_o R_s F\right)\nabla\bullet\vec{u}_t+\vec{u}_t\cdot\nabla\left(b_g F_g+b_o R_s F_o\right)+\nabla\bullet\left(b_g\Gamma_g\right)+\nabla\bullet\left(b_o R_s\Gamma_o\right)=0$$

$$\cdots\cdots \quad \text{(B.26)}$$

Then, we transform the saturation equations by introducing the time-of-flight coordinate. Introducing the time-of-flight into Eqs. B.24-26 and the following equations can be yielded dividing by porosity, ϕ , as:

$$\frac{\partial}{\partial t}\left(b_o S_o\right)+\frac{\partial}{\partial\tau}\left(b_o F_o\right)+\frac{b_o}{\phi}\left(F_o\nabla\bullet\vec{u}_t\right)+\frac{1}{\phi}\nabla\bullet\left(b_o\Gamma_o\right)=0 \quad \cdots\cdots \quad \text{(B.27)}$$

$$\frac{\partial}{\partial t}\left(b_w S_w\right)+\frac{\partial}{\partial\tau}\left(b_w F_w\right)+\frac{b_w}{\phi}\left(F_w\nabla\bullet\vec{u}_t\right)+\frac{1}{\phi}\vec{\nabla}\bullet\left(b_w\Gamma_w\right)=0 \quad \cdots\cdots \quad \text{(B.28)}$$

$$\frac{\partial}{\partial t}\left(b_g S_g+b_o R_s S_o\right)+\frac{\partial}{\partial\tau}\left(b_g F_g+b_o R_s F_o\right)+\frac{1}{\phi}\nabla\bullet\vec{u}_t\left(b_g f_g+b_o R_s f_o\right)+\frac{1}{\phi}\nabla\bullet\left(b_g\Gamma_g+b_o R_s\Gamma_o\right)=0$$

$$\cdots\cdots \quad \text{(B.29)}$$

Because streamline trajectory follows total velocity field while gravity and capillary follow phase velocity, we split equation by convective flow and capillary/gravity flow by operator splitting method. The convective equation follows time-of-flight coordinate as

$$\frac{\partial}{\partial t}\left(b_o S_o\right)+\frac{\partial}{\partial\tau}\left(b_o F_o\right)+\frac{b_o}{\phi}\left(F_o\nabla\bullet\vec{u}_t\right)=0 \quad \cdots\cdots \quad \text{(B.30)}$$

$$\frac{\partial}{\partial t}(b_w S_w)+\frac{\partial}{\partial \tau}(b_w F_w)+\frac{b_w}{\phi}(F_w \nabla \bullet \vec{u}_t)=0 \quad \cdots\cdots \quad \text{(B.31)}$$

$$\frac{\partial}{\partial t}(b_g S_g + b_o R_s S_o)+\frac{\partial}{\partial \tau}(b_g F_g + b_o R_s F_o)+\frac{1}{\phi}\nabla \bullet \vec{u}_t (b_g F_g + b_o R_s F_o)=0 \quad \cdots\cdots \quad \text{(B.32)}$$

Then capillary and gravity term is calculated on grid by

$$\frac{\partial}{\partial t}(b_o S_o)+\frac{1}{\phi}\nabla \bullet (b_o \Gamma_o)=0 \quad \cdots\cdots \quad \text{(B.33)}$$

$$\frac{\partial}{\partial t}(b_w S_w)+\frac{1}{\phi}\nabla \bullet (b_w \Gamma_w)=0 \quad \cdots\cdots \quad \text{(B.34)}$$

$$\frac{\partial}{\partial t}(b_g S_g + b_o R_s S_o)+\frac{1}{\phi}\nabla \bullet (b_g \Gamma_g + b_o R_s \Gamma_o)=0 \quad \cdots\cdots \quad \text{(B.35)}$$

APPENDIX C

MATRIX SOLVER

In a forward simulation, history matching and optimization process, the final formulation to find the solution of the system becomes following shape.

$$\mathbf{Ax} = \mathbf{b} \quad \cdots\cdots\cdots\cdots\cdots\cdots\cdots\cdots\cdots\cdots\cdots\cdots\cdots\cdots\cdots\cdots\cdots\cdots \quad (C.1)$$

where **A** is a Jacobian or sensitivity matrix, **x** and **b** are solution and residual vector, respectively. The forward simulation and inverse modeling in high resolution system often takes a large amount of computation time to solve the linear matrix system. Thus the efficient algorithm to solve linear matrix is essential to improve the efficiency of the reservoir management process. Here then we overview the algorithm that used for this study. In addition, the demonstration is made to show the performance of the each algorithm by SPE10 case.

The linear matrix solvers used for this study is listed as follows.

- **AMG1R5(6)** - The first fairly general AMG program. AMG1R5 is described in Ruge and Stuben (Stüben 1999). It was mainly written by Klaus Stuben and John Ruge at the former GMD in Birlinghoven, Germany. It is Fortran77 implementation of the original Ruge/Stuben approach. Convenient with Fortran implementation, however, the matrix needs to be symmetric positive definite because of conjugate gradient based solver.

- **JCG** - Included in ITPACK. Applicable for symmetric positive definite matrix. This is a collected algorithm based on ACM.CALGORITHM APPEARED IN ACM-TRANS. MATH. SOFTWARE, VOL.8, NO. 3,C SEP., 1982, P. 302.
- **BICGSTAB** - Bi-Conjugate Gradient Stabilized solver with preconditioned by incomplete LU decomposition. The implementation of the code is provided by by University of Tennessee and Oak Ridge National Laboratory October 1, 1993. This solver is applicable for general square matrix.
- **MGMRES_ST** - The iterative sparse solver for non-symmetric linear system by Generalized Minimal Residual Method (GMRES). The subroutine is the modified version of the original GMRES algorithm by (Saad 2003). The module specifically use a Galerkin conditioner to derive the MGMRES method with restart function.
- **DGESV** - LAPACK implementation of Gaussian elimination with partial pivoting.
- **GBAND** - Sparse band matrix solver. Implemented by the code provided by Aziz *et al.* in a book (Aziz and Settari 1979). Often used to solve implicit saturation equation matrix along streamline.
- **LSQR** - To solve non-symmetric non-square matrix with an iterative process. It is used only for the history matching purpose.
- **DGETRF** - Direct solver non-symmetric non-square matrix. It is used only for history matching, with Gauss-Newton approach.

The solvers are tested using SPE10 reservoir model. The description is shown in the verification of the simulator in Chapter II. The main purpose here is to evaluate the

efficiency of the solver by conducting first step of the linear system in SPE10. The tested solver is **AMG1R5, JCG, BICGSTAB** and **MGMRES_ST**. The direct solver is not tested due to the limitation of the memory. First, the reduction of the residual is compared as follows.

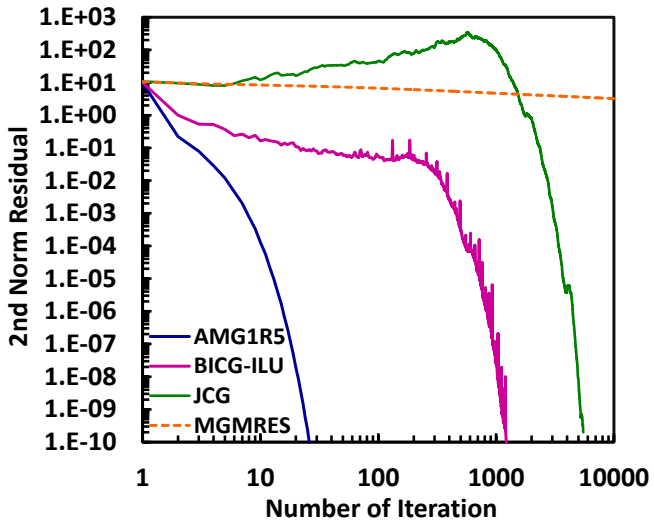

Figure C.1: Convergence behavior of tested solvers: blue by AMG, purple by BICGSTAB, green by JCG and orange by GMRES

As shown in Figure C.1, the best performance is obtained by **AMG1R5.** It needs to be mentioned here that the idea of iteration for AMG type of the solver is not equivalent with other solvers tested here. The comparisons of **JCG** and **BICGSTAB** are also significant. The main difference here could be the difference of the preconditioner used inside the algorithm. The **MGMRES_ST** here could not reduce residual of the vector until the limit of the iteration. It is often seen that GMRES-type solver is efficient for small size of the matrix, however, when the system becomes large and norm of the

matrix increases, the GMRES could not reduce the residual efficiency. In order to evaluate all the algorithm, the computation time is compared in Figure C.2 as follows.

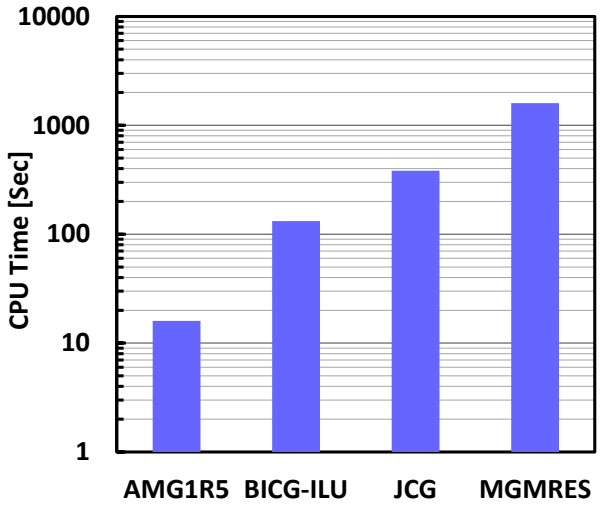

Figure C.2: Comparisons of computation time to solve a pressure matrix of quarter file spot SPE10 case.

Note that the average computation time is taken over 1000 trials through the simulation. The results indicate that the average time to solve the linear matrix by AMG is less than 20 seconds, however, it is going to take over 100 seconds by other solver. Because of these reasons, **AMG1R5** is always used for this study. In some cases, however, due to the condition of the matrix, AMG solver could not handle the linear matrix and return the error. In that case, solver is switched to **BICGSTAB** and continues the simulation.

APPENDIX D

SUMMARY OF SIMULATION VERIFICATION BY 1D CAPILLARY AND GRAVITY DRIVEN FLOW CASES

D-1 Black Oil Model

The series of 1D simulation examples are demonstrated to verify the capillary and gravity flow in 1D space. The simulation is conducted in oil and water wet case with J-function capillarity for black oil and compositional model. All the simulation cases are conducted with closed boundary condition and no viscous force due to sink and source, as shown in Figure D.1. The initial saturation distribution is heterogeneous and non-equilibrium condition. Thus, capillary force tries to equilibrate saturation for horizontal core model. The vertical core model is equilibrated by both capillarity and gravity. The first test case is horizontal model with black oil simulation, shown below.

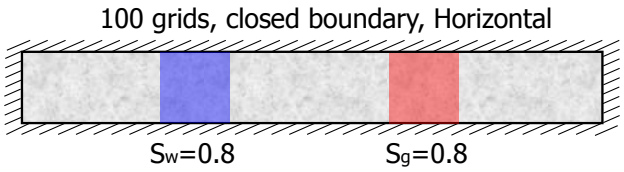

Figure D.1: Schematic 1D horizontal reservoir, capitally and gravity driven equilibrium model by black oil simulation.

The initial saturation distribution is heterogeneous and non-equilibrium condition. Thus, capillary force tries to equilibrate saturation for horizontal core model. The vertical core model is equilibrated by both capillarity and gravity. The first test case is

horizontal model with black oil simulation, the rel-perm and capillary is given by Figure D.2 and D.3, the results are shown in Figure D.4 and D.5, respectively.

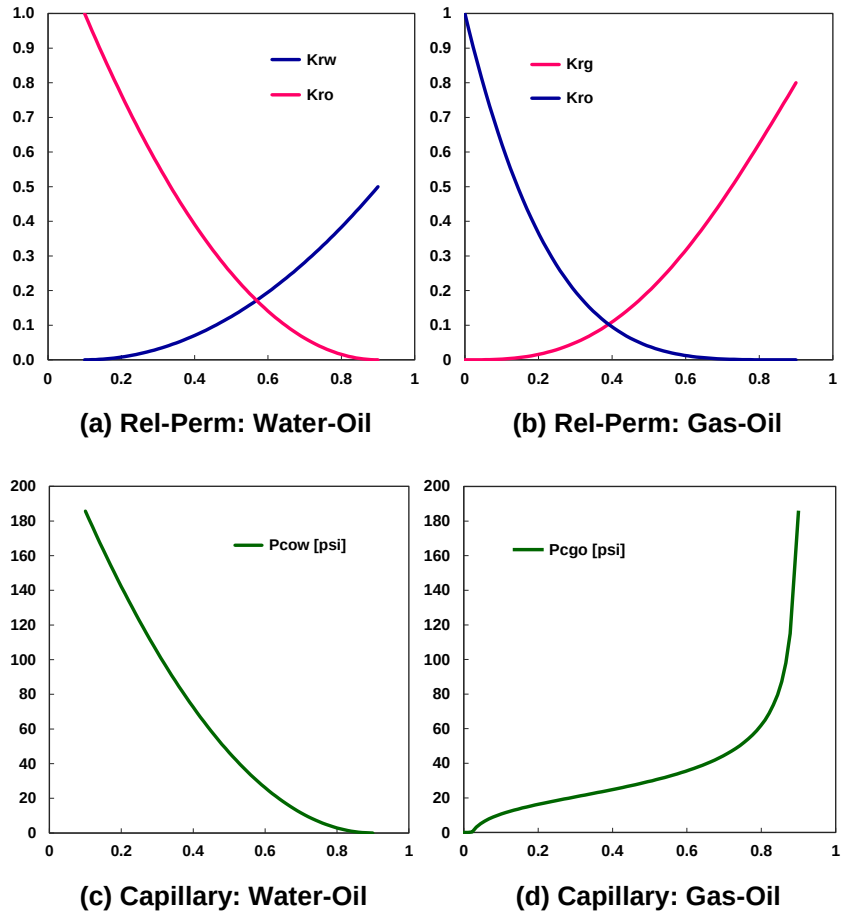

(a) Rel-Perm: Water-Oil (b) Rel-Perm: Gas-Oil

(c) Capillary: Water-Oil (d) Capillary: Gas-Oil

Figure D.2: Relative permeability and capillary pressure curves used for Black oil capillary and gravity equilibrium simulation: Water wet scenario.

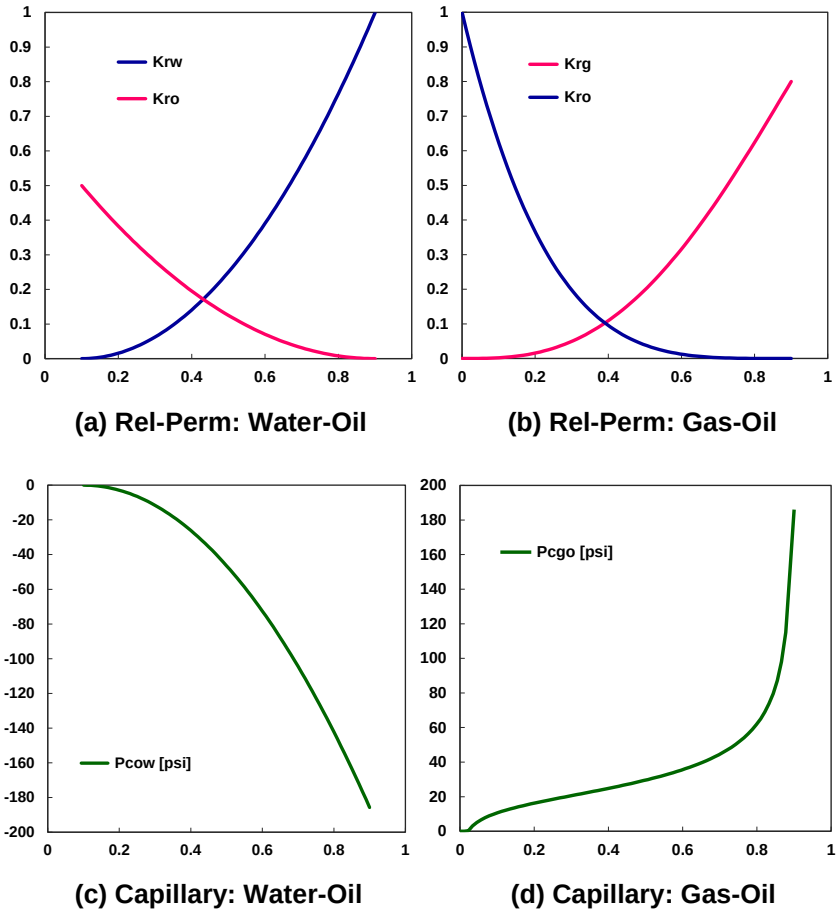

(a) Rel-Perm: Water-Oil

(b) Rel-Perm: Gas-Oil

(c) Capillary: Water-Oil

(d) Capillary: Gas-Oil

Figure D.3: Relative permeability and capillary pressure curves used for Black oil capillary and gravity equilibrium simulation: Oil wet scenario.

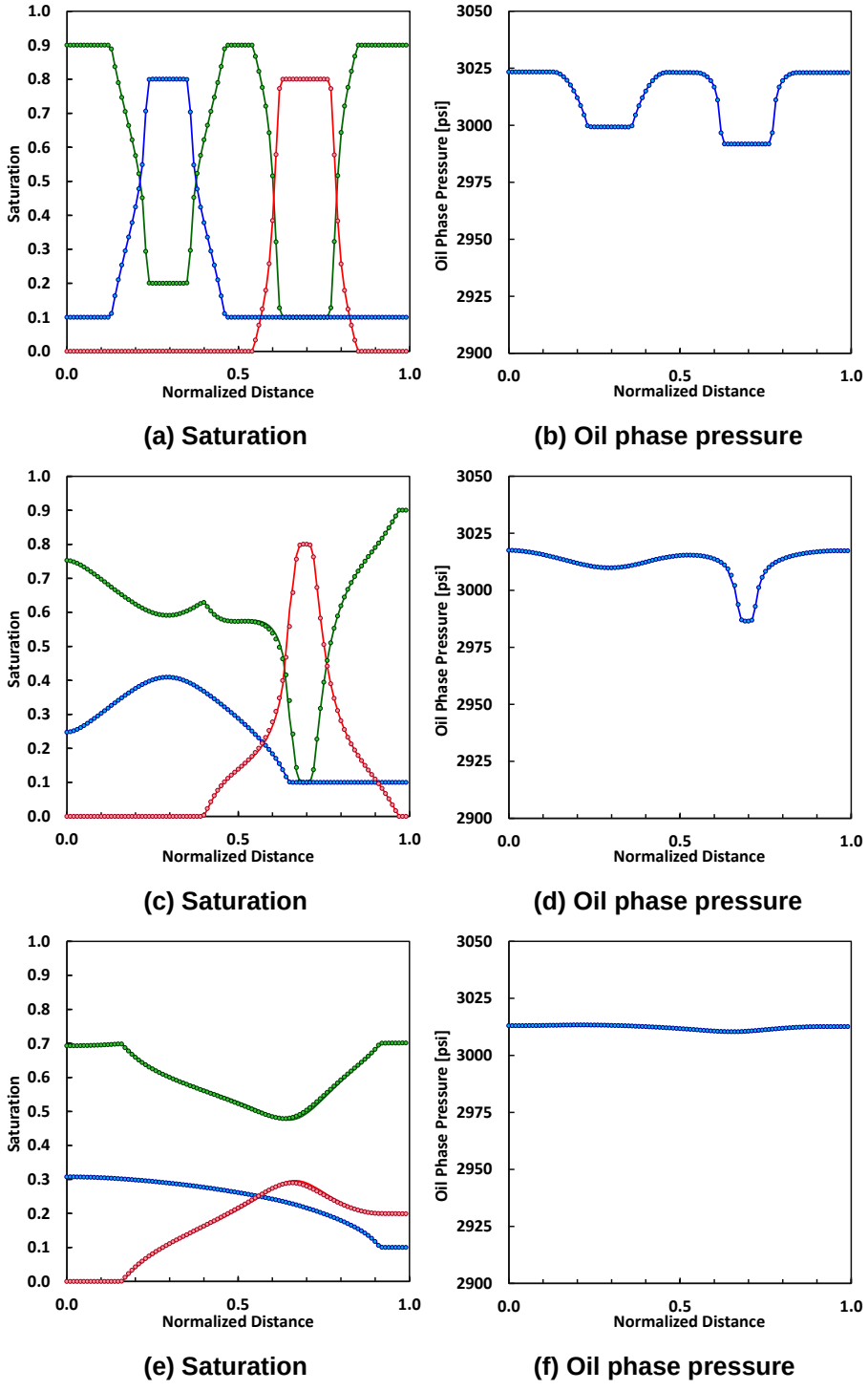

Figure D.4: Saturation (Green=Oil,Blue=Water,Red=Gas) and oil phase pressure result by water wet system. Solid line by developed model and dotted line by commercial simulator (E100). Solution by (a,b) = 1day, (c,d) = 5 days, (e,f) = 10 days, respectively.

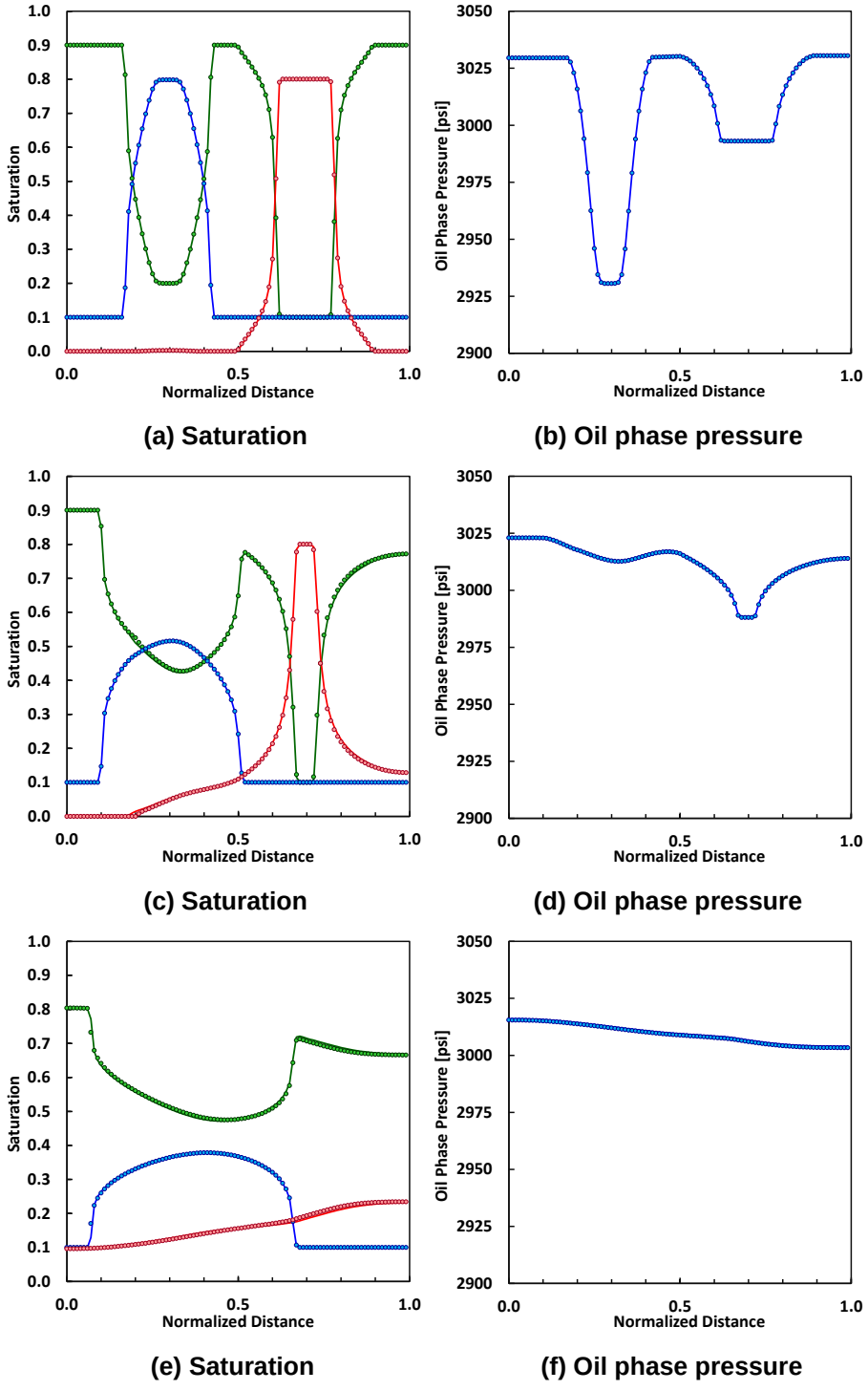

Figure D.5: Saturation (Green=Oil,Blue=Water,Red=Gas) and oil phase pressure result by oil wet system. Solid line by developed model and dotted line by commercial simulator (E100). Solution by (a,b) = 1day, (c,d) = 5 days, (e,f) = 10 days, respectively.

The simulation results with capillary flow in homogeneous field showed good agreement with commercial simulator. It can be seen that the oil wet permeability shows the clear water front in Figure D.5(e) compared with the result with water wet case, in Figure D.4(e). This is because the oil wet case lower the water pressure at high water saturation region. Thus, less dispersion of water saturation in oil wet case in general.

The equilibrium scenario continues to evaluate the case with gravity and capillarity using 1D vertical reservoir. Again the initial condition is given as heterogeneous saturation field, shown in Figure D.6. Because of the difference of the density, water segregate and gas move up towards the top of the reservoir. Use same capillary model shown in Figs D.2-3.

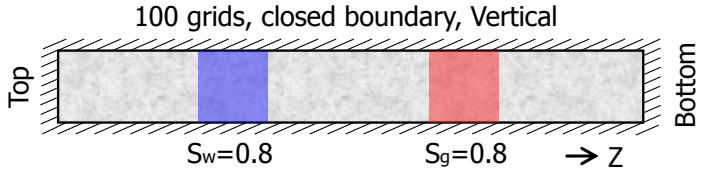

Figure D.6: Schematic 1D vertical reservoir, capitally and gravity driven equilibrium model by black oil simulation.

The results are shown in Figs D.7-8. Again the good agreement is obtained while the difference of saturation distribution with different wettability is less compared with previous case study. The model is tested in heterogeneous permeability media with J-function capillarity and results are shown in Figs. D.9-10.

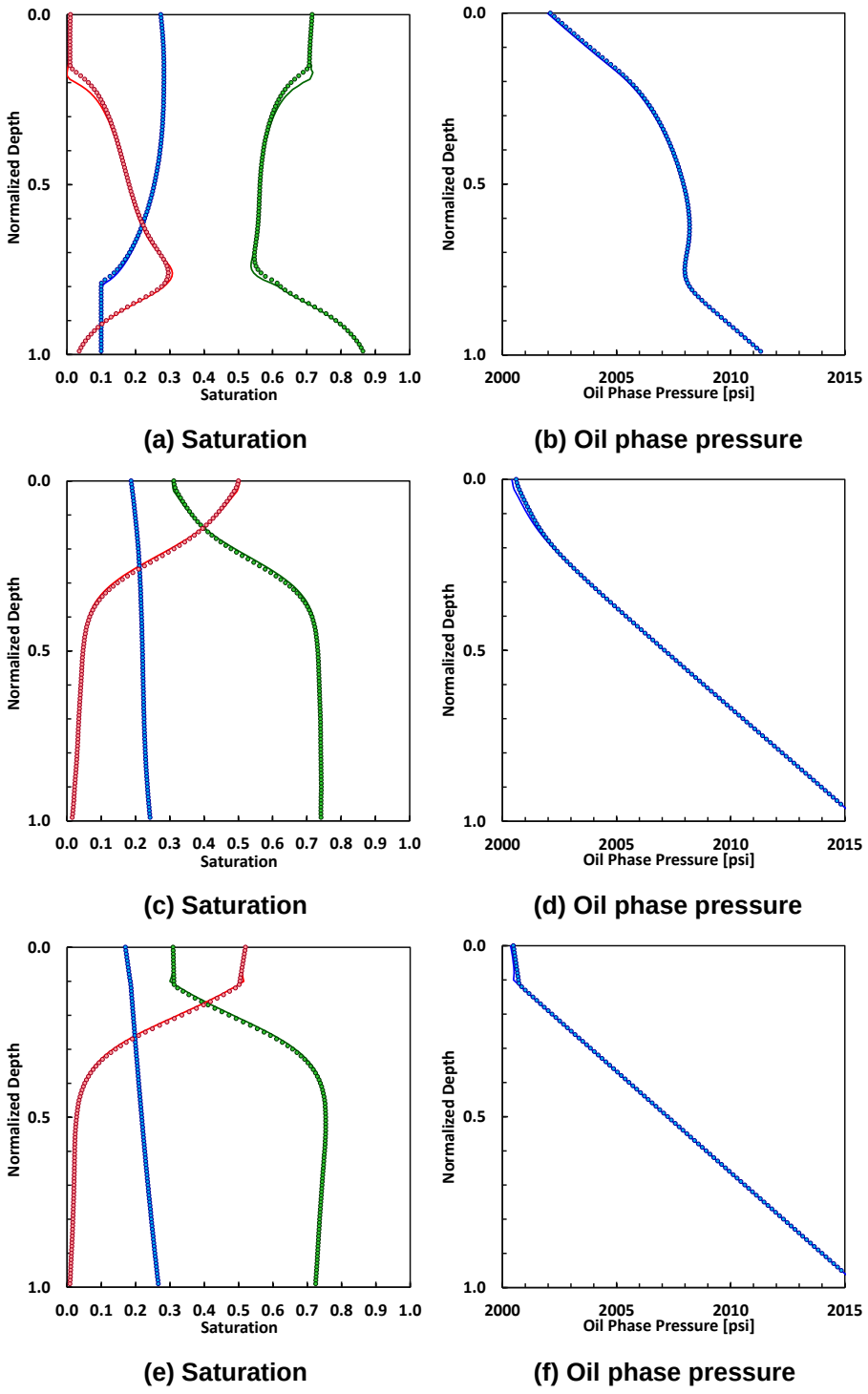

Figure D.7: Saturation (Green=Oil,Blue=Water,Red=Gas) and oil phase pressure result by water wet system with vertical reservoir model. Solution by (a,b) = 1day, (c,d) = 5 days, (e,f) = 10 days, respectively.

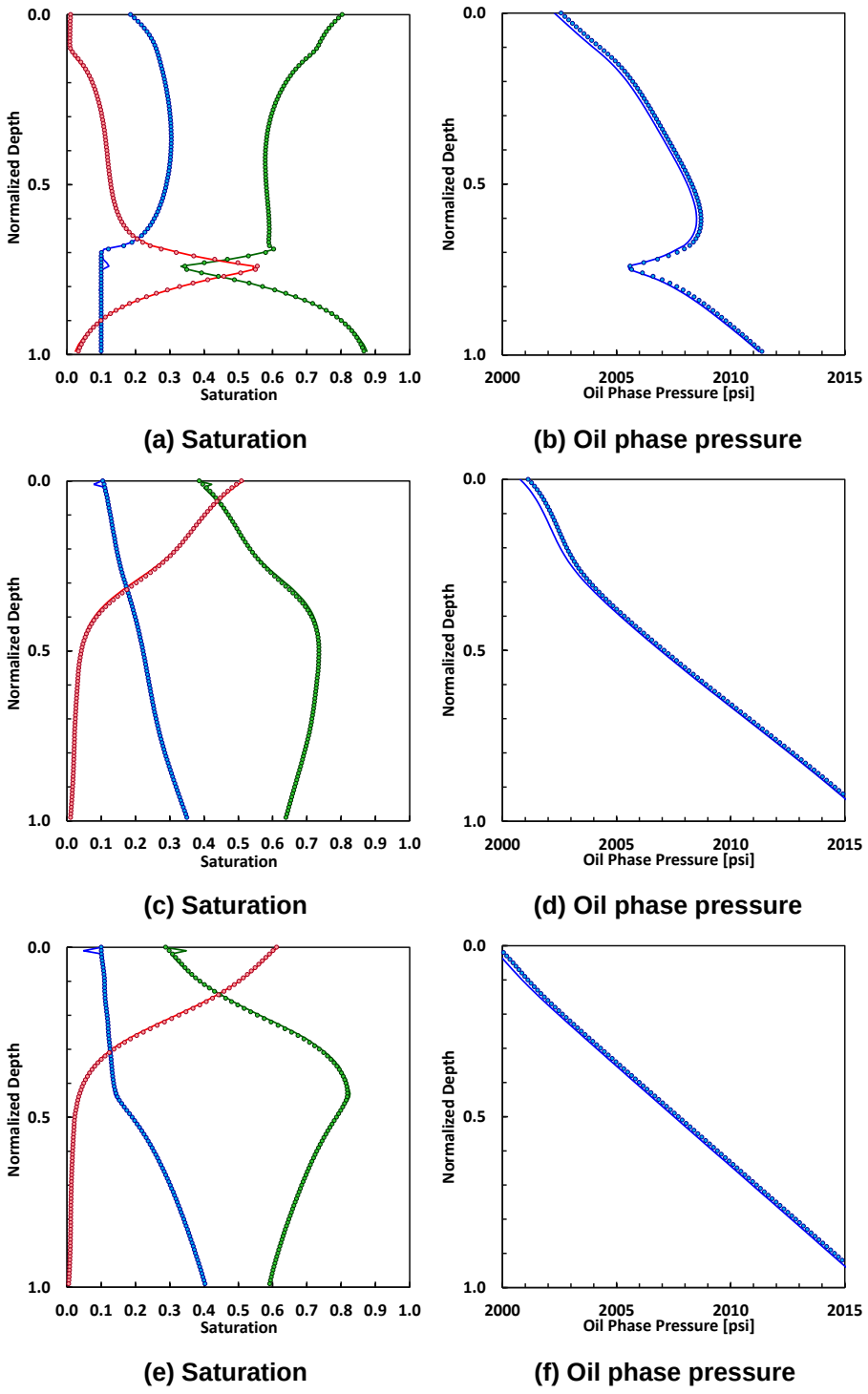

Figure D.8: Saturation (Green=Oil,Blue=Water,Red=Gas) and oil phase pressure result by oil wet system with vertical reservoir model. Solution by (a,b) = 1day, (c,d) = 5 days, (e,f) = 10 days, respectively.

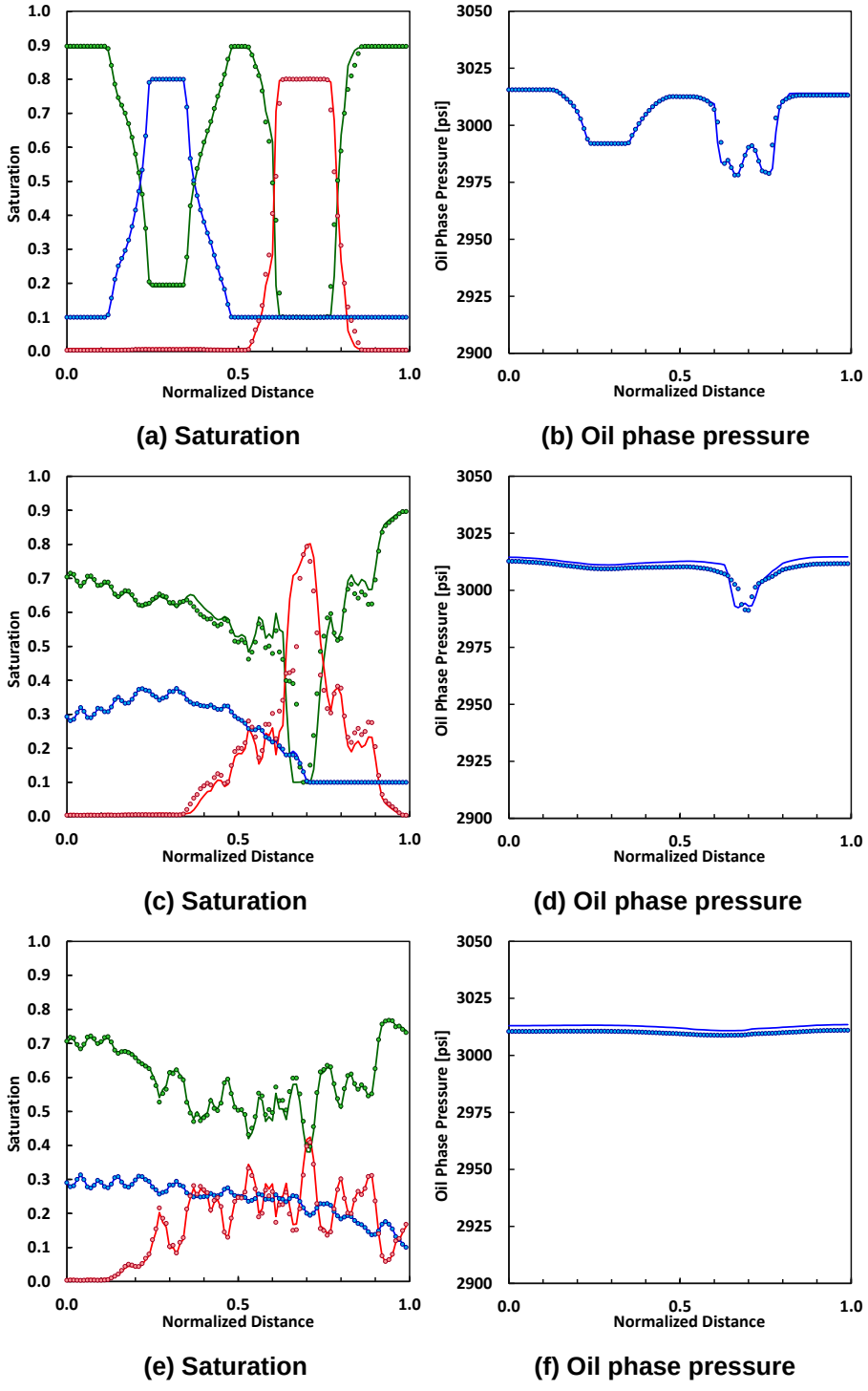

Figure D.9: Saturation (Green=Oil,Blue=Water,Red=Gas) and oil phase pressure result by Jfunction oil wet system. Solid line by developed model and dotted line by commercial simulator (E100). Solution by (a,b) = 1day, (c,d) = 5 days, (e,f) = 10 days, respectively.

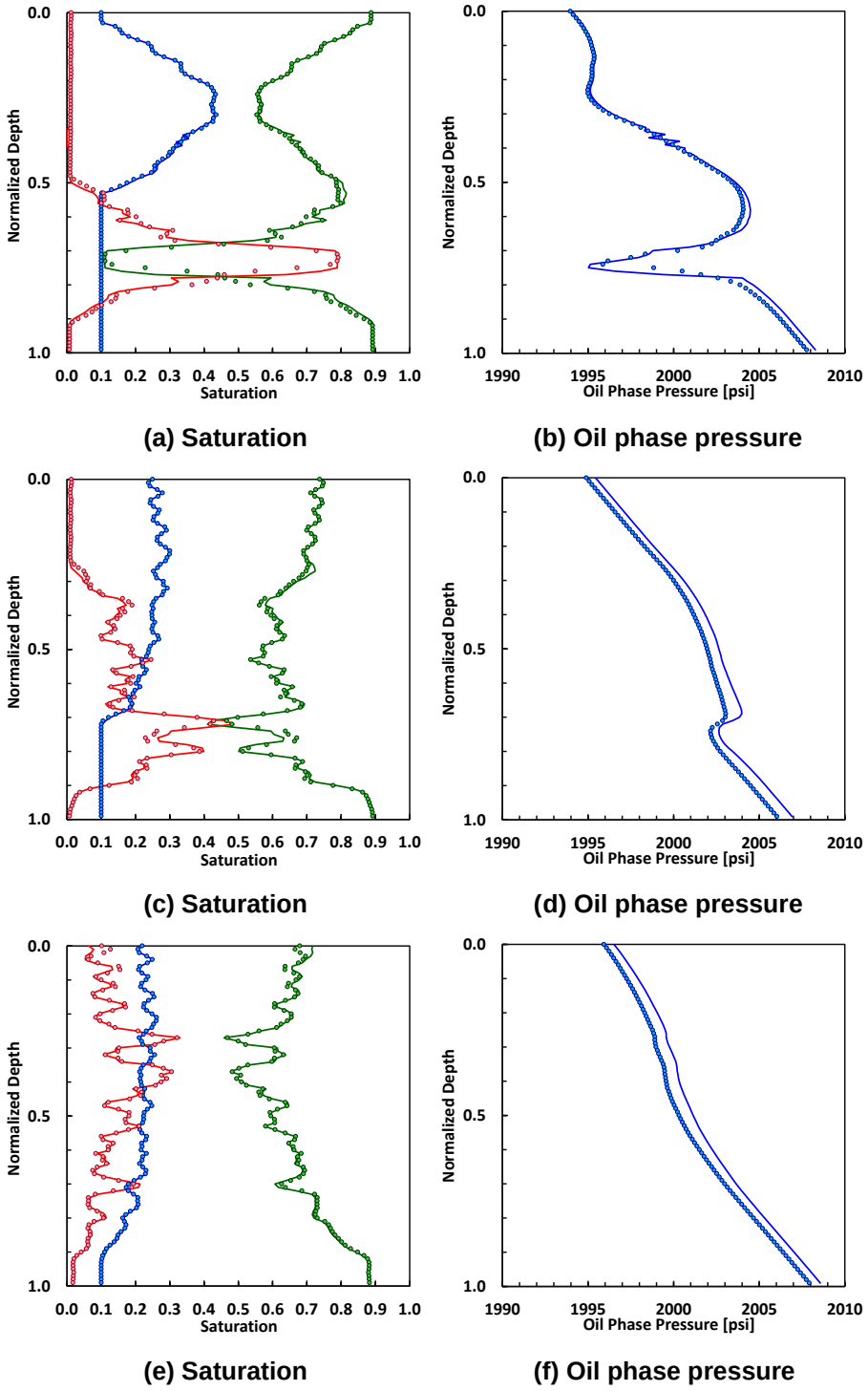

Figure D.10: Saturation (Green=Oil,Blue=Water,Red=Gas) and oil phase pressure result by Jfunction oil wet system with vertical reservoir model. Solution by (a,b) = 1day, (c,d) = 5 days, (e,f) = 10 days, respectively.

D-2 Compositional Model

The equilibrium scenario continues to evaluate the multicomponent flow model. The system is 2 hydrocarbon component and 1 water component. The water saturation is uniformly distributed by 0.25. The hydrocarbon is CO_2 and 10, where higher CO_2 concentration exist at the center as an initial condition with 2000 psi, 212 F°. The following figure shows the schematic picture of the simulation model.

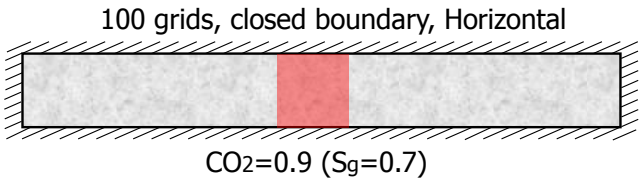

Figure D.11: Relative permeability and capillary pressure curves used for the series of test cases.

Three simulation cases are conducted: water-wet and oil-wet with homogeneous permeability (Figs D.12-13), and J-function water-wet capillary with heterogeneous permeability field (Figure D.14). The simulation case with vertical reservoir model is not shown here because of limitation of initial equilibrium in commercial simulator.

The results show good agreement with commercial simulator (Schlumberger 2012b), except commercial simulator shows lower oil phase pressure distribution. The oil wet and water wet scenario does not shows the clear differences in both pressure and saturation, because of uniform water saturation distribution. For all the senior, the CO_2 will reach boundary within a week.

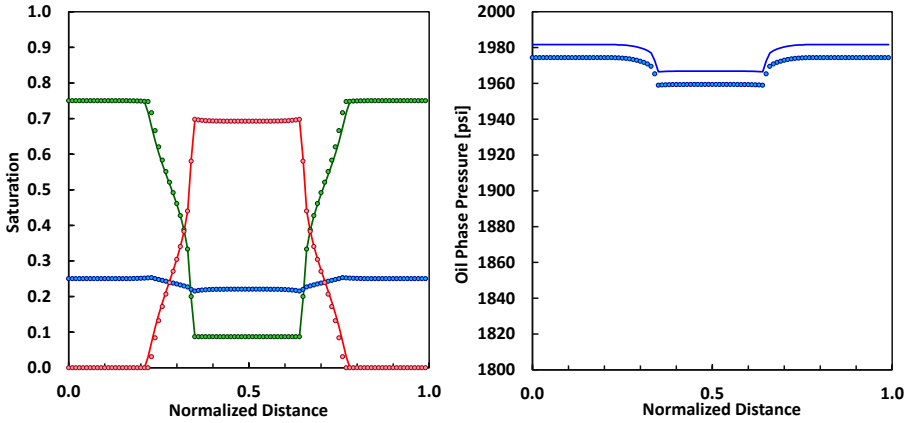

(a) Saturation

(b) Oil phase pressure

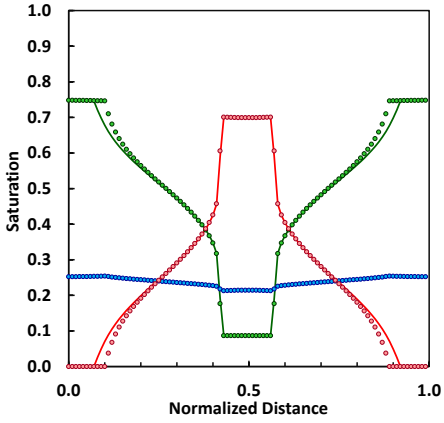

(c) Saturation

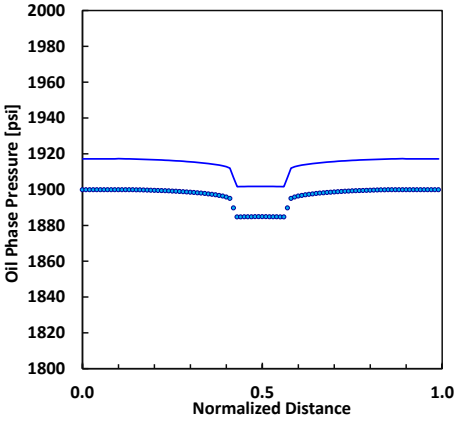

(d) Oil phase pressure

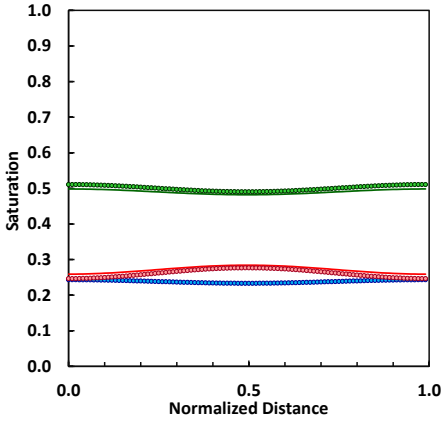

(e) Saturation

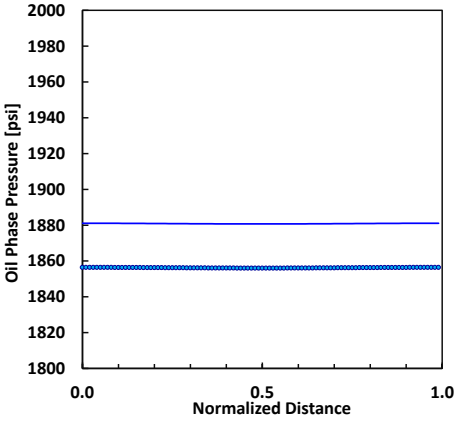

(f) Oil phase pressure

Figure D.12: Saturation (Green=Oil,Blue=Water,Red=Gas) and oil phase pressure result by water wet system. Solid line by developed model and dotted line by commercial simulator (E300). Solution by (a,b) = 1day, (c,d) = 5 days, (e,f) = 10 days, respectively.

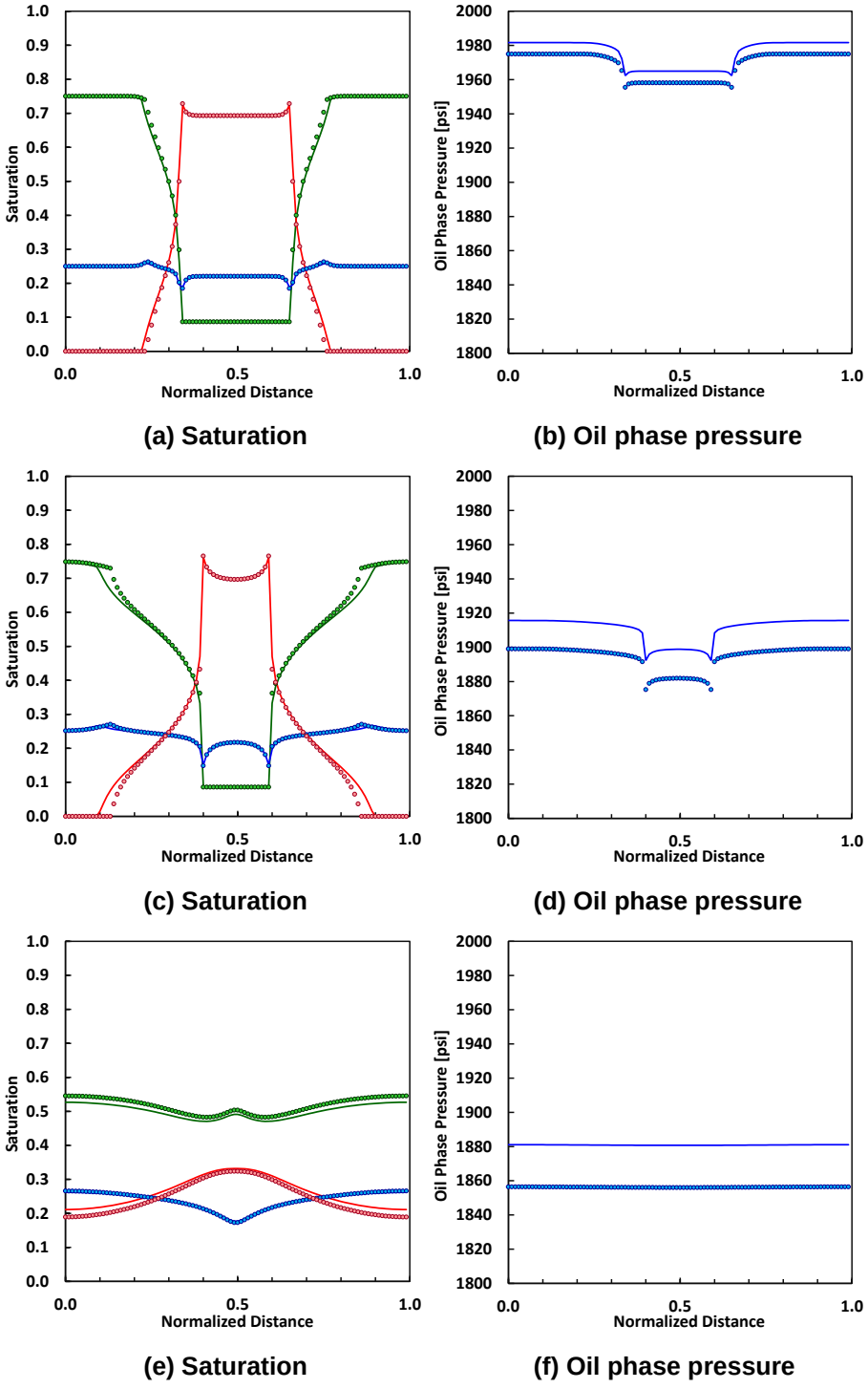

Figure D.13: Saturation (Green=Oil,Blue=Water,Red=Gas) and oil phase pressure result by oil wet system. Solid line by developed model and dotted line by commercial simulator (E300). Solution by (a,b) = 1day, (c,d) = 5 days, (e,f) = 10 days, respectively.

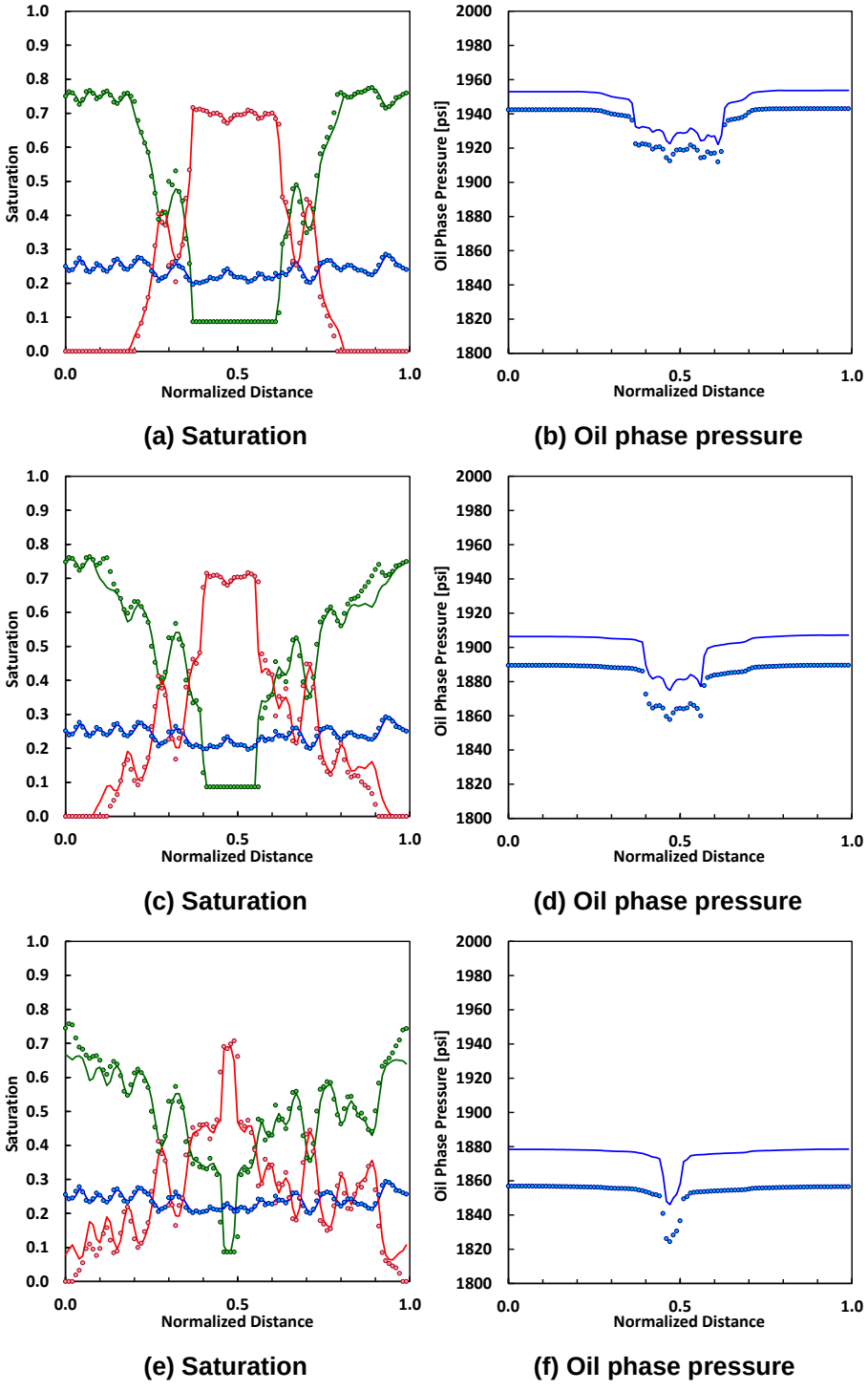

Figure D.14: Saturation (Green=Oil,Blue=Water,Red=Gas) and oil phase pressure result by Jfunction water wet system. Solid line by developed model and dotted line by commercial simulator (E300). Solution by (a,b) = 1day, (c,d) = 5 days, (e,f) = 10 days, respectively.

APPENDIX E

THERMO-EQULIBRIUM CALCULATIONS

E-1 2-Phase Flash Calculation

With flash calculations, we obtain the phase mole fractions and component mole fractions of a system in equilibrium. Phase and component mole fractions are calculated using that the fugacity of each component in each phase is equal in the equilibrium system. Consider a 2-phase (liquid and gas) system comprised of n_c hydrocarbon components. Let n be total moles, n_L, n_V be liquid, vapor phase moles, n_i be moles of component i, and n_{Li}, n_{Vi}, be moles of each phase and component i, we get the mole conservation equations as follows:

$$\sum_{i=1}^{n_c} n_i = n \quad \cdots\cdots \quad \text{(E.1)}$$

$$n_L + n_V = n \quad \cdots\cdots \quad \text{(E.2)}$$

$$\sum_{i=1}^{n_c} n_{ki} = n_k \,, k = L,V \quad \cdots\cdots \quad \text{(E.3)}$$

$$n_i = n_{Li} + n_{Vi} \quad \cdots\cdots \quad \text{(E.4)}$$

Next, consider the equations above in terms of fractions. We express as follows global mole fraction z_i, component mole fractions of gas, liquid y_{io}, y_{ig}, and phase mole fractions L, V.

$$z_i = n_i / n \quad \cdots\cdots \quad \text{(E.5)}$$

$$L = n_L / n \quad \cdots\cdots \quad \text{(E.6)}$$

$$V = n_V / n \quad \cdots\cdots \quad \text{(E.7)}$$

$$y_{io} = n_{Li} / n_L = n_{Li} / nL \quad \cdots\cdots \quad \text{(E.8)}$$

$$y_{ig} = n_{Vi} / n_V = n_{Vi} / nV \quad \cdots\cdots \quad \text{(E.9)}$$

The mass conservation law is stated in terms of fractions as follows:

$$\sum_{i=1}^{n_c} z_i = 1 \quad \cdots\cdots \quad \text{(E.10)}$$

$$\sum_{i=1}^{n_c} y_{ij} = 1, \quad j = o, g \quad \cdots\cdots \quad \text{(E.11)}$$

$$L + V = 1 \quad \cdots\cdots \quad \text{(E.12)}$$

$$Ly_{io} + Vy_{ig} = z_i \quad \cdots\cdots \quad \text{(E.13)}$$

In this phase equilibrium model, we assume the water phase as a constant and no component exchange between oil and gas phase.

$$\begin{aligned} &W = const, \\ &y_{n_c,w} = 0, y_{n_c+1,w} = 1 \end{aligned} \quad \cdots\cdots \quad \text{(E.14)}$$

For flash calculations for two-phase systems, the equilibrium ratio of each component is estimated. The Wilson's empirical equation is used to estimate initial values of equilibrium ratios K_{ig}. At the beginning of the flash calculation term, the initial values of phase compositions, y_{io}, y_{ig} are unknown parameters, so some sort of initial guess of

phase compositions be made. The Wilson's equation is used to estimate equilibrium K-values.

$$K_{ig} = \frac{p_{ci}}{p}\exp\left\{5.37(1+\omega_i)\left(1-\frac{T_{ci}}{T}\right)\right\}, \quad K_{ig} = \frac{y_{ig}}{y_{io}} \quad \cdots\cdots\cdots\cdots\cdots\cdots \quad \text{(E.15)}$$

From estimated or updated equilibrium ratios K_{ig}, we can calculate phase mole fractions, V, from material balance. Eliminating L and y_{ig} from Eqs. E.11, E.12 and E.13, we get

$$y_{io} = \frac{z_i}{1-V+VK_{ig}} \quad \cdots\cdots\cdots\cdots\cdots\cdots\cdots\cdots\cdots\cdots\cdots\cdots\cdots\cdots \quad \text{(E.16)}$$

$$y_{ig} = y_{io}K_{ig} \quad \cdots\cdots\cdots\cdots\cdots\cdots\cdots\cdots\cdots\cdots\cdots\cdots\cdots\cdots \quad \text{(E.17)}$$

From Eqs. E.16 and E.17, we get

$$\sum_{i=1}^{n_c}\left(y_{ig}-y_{io}\right) = \sum_{i=1}^{n_c}\frac{z_i\left(1-K_{ig}\right)}{1-V+VK_{ig}} = 0 \quad \cdots\cdots\cdots\cdots\cdots\cdots\cdots\cdots\cdots\cdots \quad \text{(E.18)}$$

Using Eq. E.18 the phase mole fractions V is calculated with the Newton-Raphson method. Liquid phase mole fraction L can be obtained from Eq. E.13. Using phase mole fractions L, V in Eqs. E.16 and E.17, we can obtain a component mole fraction of each phase y_{io}, y_{ig}. The component mole fractions and phase fractions obtained from this procedure are derived from Wilson's K-value, so we need to calculate the phase potential next. The volume of phase and its compressibility value are necessary to calculate the phase potential with fugacity, so the EOS calculation should be done at next step. The EOS parameters are also required to compute the compressibility factor. The Peng-Robinson EOS is used here. The general equation is given as follows.

$$P = \frac{RT}{V-b} - \frac{a}{(V+m_1 b)(V+m_2 b)} \quad \cdots\cdots \quad \text{(E.19)}$$

where a is the attraction parameter, and b is the repulsive parameter. a accounts for effects of inter-molecule force, and b accounts for effects of molecular volume. Substituting the EOS parameters A_k and B_k obtained from Eq. E.18 and the equation $PV=ZRT$, a cubic equation of the compressibility factor Z (Z-factor) is obtained as follows.

$$Z_k^3 - (1-B_k)Z_k^2 + (A_k - 2B_k - 3B_k^2)Z_k - (A_k B_k - B_k^2 - B_k^3) = 0 \quad \cdots\cdots\cdots \quad \text{(E.20)}$$

Solving the equation above for each phase, Z-factor of liquid and gas phase, Z_L and Z_V are calculated. When 3 real roots are obtained, the maximum root is Z-factor for gas phase and the minimum for liquid phase. We use Cardano's algebraic method to obtain the solutions from cubic equations.

For the phase fugacity, f_i^L and f_i^V, the following expression is used. Z_k values and other parameters have already obtained at EOS procedure.

$$\ln \frac{f_i^k}{y_{ik} p} = -\ln(Z_k - B_k) + (Z_k - 1)B'_{ik} - \frac{A_k}{2\sqrt{2}B_k}(A'_{ik} - B'_{ik})\ln\left[\frac{Z_k + (\sqrt{2}+1)B_k}{Z_k - (\sqrt{2}-1)B_k}\right] \quad \cdots$$

$$\cdots\cdots \quad \text{(E.21)}$$

Once the fugacity values of each phase are obtained, the phase equilibrium is estimated again. For the system in equilibrium conditions, f_i^L and f_i^V for each component should be equal or close enough. When the following conditions are satisfied, iterative flash calculations are terminated.

$$\left|\frac{f_i^L}{f_i^V}-1\right|<\varepsilon\,;\ \forall i \quad \left(\varepsilon=10^{-10}\right) \quad \cdots\cdots\cdots\cdots\cdots\cdots\cdots\cdots\cdots\cdots \quad \text{(E.22)}$$

If Eq. E.22 is not satisfied, the equilibrium ratios K_{ig} is renewed, and this update procedure, which includes K-value update, EOS calculations, and fugacity calculations, is repeated until an equilibrium state is reached. *K* values are renewed as follows.

$$K_{ig}^{new}=\frac{f_i^L}{f_i^V}K_{ig}^{old} \quad \cdots\cdots\cdots\cdots\cdots\cdots\cdots\cdots\cdots\cdots\cdots\cdots\cdots\cdots \quad \text{(E.23)}$$

E-2 3-Phase Flash Calculation

The equilibrium ratio of each component is estimated with changing pressure and total mole fraction after solving Eqs. E.18, 20 and 21. The 3-phase flash is performed based on Li and Nghiem (1986) and Akamine, Tanaka, and Arihara (2009). The values of equilibrium ratios K_{ig} and K_{iw} determines the phase compositions. At the beginning of the flash calculations, the initial values of phase compositions, y_o, y_{ig}, y_{iw} are unknown parameters, and thus the Wilson's equation is used to estimate K-values. From estimated or updated equilibrium ratios K_{ig}, and K_{iw}, phase mole fractions, *V* and *W* are calculated from the conservation equation. The phase mole fractions *V* and *W* are calculated by the Newton-Raphson method and liquid phase mole fraction *L* is obtained from derived *V* and *W*. Assuming no water component in the hydrocarbon phase, $y_{H2O,o}$ =0 and $y_{H2O,g}$ =0, we get $y_{H2O,w}$=z_{H2O}/*W*. After PR-EOS and fugacity calculation with Henry's constant $H_i=H_{iref}e^{v(p-p_{ref})/(RT)}$, we update K_{ig} and K_{iw} and also y_o, y_{ig} by y_{ig}=$y_{io}K_{ig}$ and y_{iw}=$y_{io}K_{iw.}$ The parameters of Henry's constant are obtained using commercial PVT software (WINPROP 2012.10, Computer Modeling Group 2012). The component fugacity in

phase, f_i^L , f_i^V and f_i^W, is calculated and K values are updated as $K_{ig}^{new} = K_{ig}^{old}\left(f_i^L / f_i^V\right)$ and $K_{iw}^{new} = K_{iw}^{old}\left(f_i^L / f_i^W\right)$. This process is continued until differences between component fugacity satisfy a specified tolerance given by $\left|f_i^L / f_i^V - 1\right| < \varepsilon, \left|f_i^L / f_i^W - 1\right| < \varepsilon$.

E-3 Solution of Cubic Equation

There are several methods available to find the solution of the cubic equation. Because a number of times conducted to solve Z-factor from Eq. E.20 the analytical method is preferred for the computational efficacy. The Cardano's method is used and the implementation is discussed here. First, the general cubic equation is described as follows.

$$f(x) = ax^3 + bx^2 + cx + d = 0 \quad \cdots\cdots \quad \text{(E.24)}$$

where $a \neq 0$. Then, change variable in Eq. E.24 as follows.

$$x = y - \frac{b}{3a} \quad \cdots\cdots \quad \text{(E.25)}$$

The division of a to both sides of Eq. E.25 eliminate y^2 from cubic equation and we get

$$y^3 + \frac{-b^2 + 3ac}{3a^2} y + \frac{2b^3}{27a^3} - \frac{bc}{3a^2} + \frac{d}{a} = 0 \quad \cdots\cdots \quad \text{(E.26)}$$

Then simplify the equation as

$$y^3 + 3py + q = 0 \quad \cdots\cdots \quad \text{(E.27)}$$

where p and q are given as

$$3p = \frac{-b^2 + 3ac}{3a^2} \quad \cdots\cdots \quad \text{(E.28)}$$

$$q = \frac{2b^3}{27a^3} - \frac{bc}{3a^2} + \frac{d}{a} \quad \cdots\cdots \quad \text{(E.29)}$$

Then, define $y = u + v$ and rearrange E.29 as follows

$$u^3 + v^3 + 3uv(u+v) + 3p(u+v)q = 0 \quad \cdots\cdots \quad \text{(E.30)}$$

Set $u^3 + v^3 + q = 0$ and we get

$$u^3 + v^3 + q = 0 \quad \cdots\cdots \quad \text{(E.31)}$$

$$u^3 v^3 = -p^3 \quad \cdots\cdots \quad \text{(E.32)}$$

Eqs.E. 31-32 find u^3 and v^3 is a root of the following quadratic equation

$$t^2 + qt - p^3 = 0 \quad \cdots\cdots \quad \text{(E.33)}$$

Eq. E.33 gives following set of solutions

$$A = \frac{-q + \sqrt{a^2 + 4p^2}}{2} \quad \cdots\cdots \quad \text{(E.34)}$$

$$B = \frac{-q - \sqrt{a^2 + 4p^2}}{2} \quad \cdots\cdots \quad \text{(E.35)}$$

Then define the three root of the E.27 as α, β, γ and we get

$$\alpha = \sqrt[3]{A} + \sqrt[3]{B} \quad \cdots\cdots \quad \text{(E.36)}$$

$$\beta = -\frac{1}{2}\left(\sqrt[3]{A} + \sqrt[3]{B}\right) + j\frac{3}{2}\left(\sqrt[3]{A} - \sqrt[3]{B}\right) \quad \cdots\cdots \quad \text{(E.37)}$$

$$\gamma = -\frac{1}{2}\left(\sqrt[3]{A} + \sqrt[3]{B}\right) - j\frac{3}{2}\left(\sqrt[3]{A} - \sqrt[3]{B}\right) \quad \cdots\cdots \quad \text{(E.38)}$$

The solutions derived from Eqs. E.36-38 is a conditional solution of Eqs. E.34-35. The three conditions are: $q^2 + 4p^3 > 0$, $q^2 + 4p^3 < 0$ and $q^2 + 4p^3 = 0$ and solve solution as follows:

If $q^2 + 4p^3 > 0$:

The A and B are real number and α, β and γ is solved by E.36-38. The equation provides one real solution and one pair of complex conjunction.

if $q^2 + 4p^3 < 0$:

The A. B are complex number and thus define $A = re^{+j\theta}$ and $B = re^{-j\theta}$, then

$$r = \sqrt{-p^3} \quad \cdots\cdots \quad \text{(E.39)}$$

$$\tan\vartheta = \frac{\sqrt{-q^2 - 4p^3}}{-q} \quad \cdots\cdots \quad \text{(E.40)}$$

$$\cos\vartheta = \frac{q}{2p\sqrt{-p}} \quad \cdots\cdots \quad \text{(E.41)}$$

And we get

$$\alpha = \sqrt{-p}\,2\cos\left(\frac{\vartheta}{3}\right) \quad \cdots\cdots \quad \text{(E.42)}$$

$$\beta = \sqrt{-p}\,2\cos\left(\frac{\vartheta - 2\pi}{3}\right) \quad \cdots\cdots \quad \text{(E.43)}$$

$$\gamma = \sqrt{-p}\,2\cos\left(\frac{\vartheta + 4\pi}{3}\right) \quad \cdots\cdots \quad \text{(E.44)}$$

if $q^2 + 4p^3 = 0$:

This case the $A = B$ and finds solution as $\beta = \gamma$ and α. If $p = 0$, the solution is not defined and better return 1.0 to avoid further issue.

E-4 Phase Stability Analysis

As phases of the compositional model appear and disappear depending on temperature, pressure, composition, etc., the phase criteria method is important. The phase stability analysis is used for phase criteria in this study, especially to avoid the number of flash calculation along streamline. The phase stability analysis determines the number of phases in a system by analyzing the stability of the system on the basis that the system is in phase equilibrium if the multicomponent system at a certain pressure and temperature shows such phase compositions that Gibbs free energy of liquid and gas phases becomes minimum(Baker, Pierce, and Luks 1982, Firoozabadi and Pan 2002). The stability calculation process is described here for Peng-Robinson EOS. The stable satisfies X_i obtained from Eq. E.45 satisfies Eq. E.46 as

$$\ln X_i + \ln \varphi_i(x_i) - \ln z_i - \ln \varphi_i(z_i) = 0 \quad \cdots\cdots \quad \text{(E.45)}$$

$$\sum_{i=1}^{n_c} X_i < 1 \quad \cdots\cdots \quad \text{(E.46)}$$

z_i is the system's global mole fraction. Component mole fractions of the liquid phase are used for initial values of z_i, and mole fractions of the newly generated gas phase are given to x_i. φ_i is fugacity coefficient. Eq. E.45 is solved for X_i by the sequential substitution method. An initial estimate of X_i is set with an equilibrium constant K_{gi} that is obtained from Wilson's empirical equation, Eq. E.14, as follows:

$$X_i = K_{gi} z_i \quad \cdots\cdots \quad \text{(E.47)}$$

$$x_i = \frac{X_i}{\sum_{j=1}^{n_c} X_j} \quad \cdots\cdots \quad \text{(E.48)}$$

With this initial value, X_i and x_i are renewed until the equation is satisfied. The X_i is updated with the following Eq. E.49. Also, x_i is updated with Eq. E.48.

$$X_i = \exp\left[\left(\ln z_i + \ln \varphi_i(z) - \ln \varphi_i(x)\right)\right] \quad \cdots\cdots \quad \text{(E.49)}$$

As we may not achieve X_i convergence, or we may have made an incorrect assumption even if Eq. E.46 is satisfied, calculations are repeated with the same initial value after altering the gas and liquid phases.

$$X_i = \frac{z_i}{K_i} \quad \cdots\cdots \quad \text{(E.50)}$$

If solution of X_i could not find by Eq. E.45, or if X_i satisfies Eq. E.46, the system is considered as stable and a single-phase state. On the other hand, if Eq. E.46 is not satisfied, the system is considered as unstable, and a two-phase state. In this case, the equilibrium constant K_{gi} is given as follows:

$$K_{gi} = \frac{z_i}{x_i} \quad \cdots\cdots \quad \text{(E.51)}$$

Figure E.1 shows a flow chart for the phase stability analysis. If the phase stability analysis infers a single phase, we need to decide whether the phase is liquid or vapor. Phase determination is performed using the parameters of Peng-Robinson EOS, *A* and *B*,

and compressibility factor, *z*. Figure E.2 illustrates the phase determination criteria with Peng-Robinson EOS.

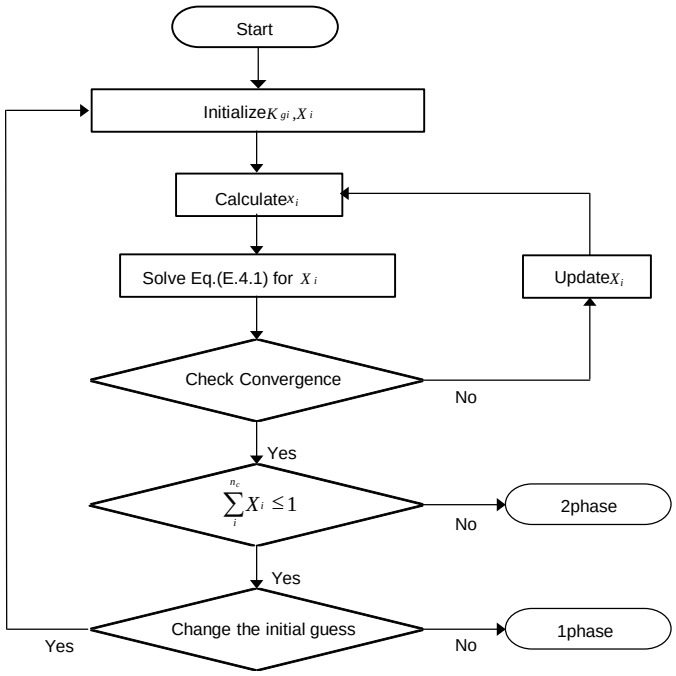

Figure E.1: A flow diagram of phase stability analysis.

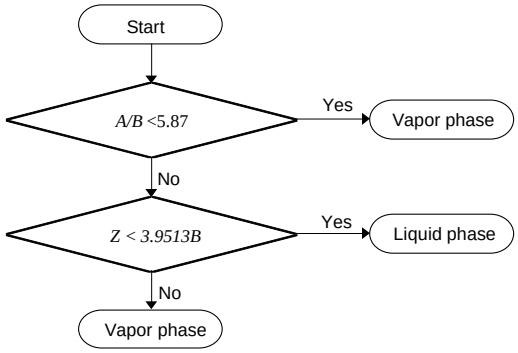

Figure E.2: Phase determination with Peng-Robinson EOS.

APPENDIX F

PVT AND ROCK TABLE

F-1 Black Oil PVT Data

The following PVT tables are given for 3phase black oil simulation. Figure F.1 shows the formation volume factor and viscosity of oil phase with variable bubble point pressure condition due to solution GOR, which is shown in Figure F.2.

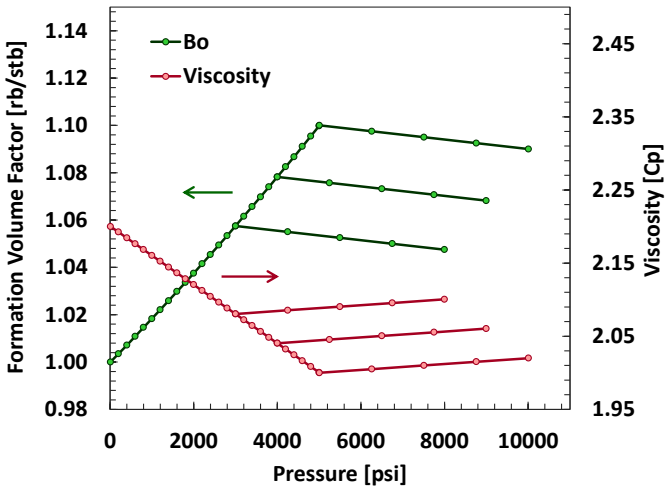

Figure F.1: Formation volume factor and viscosity for oil phase.

The oil property shown in Figure F.1 and F.2 is used by the simulation with gas phase. Although there is 3 branch of parameter in Figure F.1 and F.2, the branch point changes arbitrary as bubble point pressure changes. For example, if oil phase does not have solution GOR, then formation volume factor is lower than 1.0 calculated by interpolation of extending branch starting from 1.0.

The formation volume factor and viscosity of gas phase is shown in Figure F.3.

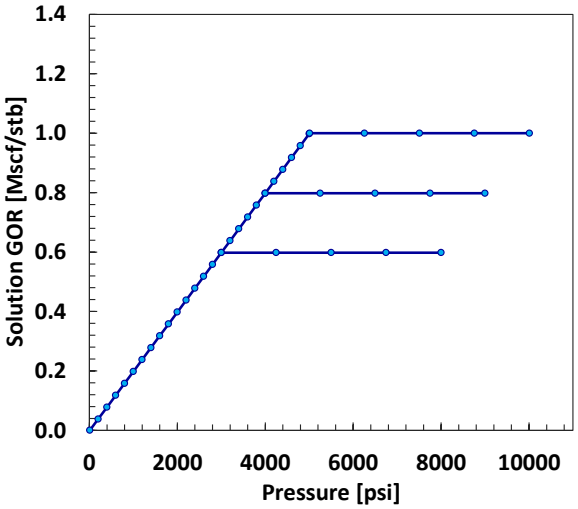

Figure F.2: Pressure vs. solution GOR for oil phase.

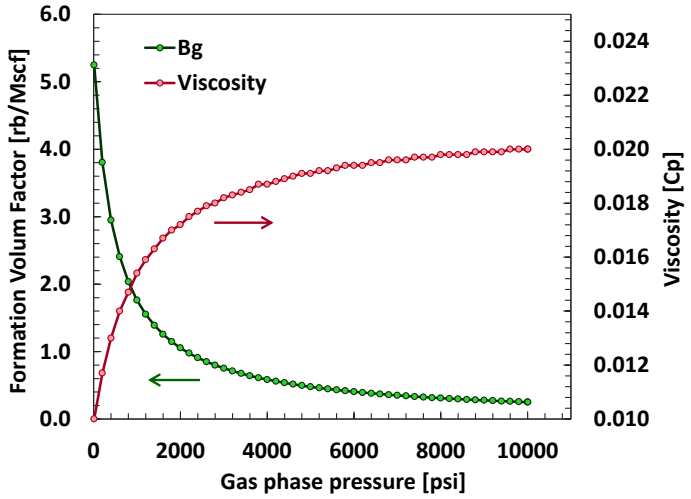

Figure F.3: Formation volume factor and viscosity for gas phase.

F-2 Compositional Model

In a compositional simulation run, the fluid PVT is calculated by Equation-of-State based on parameters assigned by each component. Through the study here, maximum 7 component is used. All the parameters used for these component is shown below.

Table F.1: Parameters used for equation of state

Component Name	Critical Pressure [psi]	Critical Temperature [R]	Critical Volume [cft/lb-mol]	Molecular Weight [g]	Acentric Factor
C1	667.78	343.08	1.5994	16.04	0.012
C3	616.35	665.64	3.2114	44.10	0.1524
C6	477.03	913.50	5.4271	86.18	0.275
C10	367.55	1119.78	8.40538	134.0	0.443774
C15	268.20	1293.48	12.684	206.0	0.651235
C20	211.03	1409.22	16.846	275.0	0.816053
CO2	1069.87	547.56	1.5058	44.01	0.225

Table F.2: Binary coefficient parameters used for equation of state

Name	C1	C3	C6	C15	C20	CO2
C1	0.000					
C3	0.000	0.000				
C6	0.000	0.000	0.000			
C6	0.000	0.000	0.000	0.000		
C15	0.050	0.050	0.000	0.000	0.000	
C20	0.050	0.124	0.025	0.000	0.000	0.000
CO2	0.103	0.135	0.150	0.150	0.150	0.150

F-3 Rock Table

We use relative permeability and capillary pressures following Corey and Ferreira (Corey 1954, Ferreira and Descant 1986) respectively. These models describe the relative-permeability and capillary pressures as a function of saturation, porosity and permeability of each grid.

$$p_c = \sigma \cdot J(S) \cdot \sqrt{\phi k^{-1}} \quad \cdots\cdots \quad (F.1)$$

$$J(S_w) = c_{pc} \begin{cases} (S_{wn} - S_w)^{n_{pc}} & S_{wr} \le S_w \le S_{wn} \le 1 - S_{or} \\ -(S_w - S_{wn})^{n_{pc}} & S_{wn} \le S_w \le 1 - S_{or} \end{cases} \quad \cdots\cdots \quad (F.2)$$

$$J(S_g) = A\left(\frac{S_g - S_{gi}}{1 - S_{or} - S_{gi}}\right)^{-n_A} - B\left(\frac{1 - S_{or} - S_g}{1 - S_{or} - S_{gi}}\right)^{-n_B} + C \quad \cdots\cdots \quad (F.3)$$

The capillary pressure for water/oil and gas/oil is dependent upon the Leverett J-function (Leverett 1941) as shown in Eq. F.1. The capillary pressure is first calculated by grid block saturation as shown in Eqs. F.2 and 3 or Figs. 4-5, then augmented by grid porosity and permeability. Eq. F. 2 is used to find capillary pressure between water/oil. The gas-oil capillary pressure is calculated using Eq. F.3. The parameter for the surface tension is assumed to be a constant and homogeneous. The relative permeability of oil and water phase is calculated by Corey's model as

$$k_{rw} = k_{rw}(S_{oir})\left(\frac{S_w - S_{wr}}{1 - S_{wr} - S_{or}}\right)^{n_w} \quad \cdots\cdots \quad (F.4)$$

$$k_{row} = k_{ro}(S_{wc})\left(\frac{1 - S_w - S_{or}}{1 - S_{wr} - S_{or}}\right)^{n_o} \quad \cdots\cdots \quad (F.5)$$

We use gas-oil relative permeability as

$$k_{rg} = \left(1 - \frac{S_o - S_{or}}{S_m - S_{or}}\right)^{nc} \left(1 - \left(\frac{S_o - S_{or}}{1 - S_{or}}\right)^{nc}\right), \quad k_{rog} = \left(\frac{S_o - S_{or}}{1 - S_{or}}\right)^{2*nc} \quad \cdots\cdots\cdots\cdots\cdots\cdots \quad \text{(F.6)}$$

The oil phase relative permeability, k_{ro}, for three phase flow is calculated using Stone's 2nd model. The 3 different wettability cases are prepared and used through the study. The Table F.3 and F.4 shows the 3 wettability cases and coefficient for relative permeability and capillary curve.

Use of Table F.3 and F.4 provide 9 cases of wettability scenario for both oil-water and gas-water property. The following Figs. F.4-5 shows the oil-water properties for both relative permeability and capillary by oil, water and mixed wet.

Table F.3: Parameters used to define Relperm and default capillary curve – Functions and parameters

Simulation Case	Capillary Equation	k_{rom},k_{rwm},k_{rgm}	n_w/n_g, n_o
Water Wet Case 1	Wat(10),Gas(11)	1.0,0.5,0.8	2
Water Wet Case 2	Wat(10),Gas(11)	1.0,0.5,0.8	4
Water Wet Case 3	Wat(10),Gas(11)	1.0,0.5,0.8	8
Mixed Wet Case 1	Wat(11),Gas(11)	1.0,1.0,1.0	2
Mixed Wet Case 2	Wat(11),Gas(11)	1.0,1.0,1.0	4
Mixed Wet Case 3	Wat(11),Gas(11)	1.0,1.0,1.0	8
Oil Wet Case 1	Wat(10),Gas(11)	0.5,1.0,0.8	2
Oil Wet Case 2	Wat(10),Gas(11)	0.5,1.0,0.8	4
Oil Wet Case 3	Wat(10),Gas(11)	0.5,1.0,0.8	8

Table F.4: Parameters used to define Relperm and default capillary curve – Exponents				
n_{pca}/n_{pcb} oil-wat	n_{pca}/n_{pcb} oil-gas	Cpc	A,B	C
2	1.0,0.5	1000	2	20
4	0.5,0.25	1500	8	20
8	0.25,0.125	3500	32	20
2	1.0,0.5	-	2	10
4	0.5,0.25	-	8	10
8	0.25,0.125	-	32	10
2	1.0,0.5	-	2	20
4	0.5,0.25	-	8	20
8	0.25,0.125	-	32	20

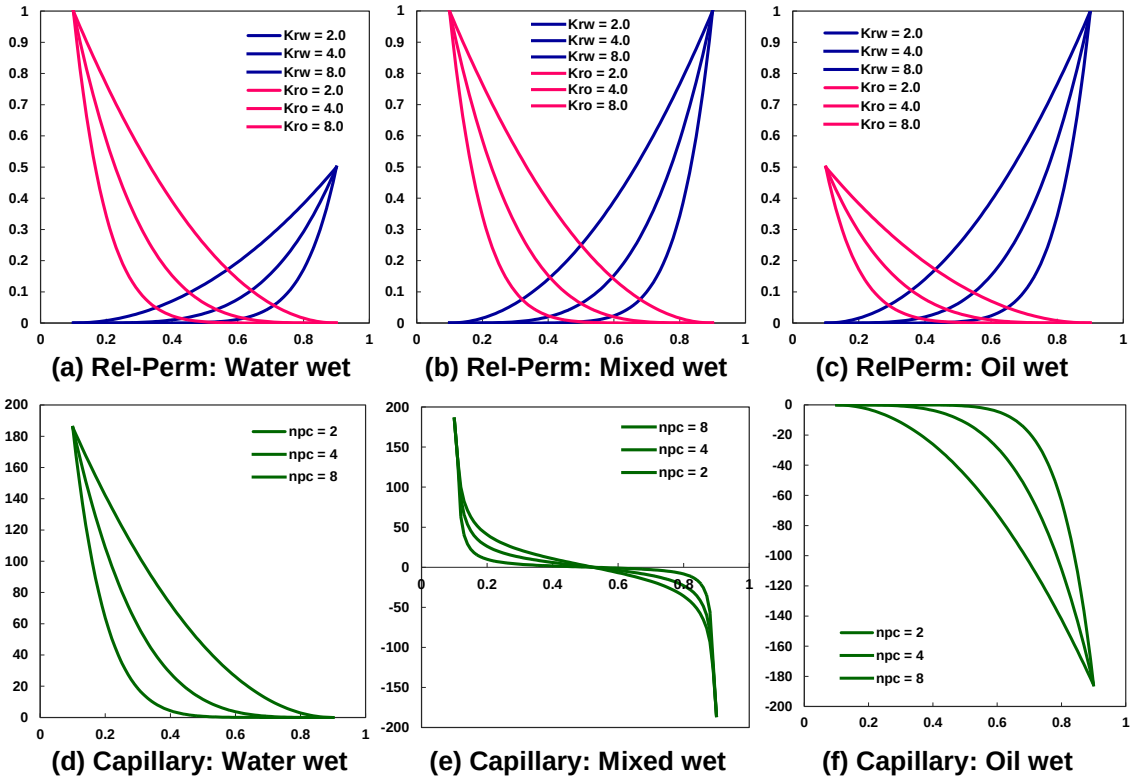

(a) Rel-Perm: Water wet (b) Rel-Perm: Mixed wet (c) RelPerm: Oil wet

(d) Capillary: Water wet (e) Capillary: Mixed wet (f) Capillary: Oil wet

Figure F.4: Relative permeability and capillary pressure curves for oil-water phase (x axis is water phase saturation).

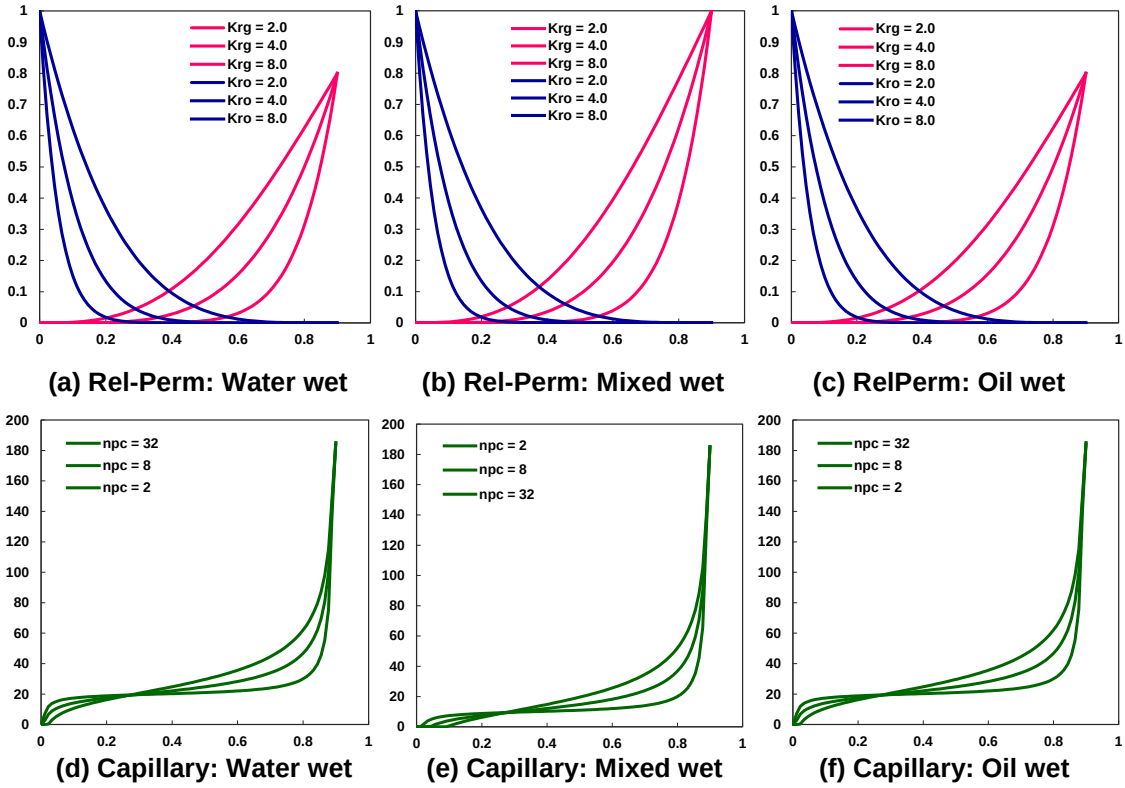

Figure F.5: Relative permeability and capillary pressure curves for oil-gas phase (x axis is gas phase saturation).

F-4 Formulations of PVT and Tock Table and Partial Derivatives

A. 3 Phase Relative Permeability

Oil phase Relative permeability is calculated by Stone's 2nd model as

$$k_{ro} = k_{rocw}\left\{\left(\frac{k_{row}}{k_{rocw}} + k_{rw}\right)\left(\frac{k_{rog}}{k_{rocw}} + k_{rg}\right) - k_{rg} - k_{rw}\right\} \quad \cdots\cdots\cdots\cdots\cdots\cdots \quad (F.7)$$

where,

k_{ro} : oil relative permeability

k_{rg} : gas relative permeability

k_{rw} : water relative permeability

k_{rog} : gas relative permeability to oil phase

k_{row} : water relative permeability to oil phase

k_{rocw} : relative permeability for oil by connate water.

B. Porosity

The porosity of the rock is calculated based on slightly compressible model as

$$\phi = \phi_0 e^{c_r(p-p_0)} \quad \cdots\cdots\cdots\cdots\cdots\cdots\cdots\cdots\cdots\cdots\cdots\cdots\cdots\cdots\cdots\cdots \quad (F.8)$$

where

c_r : rock compressibility [1/psi]

p_0 : reference pressure [psi]

ϕ_0 : reference porosity

The partial difference of the porosity with respect to pressure is calculated as

$$\frac{\partial \phi}{\partial p} = -\frac{1}{\phi} c_r \quad \cdots\cdots \quad (F.9)$$

C. Formation Volume Factor (Black Oil Model)

The formation volume factor of the hydrocarbon phase is given by table input and water by slightly compressible fluid as

$$B_o, B_g = table \quad \cdots\cdots \quad (F.10)$$

$$B_w = B_{w0} e^{c_w (p - p_0)} \quad \cdots\cdots \quad (F.11)$$

The partial difference of the porosity with respect to pressure is calculated as

$$\frac{\partial B_g}{\partial p} = \frac{B_g (p + \delta) + B_g (p)}{\delta} \quad \cdots\cdots \quad (F.12)$$

The same treatment is made for oil phase. For water phase, use same formulation with porosity as

$$\frac{\partial B_w}{\partial p} = -\frac{1}{B_w} c_w \quad \cdots\cdots \quad (F.13)$$

Whenever the input data of fluid properties are given by the table, it is linearly interpolated from the reciprocals formation volume factor, B_α, between data points, rather than the values themselves. This interpolation can improve convergence in addition to the accuracy of the solution. The typical gas formation volume factor is given by following table data.

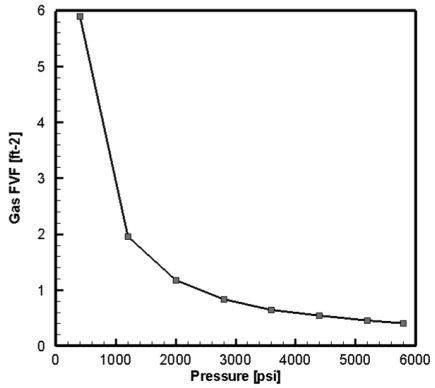

Figure F.6: Gas formation volume factor.

Figs. F.6 and F.7 shows the same formation volume factor derived with linearly or reciprocally interpolated method.

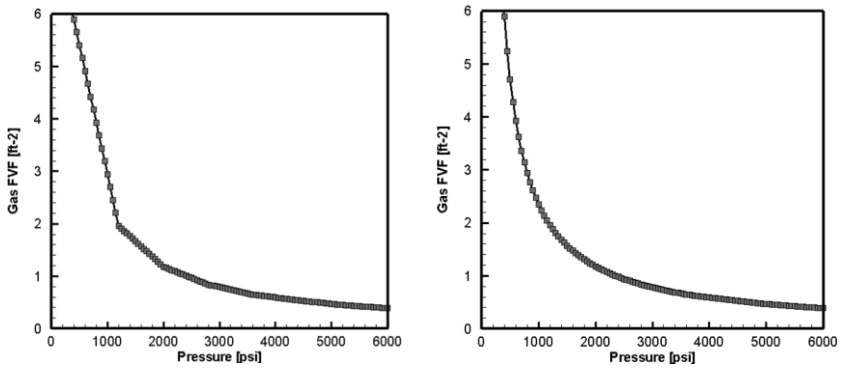

(a) Liner interpolation (b) Linear interpolation of the reciprocals

Figure F.7: Gas formation volume factor by 50 psi interval.

The result of the interpolated formation volume factor shown in Figure F.7 shows the difference and it is clear that linear interpolation of the reciprocals show the smooth results. This smoothness is important for reservoir simulation in two reasons. First, is going to follow the realistic fluid with a small number of the table data. Second, from a

mathematical point of view, this smooth data improves convergence behavior of the Newton Raphson iteration through pressure solution.

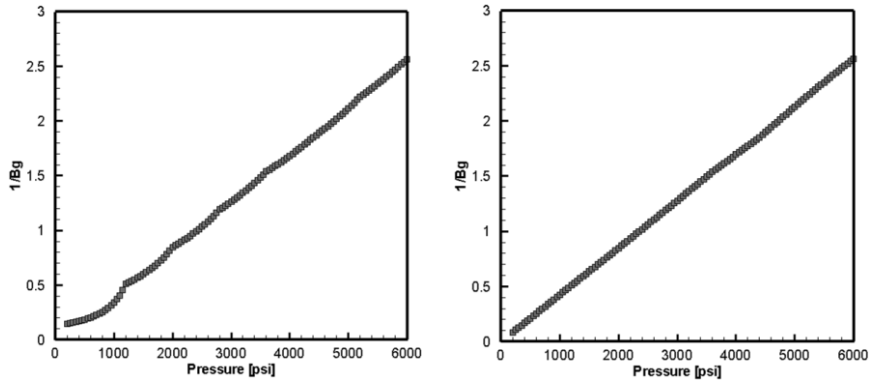

(a) Liner interpolation (b) Linear interpolation of the reciprocals

Figure F.8: Reciprocal of gas formation volume factor.

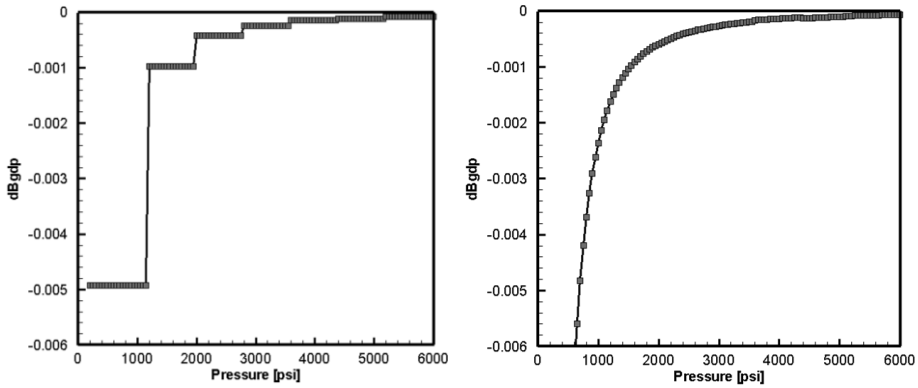

(a) Liner interpolation (b) Linear interpolation of the reciprocals

Figure F.9: Pressure derivatives of gas formation volume factor.

The Figs. F.4.8a and F.4.9a are the result of $1/B_g$ and $dB_g dp$ which was calculated from Figure. F.7a. Alto the result of Figure F.4.8b are the result of $1/B_g$ and $dB_g dp$ derived from Figs. F.7-8 of (b). We can find that the result of (b) in Figs. F.8-9 shows a

smooth curve again while the result of linear interpolated data shows not a smooth one. The compressibility of gas equation can be calculated using $1/B_g$ and $dB_g dp$ as shown in Figure F.10. The result of the Figure 10a is calculated from linear interpolation and Figure F.10b is the result from linear interpolation of the reciprocals.

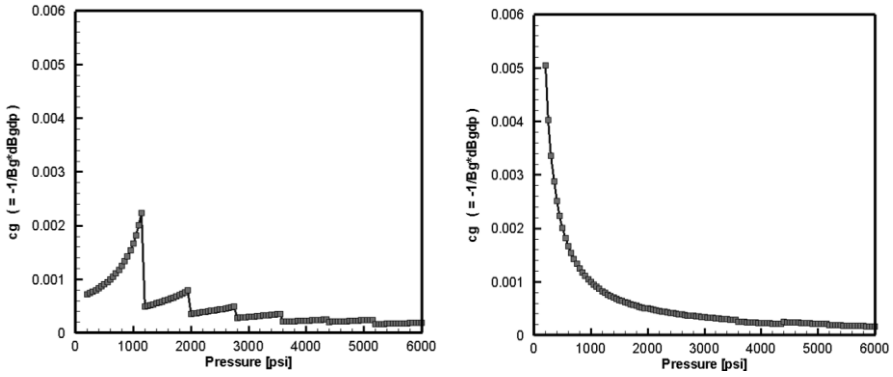

(a) Liner interpolation **(b) Linear interpolation of the reciprocals**

Figure. F.10: Gas compressibility.

The smooth curve of gas compressibility is of importance for accumulation term in pressure equation. Figure F.10a will provide step-like change of the accumulation term. In contrast, as shown in Figure F.10b, interpolation from reciprocals avoids these issues in addition to keep more realistic properties.

D. Molar Density (Compositional Model)

The molar density of the hydrocarbon phase (oil, gas phase) is calculated as follows

$$\rho_j = \frac{p}{z_j RT} \quad \cdots\cdots\cdots\cdots \quad \text{(F.14)}$$

where

ρ_j : molar density of the j phase [lb-mol/ft^3]

z_j : Compressibility factor of j phase ($j = o,g$)

The Z factor is calculated by cubic equation and system pressure (oil phase pressure) is used for oil and gas phase.

The derivative of the molar density in hydrocarbon phase is calculated as follows

$$\frac{\partial \rho_j}{\partial p} = \frac{1}{zRT} - \frac{1}{z^2 RT}\frac{\partial z}{\partial p} \quad \cdots\cdots\cdots\cdots \quad \text{(F.15)}$$

where the derivative of the phase compressibility is calculated as

$$\frac{\partial z}{\partial p} = \frac{\partial z}{\partial A}\frac{\partial A}{\partial p} + \frac{\partial z}{\partial B}\frac{\partial B}{\partial p} \quad \cdots\cdots\cdots\cdots \quad \text{(F.16)}$$

$$\frac{\partial z}{\partial A} = \frac{B - z}{3z^2 - 2(1-B)z + A - 2B - 3B^2} \quad \cdots\cdots\cdots\cdots \quad \text{(F.17)}$$

$$\frac{\partial z}{\partial B} = \frac{-z^2 + z(6B+2) + A - 2B - 3B^2}{3z^2 - 2z(1-B) + A - 2B - 3B^2} \quad \cdots\cdots\cdots\cdots \quad \text{(F.18)}$$

$$\frac{\partial A}{\partial p} = \frac{a}{(RT)^2} \quad \cdots\cdots\cdots\cdots \quad \text{(F.19)}$$

$$\frac{\partial B}{\partial p} = \frac{b}{RT} \quad \cdots\cdots \quad \text{(F.20)}$$

Here the coefficient of *A*, *B*, *a* and *b* are the values derived by cubic EOS in Appendix E. The molar density of the water phase is calculated as follows

$$\rho_{H_2O} = \frac{\rho_{w0}}{453.59}\left(1 + c_w\left(p - p_0\right)\right) \quad \cdots\cdots \quad \text{(F.21)}$$

where

ρ_{w0} : molar density of water at reference condition [lb-mol/ft^3]

When the Henry's coefficient is given and hydrocarbon component dissolves into water phase, the partial mole volume of water and dissolved component is calculated to update molar density of the water phase. First, update partial molar volume of the component is calculated as

$$V_{H_2O} = \frac{y_{H_2O,w}}{\rho_{H_2O}} \quad \cdots\cdots \quad \text{(F.22)}$$

$$V_{sol} = \sum_{i=1}^{n_c} V_i^{\infty} y_{iw} \quad \cdots\cdots \quad \text{(F.23)}$$

where V_i^{∞} is the partial molar volume at infinite dilution, given by constant coefficient. Then the molar volume is updated by

$$\rho_w = \frac{1}{V_{H_2O} + V_{sol}} \quad \cdots\cdots \quad \text{(F.24)}$$

The derivative of the molar density of water with respect to pressure is calculated as follows.

$$\frac{\partial \rho_w}{\partial p} = \frac{\partial}{\partial p}\left(\frac{1}{V_{H_2O} + V_{sol}}\right) = \frac{-1}{\left(V_{H_2O} + V_{sol}\right)^2}\left(V_{sol}\frac{\partial V_{H_2O}}{\partial p} + V_{H_2O}\frac{\partial V_{sol}}{\partial p}\right) \quad \cdots\cdots \quad (F.25)$$

$$\frac{\partial V_{H_2O}}{\partial p} = y_{H_2O}\frac{\partial}{\partial p}\left(\frac{1}{\rho_{H_2O}}\right) = \frac{-y_{H_2O}}{\rho_{H_2O}^2}\frac{\partial \rho_{H_2O}}{\partial p} \quad \cdots\cdots \quad (F.26)$$

$$\frac{\partial V_{sol}}{\partial p} = 0 \quad \cdots\cdots \quad (F.27)$$

$$\frac{\partial \rho_{H_2O}}{\partial p} = \frac{\rho_{w0} c_w}{453.59} \quad \cdots\cdots \quad (F.28)$$

E. Viscosity (Black Oil Model)

The viscosity of the hydrocarbon phase is given by the table and

$$\mu_o, \mu_g = table \quad \cdots\cdots \quad (F.29)$$

The partial difference of the porosity with respect to pressure is calculated as

$$\frac{\partial \mu_g}{\partial p} = \frac{\mu_g(p+\delta) + \mu_g(p)}{\delta} \quad \cdots\cdots \quad (F.30)$$

The same treatment is made for the interpolation of the data, as discussed in formation volume factor. The viscosity of the water phase is calculated based on slightly viscous model as

$$\mu_w = \mu_{w0} e^{c_{\mu_w}(p - p_0)} \quad \cdots\cdots \quad (F.31)$$

where

c_{uw} : water viscosibility [1/psi]

μ_{w0} : reference viscosity

The partial difference of the porosity with respect to pressure is calculated as

$$\frac{\partial \mu_w}{\partial p} = \frac{1}{\mu_w} c_{\mu_w} \quad \cdots\cdots \quad \text{(F.32)}$$

F. Viscosity (Compositional Model)

The same equation is used to calculate the viscosity of the water phase. The viscosity of the hydrocarbon phase is used with Lorentz-Bray-Clark (Lohrenz, Bray, and Clark 1964) and the implementation of their model is discussed here.

For the viscosity of the hydrocarbon phase in low pressure condition, use the experimental equation derived by Steil & Thodos (Stiel and Thodos 1961). Their model uses different equations up to the change of the reduced temperature as

$$\begin{cases} \mu_i \xi_i = 34 \times 10^{-5} T_{ri}^{0.94} & (T_{ri} \le 1.5) \\ \mu_i \xi_i = 17.78 \times 10^{-5} \times \left[4.58 T_{ri} - 1.67\right]^{0.625} & (T_{ri} \ge 1.5) \end{cases} \quad \cdots\cdots \quad \text{(F.33)}$$

where

$$\xi_i = \frac{5.440 \left[T_{ci}\right]^{1/6}}{m w_i \left[P_{ci}\right]^{2/3}} \quad \cdots\cdots \quad \text{(F.34)}$$

$$T_{ri} = \frac{T}{T_{ci}} \quad \cdots\cdots \quad \text{(F.35)}$$

In order to apply to the multiphase multicomponent problem, use experimental equation (Herning and Zipperer 1936) to derive phase viscosity and add correlation by pressure condition, Viscosity by Herning & Zipper's model is given by

$$\mu_j^* = \frac{\sum_{i=1}^{n_c} y_{ij}\mu_i\sqrt{mw_i}}{\sum_{i=1}^{n_c} y_{ij}\sqrt{mw_i}} \quad \cdots\cdots\cdots\cdots \quad (F.36)$$

Then, define reduced molar density as follows.

$$\rho_{rj} = \rho_j \sum_{i=1}^{n_c} y_{ij} V_{ci} mw_i \quad \cdots\cdots\cdots\cdots \quad (F.37)$$

Then, add the correlation up to the reduced density by high pressure and low pressure case. Define high pressure as $\rho_{rj} \le 0.18$ and the phase viscosity is calculated as

$$\mu_j = \mu_j^* + 2.05\frac{\rho_j}{10^4\xi} \quad \cdots\cdots\cdots\cdots \quad (F.38)$$

where

$$\zeta = \frac{5.440\left[\sum_{i=1}^{n_c} y_{ij}T_{ci}\right]^{\frac{1}{6}}}{\left[\sum_{i=1}^{n_c} y_{ij}mw_i\right]^{\frac{1}{2}}\left[\sum_{i=1}^{n_c} y_{ij}P_{ci}\right]^{\frac{2}{3}}} \quad \cdots\cdots\cdots\cdots \quad (F.39)$$

Define low pressure by $\rho_{rj} > 0.18$ and the phase viscosity is calculated as

$$\mu_j = \mu_j^* + \frac{\left[\eta(\rho_{rj})^4 - 10^{-4}\right]}{\zeta} \quad \cdots\cdots\cdots\cdots \quad (F.40)$$

where

$$\eta(\rho_{rj}) = a + b\rho_{rj} + c\rho_{rj}^2 + d\rho_{rj}^3 + e\rho_{rj}^4 \quad \cdots\cdots\cdots\cdots \quad (F.41)$$

where the coefficient is given as a = 0.1023, b = 0.023364, c = 0.058533, d = -0.04075, e = 0.0093324. This value needs to be modified whenever the parameter of the commercial simulator is modified.

Then the partial derivative of the viscosity of the hydrocarbon phase is calculated as follows

If $\rho_{rj} \le 0.18$

$$\frac{\partial \mu_j}{\partial p} = \frac{2.05}{10^4 \zeta} \frac{\partial \rho_j}{\partial p} \quad \cdots\cdots\cdots\cdots \quad \text{(F.42)}$$

If $\rho_{rj} > 0.18$

$$\frac{\partial \mu_j}{\partial p} = \frac{4\eta(\rho_{rj})^3}{\zeta} \frac{\partial \eta(\rho_{rj})}{\partial p} \quad \cdots\cdots\cdots\cdots \quad \text{(F.43)}$$

where

$$\frac{\partial \rho_j}{\partial p} = \frac{\partial \rho_j}{\partial p} \sum_{i=1}^{n_c} y_{ij} V_{ci} m w_i \quad \cdots\cdots\cdots\cdots \quad \text{(F.44)}$$

$$\frac{\partial \eta(\rho_{rj})}{\partial p} = \frac{\partial \rho_j}{\partial p} \left(a + b\rho_{rj} + c\rho_{rj}^2 + d\rho_{rj}^3\right) \quad \cdots\cdots\cdots\cdots \quad \text{(F.45)}$$

where the coefficients are given as a = 0.023364, b = 0.117066, c = 0.122274, d = 0.0373296.3